Mathematical Modelling of Bubble Nucleation in Acoustic Fields

by

Matheus Oliveira de Andrade

A dissertation submitted for

the degree of Doctor of Philosophy

at UCL

Department of Mechanical Engineering

UCL

Torrington Place

London WC1E 7JE

Declaration

I, Matheus Oliveira de Andrade, confirm that the work presented in this thesis is my own. Where information has been derived from other sources, I confirm that this has been indicated in the thesis.

Abstract

Ultrasound-induced bubble activity is a promising phenomenon underlying the non-invasive ablation of soft tissue via histotripsy. Histotripsy is a non-invasive, repeatable and non-ionizing modality of surgery that takes advantage of the bioeffects of ultrasound propagation in attenuating media, employing heat deposition and ultrasound tensile pressures to different extents in triggering the nucleation of bubbles within millimetric volumes of soft tissue. Central to the clinical translation of histotripsy as a surgical modality are the challenges of establishing operating windows in which bubble nucleation takes place in terms of electrical power provided to the transducer, pulse duration, medium temperature, and ultrasound waveforms. The models developed herein aim to aid in the design of effective histotripsy protocols to be employed with current clinical high intensity focused ultrasound (HIFU) systems, as well as the understanding of the fundamental mechanisms that affect bubble formation and activity in soft tissue. While a number of studies have explored the effects of different experimental parameters in histotripsy, a rigorous formulation of the physics of metastable volumes under HIFU sonication is absent from the literature. The main objectives of this thesis are: (i) to evaluate the current understanding of ultrasound bubble nucleation, integrating knowledge from experimental and theoretical sources towards evaluating its limitations and synthesizing new information; (ii) to design and derive models of bubble nucleation in ultrasound pressure and temperature fields that are parameterised and validated against existing experimental evidence in histotripsy; and (iii) to assess the scope, validity and limitations of any models developed herein through quantitative and qualitative comparison of simulations with published experimental evidence.

Contents

List of Figures

List of Tables

List of Symbols

U	Internal energy	
T	Temperature	Liquid (T_l), Vapour (T_v), Critical (T_c), Reduced (T_r), Initial temperature (T_0), Peak temperature (T_{peak})
S	Entropy	
P	Thermodynamic pressure	Liquid (P_l), Vapour (P_v), Critical (P_r), Reduced (P_r), Internal pressure (P'), Nucleation pressure threshold (P_l^N)
V	Volume	
μ	Chemical potential	Liquid (μ_l), Vapour (μ_v)
N	Number of molecules	
G	Gibbs free energy	
σ	Surface tension	Bulk (σ_∞) or Effective (σ_E) surface tension
A	Nucleus surface area	
r	Nucleus radius	
W^*	Critical work of nucleation	
J_{ss}	Steady-state nucleation rate	
J_0	Nucleation rate kinetic factor	
k_B	Boltzmann constant	
m	Molecular mass	

ρ	Density	Liquid (ρ_l), Vapour (ρ_v), Critical (ρ_c),
Δt_N	Mean lifetime of the metastable fluid	
P_l^N	Nucleation pressure threshold	
ζ	Poynting correction factor	
$\Delta\phi_s$	Substrate surface energy variation	
Ψ	Activity factor	
I	Acoustic intensity	
Q_A	Acoustic heating rate	
p	Time-dependent acoustic pressure	
P_{elec}	Electrical power	
c_0	Small-signal speed of sound	
Q_{WS}	Weak shock theory heating rate	
w_p	Perfusion rate	
κ	Thermal conductivity	
C	Specific heat	Note: When used as a constant
β	Non-linearity parameter for acoustic simulations	
$Z(n,t)$	Bubble population distribution	
$C(n,t)$	Equilibrium bubble population distribution	Note: When used as a function of n and t
n	Number of molecules inside a bubble	
Z_n	Distribution of n-sized bubbles	
C_n	Equilibrium distribution of n-sized bubbles	

v	Hydrodynamic advective term
f_n	Arrival transition frequency to size n
g_n	Departure transition frequency from size n
B	Curvature of W^*
Δ^*	Width of the critical region
l_r	Fundamental hydrodynamic length scale
D	Hydrodynamic diffusive coefficient
$\bar{r}$	Average bubble population radius
N_T	Total number of nuclei in a population
η	Viscosity
$\dot{r}$	Bubble wall velocity
$\ddot{r}$	Bubble wall acceleration
ΔH_v	Enthalpy of vaporization
κ	Thermal conductivity
$Y(r,t)$	Normalised distribution of bubbles with respect to equilibrium
χ	Wavenumber for quasi-stationary solutions
τ	Time-lag of nucleation

List of Publications

1. Froghi, Saied, **Matheus Oliveira de Andrade**, Layla Mohammad Hadi, Pierre Gelat, Hassan Rashidi, Alberto Quaglia, Barry Fuller, Nader Saffari, and Brian Davidson. 2023. "Liver Ultrasound Histotripsy: Novel Analysis of the Histotripsy Site Cell Constituents with Implications for Histotripsy Application in Cell Transplantation and Cancer Therapy" Bioengineering 10, no. 2: 276. https://doi.org/10.3390/bioengineering10020276
2. Froghi, Saied, Andrew Hall, Arif Hanafi Bin Jalal, **Matheus Oliveira de Andrade**, Layla Mohammad Hadi, Hassan Rashidi, Pierre Gélat, Nader Saffari, Brian Davidson, and Alberto Quaglia. 2023. "Ultrasound Histotripsy on a Viable Perfused Whole Porcine Liver: Histological Aspects, Including 3D Reconstruction of the Histotripsy Site" Bioengineering 10, no. 3: 278. https://doi.org/10.3390/bioengineering10030278
3. **Matheus O. de Andrade**, Reza Haqshenas, Ki Joo Pahk, Nader Saffari, Mechanisms of nuclei growth in ultrasound bubble nucleation, Ultrasonics Sonochemistry, Volume 88, 2022, 106091, ISSN 1350-4177, https://doi.org/10.1016/j.ultsonch.2022.106091 .
4. Nyamapfene, S. Lynch, I. Burova and **M. O. de Andrade**, "MATLAB and Python Open Book Assessments: Lessons from Two UK Institutions," 2022 IEEE Global Engineering Education Conference (EDUCON), 2022, pp. 2022-2027, https://doi.org/10.1109/EDUCON52537.2022.9766577.
5. **M. O. de Andrade**, M. Zurita, I. Burova and A. Nyamapfene, "Assessing higher levels of learning through real-life problems in engineering mathematics," 2022 IEEE Global Engineering Education Conference (EDUCON), 2022, pp. 2002-2006, https://doi.org/10.1109/EDUCON52537.2022.9766484 .
6. **de Andrade, M.O.**, Haqshenas, S.R., Pahk, K.J. and Saffari, N., 2021. Modeling the Physics of Bubble Nucleation in Histotripsy. IEEE

Transactions on Ultrasonics, Ferroelectrics, and Frequency Control, 68(9), pp.2871-2883.

7. Sehmbi, A.S., Froghi, S., **de Andrade, M.O.,** Saffari, N., Fuller, B., Quaglia, A. and Davidson, B., 2021. Systematic review of the role of high intensity focused ultrasound (HIFU) in treating malignant lesions of the hepatobiliary system. HPB, 23(2), pp.187-196.
8. Pahk, K.J., Lee, S., Gélat, P., **de Andrade, M.O.** and Saffari, N., 2021. The interaction of shockwaves with a vapour bubble in boiling histotripsy: The shock scattering effect. Ultrasonics Sonochemistry, 70, p.105312.
9. **de Andrade, M.O.**, Haqshenas, S.R., Pahk, K.J. and Saffari, N., 2019. The effects of ultrasound pressure and temperature fields in millisecond bubble nucleation. Ultrasonics sonochemistry, 55, pp.262-272.
10. Pahk, K.J., **de Andrade, M.O.**, Gélat, P., Kim, H. and Saffari, N., 2019. Mechanical damage induced by the appearance of rectified bubble growth in a viscoelastic medium during boiling histotripsy exposure. Ultrasonics sonochemistry, 53, pp.164-177.
11. Pahk, K.J., **de Andrade, M.O.**, Kim, H. and Saffari, N., 2019, March. The effects of the size of a boiling bubble on lesion production in boiling histotripsy. In Journal of Physics: Conference Series (Vol. 1184, No. 1, p. 012007). IOP Publishing.
12. Platt, G.M., Domingos, R.P. and **de Andrade, M.O.,** 2014. Application of the Firefly and Luus–Jaakola algorithms in the calculation of a double reactive azeotrope. Computational Science & Discovery, 7(1), p.015002.
13. Platt, G.M., Domingos, R.P. and **de Andrade, M.O.**, 2013, February. Calculation of a double reactive azeotrope using stochastic optimization approaches. In Journal of Physics: Conference Series (Vol. 410, No. 1, p. 012020). IOP Publishing.

Acknowledgements

I want to thank my supervisor Professor Nader Saffari for his unwavering support, guidance, and kindness over these seven years.

Immense gratitude goes to my friends Dr Pierre Gelat, Dr Ki Joo Pahk, and Dr Reza Haqshenas for teaching me acoustics, histotripsy, and nucleation theory.

I also want to thank Professor Brian Davidson and Professor Alberto Quaglia for their clinical practice guidance and much appreciated help with histopathology.

Thank you to my dear friends Celine and Marina for inspiring me and making UCL feel like home. This is also true for my Roberts 509 colleagues and the UCL Mechanical Engineering student and staff community.

Thank you to my chosen family, Vice, Thayna, Clarissa, Anna, Diego, Léa, Everrette, Alex, Martin, Melanie, Jamie and Priya, for your friendship, kindness and for sharing my happiest moments whether in Rio de Janeiro, Arraial do Cabo, São Paulo, or London.

Finally, thank you to my mum, dad, sister, niece and nephew for the love, encouragement and support, but primarily for never letting me forget to believe in myself.

UCL Research Paper Declaration Form

referencing the doctoral candidate's own published work(s)

Please use this form to declare if parts of your thesis are already available in another format, e.g. if data, text, or figures:

- *have been uploaded to a preprint server*
- *are in submission to a peer-reviewed publication*
- *have been published in a peer-reviewed publication, e.g. journal, textbook.*

This form should be completed as many times as necessary. For instance, if you have seven thesis chapters, two of which containing material that has already been published, you would complete this form twice.

1. **For a research manuscript that has already been published** (if not yet published, please skip to section 2)

a) **What is the title of the manuscript?**

Modeling the Physics of Bubble Nucleation in Histotripsy

b) **Please include a link to or doi for the work**

https://ieeexplore.ieee.org/document/9483922

c) **Where was the work published?**

IEEE Transactions on Ultrasonics, Ferroelectrics, and Frequency Control

d) **Who published the work?** (e.g. OUP)

IEEE

e) **When was the work published?**

14 July 2021

f) **List the manuscript's authors in the order they appear on the publication**

Matheus O. de Andrade, Seyyed Reza Haqshenas, Ki Joo Pahk, Nader Saffari.

g) **Was the work peer reviewed?**

Yes

h) **Have you retained the copyright?**

No

i) **Was an earlier form of the manuscript uploaded to a preprint server?** (e.g. medRxiv). If 'Yes', please give a link or doi)

No

If 'No', please seek permission from the relevant publisher and check the box next to the below statement:

☒

*I acknowledge permission of the publisher named under **1d** to include in this thesis portions of the publication named as included in **1c**.*

2. **For a research manuscript prepared for publication but that has not yet been published** (if already published, please skip to section 3)

   a) **What is the current title of the manuscript?**

      Click or tap here to enter text.

   b) **Has the manuscript been uploaded to a preprint server?** (e.g. medRxiv; if 'Yes', please give a link or doi)

      Click or tap here to enter text.

   c) **Where is the work intended to be published?** (e.g. journal names)

      Click or tap here to enter text.

   d) **List the manuscript's authors in the intended authorship order**

      Click or tap here to enter text.

   e) **Stage of publication** (e.g. in submission)

      Click or tap here to enter text.

3. **For multi-authored work, please give a statement of contribution covering all authors** (if single-author, please skip to section 4)

As the primary author, I conducted the comprehensive research, computational model development, result generation, analysis, and conclusion formulation for this study. Reza Haqshenas contributed to enhancing the theoretical understanding of the models, providing essential insights that refined our approach. Ki Joo Pahk assisted in proofreading and editing the manuscript, ensuring its clarity and coherence. Nader Saffari, my supervisor, offered overarching guidance and support, shaping the research direction and execution.

4. **In which chapter(s) of your thesis can this material be found?**

   Chapter 4

5. **e-Signatures confirming that the information above is accurate** (this form should be co-signed by the supervisor/ senior author unless this is not appropriate, e.g. if the paper was a single-author work).

   Candidate

Matheus Oliveira de Andrade

Date:

18 March 2024

Supervisor/ Senior Author (where appropriate)

Nader Saffari

Date:

18 March 2024

UCL Research Paper Declaration Form

referencing the doctoral candidate's own published work(s)

Please use this form to declare if parts of your thesis are already available in another format, e.g. if data, text, or figures:

- *have been uploaded to a preprint server*
- *are in submission to a peer-reviewed publication*
- *have been published in a peer-reviewed publication, e.g. journal, textbook.*

This form should be completed as many times as necessary. For instance, if you have seven thesis chapters, two of which containing material that has already been published, you would complete this form twice.

1. **For a research manuscript that has already been published** (if not yet published, please skip to section 2)

a) **What is the title of the manuscript?**

Mechanisms of nuclei growth in ultrasound bubble nucleation

b) **Please include a link to or doi for the work**

https://doi.org/10.1016/j.ultsonch.2022.106091

c) **Where was the work published?**

Ultrasonics Sonochemistry

d) **Who published the work?** (e.g. OUP)

Elsevier

e) **When was the work published?**

12 July 2022

f) **List the manuscript's authors in the order they appear on the publication**

Matheus O. de Andrade, Reza Haqshenas, Ki Joo Pahk, Nader Saffari.

g) **Was the work peer reviewed?**

Yes

h) **Have you retained the copyright?**

Yes

i) **Was an earlier form of the manuscript uploaded to a preprint server?** (e.g. medRxiv). If 'Yes', please give a link or doi)

No

If 'No', please seek permission from the relevant publisher and check the box next to the below statement:

☒

*I acknowledge permission of the publisher named under **1d** to include in this thesis portions of the publication named as included in **1c**.*

2. **For a research manuscript prepared for publication but that has not yet been published** (if already published, please skip to section 3)

   a) **What is the current title of the manuscript?**

      Click or tap here to enter text.

   b) **Has the manuscript been uploaded to a preprint server?** (e.g. medRxiv; if 'Yes', please give a link or doi)

      Click or tap here to enter text.

   c) **Where is the work intended to be published?** (e.g. journal names)

      Click or tap here to enter text.

   d) **List the manuscript's authors in the intended authorship order**

      Click or tap here to enter text.

   e) **Stage of publication** (e.g. in submission)

      Click or tap here to enter text.

3. **For multi-authored work, please give a statement of contribution covering all authors** (if single-author, please skip to section 4)

As the primary author, I conducted the comprehensive research, computational model development, result generation, analysis, and conclusion formulation for this study. Reza Haqshenas contributed to enhancing the theoretical understanding of the models, providing essential insights that refined our approach. Ki Joo Pahk assisted in proofreading and editing the manuscript, ensuring its clarity and coherence. Nader Saffari, my supervisor, offered overarching guidance and support, shaping the research direction and execution.

4. **In which chapter(s) of your thesis can this material be found?**

   Chapter 5

5. **e-Signatures confirming that the information above is accurate** (this form should be co-signed by the supervisor/ senior author unless this is not appropriate, e.g. if the paper was a single-author work).

   Candidate

Matheus Oliveira de Andrade

Date:

18 March 2024

Supervisor/ Senior Author (where appropriate)

Nader Saffari

Date:

18 March 2024

Em memória de vovó Olinda

Chapter 1

Motivation

The defining feature of ultrasound is that it is a versatile and efficient energy source. Ultrasound is versatile because it allows for the simultaneous manipulation of pressure and temperature fields in real-world media such as liquid mixtures, viscoelastic materials, and soft tissue. This control can be spatially limited to the focal volume of a bowl-shaped transducer, where waves of central frequency above 20 kHz are applied continuously or in bursts of specific period and intensity. Furthermore, ultrasound is efficient in the thermodynamic sense of the word: the reorganisation of mechanical into thermal energy is not merely a thermoviscous loss but often the desired outcome of a procedure (Sapozhnikov, 2015).

Cavitation, the detectable activity of bubble activity in a liquid, can be controlled by ultrasound propagation to various extents depending on whether the bubble population is known or how it can be modified to a desired quality. In this sense, cavitation adds versatility to the modes of energy exchange via ultrasound. It transforms ultrasound from a strictly thermal and mechanical tool into a technology that can drive, enhance, or monitor a range of chemical, electrical and biomedical phenomena that occur within and around bubbles. A more detailed definition of cavitation in the scope of this thesis is given in section 2.1.2.

The grand challenges to the widespread realisation of ultrasound technologies are somewhat common across its landscape of industrial and biomedical applications, they often gravitate around:

- the need to achieve detailed temporal and spatial control of cavitation,
- upscaling cavitation as a process intensification approach,
- improving the translatability of novel ultrasound technologies.

These challenges are shared to a different extent across applications as wide-ranging as improving the yield, selectivity, and sustainability of processes in food and biofuel production, wastewater treatment and chemical synthesis; or

controlling and monitoring the delivery of chemical, ablative, or radiation therapies to organs of difficult access. Ultrasound is at its most effective when the intended application exploits patterns of cavitation, and its interaction with the surrounding environment, that are mechanistic elements of well-understood wider physical processes, such as

(i) increased mass and heat transfer via convection or turbulent mixing,
(ii) non-linear ultrasound heat deposition amplified by viscous heating,
(iii) decreased electrode passivation via microstreaming,
(iv) permeabilization of biological media via micro-jetting or streaming,
(v) targeted cargo delivery via micro/nano-bubbles,
(vi) production of radicals or oxygen reactive species via bubble collapse,
(vii) contrast enhancement in ultrasound monitoring,
(viii) cavitational damage of surfaces.

These are phenomena that act over intersecting (but distinct) time and length scales, resulting in compound physical, chemical and biomedical effects that can be detected experimentally (Kooiman *et al.*, 2020; Meroni *et al.*, 2022). The key idea is the detection of a desired outcome at an appropriate scale (Gateau *et al.*, 2011; Khokhlova *et al.*, 2014; Geoghegan *et al.*, 2022). Ultrasound cavitation is an empirical field in essence, mostly preoccupied with the occurrence, behaviour and outcomes of cavitation that manifest at time and length scales appropriate for detection.

The window of cavitation initiation and detection via acoustic means is highly sensitive to the composition and concentration of impurities in the propagation medium, at times presenting unpredictable behaviour that springs from the heterogeneity of real-world fluids (Bader, Vlaisavljevich and Maxwell, 2019). This window comprises important metrics such as local ultrasound pressure, acoustic waveforms, and medium temperature. This sensitivity of nucleation to experimental protocols and purity of the medium has been frequently interpreted as evidence that the nucleation pressure of water is a stochastic quantity that is difficult to define or even impossible to predict. Nonetheless, a now extensive body of evidence shows that the ability of water to sustain ultrasound

negative pressures can be studied in detail by considering the effects of high-magnitude shockwaves in micro/nanoscopic bubbles (Davitt, Arvengas and Caupin, 2010; Maxwell et al., 2013).

At the nanoscale in particular, the conceptualisation of a bubble requires a joint acoustic and thermodynamic description(Caupin, 2005; Caupin and Herbert, 2006; Caupin and Stroock, 2013; González *et al.*, 2014; Bruot and Caupin, 2016; Menzl *et al.*, 2016). The task then becomes an enquiry on how ultrasound affects nano-sized volumes in a liquid, at scales where molecular fluctuations in matter can act as hotspots for rupture at larger scales. Such a thermodynamic enquiry into cavitation is needed because the existing models that assume a stable liquid lose their validity, as bubble nucleation is a phenomenon that occurs during metastable states. Metastable states occur when water exists under pressures lower than its equilibrium pressure for a given temperature, such as the negative pressures induced by ultrasound waves. In the metastable state of liquids, a multitude of often undetected nanobubble embryos come in and out of existence naturally from thermal fluctuations in the liquid at molecular scales (Balibar and Caupin, 2003; Caupin, 2005, 2015; Caupin and Stroock, 2013; Bruot and Caupin, 2016). An understanding of this interface between ultrasound-driven nanoscopic bubbles with local thermodynamic effects is the very knowledge boundary that this research aims to delineate and push backwards.

The questions addressed in this thesis are a contribution to a broader discourse in ultrasound cavitation, largely in the biomedical field, that has changed in tone over the years. Cavitation was initially seen as a potentially harmful effect (Holland, 1989; Holland and Apfel, 1989; Apfel and Holland, 1991; Hedrick and Hykes, 1991; Miller and Brayman, 1997; Church, 2002), then as an activation approach for stabilised microbubble populations (Ward and Wu, 1999; Stride and Saffari, 2003; Ferrara, Pollard and Borden, 2007), paving the way to a novel non-invasive surgery technique that relies on cavitation on demand (Maxwell *et al.*, 2012; Xu, Bigelow and Lee, 2013; Xu *et al.*, 2014; Khokhlova *et al.*, 2015). This compound of belief systems contributed to the transformation of the literature from showing concerns about the safety of ultrasound imaging into excitement over the

possibilities brought about by the interactions of cavitation and soft tissue. Research efforts evolved from establishing operating windows that reduce the likelihood of cavitation, to designing protocols where cavitation is induced in under ten milliseconds or within as much as two cycles of a MegaHertz wave (Vlaisavljevich, 2015; Vlaisavljevich, Lin, *et al.*, 2015). This necessity to control ultrasound cavitation so closely warrants focus on ultrasound bubble nucleation, the very beginning of the cavitation process in the absence of pre-existing microbubbles. Here, it is necessary to integrate the literature on ultrasound cavitation and water thermodynamics, where histotripsy is a notable example of the synergy between the molecular and macroscopic realms of matter.

Histotripsy is a family of techniques where focused ultrasound is used to non-invasively nucleate and drive the oscillations of bubbles within a volume of soft tissue, leading to the mechanical injury of surrounding areas (Khokhlova *et al.*, 2015; de Andrade *et al.*, 2021). Within the scope of this thesis histotripsy refers exclusively to 'endogenous' histotripsy, which is histotripsy without the use of any administered contrast agents or nuclei that can aid the initiation of histotripsy. In a review of the spectrum of methods used in histotripsy (Williams *et al.*, 2023) classified the current methods as boiling, shock-scattering, intrinsic threshold or hybrid histotripsy. These methods rely on the application of short and high-amplitude pulses of focused ultrasound, which aims to initiate violent bubble activity and acoustic streaming at the focus to fractionate tissue into subcellular debris. The differences between these modes of initiating histotripsy are mainly the pulse duration, ultrasound waveforms and corresponding peak-focal positive P_L^+ and negative P_L^- pressures to achieve the desired character of bubble activity (Williams *et al.*, 2023). Other important characteristics of histotripsy methods also include the ultrasound central frequency f [MHz], the electrical power provided to the transducer and the net acoustic power output, the pulse repetition frequency (PRF), and duty cycles used (Maxwell *et al.*, 2012).

Boiling histotripsy (BH) is characterised by the presence of non-linear shockwaves with high-amplitude peak-positive pressures P_L^+ (> 50 MPa). In this regimen non-linear propagation is essential so that the waveform is distorted and

contains high harmonics which are readily absorbed and turned into heat as described by the power-law of attenuation. Non-linear propagation and the presence of shockwaves leads to acoustic heating rates that are greater than their linear counterpart, achieving boiling temperatures within ten milliseconds of sonication (Filonenko and Khokhlova, 2001). Sonication pulses are delivered at a low PRF (0.5 – 1 Hz) and duty cycle (1 – 2%) to avoid for undesired build-up of heat in the tissue volumes immediately around the ultrasound focus.

Conversely, in shock-scattering and intrinsic pressure histotripsy, the pulses are shorter and delivered more frequently in the case of shock-scattering histotripsy. This ensures that no significant heat deposition happens, and that any bubble formation is either directly caused by the peak-negative focal pressures P_L^- or activated by an interaction of incoming waves and those reflected from existing bubbles at physiological, or ambient, temperatures (Khokhlova *et al.*, 2015).

Table 1-1. Comparison between bubble initiation protocols in histotripsy (V. A. Khokhlova et al. 2015; Maxwell et al. 2012; Vlaisavljevich et al. 2016).

	f (MHz)	P_L^+ (MPa)	P_L^- (– MPa)	Number of cycles	PRF (Hz)
Boiling	1 – 5	> 40	15 – 20	3 - 20	0.5 – 1
Hybrid	1 – 1.5	> 90	15 – 20	-	0.5 – 100
Shock-scattering	0.5 – 1	> 50	12 – 25	3000 – 10000	10 – 1000
Intrinsic Pressure	0.3 – 3		> 28	≤ 2	-

Intrinsic pressure histotripsy is the term given to bubble nucleation that happens as a direct consequence of peak-negative ultrasound pressures. This technique builds onto the idea that the highest acoustically attainable tensile pressure in water-like media is around -30 MPa at ambient temperatures (Vlaisavljevich *et al.*, 2016), and that bubbles can be reliably nucleated at this pressure threshold. The mechanism that depends on the interaction of the incoming field and a reflecting bubble is termed shock-scattering histotripsy and operates with much similarity to shockwave lithotripsy(Coleman and Saunders, 1993). Shock-scattering histotripsy is remarkable in that the formation of the first bubble nucleus could take from a few to thousands of pulses, but once this initial seed is nucleated, cavitation clouds follow from the interactions of incoming

shockwaves reflected at the bubble wall and the medium undergoing therapy. This taxonomy of histotripsy is widely accepted in the literature and is helpful because it allows *a priori* description of the HIFU focal volume during nucleation.

This thesis makes an argument that boiling and intrinsic histotripsy share a fundamental thermodynamic description that considers the interaction between ultrasound fields and the hydrodynamics of thermal fluctuations in liquid water. This fuller description of ultrasound nucleation allows for characterising an equation of state of water at negative pressures by recording density changes in the ultrasound focal volume during the tensile cycle of a focused 1 MHz ultrasonic beam. The sharp focusing provided by single and multi-element bowl-shaped transducers minimises the likelihood that pre-existing bubbles or impurities manifest stochastic behaviour, but also amplifies the likelihood that deterministic, or intrinsic, behaviour is dictated by characteristics of the medium. This behaviour of nucleation in focused fields and small volumes is explored in detail in Chapter 3.

It is within the ultrasound focus that naturally-occurring nanoscopic density fluctuations in the liquid become a plausible trigger for ultrasound-induced nucleation. Although this technique was first employed by (Sankin and Teslenko, 2003) to verify the existence of nano-sized preferential nucleation sites in water, later experiments were interpreted as evidence that the nucleation pressure threshold of water in ultrasound follows a temperature-dependent behaviour that is appropriately described by the relatively simple classical nucleation theory (Davitt, Arvengas, et al. 2010; Herbert et al. 2006; Caupin et al. 2012). In the field of biomedical ultrasound, the investigation of the nucleation threshold of water as an approximation of soft tissue contributed to the current momentum around seeing histotripsy as a clinical possibility. This thesis aims to contribute to the realisation of histotripsy as a widespread therapeutic possibility by formalising a mathematical and numerical description of the thermodynamics of bubble nucleation in ultrasound.

1.1 Objectives

The specific objectives of this work are:

- To evaluate the current understanding of ultrasound bubble nucleation, integrating knowledge from experimental and theoretical sources towards evaluating its limitations and synthesizing new information.
- To design and derive models of bubble nucleation in ultrasound pressure and temperature fields that are parameterised and validated against existing experimental evidence in histotripsy.
- To assess the scope, validity and limitations of any models developed herein through quantitative and qualitative comparison of simulations with published experimental evidence.

1.2 Thesis outline and contributions

This dissertation consists of seven Chapters, three of them consisting of original research. The initial sections focus on identifying the critical parameters involved in ultrasound-induced bubble nucleation and the effects of non-linear acoustic fields in the thermodynamics of bubble nucleation. Then, attention is given to the effects of non-linear acoustic propagation on bubble nucleation, the varied time and length scales of the process, the similarities and differences between ultrasound-induced boiling and cavitation, and the role of dissolved gas in the process of nucleation.

This dissertation comprises an original framework for physical reasoning followed by mathematical and computational modelling of nucleation in ultrasound. This modelling framework is parameterised and assessed against the existing literature on histotripsy bubble nucleation. As with any models of reality, mathematical models are idealised and limited in the descriptions of phenomena that can be verified experimentally, possessing a range of limitations that are conceptual, numerical, and contextual. An earnest effort is made to disclose these limitations critically and highlight avenues where knowledge in ultrasound bubble

nucleation can be synthesised by integrating empirical practice and physical-mathematical reasoning. It is important to recognise that modelling does not attempt to replace empirical practice, but aims to describe, inform, and optimise the design of experiments.

The original contributions brought by this thesis to the field of biomedical ultrasound, and acoustic nucleation in general, are divided into three main landmarks throughout this thesis:

- **Contribution 1**: Developing, evaluating, and describing a mathematical model for the numerical study of ultrasound bubble nucleation (de Andrade *et al.*, 2019, 2021).
- **Contribution 2**: Proposing a dimensional model to quantify thermal and hydrodynamic equivalence between boiling and cavitation bubbles (de Andrade et al., 2022).
- **Contribution 3**: Proposing a quasi-stationary model of bubble nucleation for non-linear ultrasound propagation at MegaHertz frequencies (Chapter 6).

These contributions are fully contextualised by the literature review in Chapter 2, which sets out to synthesise existing research and highlight existing gaps in knowledge. An outline of Chapters consisting original research is as follows:

- **Chapter 3** describes the mathematical modelling of bubble nucleation via classical nucleation theory (CNT). In this Chapter, a rigorous and somewhat fundamental derivation of a nucleation model is described, and reasoning for the choice of parameters to be used in ultrasound nucleation is given. Chapter 3 aims to critique the idea that the classical nucleation theory is invalid *because* nucleation is often heterogeneous in real-world media. This Chapter also evaluates the mathematical representation of both homogeneous and heterogeneous nucleation, showing that there is little practical reason to see this distinction as an obstacle for the implementation of the classical nucleation theory in ultrasound.

- **Chapter 4** describes and exemplifies the coupling of the CNT model with a wide-angle approximation to the Westervelt equation towards describing nucleation in boiling histotripsy. This Chapter outlines the type of numerical procedures and analysis that would be required for the detailed simulation of nucleation events in non-linear, high-intensity ultrasound fields. As a contribution, this Chapter exemplifies the application of the thermodynamic models derived in Chapter 3 to a numerically-obtained histotripsy protocol and provides insight into the relative importance of high temperatures and negative pressures for bubble nucleation.
- **Chapter 5** introduces a model to quantify the dominance of acoustic or thermal effects during of nucleation, using histotripsy protocols as examples. This Chapter provides a kinetic critique of the models developed in Chapter 3, in that these models essentially depict bubbles that grow because of their contents and ignore the possibility that bubble (radial) growth can precede and therefore induce mass transfer. In summary, this Chapter outlines the mathematical steps toward including Rayleigh-Plesset-type equations in the description of bubble nucleation. This allows for a dimensional comparison of the key mechanisms of bubble growth, namely vapour and heat transfer, the inertia of the bubble wall, and the viscosity of the liquid.
- **Chapter 6** evaluates whether the timescales of ultrasound are sufficiently long for the validity of quasi-stationary (time-dependent) modelling. This Chapter aims to delimit the timescales at which the stationary models in Chapters 3 and 5 are valid, as well as to lay the foundations of transient formulations of bubble nucleation in ultrasound. Close attention is given to the intrinsic timescales of bubbles nucleated by an acoustic wave at low temperatures (cavitation) and bubbles nucleated by an acoustic wave at high temperatures (boiling) with or without heat transfer to the bubble core.
- **Chapter 7** finally provides a summary of this thesis and envisions future steps in this research.

Chapter 2

Literature Review

This chapter presents a review of the literature on ultrasound-induced nucleation, which forms the basis for defining the research questions tackled in the subsequent original chapters of this dissertation. This review aims to summarise key articles, reviews and book Chapters used throughout the research development presented in Chapters 3 – 7. The existing literature was interrogated with the following questions in mind:

(i) What are the appropriate statistical methods for the quantification of nucleation?

(ii) Are there differences between bubbles nucleated by ultrasound at high and low temperatures?

(iii) What are the key thermodynamic theories, methods, and parameters needed to numerically evaluate the phase stability of a fluid and acoustic propagation in biological tissue?

2.1 Therapeutic Ultrasound

Focused ultrasound therapy is a highly targeted, non-ionising modality of procedures that take advantage of the bioeffects of ultrasound propagation to perform minimally or entirely non-invasive therapy. An extracorporeal transducer is submerged in an intermediary medium, generally purified and de-gassed water, and the ultrasound waves propagate first through water and then through the tissue towards a surgical target. Because the density and sound speed of water and tissue are similar, a minor impedance mismatch minimises sound reflection from skin and organs. Focused ultrasound has the advantage of causing minimal damage to neighbouring tissue and the potential to reduce risks of post-operatory infection and the demand for sterile clinical resources if applied fully non-invasively (Maxwell *et al.*, 2012).

Interest in the biological effects of ultrasound-initiated phenomena dates to 1912, when Paul Langevin observed that apparatus used for underwater obstacle detection could generate sound waves of sufficient strength to kill small fish (Hill, 1982). Since then, substantial work has aimed to identify bioeffects and underlying mechanisms for cell and tissue damage after acoustic irradiation (Fry *et al.*, 1977; Williams, 1986; Carstensen, 1987; Miller, 1987; Barnett *et al.*, 1994; Miller, Miller and Brayman, 1996; Fowlkes and Holland, 2000; Dalecki, 2004; Wang *et al.*, 2013). Over the years, the effects of ultrasound propagation in biological media were split into two categories. One for thermal bioeffects resulting from ultrasound heat deposition, and another for mechanical bioeffects resulting from phenomena such as bubble activity and acoustic radiation forces (O'Brien Jr, 2007; Azhari, 2010; Miller *et al.*, 2012; Boissenot *et al.*, 2016).

2.1.1 Thermal bioeffects of ultrasound

Thermal bioeffects were the first to find clinical application due to a better understanding of their physical mechanisms (Paliwal and Mitragotri, 2008). These are exploited in high intensity focused ultrasound (HIFU) therapy. HIFU uses focused ultrasound beams operating at the MegaHertz frequency range (0.8 – 10 MHz) to achieve intensities as high as 20×10^3 W cm^{-2}. This modality of treatment is used to raise and maintain focal temperatures above 55 ˚C for 1 s or longer and induce coagulative necrosis and cell death in a sharply demarcated focal volume (Gail ter Haar and Coussios 2007). Ultrasound heating happens because soft tissue absorbs the mechanical energy of sound waves and part of it becomes heat through thermoviscous loss (Fry *et al.*, 1950). This process is amplified when non-linear propagation causes the formation of shock waves, where the higher harmonics of shockwaves are readily absorbed by tissue and increase heat deposition rates (Filonenko and Khokhlova, 2001).

Clinical applications of HIFU vary between extra- and intra-corporeal depending on the accessibility of the target organ and the gas or cartilaginous composition of its surroundings. HIFU can be applied through the skin for organs that are readily accessible such as the kidney, but in organs like the prostate it might be necessary to insert the transducer into the body through the rectum. The

acoustic window that is available for HIFU therapy helps define transducer properties such as frequency, aperture, and focal length (Izadifar *et al.*, 2020a). From the given power-law of attenuation (Waters *et al.*, 2000; Sapozhnikov, 2015) it is known that higher frequencies are more readily absorbed and turned into heat. However, the larger wavelengths of lower frequencies warrant longer focal lengths and deeper HIFU penetration into the body. Therefore, transrectal and interstitial transducers therefore often operate at higher frequencies than their extracorporeal counterparts.

Although the focal volume of HIFU systems are often ellipsoids (cigar-shaped lesions), surgical targets of the order of centimetres can generally be treated with HIFU. Consequently, HIFU therapy is the most safe and effective when combined to real-time imaging for guidance and monitoring of treatments. In a review of the literature, (Siedek, et al. 2019) identified a range of oncological, neurological, musculoskeletal, cardiovascular, and endocrine applications and listed their regulatory approval in several regions according to the monitoring modality: Magnetic Resonance-Guided HIFU or Ultrasound-Guided HIFU.

Monitoring strategies to HIFU are often constrained by the possibility of assessing thermally induced contrast phenomena with techniques such as magnetic resonance imaging (MRI) or ultrasound imaging (Geoghegan *et al.*, 2022). On the one hand, MR-guided HIFU provides high anatomical resolution and is not limited by overlying fat tissue, enabling estimation of dosimetry within an error window of 1˚C. On the other hand, MRI guidance is limited by low spatial and temporal resolutions. As an alternative, ultrasound imaging is less expensive and possesses greater spatial and temporal resolution. Ultrasound monitoring and guidance allows for an immediate verification of the acoustic window since the same form of energy is being utilised for imaging and intervention. In B-mode imaging bubbles scatter more of the incident US field than soft tissue, allowing for a correlation with the ablation zone, but failing to delineate the coagulation boundary of treatment (Izadifar *et al.*, 2020b). Here, alternative modes of monitoring gain space in ultrasound-induced thermal ablation. For example, the intravenous administration of contrast agents allows for the determination of non-

perfused regions where the vasculature has been compromised by thermal lesioning. Moreover, elastography-based techniques such as shear wave elastography and acoustic radiation force impulse imaging can be applied to evaluating differences in tissue stiffness caused by ablation therapy (Geoghegan *et al.*, 2022).

2.1.2 Ultrasound cavitation

Early evidence of ultrasound-induced cavitation in-vivo (G R ter Haar and S Daniels, 1981; ter Haar *et al.*, 1982) was detected within attempts to characterise the therapeutic effects of heat-based HIFU effects. In ultrasound fields, cavitation bubbles respond mechanically to the time-dependent oscillations in acoustic pressure. When the pressure is positive, it compresses the bubble, reducing its size. When the acoustic pressure is negative, it stretches the bubble in all directions. A schematic of this process can be seen in Figure 2-1.

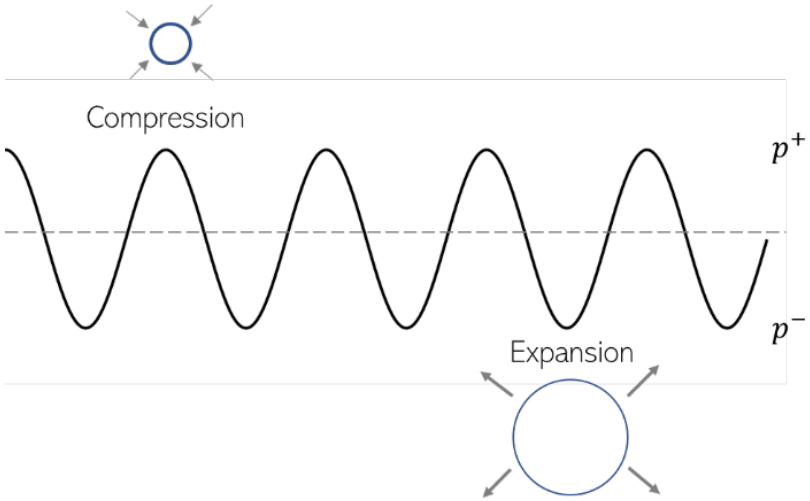

Figure 2-1. Schematic of the mechanical effects of an acoustic field in a free bubble.

The most well-known mechanical effect of naturally occurring cavitation is the damage it can cause to metallic surfaces such as ship propellers or plumbing tubes; as shown in Figure 2-2. Cavitation has such destructive potential because whenever a surface is sufficiently close to an oscillating bubble, this bubble collapses onto the surface as a powerful jet (Plesset and Chapman, 1971). The physical mechanism at play is the creation of a stagnation point in pressure potential between the bubble and the boundary, which attracts fluid toward itself

(Tomita *et al.*, 2009; Kim and Kim, 2012). For biological tissues, especially vasculature, this understanding signifies the possibility of directing bubble jetting towards an elastic surface (the vessel wall), and a therapeutic opportunity to permeabilise endothelial walls. This type of bubble behaviour is appropriately characterised by a solution of mass and momentum conservation equations through boundary element methods.

The response of spherical bubbles to a pressure field can be modelled by a radial approximation the Navier-Stokes equation in the presence of heat and mass transport (Christopher Earls Brennen, 2013; Christopher E. Brennen, 2013a, 2013c). Although the original model was derived by Lord Rayleigh and augmented by M. Plesset (Plesset, 1949), further improvements were derived as efforts of accounting for the presence of pollutant gas, acoustic driving, viscosity, and sound emissions from the bubble (Lauterborn and Mettin, 2015). These models often contain a mix of differential equations that treat a spherical bubble as a non-linear harmonic oscillator. The action of a stable gas bubble within soft tissue or a liquid solution has been subject to intense research in biomedical ultrasound. The most recent understanding is that bubbles interact with cells via a mix of thermal, chemical, and predominantly mechanical pathways (Kooiman *et al.*, 2020) such as:

- Direct mechanical action as forces from the bubble wall, or bubble translation in liquid media, as well as secondary radiation forces or the formation of shockwaves upon bubble collapse.
- Microstreaming as flow up to 1 mm/s that is generated from stable or transient cavitation, generating shear stresses on surfaces and increasing convection, and micro jetting as the asymmetric collapse of bubbles onto surfaces, that can cause direct mechanical damage.

Most importantly, these effects of acoustic excitation of pre-existing bubbles were proposed as mechanistic elements in applications such as drug delivery to tumours, aiming to confine the cytotoxic effects of chemotherapeutics to tumours, improve the permeability of the endothelial wall, and overcome gradients in interstitial fluid pressure (Coussios and Roy, 2008; Wu and Nyborg, 2008; Kooiman

et al., 2020). Linearised versions of this mathematical treatment are those concerned with small oscillatory amplitudes that allow for the conceptualisation of a resonance frequency. For oscillations that depart from equilibrium, the reorganisation of the inertial energy of the bubble's wall into heat or chemical reactions at its core, coupled with varied extents of heat and mass transfer from the surrounding liquid (Christopher E. Brennen, 2013c; Pahk *et al.*, 2018), might induce a distinctive distribution of energy across the detectable frequency spectrum through the presence of broadband emissions. This distribution is correlated to a noticeable presence of high harmonics in the backscattered signal of a passive cavitation detection hydrophone during cavitation (Bawiec *et al.*, 2021). This characterises violent rebound and collapse of bubbles, that can fragment tissue to subcellular levels (Mitragotri, 2005; Paliwal and Mitragotri, 2008; Hoogenboom *et al.*, 2015). This type of transient bubble activity is also theoretically capable of selectively inducing mechanical damage to materials of different mechanical strengths (Hwang *et al.*, 2006; Styn *et al.*, 2011; Vlaisavljevich, 2015; Mancia *et al.*, 2017, 2019), such as the vasculature and the parenchyma (Ki Joo Pahk *et al.*, 2019).

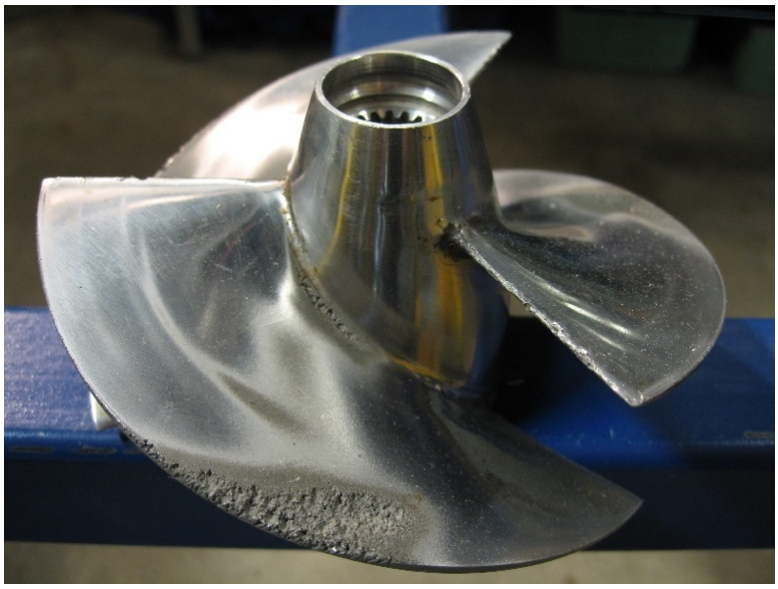

Figure 2-2. Cavitation damage in a propeller. Photographed by Erik Axdahl, uploaded on Wikimedia Commons on 20 May 2006. Original replicated under a Creative Commons license.

The combined potential hazards and benefits of cavitation point to the challenge of defining a "true" or "intrinsic" pressure threshold for cavitation in water

in the absence of pre-existing cavitation nuclei (Greenspan and Tschiegg, 1967, 1982; Sankin and Teslenko, 2003; Caupin and Herbert, 2006; Caupin, 2015; Gallo *et al.*, 2016). This question has been solved in practical terms by boiling histotripsy (Canney, T. D. Khokhlova, *et al.*, 2010; Canney, V. A. Khokhlova, *et al.*, 2010; Khokhlova, Canney, *et al.*, 2011), and with statistical merit by intrinsic threshold histotripsy (Vlaisavljevich, Lin, *et al.*, 2015; Vlaisavljevich *et al.*, 2016), however has been long documented in the literature of water thermodynamics where ultrasound is used to evaluate the properties of liquid water under negative pressures (Sankin and Teslenko, 2003; Ando, Liu and Ohl, 2012).

2.1.2.1 Cavitation detection

There is a wide range of techniques that can used to detect or map cavitation activity resulting from ultrasound propagation. Each of them has strengths and weaknesses that should be considered in terms of the type of evidence sought in an experiment. Cavitation can be detected or mapped via primary or secondary measurements of parameters of the acoustic field (Izadifar, Babyn and Chapman, 2019). Optical methods often yield primary evidence of bubbles, such as an image or a time-series of images at a high framerate displaying spatial/temporal change of bubbles, or direct measurements of a laser beam scattered from a bubble as it oscillates. As a limitation, these techniques require that the experiment is performed in optically transparent media and output data that informs size, shape and spatial distribution of bubbles. These methods are also generally unfeasible for in-vivo applications (Cleveland and McAteer, 2012).

As an alternative, acoustic methods can be employed to detect sound emissions from a bubble as it oscillates, collapses, or interacts with an incoming sound field. Acoustic methods are broadly categorised between active and passive methods (McLaughlan *et al.*, 2010), where the distinguishing feature relies on whether the signal that is sought is the consequence of a continuous sound field emitted towards the detection volume (active cavitation detection), or whether the receiving transducers simply record the pressure oscillations in the fluid in time and space as a response to a pulsed beam (passive cavitation detection) (Haworth *et*

al., 2012). This family of methods can yield a range of useful data for the characterisation and detection of cavitation and bubble activity, such as:

(i) Time-series measurements of voltage oscillations which can be decomposed for analysis of harmonics;
(ii) 2D and 3D imaging and mapping of the cavitation field.

Acoustic methods are not hindered by some of the limitations of optical methods such as a transparent medium, but they possess limitations of their own such as a possible interference with the cavitation process, and susceptibility to noise. However, the evidence obtained in cavitation detection via acoustic methods is secondary and depends on a mechanistic understanding of the relationship between bubble radial dynamics and the subsequent sound emissions (Izadifar, Babyn and Chapman, 2019).

2.1.2.2 The nucleation pressure threshold in water

Figure 2-3 shows a timeline of landmark developments in understanding cavitation/nucleation thresholds in water. This timeline opens space for a different narrative for histotripsy, in that it broadens the horizon of contributions toward the development of what is sometimes viewed as a strictly biomedical technique. For example, static pressures of -27.7 MPa had been achieved in water at 10 °C before the liquid ruptured into bubbles much before the development of intrinsic pressure threshold histotripsy (Briggs, 1950). Briggs was the first to report a temperature dependence of the process after observing that the pressures reached at 50 °C were limited to about -22 MPa. These results were obtained using the centrifugation method, where a tube filled with water is rotated at high speeds, and the centrifugal force creates negative pressures in the axis of rotation.

Moreover, (Galloway, 1954) used a standing wave produced by a spherical resonator to stretch water for a range of time intervals. One of his most important findings is that cavitation pressure amplitudes in water increase as the period of water under tension decreases, foreshadowing an understanding of the effect of ultrasound frequencies in bubble nucleation that was later conceptualised into the mechanical index (Apfel and Holland, 1991). This trend was subsequently

confirmed by (Greenspan and Tschiegg, 1967), who measured nucleation pressure thresholds of -16 MPa for an exposure time of minutes and -21 MPa for an exposure time of seconds in water.

Acoustic cavitation in naturally occurring (untreated) water or bubbly media also has predecessors in the field of water nucleation research. (Strasberg, 1959) investigated ultrasound cavitation thresholds in tap water and found highly scattered results with few discernible trends. Some significant findings were a decrease of the achievable pressure magnitudes with increasing air content, an increase of the achievable pressure magnitude with increasing static pressure applied to the liquid, and an increase in the pressure magnitude with increasing time where the fluid is left at rest. These are trends that have been exhaustively revisited and confirmed staking their claim as common knowledge within ultrasound cavitation (Bader *et al.*, 2012).

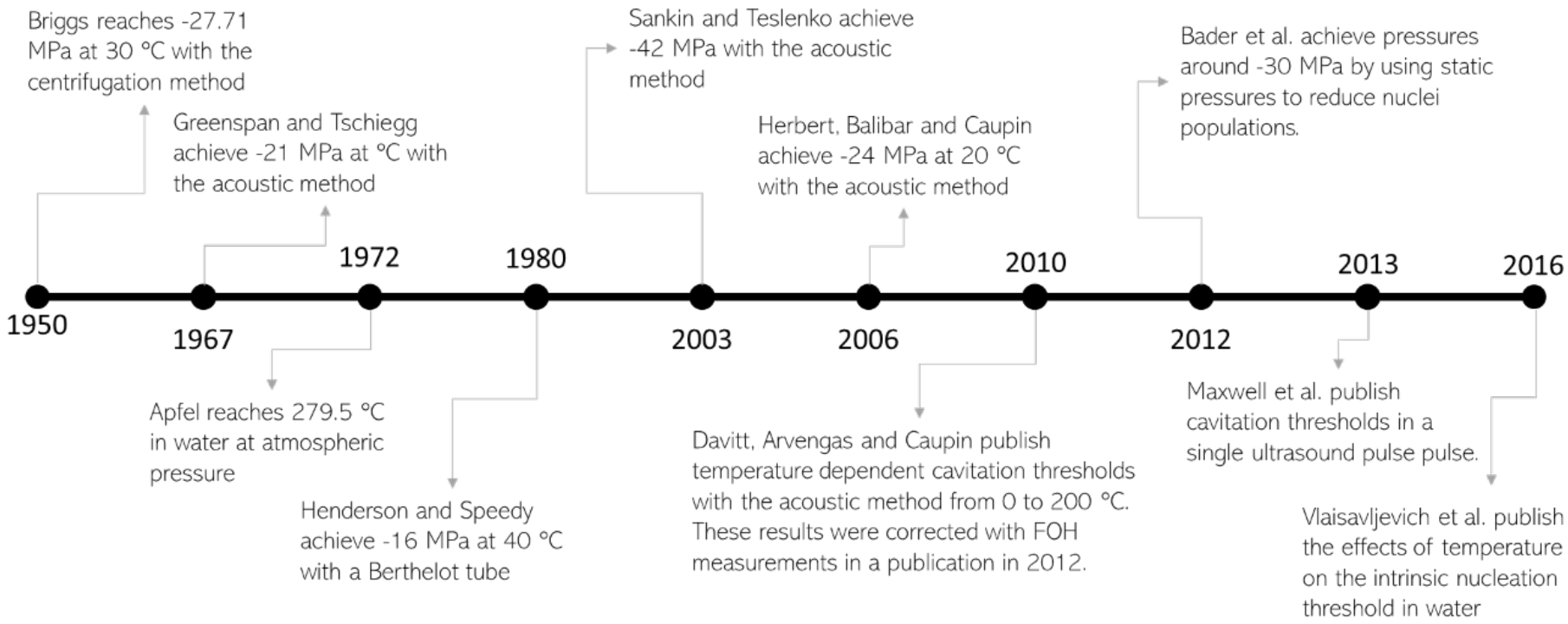

Figure 2-3. Timeline of important developments in the search for the cavitation threshold in water.

More recently, (Sankin and Teslenko, 2003) used acoustic shockwaves with focal peak negative pressures of -42 MPa to induce nucleation in distilled water. These were the lowest acoustic pressures achieved in liquid water and inspired a wave of future experiments. Their experimental set-up characterises the first evidence of what is now seen as the intrinsic threshold method. At a similar time, the first publication on histotripsy described a method where several ultrasound pulses were employed to generate *cavitation* clouds at the ultrasound focus (Xu *et al.*, 2003). This method relied on the chance that "stochastic" cavitation would occur at the ultrasound focus or that there would be a pre-existing bubble that would initiate the cavitation process. This process is currently called shock-scattering histotripsy .

The integrated view of ultrasound-induced nucleation proposed in this thesis takes shape from the work of (Herbert, Balibar and Caupin, 2006). In this seminal work, the authors used a confocal 30 MHz hydrophone to detect echo produced from cavitation bubbles. This work analysed ultrasound cavitation through its essential statistics, where the excitation voltage of a 1 MHz transducer was gradually increased for subsequent experiments consisting of 1000 identical repetitions. The distribution of the magnitude of detectable echo was computed, and "cavitation" events were coded as those with echo distributions above a noise threshold of 5 V. Over each of the thousand repetitions for a given excitation voltage, a probability of cavitation was calculated from a thousand samples. The compound analysis of every probability of cavitation for each of the several excitation windows then yields a probability cumulative function.

The important feature of this distribution function is that it was shaped like a sigmoid, which is a continuous approximation of a threshold phenomenon. Within this statistical analysis, the median electric voltage is defined as the nucleation threshold, since it poses a one in two probability that cavitation takes place. The authors then use constitutive models and acoustic characterisation to relate excitation frequencies to the focal peak negative pressure. This worked confirmed the findings of (Galloway, 1954; Greenspan and Tschiegg, 1967) and clarified the role of experimental volumes and periods within classical nucleation theory. It was

also pushed forward in 2010, where (Davitt, Arvengas and Caupin, 2010) published temperature-dependent pressure thresholds within six cycles of a 1.03 MHz transducer at a pulse repetition frequency of 1.75 Hz. Their results reported ultrasound pressures as low as -24 MPa at 0 °C and -15 MPa at 100 °C before nucleation takes place (Caupin *et al.*, 2012).

Table 2-1. Selective list of temperature-dependent nucleation thresholds in water.

Reference	f (MHz)	p^- (MPa)	Mean error (MPa)	T (°C)
(Davitt, Arvengas and Caupin, 2010; Caupin *et al.*, 2012)	1.1	34	± 1	1
		33		3
		34		5
		32		7
		32		9
		31		11
		31		13
		30		16
		30		20
		28		29
		26		38
		25		48
(Vlaisavljevich *et al.*, 2016)	1	29.8	0.7	10
		28.9	0.6	20
		24.7	1.9	40
		21.8	2	60
		17.4	2.4	80
		14.9	3.5	90

Table 2-1 outlines temperature-dependent nucleation pressure thresholds obtained with the acoustic method by two independent groups. It can be noted that there are small discrepancies within results, likely to arise from the methodology employed to detect bubble nucleation and to measure the acoustic field itself. In the first set of experiments an extrapolation of the International Association for the Properties of Water and Steam (IAPWS) equations of state is used to convert the density of the liquid into a focal pressure (Caupin *et al.*, 2012). In the second set of experiments, a combined optical and acoustic approach is used to detect cavitation activity, and any pressures below – 25 MPa are obtained by direct measurement of pressures with a fibre-optic probe hydrophone immersed in 1,3-butadienol (Vlaisavljevich *et al.*, 2016).

2.1.3 Boiling Histotripsy

Boiling histotripsy (Canney, T. D. Khokhlova, *et al.*, 2010; Canney, V. A. Khokhlova, *et al.*, 2010; Khokhlova, Canney, *et al.*, 2011) occurs when millisecond-long pulses heat focal tissue to temperatures that are favourable for vapour bubble nucleation and growth (de Andrade *et al.*, 2019). In boiling histotripsy, an ultrasound source generates acoustic waves which travel through water and then soft tissue onto a treatment zone. Non-linear propagation effects cause the formation of shock fronts of about 80 MPa in a small sub-volume within the HIFU focal region (Khokhlova *et al.*, 2015). The high harmonic components of these shockwaves are promptly absorbed by soft tissue and cause non-linear heating of the treatment zone. This interaction between HIFU and soft tissue can increase the temperature of the treatment zone beyond 100 °C in a few milliseconds (Canney, V. A. Khokhlova, *et al.*, 2010), leading to the formation of a boiling bubble.

Table 2-2 summarises boiling histotripsy protocols in terms of the excitation frequency (MHz), target medium, and peak positive and negative focal pressures. This data shows that the most experiments in boiling histotripsy are performed at peak-positive pressures above 60 MPa and peak-negative focal pressures from - 12 to - 20 MPa with frequencies ranging from 1 to 3.5 MHz, although most protocols are carried at 2 MHz ultrasound frequency.

Table 2-2. Selective list of boiling histotripsy protocols.

Reference sorted by publication date	f (MHz)	Medium	p^+ (MPa)	p^- (MPa)	Pulse duration (ms)
(Canney, T. D. Khokhlova, *et al.*, 2010)	2.158	Ex vivo bovine liver	36	9	10
		Ex vivo bovine heart	70	12	
(Canney, V. A. Khokhlova, *et al.*, 2010)	2.158	Ex vivo bovine liver	67	12	4 – 52
(Khokhlova, Canney, *et al.*, 2011)	2.158	Ex vivo bovine heart	67	12	1 - 500
		Tissue-mimicking gel	76	13.5	
(Wang *et al.*, 2013)	2.158	Ex vivo bovine heart	73	12	4.5
		Ex vivo bovine liver	73	12	
(Pahk *et al.*, 2015)	1.1	Ex vivo porcine liver	74	14.4	10
	2.0		101	16.7	
(Pahk *et al.*, 2016)	2.0	In vivo rat liver	94	15	10
			101	17	
(Pahk *et al.*, 2017)	2.0	Tissue-mimicking gel	85.4	15.6	10
(Schade *et al.*, 2019)	1.5	In vivo carcinoma Eker rat	85	17	10
			100	20	
(Khokhlova, Schade, *et al.*, 2019)	1.5	In vivo porcine kidney and liver	80	12-18	1 - 10
(Kisoo Joo Pahk *et al.*, 2019)	2.0	Human breast adenocarcinoma	85	14	10
(K J Pahk, 2021)	2	Tissue-mimicking gel	89.1	14.6	4, 6
	3.5		72.4	13.8	5, 5
	5		69.2	12.5	5, 5

Computational models of histotripsy bubble dynamics have shown that histotripsy pressure and temperature fields can drive a nanometric initial bubble up to micrometre dimensions (Bader and Holland, 2016). Moreover, simulations of the induced shear stress fields in boiling histotripsy have shown that there is a possibility that bubbles in viscoelastic media selectively rupture the parenchyma, whilst sparring the vasculature, due to their different mechanical properties (Ki Joo Pahk *et al.*, 2019; K. J. Pahk *et al.*, 2019).

As illustrated in Figure 2-4, it has been proposed that the backscattering of incident shocks on the vapour bubble surface are sufficient to create regions of tensile pressure that are capable of inducing cavitation, in a process analogous to shock-scattering histotripsy (Pahk, 2021; Pahk et al., 2021). This hypothesis has been further tested in developing protocols for boiling histotripsy where the amplitude of the incident field is immediately reduced after the formation of the first boiling bubble, where no signs of cavitation can be seen (Pahk, 2021). Concurrently, analysis of inertial cavitation produced by HIFU pulses concluded an enhanced growth of gas bubbles in transparent agarose gels in the presence of shockwaves, with the growth of new bubbles in the pre-focal region of the medium (Bawiec *et al.*, 2021).

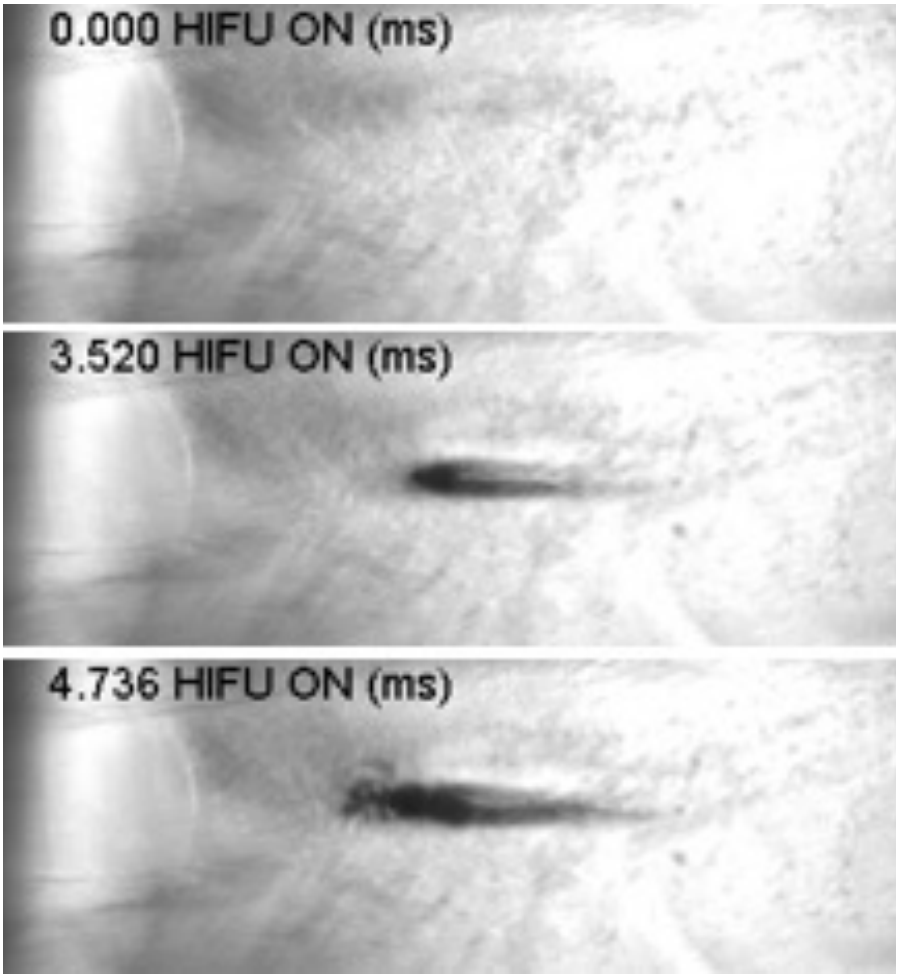

Figure 2-4. Boiling histotripsy in a tissue phantom recorded in video format by a high-speed camera. The transducer is placed at the left of the selected region of visualisation, and acoustic propagation occurs from left to right. Top picture: Intact phantom before sonication. Middle picture: Formation of a boiling bubble at the ultrasound focus. Bottom picture: Formation of a pre-focal cavitation cloud. Reproduced from (Pahk et al. 2021).

A minimal set-up for boiling histotripsy experiments can be achieved by using a fixed 2 MHz bowl shaped transducer (Sonic Concepts H-148, Bothell, WA, USA) in a water tank filled with degassed, de-ionised water at room temperature. To ensure shock formation, the transducer must be driven via a linear radiofrequency (RF) power amplifier at high powers to cause non-linear propagation and shock-formation, for example powers exceeding 150 W for a Sonic Concepts H148 transducer. The input to the power amplifier is provided by two function generators in series, one commanding the pulses and one generating sinusoidal waves. The pulse-controlling function generator is set-up to output a square wave at a certain pulse repetition frequency (PRF). The duty cycle in boiling

histotripsy is the portion of the square wave where the ultrasound is activated and is often low (between 1 – 5%). For example, for a histotripsy pulse of 10 ms, a PRF of 1 Hz might be used with a duty cycle of 1%, where 1% of 1 second is 10 ms. The sinusoidal function generator is gated to the pulse generator, and only outputs a signal when the input square wave exceeds a certain threshold. This function generator must output a sinusoidal signal of the same frequency of the transducer (2 MHz, for example) where the amplitude of this signal in peak-to-peak voltage determines the electric power at which the transducer will be excited by the output of the power amplifier. Figure 2-5 provides a schematic of boiling histotripsy pressure fields within this context.

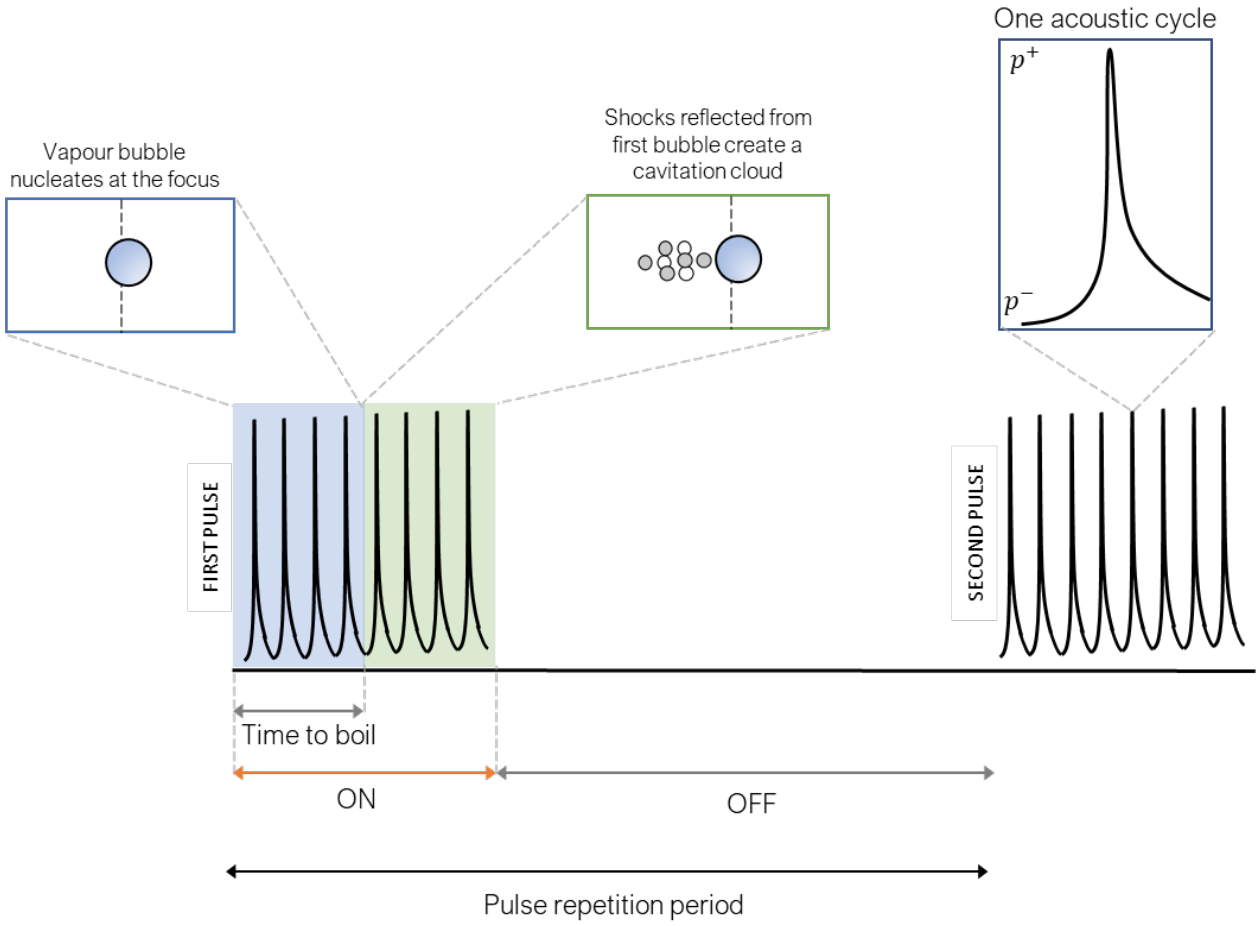

Figure 2-5. Schematic of boiling histotripsy pulse inducing nucleation.

Potential applications of BH include the mechanical ablation of benign prostatic hyperplasia (BPH), liver, and kidney tumours, in inducing anti-tumour immune responses, thrombolysis and decellularising soft tissue (Wang *et al.*, 2014, 2018; Bader *et al.*, 2019). Comprehensive reviews on the clinical applications of

histotripsy can be found in references (Roberts, 2014; Khokhlova *et al.*, 2015; Williams *et al.*, 2023). Pre-clinical studies of BH in *ex-vivo* bovine liver, kidney and heart tissue, and *in-vivo* porcine liver and kidney, have reported complete tissue emulsification and cell destruction in millimetre-sized treatment zones around the HIFU focus (Khokhlova *et al.*, 2015). In addition, the feasibility of generating transcutaneous centimetre-sized treatment zones with boiling histotripsy has been demonstrated in an *in-vivo* porcine model via translation of the HIFU focus by a millimetre after the delivery of 30 histotripsy pulses (Khokhlova *et al.*, 2016). Histotripsy has been tested in a phase I non-randomised clinical trial for the ablation of malignant tumours in eight patients using the HistoSonics VORTX Rx Treatment system. Results reported over 75% ablation efficiency in tumours up to 1.3 cm of diameter with no procedure-related significant adverse effects. Moreover, a study on the safety of histotripsy treatment of benign prostatic hyperplasia on twenty-five male patients showed the safety of histotripsy and reported improvement in lower urinary tract symptoms (Schuster *et al.*, 2018).

2.1.4 Intrinsic and shock-scattering histotripsy

At first, a striking difference between boiling histotripsy and shock-scattering histotripsy was the “all-or-nothing” character of shock-scattering histotripsy, where bubbles could take from one to thousands of pulses to nucleate (Xu, Fowlkes, Ludomirsky, *et al.*, 2005; Xu, Fowlkes, Rothman, *et al.*, 2005). This contrasted with the repeatability of boiling histotripsy (Khokhlova, Canney, *et al.*, 2011; Khokhlova, Simon, *et al.*, 2011). The issues with the repeatability of shock-scattering histotripsy were then addressed considering the work of (Herbert, Balibar and Caupin, 2006; Davitt, Arvengas and Caupin, 2010). In 2012, a study built onto the results of (Strasberg, 1959) and showed that pressures up to -30 MPa could be achieved in water that had been subjected to high static pressures (Bader *et al.*, 2012). Later, (Maxwell *et al.*, 2013) investigated ultrasound pressure thresholds that could generate cavitation in a few cycles of the acoustic wave, similarly to what (Sankin and Teslenko, 2003; Herbert, Balibar and Caupin, 2006; Davitt, Arvengas and Caupin, 2010; Caupin *et al.*, 2012) had previously achieved.

Table 2-3. Nucleation parameters for microtripsy, intrinsic pressure histotripsy, shock-scattering histotripsy.

Reference	f (MHz)	Tissue	Modality	p^- (-MPa)
(Parsons *et al.*, 2006)	0.75	Ex vivo porcine heart	Shock-scattering	22
(Roberts *et al.*, 2006)		Ex vivo rabbit kidney		22
(Hall *et al.*, 2009)		Ex vivo canine prostate		20
(Maxwell *et al.*, 2011)	1	Tissue-mimicking gel		19
(Maxwell *et al.*, 2013)	1.1	Distilled water 10% O2	Intrinsic pressure	27.4
		Unfiltered water 90% O2		26.2
		Tissue-mimicking gel (5% what)		27.3
		Tissue-mimicking gel (15% what)		28
		Ex vivo canine blood		26.9
		Ex vivo canine blood clot		26.8
		Ex vivo canine kidney		29.4
(Vlaisavljevich *et al.*, 2013)	1	In vivo porcine liver		17
(Lin *et al.*, 2014)	0.5	Ex vivo canine kidney	Microtripsy	28.5
		Ex vivo canine liver		29.3
		Tissue-mimicking gel		24.5
(Zhang *et al.*, 2015)	1	Blood clot		36

This new intersection of well-established nucleation research with therapeutic ultrasound was then explored in a series of publications on the effects of tissue properties (Vlaisavljevich *et al.*, 2014; Vlaisavljevich, Lin, *et al.*, 2015), ultrasound parameters (Vlaisavljevich, Aydin, *et al.*, 2015; Vlaisavljevich, Lin, *et al.*, 2015; Vlaisavljevich *et al.*, 2017), and, most importantly, temperature (Vlaisavljevich, Xu, *et al.*, 2015; Vlaisavljevich *et al.*, 2016) into the pressure threshold for low MegaHertz acoustic nucleation in water. The newly found repeatability of bubble nucleation for histotripsy in soft tissue warranted a different branding to the improved protocol to avoid confusion with the less predictable shock-scattering histotripsy. The new method is now commonly referred to as intrinsic-threshold histotripsy (Maxwell *et al.*, 2013; Vlaisavljevich *et al.*, 2016), a phenomenon that occurs when the focal peak negative ultrasound pressures surpass the local tensile strength of the medium. A modification of this technique was named Microtripsy due to the highly localised and repeatable lesions it could

create (Lin *et al.*, 2014). Table 2-3 summarises frequencies, media and modalities of cavitation-based histotripsy, accompanied by the peak-negative focal pressure reported by the authors.

2.1.5 Model of Acoustic Propagation

The literature of histotripsy is closely tied to the simulation of high-intensity focused acoustic beams for determination of peak focal pressures and heating rates. The Khokhlov–Zabolotskaya–Kuznetsov (KZK) equation models high-intensity axially symmetric acoustic beams and has been widely used to simulate acoustic propagation in histotripsy (Bailey *et al.*, 2003; Khokhlova *et al.*, 2006; Canney *et al.*, 2008; Canney, V. A. Khokhlova, *et al.*, 2010). The KZK equation in the propagation direction z is given by:

$$\frac{\partial^2 p}{\partial z \partial \tau} - \frac{c_0}{2}\nabla_\perp^2 p = L(p) + \frac{\beta}{2\rho_0 c_0^3}\frac{\partial^2 p^2}{\partial \tau^2}, \qquad 2.1$$

where p is acoustic pressure, τ is the retarded time coordinate $\tau = t - z/c_0$, c_0 is the small-signal speed of sound, β is the coefficient of non-linearity, and ρ_0 is the density in the equilibrium state.

The effects of attenuation and dispersion are considered by the term $L(p)$, which is defined as (Soneson, 2017)

$$L(p) = \frac{2}{c_0}\frac{\partial}{\partial \tau}\left[\alpha(\omega) * p(\omega)\right], \qquad 2.2$$

where $p(\omega)$ and $\alpha(\omega)$ are, respectively, the frequency-dependent pressure and absorption, and the operator $*$ denotes a convolution. Ultrasound absorption can be modelled by a power-law in frequency (Waters *et al.*, 2000):

$$\alpha(\omega) = \alpha_0 |\omega|^y, \qquad 2.3$$

where α_0 is the absorption coefficient and y is a real positive constant below two. Phase velocity dispersion is given by the imaginary component of α and is

calculated using the differential form of the Kramers-Kröning relations (O'Donnell, Jaynes and Miller, 1981).

As a limitation of the KZK equation, the transverse Laplacian $\nabla_{\perp}^{2} = \partial^{2}/\partial x^{2} + \partial^{2}/\partial y^{2}$ operates on the plane perpendicular to the propagation direction z and approximates diffraction in Eq. 2.1. This approximation introduces errors at field points that are more than 20° away from the propagation axis (Soneson, 2017). For highly focused HIFU sources, the KZK equation should be solved within a wide-angle approximation (Sapozhnikov, 2015). Within this thesis, all numerical simulation of acoustic propagation was simulated for a 2 MHz bowl-shaped transducer (Sonic Concepts, H148) and a 1.1 MHz bowl-shaped transducer (Sonic Concepts, H102), both with a central opening of approximately 1 cm. Tables 2-4, 2-5 and 2-6 detail the geometry of both transducers, the material and thermoacoustic properties used within simulations.

The HITU Simulator is an open source for simulating axisymmetric high-intensity focused ultrasound (HIFU) beams in MATLAB (The Mathworks, Inc., Natick, MA). This package was employed to solve a wide-angle parabolic approximation to transverse Laplacian in the KZK Equation (Soneson, 2017). The wide-angle parabolic approximation improves the calculation of the diffraction term $\nabla_{\perp}^{2} p$ in Eq. 2.1 by using an approximate solution to the full Laplacian Δ (Yuldashev, Mezdrokhin and Khokhlova, 2018). This results in accurate numerical results for field points within 45° of the propagation axes, with errors below 0.07% at the focus, 0.5% in the area around the focus and a maximum error that does not surpass 2.5% in the whole field. The simulations computed acoustic propagation for 5.32 cm in water followed by propagation in 2 cm of liver tissue.

Table 2-4. Transducer geometry used for KZK simulations.

Parameter	Value (cm)	
	H102	H148
Transducer outer radius	3.2	3.2
Transducer inner radius	1	1.13
Focusing depth	6.32	6.32

Table 2-5. Tissue properties used in the acoustic simulations (Pahk *et al.*, 2015).

Property	Water	Liver
Speed of sound ($m \cdot s^{-1}$)	1482	1575
Mass density ($kg \cdot m^{-3}$)	1000	1060
Attenuation at 1 MHz ($dB \cdot m^{-1}$)	0.217	52
Power of attenuation vs frequency curve	2	1.1
Non-linearity coefficient	3.5	4.4

Table 2-6. Tissue properties used in the BHTE equations (Pahk *et al.*, 2015).

Property	Water	Liver
Specific heat ($J \cdot kg^{-1} \cdot °C^{-1}$)	4180	3628
Thermal conductivity ($W \cdot m^{-1} \cdot °C^{-1}$)	0.6	0.57
Blood perfusion rate ($kg \cdot m^{-3} \cdot s^{-1}$)	-	0 – 19

2.1.6 Model of Heat Deposition

Once the acoustic field is computed, the volumetric heat deposition rates can be calculated as:

$$Q_A = \frac{1}{\rho_0 c_0} \sum_{n}^{\square} \left[Re(\alpha_n) |p_n|^2 - \frac{d}{dz} \langle p^2 \rangle \right], \tag{2.4}$$

where p_n represents the pressure amplitude of the n-th harmonic of $p(\tau)$.

$$p(\tau) = \sum_{n}^{\square} \left(p_n e^{-i\omega n\tau} + p_n^* e^{i\omega n\tau} \right). \tag{2.5}$$

The Bioheat Transfer Equation (BHTE) is then used to model heat transfer in soft tissue. This equation is an augmentation of the heat diffusion equation in the presence of a heat source Q_A and a heat sink due to blood flow. Assuming a uniform tissue thermal conductivity k, and neglecting metabolic processes, the BHTE can be written as (Huang and Horng, 2015):

$$\rho C \frac{\partial T}{\partial t} = k\nabla^2 T - w_p C(T - T_0) + Q_A \quad 2.6$$

Where T_0 is the initial temperature, T is the local tissue temperature, ρ is the tissue density, C is the specific heat of tissue, w_p is the perfusion rate of tissue, k is the thermal conductivity, and Q_A represents the ultrasound heat source. This equation is widely used in the modelling of hyperthermia in tumours due to its simplicity and ability to predict temperature fields in HIFU therapy applications (Huang and Horng, 2015).

2.2 Thermodynamic Stability of Liquids

Stability criteria for liquid phases determine the physical conditions in which mass transfer between two phases of a fluid and the mechanism by which phase transition will be initiated (Debenedetti, 1991). Phase change is a direct consequence of thermodynamic instability, and bubble nucleation is the mechanism by which metastable liquid phases relax towards stability through a first-order phase transition (Kashchiev, 2000). Considering an isolated system, thermodynamic equilibrium requires (Beegle, Modell and Reid, 1974)

$$dS|_{U,V,N} \leq 0, \quad 2.7$$

where S, U, V and N represent the system's entropy, internal energy, volume and number of molecules, respectively.

Equation 2.7 states that any changes to the given state of the liquid will lead to a decrease in entropy. This means that no spontaneous process is possible at

equilibrium because the system is at its maximum value in entropy $S = S_{max}$. This condition is equivalent to

$$dU|_{S,V,N} \geq 0, \tag{2.8}$$

which states that an equilibrium state minimises the system's internal energy. These inequalities are necessary and sufficient for thermodynamic equilibrium (Gibbs, 1878).

2.2.1 Vapour-Liquid Equilibrium

Vapour-liquid equilibrium (VLE) conditions can be obtained by considering a finite, two-phase isolated system with liquid and vapour phases separated by a flat surface. Using the subscripts *l*, *v*, and *s* to denote liquid, vapour and surface phases, respectively, one can use the First Law of thermodynamics to write

$$dU_l = T_l dS_l - P_l dV_l + \mu_l dN_l, \tag{2.9}$$

$$dU_v = T_v dS_v - P_v dV_v + \mu_v dN_v, \tag{2.10}$$

for the liquid and vapour phases, and

$$dU_s = T_s dS_s + \sigma_s dA + \mu_s dN_s, \tag{2.11}$$

for the surface phase.

In these equations P, T, μ and σ represent pressure, temperature, chemical potential and surface tension of the respective phase and A denotes area between liquid and vapour phases.

Using the equilibrium criterium $S_{tot} = S_{max}$ such that $dS_{tot} = dS_l + dS_v + dS_s = 0$, Equations 2.9 – 2.11 can be used to derive the result

$$dS_{tot} = \left(\frac{1}{T_v} - \frac{1}{T_s}\right) dU_v + \left(\frac{1}{T_l} - \frac{1}{T_s}\right) dU_l + \left(\frac{P_v}{T_v} - \frac{P_l}{T_l}\right) dV_v + \left(\frac{\mu_v}{T_v} - \frac{\mu_s}{T_s}\right) dN_v + \left(\frac{\mu_l}{T_l} - \frac{\mu_s}{T_s}\right) dN_l. \quad 2.12$$

From Equation 2.8, $dS_{tot} = 0$ needs to hold in all directions, i.e.

$$dS_{tot}|_{U_l,V_v,V_l,N_v,N_l} = dS_{tot}|_{U_v,V_v,V_l,N_v,N_l} = \cdots = dS_{tot}|_{U_v,U_l,V_v,V_l,N_l} = dS_{tot}|_{U_v,U_l,V_v,V_l,N_v} = 0. \quad 2.13$$

This leads to the following results:

Solving for $dU_v \neq 0$:

$$\left(\frac{1}{T_v} - \frac{1}{T_s}\right) dU_v = 0, \quad T_v = T_s. \quad 2.14$$

Solving for $dU_l \neq 0$:

$$\left(\frac{1}{T_l} - \frac{1}{T_s}\right) dU_l = 0, \quad T_l = T_s (= T_v). \quad 2.15$$

Solving for $dV_v \neq 0$:

$$\left(\frac{P_v}{T_v} - \frac{P_l}{T_l}\right) dV_v = 0, \quad P_v = P_l. \quad 2.16$$

A similar approach in $dN_v \neq 0$ and $dN_l \neq 0$ will also yield $\mu_l = \mu_s = \mu_v$.

These results show that chemical potentials, pressure and temperature need to be equal in all phases at VLE. The chemical potentials and temperature need to be constant in both space and time; otherwise, heat and mass transfer will occur (Vehkamäki, 2006). The pressure does not need to be constant in space, only in time, as is the case for equilibrium mixtures under the influence of a gravitational field (Debenedetti, 1988).

The VLE pressure of water can be computed as given by the International Association for the Properties of Water and Steam (IAPWS) (Wagner and Pruß, 2002)

$$\ln\left(\frac{P_v}{P_c}\right) = (\alpha_1 x + \alpha_2 x^{1.5} + \alpha_3 x^3 + \alpha_4 x^{3.5} + \alpha_5 x^4 + \alpha_6 x^{7.5}) T_r^{-1}. \quad 2.17$$

In this equation, P_c is the critical pressure of water and $x = 1 - T_r$, where T_r is the reduced temperature T/T_c having T_c as the critical temperature of water. The values for α are $\alpha_1 = 7.85951783$, $\alpha_2 = 1.84408259$, $\alpha_3 = 11.7866497$, $\alpha_4 = 22.680\,741\,1$, $\alpha_5 = 15.9618719$ and $\alpha_6 = 1.80122502$.

2.2.2 The Spinodal Limit of Stability

Thermodynamic quantities such as entropy and internal energy are virtually impossible to be controlled in an experiment. In focused ultrasound procedures, the thermodynamic variables which can be controlled are the acoustic pressure and the medium temperature. For example, in ex-vivo and in-vivo experiments, the temperature can be altered via acoustic heat deposition. For in-vitro experiments, ultrasound might solely be used to change the pressure in a medium. It is then useful to define the system's free energy by connecting it to a thermodynamic bath. A thermodynamic bath is a theoretical device representing an equilibrium system much bigger than the system under consideration. The bath is assumed to be so large that it can freely exchange heat and volume with the smaller system without changing its intensive properties (Vehkamäki, 2006). An isothermal and isobaric system without mass flux across its boundaries is desirable for this work. This leads to the choice of the Gibbs free energy defined as

$$G = U - TS + PV, \quad 2.18$$

where T and P are, respectively, the temperature and pressure of the system. This system is free to exchange heat and volume with its surroundings whilst keeping its pressure, temperature and number of molecules constant.

The minimum in free energy takes place at $\left(\frac{\partial^2 G}{\partial V^2}\right)_T > 0$. From the thermodynamic definition of pressure $\left(\frac{\partial G}{\partial V}\right)_T = -P$, it follows that

$$-\left(\frac{\partial P}{\partial V}\right)_T = \frac{1}{VK_T} > 0, \qquad 2.19$$

where K_T denotes the liquid's isothermal compressibility.

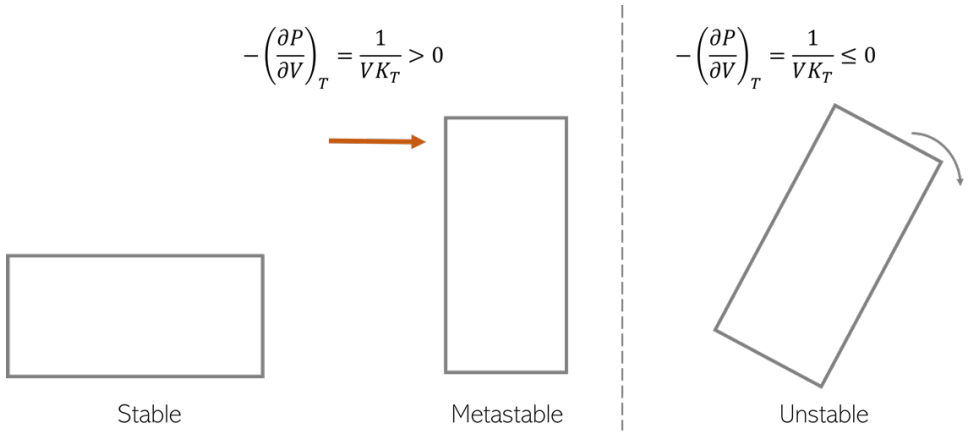

Figure 2-6. Schematic of phase stability.

In continuum thermodynamics, the isothermal limit of stability is obtained as $P \to P^S(T)$, where $P^S(T)$ is the spinodal pressure, an envelope in the P-V plane where $K_T \equiv -\left(\frac{\partial \ln V}{\partial P}\right)_T \to \infty$ (Speedy, 1982, 2002). At the spinodal, density fluctuations grow without limit due to the divergent liquid compressibility (Herbert, Balibar and Caupin, 2006). This process is illustrated in Figure 2-7. At the spinodal limit, the energy barrier that delays nucleation disappears, and a new phase forms spontaneously in a spinodal decomposition process (Lienhard, Shamsundar and Biney, 1986). In Figure 2-7 the spinodal and vapour-liquid equilibrium curves of a van der Waals fluid are plotted as an example. The vapour-liquid equilibrium (VLE) curve (black solid curve) is an upper limit of the metastable region, whilst the liquid (solid blue curve) and vapour spinodal (dashed blue curve) are the lower bounds of the metastable region. Liquid and vapour metastable regions meet at the critical point of the fluid.

This means that the first step into investigating bubble nucleation in HIFU is finding an approximation for the metastable envelope in a pressure-volume-temperature (P-V-T) diagram of the liquid under consideration. A fluid's metastable region is bound by its spinodal locus and the VLE curve. The spinodal of liquids

can be numerically approximated by applying the stability conditions $\left(\frac{\partial G}{\partial V}\right)_T = 0$ and $\left(\frac{\partial^2 G}{\partial V^2}\right)_T > 0$ to a suitable equation of state (EoS).

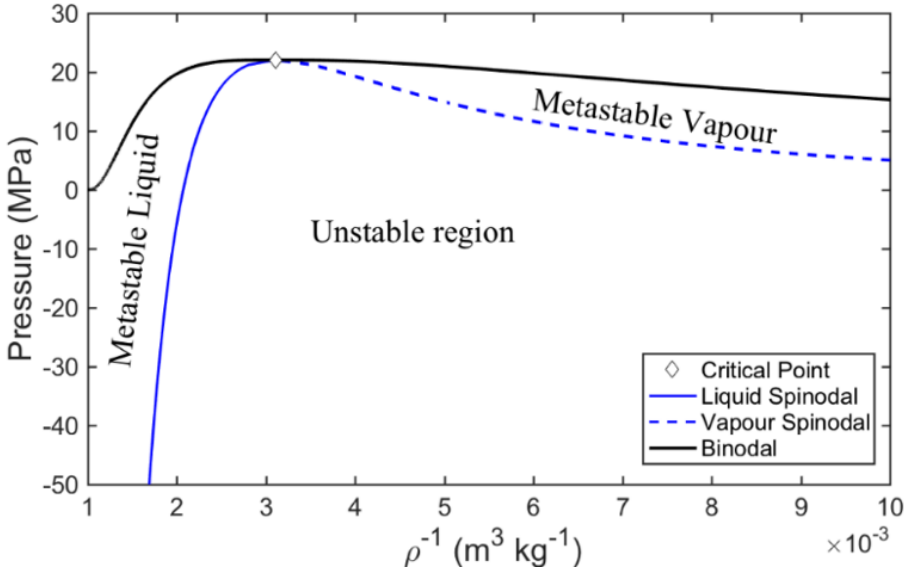

Figure 2-7 Representation binodal (VLE curve) and spinodal in a van der Waals fluid. Parameters outlined in Table 2-7.

The simplest EoS used for obtaining the spinodal pressure in liquids are the van der Waals, Redlich-Kwong (Redlich and Kwong, 1949) and Peng-Robinson (Peng and Robinson, 1976a) equations. These are cubic EoS capable of describing P-V-T relationships in fluids analytically in both liquid and vapour phases. All cubic EoS can be formulated in a general form with five parameters (Carey, 1988a).

$$P = \frac{RT}{V-b} + \frac{\phi_1(V-b)}{(V-b)(V^2+\phi_2 V+\phi_3)} \qquad 2.20$$

The constants for Equation 2.20 are given as:

Table 2-7. Parameters for cubic equations of state

	Model Parameters			Critical Parameters	
	ϕ_1	ϕ_2	ϕ_3	$\frac{bP_c}{RT_c}$	$\frac{aP_c}{(RT_c)^2}$
Van der Waals (vdW)	a	0	0	0.125	0.42188
Redlich-Kwong (RK)	$aT_r^{-0.5}$	b	0	0.08664	0.42748
Peng-Robinson (PR)	$a\alpha(T_r)$	$2b$	$-b^2$	0.0778	0.45724

where $T_r = T/T_c$ is the reduced temperature. The parameters a and b are fluid-dependent. They are obtained from replacing T_c, P_c and R in the expressions $\frac{bP_c}{RT_c}$ and $\frac{aP_c}{(RT_c)^2}$ and equalling this to the values shown in Table 2-7. The parameter $\alpha(T_r)$ is given by

$$\alpha(T_r) = [1 + (0.37464 + 1.54226w - 0.2699w^2)(1 - T_r^{0.5})]^2 \qquad 2.21$$

where w denotes the acentric factor (Pitzer, 1955; Pitzer *et al.*, 1955), a substance-specific constant.

The spinodal curve might be obtained either numerically or analytically from Equations 2.20 - 2.21 by applying the stability condition $-\left(\frac{\partial P}{\partial V}\right)_T = 0$ (Debenedetti, 1991).

For a van der Waals fluid, the spinodal pressure as a function of the reduced density $\rho_r = \rho/\rho_c$, where ρ_c is the critical density of water is given by

$$P_r^S = (3 - 2\rho_r)\rho_r^2. \qquad 2.22$$

The Redlich-Kwong equation for the spinodal pressure reads

$$P_r^S = 3.5412\left[\left(\frac{\rho_r^5}{2 + 0.2599\rho_r}\right)^{\frac{1}{3}}\left(\frac{1 + 0.2599\rho_r}{1 - 0.2599\rho_r}\right)^{\frac{2}{3}}\right] \times \left(\frac{1 - 0.676\rho_r - 0.5198\rho_r}{1 + 0.676\rho_r + 0.5198\rho_r}\right). \qquad 2.23$$

Finally, for the Peng-Robinson equation

$$P_r^S = \frac{\alpha(T_r)\rho_r^2(0.0394 - 0.0028\rho_r^2 - 0.0209\rho_r)}{0.0861 - 0.0061\rho_r^2 + 0.0457\rho_r}. \qquad 2.24$$

The liquid spinodal pressure predicted by the vdW and RK equations is substance independent. In most cases, the PR spinodal pressure curve is seen as an upper boundary for the spinodal pressure (Debenedetti, 1991).

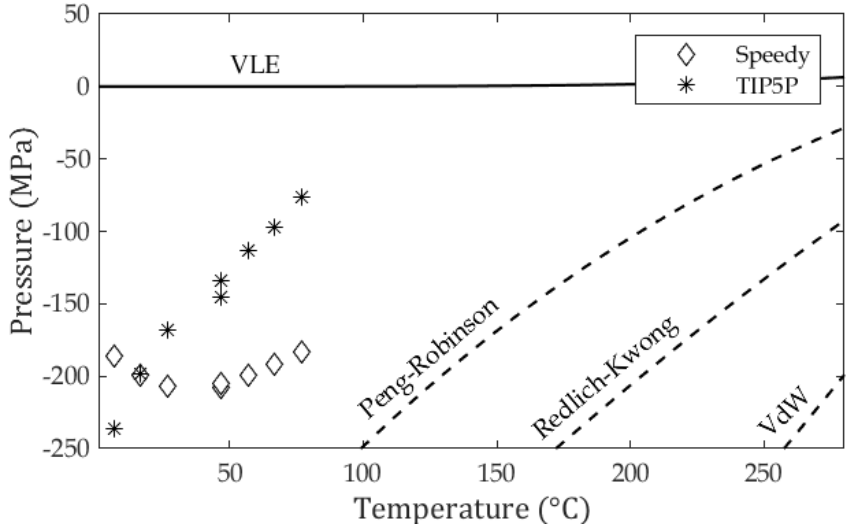

Figure 2-8. Comparison between temperature-dependent spinodal and the temperature-dependent vapour-liquid equilibrium pressure of water, spinodal pressures predicted by Eqs. 2.22 – 2.24 and numerical data obtained from the TIP5P and Speedy EoS.

Alternatively, EoS such as the Speedy EoS (Speedy, 1982) and the Five-site Transferable Interaction Potential (TIP5P) have been combined with van der Walls-Cahn-Hilliard theory to obtain predictions of the spinodal locus of water (Caupin, 2005). Analytical predictions of the water spinodal alongside Walls-Cahn-Hilliard theory numerical results and the VLE pressure of water are shown in a P-T diagram in Figure 2-9. In this figure, the regions between the VLE curve and the liquid spinodal are where the liquid is metastable, and nucleation might occur.

2.2.3 Liquid Metastability

Pure liquids are notable for the ability to withstand tensile pressures, possibly as low as -150 MPa, before a vapour phase appears, entering what is termed a metastable state (Azouzi *et al.*, 2013). Metastable liquid phases are those where the fluid is stretched below its saturation pressure or superheated above the boiling point (Herbert, Balibar and Caupin, 2006). Under HIFU sonication,

metastability might be induced in a liquid momentarily at the tensile part of the acoustic wave or through heat deposition via sound attenuation in thermoviscous media (Copelan *et al.*, 2015).

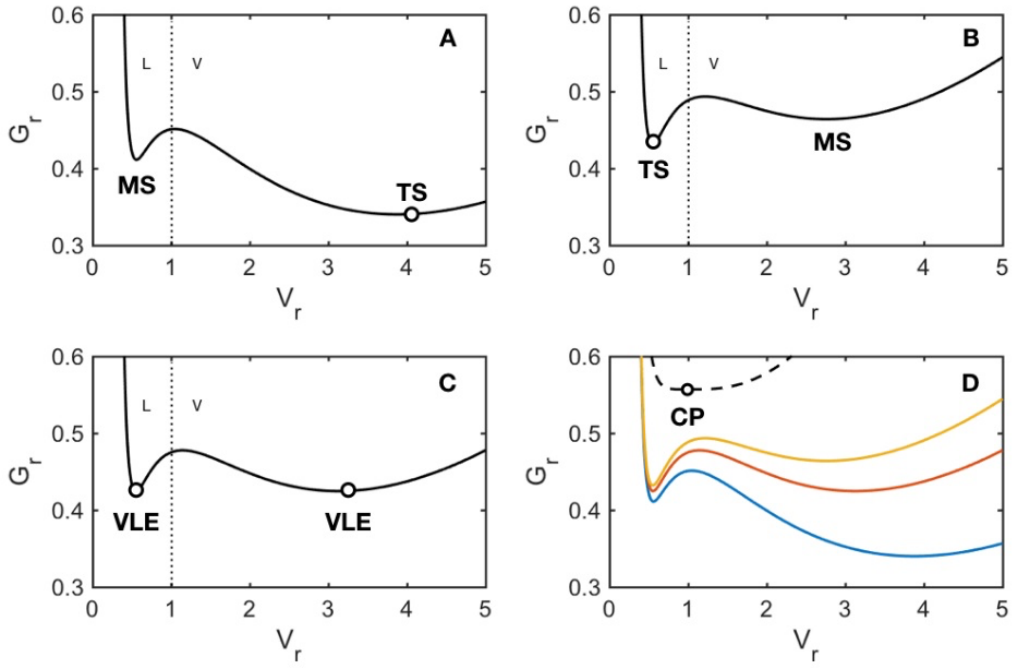

Figure 2-9. Reduced Gibbs free energy as a function of the reduced volume in a van-der-Waals fluid. (A) metastable liquid. (B) Metastable vapour. (C) VLE. (D) Comparison of cases A, B and C.

Thermodynamically, metastable phases (MS) are somehow *less-than-stable* phases. They correspond to local minima of the free energy in the system, whilst truly stable (TS) phases define the global free energy minimum at the same thermodynamic conditions (Kashchiev, 2000). Figure 2-10 illustrates the free energy of a van der Waals fluid as a function of its reduced volume. Taking V_r as the reduced volume of a liquid such that $V_r = \frac{V}{V_c}$, $V_r < 1$ represents liquid phases, whilst $V_r > 1$ represents vapour phases. $V_r = 1$ constitutes the critical point (CP) where any distinction between liquid and vapour phases disappears (Guggenheim, 1950).

Figure 2-9A represents the reduced Gibbs free energy of a metastable liquid. Although a metastable liquid has *some* stability in the liquid phase (it has a local G_r minimum), true stability can only be achieved upon the nucleation of a vapour bubble and subsequent mass transfer to the vapour phase. The same is

valid for Fig. 2-9B, which shows a metastable vapour, and proper stability will be achieved upon droplet formation in the vapour. Finally, Fig. 2-9C shows vapour-liquid equilibrium, the final stage of a first-order phase transition (Kashchiev 2000). At equilibrium, the system has two minima of the same depth. For this reason, no specific phase will be a global minimum, and both phases can coexist.

Metastability is only viable because phase transformations are delayed by the energetic costs of creating an interface in the bulk of a liquid. This is manifested as the barrier in the free energy that separates local from global minima and needs to be overcome before nucleation (Vehkamäki 2006). This barrier is illustrated as the maxima between all local and global minima in Figure 2-9.

2.3 The IAPWS model of water

Physical constants (Table 9) and expressions for thermodynamic properties of water were taken from the 1995 release by the International Association for the Properties of Water and Steam (IAPWS) (Wagner & Pruß 2002). Such values have been used in previous theoretical and experimental works on nucleation (Delale et al. 2003; Caupin et al. 2012). The expression for surface tension (Equation 4.20) was obtained from a revision of the 1994 IAPWS Secretariat release (Vargaftik et al. 1983).

Table 2-8. Physical constants. (Wagner & Pruß 2002)

Property	Symbol	Value	Unit
Molar mass	M	18.015 268 × 10^{-3}	kg mol^{-1}
Specific gas constant	R	461.518 05	J kg^{-1} K^{-1}
Acentric factor	ω	0.348	ND
Critical properties of water			
Temperature	T_c	647.096	K
Pressure	P_c	22.064	MPa
Density	ρ_c	322	kg m^{-3}
Viscosity	η_c	1 × 10^{-6}	Pa s

2.3.1 Vapour Pressure

The expression for the vapour pressure of water is given as

$$\ln\left(\frac{P_V}{P_c}\right) = (\alpha_1 x + \alpha_2 x^{1.5} + \alpha_3 x^3 + \alpha_4 x^{3.5} + \alpha_5 x^4 + \alpha_6 x^{7.5}) T_r^{-1}\,, \qquad 2.25$$

where $x = 1 - T_r$ and the values for α can be found in Table 2-9.

Table 2-9. Coefficients α for Equation 2.25 representing the vapour pressure of water. Obtained from (Wagner & Pruß 2002).

α_1	7.859 517 83
α_2	1.844 082 59
α_3	11.786 649 70
α_4	22.680 741 10
α_5	15.961 871 90
α_6	1.801 225 02

2.3.2 Saturated Densities

The IAPWS equations for the densities of the saturated liquid ρ_L and vapour ρ_V are such that

$$\rho_L = \rho_c(1 + b_1 x^{\frac{1}{3}} + b_2 x^{\frac{2}{3}} + b_3 x^{\frac{5}{3}} + b_4 x^{\frac{16}{3}} + b_5 x^{\frac{43}{3}} + b_6 x^{\frac{110}{3}}), \quad 2.26$$

and

$$\ln\left(\frac{\rho_V}{\rho_c}\right) = c_1 x^{\frac{2}{6}} + c_2 x^{\frac{4}{6}} + c_3 x^{\frac{8}{6}} + c_4 x^{\frac{18}{6}} + c_5 x^{\frac{37}{6}} + c_6 x^{\frac{71}{6}}, \quad 2.27$$

where the values for constants b and c can be found in Table 6.

Table 2-10. Coefficients b and c for Equations 2.26 and 2.27 representing the saturated liquid and vapour densities of water. Obtained from (Wagner & Pruß 2002).

b_1	1.992 740 64	c_1	- 2.031 502 40
b_2	1.099 653 42	c_2	- 2.683 029 40
b_3	- 0.510 839 303	c_3	- 5.386 264 92
b_4	- 1.754 934 79	c_4	- 17.299 160 50
b_5	- 45.517 035 2	c_5	- 44.758 658 10
b_6	-6.746 944 50×10^5	c_6	- 63.920 106 30

2.3.3 Viscosity

The dynamic viscosity of pure water η was obtained from the Release on the IAPWS Formulation 2008 for the Viscosity of Water Substance (Sengers & Parsi 2009; Huber et al. 2009). η is of the form:

$$\eta = \eta_0 \eta_1 \eta_2, \quad 2.28$$

where $\eta_2 = 1$ away from the critical point (Huber et al. 2009). η_0 and η_1 are defined as (Huber et al. 2009; Sengers & Parsi 2009)

$$\eta_0(T) = 100\sqrt{T_r}\left(\sum_{i=0}^{3}\frac{H_{0_i}}{T_r^i}\right)^{-1}, \qquad 2.29$$

and

$$\ln(\eta_1) = \rho_r \sum_{i=0}^{5}\left[\left(\frac{1}{T_r}-1\right)^i \sum_{j=0}^{6} H_{1_{ij}}(\rho_r - 1)^j\right], \qquad 2.30$$

where ρ_r is the reduced density of the liquid, the coefficients of H_0 are defined in Table 12 and coefficients for H_1 defined in Table 2-11.

Table 2-11. Coefficients i and H_0 for Equation 2.29 of the viscosity of water. (Huber et al. 2009; Sengers & Parsi 2009)

i	H_{0_i}
0	1.677 52
1	2.204 62
2	0.636 656 4
3	-0.241 605

Table 2-12. Coefficients i, j and H_1 for Equation 2.30 of the viscosity of water. (Huber et al. 2009; Sengers & Parsi 2009)

i	j	$H_{1_{ij}}$
0	0	5.20094×10^{-1}
1	0	8.50895×10^{-2}
2	0	-1.08374
3	0	-2.89555×10^{-1}
0	1	2.22531×10^{-1}
1	1	9.99115×10^{-1}
2	1	1.88797
3	1	1.26613
5	1	1.20573×10^{-1}
0	2	-2.81378×10^{-1}
1	2	-9.06851×10^{-1}
2	2	-7.72479×10^{-1}
3	2	-4.89837×10^{-1}
4	2	-2.57040×10^{-1}
0	3	1.61913×10^{-1}
1	3	2.57399×10^{-1}
0	4	-3.25372×10^{-2}
3	4	6.98452×10^{-2}
4	5	8.72102×10^{-3}
3	6	-4.35673×10^{-3}
5	6	-5.93264×10^{-4}

Where zero terms in $H_{1_{ij}}$ were not included in Table 2-12.

The range of validity of Equation A.4 is given by (Sengers & Parsi 2009)

$$\begin{cases} 0\ ^\circ\mathrm{C} \le T \le 150\ ^\circ\mathrm{C} & 0\ \mathrm{MPa} \le P_L \le 500\ \mathrm{MPa}, \\ 150\ ^\circ\mathrm{C} \le T \le 600\ ^\circ\mathrm{C} & 0\ \mathrm{MPa} \le P_L \le 350\ \mathrm{MPa}, \\ 600\ ^\circ\mathrm{C} \le T \le 900\ ^\circ\mathrm{C} & 0\ \mathrm{MPa} \le P_L \le 300\ \mathrm{MPa}. \end{cases}$$

2.3.4 Enthalpy of Vaporisation

The molecular enthalpy of vaporisation of water $\Delta H_v = H_V - H_L$ is calculated from the Clapeyron equation (Polling et al. 2001) and approximated with the 1995 IAPWS formulation for vapour pressures and saturated densities where $\Delta V_v = \frac{1}{\rho_V} - \frac{1}{\rho_L}$ is the difference in volume of the saturated vapour and liquid, (Wagner & Pruß 2002):

$$\frac{dP_V}{dT} = \frac{\Delta H_V}{T\Delta V_V} \approx \left(\frac{1}{\rho_L} - \frac{1}{\rho_V}\right)\left(\frac{dP_V}{dT}\right) T \times 10^3 \qquad 2.31$$

2.3.5 Thermal Conductivity

The thermal conductivity of liquid water away from the critical point κ was obtained from the Revised Release on the IAPWS Formulation 1985 for the Thermal Conductivity of Ordinary Water Substance (Sengers & Watson 1986). κ is of the form:

$$\kappa = \kappa_0 \kappa_1 \kappa_2, \qquad 2.32$$

where $\kappa_2 = 1$ away from the critical point. κ_0 and κ_1 are defined as (Sengers & Watson 1986)

$$\kappa_0(T) = \sqrt{T_r}\left(\sum_{i=0}^{3} \frac{L_{0_i}}{T_r^i}\right)^{-1}, \qquad 2.33$$

and

$$\ln(\kappa_1) = \rho_r \sum_{i=0}^{5}\left[\left(\frac{1}{T_r} - 1\right)^i \sum_{j=0}^{6} L_{1_{ij}} (\rho_r - 1)^j\right], \qquad 2.34$$

where ρ_r is the reduced density of the liquid, the coefficients of L_0 are defined in Table 2-13 and coefficients for L_1 defined in Table 2-14.

Table 2-13. Coefficients i and L_0 for Equation 2.33 of the thermal conductivity of water. (Sengers & Watson 1986)

i	L_{0_i}
0	1.000
1	6.978 267
2	2.599 096
3	-0.998 254

Table 2-14. Coefficients for L_1 in Equation 2.34 of the thermal conductivity of water. (Sengers & Watson 1986)

j	$L_{1_{0j}}$	$L_{1_{1j}}$	$L_{1_{2j}}$	$L_{1_{3j}}$	$L_{1_{4j}}$
0	1.3293046	1.7018363	5.2246158	8.7127675	-1.8525999
1	-0.40452437	-2.2156845	-10.124111	-9.5000611	0.93404690
2	0.24409490	1.6511057	4.9874687	4.3786606	0
3	0.018660751	-0.76736002	-0.27297694	-0.91783782	0
4	-0.12961068	0.37283344	-0.43083393	0	0
5	0.044809953	-0.11203160	0.13333849	0	0

Where the rage of validity of Equation 2.34 is given by (Sengers & Parsi 2009)

$$\begin{cases} 0\,^{\circ}\mathrm{C} \leq T \leq 125\,^{\circ}\mathrm{C} & P_L \leq 400\ \mathrm{MPa}, \\ 125\,^{\circ}\mathrm{C} \leq T \leq 250\,^{\circ}\mathrm{C} & P_L \leq 200\ \mathrm{MPa}, \\ 250\,^{\circ}\mathrm{C} \leq T \leq 400\,^{\circ}\mathrm{C} & P_L \leq 150\ \mathrm{MPa}. \end{cases}$$

2.4 Chapter Summary

In this Chapter, an integrative literature review was carried out to pose the initial research questions that guided the development of original work in Chapters 3 – 6 in this thesis, which are summarised in Chapter 7. Through a review of the literature, it has been identified that there is a wide range of empirical work on

ultrasound-induced cavitation that can be used to inform and guide the process of modelling ultrasound bubble nucleation mathematically. Amongst the ultrasound-based techniques that exploit the nucleation and activity of bubbles, histotripsy is highlighted as a leading example with regards to the repeatability of the bubble nucleation process. The findings of this literature delineate novel ways to integrate knowledge and findings in domains such as phase-equilibrium thermodynamics and ultrasound cavitation, which were previously thought to be unrelated, into a coherent and novel whole for the simulation, planning and optimisation of histotripsy protocols.

Currently, boiling and intrinsic pressure histotripsy are parameterised and planned in terms of the mechanistic trigger assumed to cause bubble nucleation following from extensive empirical validation carried out over the past fifteen years. This understanding is materialised as the achievement of temperatures around 100 $^{\circ}$C within milliseconds timescales for boiling histotripsy (the time-to-boil), and pressures below – 28 MPa for intrinsic pressure histotripsy. Nonetheless, when the literature on phase equilibrium thermodynamics is taken into consideration, it is possible to hypothesise that both techniques exist at different extremes of a single process. Here, a research opportunity to integrate empirical and theoretical evidence between two fields arises. At the forefront of this opportunity is the need for a more informative distinction between cavitation and nucleation. Through this literature review it has been found that a convincing argument can be made for the terminology of cavitation being used to refer to the detectable activity of bubbles in the presence of an acoustic field, and nucleation as the mechanism by which a metastable fluid relaxes towards stability through the creation of a new phase.

A detailed look into the techniques used for research on ultrasound-induced nucleation reveals important established knowledge about the phenomenon, summarised as:

(i) Nucleation thresholds are highly sensitive to the timescales at which tensile pressures are applied, and acoustic methods can reach significantly higher magnitude tensile pressures in shorter time periods as compared to techniques such as a Berthelot tube. It was

found that sonication with acoustic shockwaves have been the most successful and repeatable method for investigating liquid water deep into its metastable zone with regards to a varying pressure. In this way, the mechanistic understanding of histotripsy in all its varieties is characterised as an informative case-study of the broad phenomenon of nucleation in water.

(ii) Although the literature in boiling histotripsy suggests that bubble formation takes place as an analogue of boiling in untreated water volumes at atmospheric pressure, previous empirical evidence has demonstrated that water is able to sustain superheats as high as 279.5 ˚C before boiling. Moreover, recent evidence has shown that an equation of state can be defined for metastable water from 0 to 200 ˚C within ultrasound experiments, contesting that the fundamental mechanism at play in boiling histotripsy shares features to the literal meaning of boiling in everyday life. This brings to question the appropriacy of parametrising boiling histotripsy protocols such that the main energetic objective is to reach temperatures around 100 ˚C. Here, a need to understand the intricate interplay between pressures and temperatures in the nucleation of a gas phase in a liquid is revealed.

(iii) Nucleation thresholds as a phenomenon require investigation in purified, de-gassed liquids. In the presence of pre-existing bubbles, the nucleation threshold will be drastically reduced in magnitude unless the fluid has been subjected to a static positive pressure field that forces the gas within bubbles back into solution in the liquid. Although this finding involves material restrictions to the performance of histotripsy protocols, it also justifies focused ultrasound as a preferred methodology, since the small focal volumes and short tensile periods minimise the possibility that an experiment will be affected by impurities in the fluid.

(iv) The protocol identified as the most rigorous and practical for the detection of bubble nucleation in acoustic fields employs

hydrophones to detect acoustic emissions from cavitation bubbles. Within this signal, a threshold can be established to distinguish between noise and bubble activity. By extensive repetition of pulsed ultrasound sonication at fixed parameters, it is possible to approximate a cumulative density function for the probability of nucleation. This function has been repeatedly shown to take the shape of a sigmoid, which can be interpreted as a threshold phenomenon with a degree of uncertainty. Finally, the median of such cumulative distribution can be assigned as the nucleation threshold of a medium with known precision and quantification of uncertainty.

The questions and issues listed above give rise to the need of a quantitative framework to evaluate the occurrence of bubble nucleation and cavitation in ultrasound fields. This framework is required to connect practical ultrasound parameters such as electrical powers provided to transducers, pulse repetition frequencies and duty cycles to their resulting effects in the propagation medium, such as waveforms, peak-focal pressures, heating rates, and the probability of bubble nucleation. In this literature review, it has been identified that in the absence of pre-existing bubbles, the formation of a new phase in a liquid can happen through two related, but distinct, mechanisms. The first is nucleation, which is the way in which a single-phase fluid stretched below its vapour pressure at constant temperature relaxes towards becoming a two-phase system. The second, and less frequent, is spinodal decomposition, a phenomenon that takes place instantaneously should a fluid be brought to an unstable thermodynamic state. The fundamental theory identified for the treatment of bubble nucleation in acoustic fields was the theory of phase equilibrium in pure water volumes. This theory uses metrics of free energy such as the chemical potential of a substance to yield a numerical reference to its likelihood of changing phases. The theory of phase equilibrium underpins the development of the models shown in Chapters 3 and 4, which demonstrate the practical application of these concepts in simulating nucleation in boiling histotripsy.

Moreover, within the theory of phase equilibrium there is an intrinsic dependence of parameters on both pressure and temperature of the liquid. On the one hand, this suggests that a joint thermodynamic and hydrodynamic approach is needed for appropriate understanding of bubble nucleation and the growth of bubble nuclei. This approach should merge existing modelling frameworks such as that of vapour-liquid equilibrium and of bubble dynamics into synthesising joint energetic and dynamic information about bubbles and is explored in further depth in Chapter 5. Regrettably, this two-way dependence of phase equilibrium on pressure and temperature can create a large number of logistical challenges for the modelling process for ultrasound propagation. That is, if every variable needs to be evaluated in terms of both temperature and pressure, the timescales of analysis are then refined into the shortest timescales within acoustic simulations, and this would imply a large computational cost and unwarranted complexity. Throughout this thesis, this challenge is addressed with a blend of practical logistic assumptions and mathematical analysis:

(i) Through the literature review, it was found that the sensitivities of parameters such as density and thermal conductivity to the liquid's pressure are negligible at pressures below atmospheric pressure, and expressions for their behaviour at negative pressures are scarce or inexistent. Therefore, a simplifying assumption that the viscosity and thermal conductivity of water do not vary with pressure is made herein *a* priori.

(ii) This heuristic question brings forth an important research question regarding the intersections of phase-change thermodynamics and acoustics. At the heart of the question is evaluating whether the timescales of ultrasound propagation are sufficiently long such that thermodynamic processes can reach their steady-state form as represented by the theory of thermodynamic stability. This constrain to the modelling process is analysed mathematically and discussed in Chapter 6.

Chapter 3

A Thermodynamic Model of Bubble Nucleation

Acknowledgement: The contents of this chapter are based on (de Andrade et al., 2021). Figures 3-2, 3-3, 3-4, 3-5, 3-6 and 3-7 have been reproduced with authorisation of the publisher.

This Chapter establishes the thermodynamic basis for modelling bubble nucleation in focused ultrasound fields. It presents an overview of the thermodynamic stability of liquid and vapour phases and exemplifies the concept of metastability at temperatures and pressures relevant to ultrasound-induced bubble nucleation.

In this Chapter, a mathematical model of nucleation of bubbles that grow exclusively by vapour (diffusive) transport from the medium is developed from the first principles. This first-order, steady-state approximation is parameterised with experimental data of bubble nucleation in water at both low and high temperatures taken from Tables 2-1, 2-2 and 2-3 presented in Chapter 2. Thermodynamic quantities of water are calculated with the IAPWS expressions reviewed in section 2.3 of the literature review.

Within this Chapter it is argued that a surface activity coefficient can account for both homogeneous and heterogeneous nucleation events. This results in a temperature-dependent activity factor that can harmonise Classical Nucleation Theory (CNT) (Kashchiev, 2000) predictions and focused ultrasound experiments when multiplied by the surface tension of water. The models and results discussed within this Chapter are largely based on previously published results in (de Andrade *et al.*, 2019). Outline of simplifying assumptions and their impact on applicability or generalisability of results presented in this chapter:

- Homogeneous Liquid Assumption: The initial state of the system is considered to be a homogeneous liquid, modelled herein with the properties of pure water. This simplification overlooks the presence of micro-heterogeneities or pre-existing nuclei in the liquid, which could influence the nucleation process. The impact is a potentially oversimplified view of nucleation initiation, particularly in systems where impurities or surface irregularities play a significant role. Improvements in the model to avoid assumption are proposed as avenues for future work in Chapter 7.
- Constant Chemical Composition: The chemical composition of the liquid is assumed constant, simplifying the model by not accounting for possible changes in chemical potential due to chemical reactions. This assumption limits the model's applicability to systems where chemical reactions occur during nucleation. Improvements in the model to avoid assumption are proposed as avenues for future work in Chapter 7.
- Time-Independent Nucleation in a Transient Acoustic and Temperature Field: The model assumes the nucleation process to be time-independent, despite the transient nature of the acoustic field and subsequent temperature fields. This simplification overlooks the dynamic interactions between the nucleating bubbles and the fluctuating pressures and temperatures, potentially limiting the model's accuracy in predicting nucleation under varying acoustic conditions. This is discussed in detail in Chapter 6.
- Time-Averaged Approximation for Ultrasound Nucleation: The approximation assumes that changes in pressure and temperature are negligible over a small integration interval, allowing for a time-averaged approach. This assumption may not capture the nuances of rapid or significant fluctuations in the acoustic field, affecting the model's predictive power for nucleation rates in highly dynamic environments. This is discussed in detail in Chapter 6.

- Phenomenological Approximation to Nucleation Pressure Threshold: The model employs a phenomenological approach to determine the nucleation pressure threshold, relying on finding a linear regression for the surface temperature with respect to the pressure and temperature in the liquid as taken from experimental studies. This method's accuracy depends on the accuracy of the experimental results used to parameterise the surface tension.
- Temperature-Dependent Scaling Factor for Surface Tension: The introduction of a temperature-dependent scaling factor for surface tension aims to align theoretical predictions with experimental data. However, this approach assumes a specific relationship between temperature and surface tension that may not hold across all conditions or for all substances, potentially limiting the model's accuracy and generalisability.
- Impact of Substrates on Nucleation: The model differentiates between homogeneous and heterogeneous nucleation based on the presence and type of substrates (impurities), simplifying the complex interactions at play. This approach may not fully capture the nuances of nucleation in systems with a mix of stabilising and destabilising impurities or accurately predict the impact of substrates on nucleation rates and thresholds.

3.1 Free Energy of Bubble Nucleation

In an isolated system, bubble nucleation is the transition from an initial state consisting of a homogeneous liquid to a final stage consisting of a bubble embryo surrounded by the liquid. The initial internal energy of the homogeneous liquid has the form:

$$U_0 = T_0 S_0 - P_0 V_0 + \mu_l^0 N_l^0. \qquad 3.1$$

In Equation 3.1, $U, T, S, P, V, \mu,$ and N represent the liquid's internal energy, temperature, entropy, pressure, volume, chemical potential, and number of molecules, respectively. A zero subscript or superscript refers to initial conditions of the system. Where σ represents the surface tension of the liquid, the final internal energy of the system has contributions from the liquid, vapour, and surface phases:

$$U = T_0 S - P_v V_v - P_l V_l + \sigma A + \mu_v N_v + \mu_l N_l + \mu_s N_s. \quad 3.2$$

Assuming that the pressure in the liquid is constant between the two stages ($P_0 = P_l$) and that this is a mass conservative system ($N_{tot} = N_l^0$), a Gibbs potential can be used with equations 3.1 and 3.2 to derive the free energy barrier for this process. The Gibbs free energy in the initial state is:

$$G_0 = U_0 - T_0 S_0 + P_0 V_0 = \mu_l^0 N_l^0, \quad 3.3$$

and the free energy at the final state is:

$$\begin{aligned} G &= U - T_0 S + P_0 (V_l + V_v) \\ &= P_0 (V_l + V_v) - P_l V_l - P_v V_v + \sigma A + \mu_l N_l + \mu_v N_v + \mu_s N_s. \end{aligned} \quad 3.4$$

By assuming that the chemical composition of the liquid remains constant ($\mu_l^0 = \mu_l$), the free energy of bubble formation is given by:

$$\begin{aligned} \Delta G = G - G_0 = (P_l - P_v) V_v + \sigma A - (\mu_l - \mu_v) N_v \\ - (\mu_l - \mu_s) N_s. \end{aligned} \quad 3.5$$

This expression is derived under the assumption that the initial homogeneous liquid system is much larger than the bubble embryo. Literature data on the size of ultrasound-induced bubble nucleation (Davitt, Arvengas and Caupin, 2010) estimates bubble nuclei to be of the order of nanometres at nucleation. For HIFU nucleation, the initial homogeneous system would be as large as the focal volume of the transducer being used.

3.1.1 Unstable Equilibrium

Metastable and truly stable phases are separated by a local maximum $\left(\frac{\partial \Delta G}{\partial V}\right)_{T,P,N}$ in the change of free energy in the system. This local maximum corresponds to the energy barrier that needs to be overcome so that nucleation can occur and defines the critical point of nucleation (Vehkamäki, 2006). The critical point of nucleation is a state of unstable equilibrium, for it demarks the boundary between thermodynamic conditions of spontaneous growth or spontaneous collapse of embryos of the new phase (Kashchiev, 2000). Assuming isothermal, isobaric nucleation and applying the condition of criticality to Eq. 3.5 yields

$$\left(\frac{\partial \Delta G}{\partial V}\right)_{T,P,N} = (P_l - P_v) + \sigma\left[\frac{dA}{dV}\right] + \left[\frac{d\sigma}{dV}\right]A = \\ (P_l - P_v) + \sigma\left(\frac{dA}{dr}\right)\left(\frac{1}{\frac{dV}{dr}}\right) + \left(\frac{d\sigma}{dr}\right)\left(\frac{1}{\frac{dV}{dr}}\right)A = 0. \qquad 3.6$$

If the embryos of the new phase are assumed to be spherical, Eq. 3.6 yields the generalised Laplace equation

$$P_v - P_l = \frac{2\sigma}{r} + \left(\frac{d\sigma}{dr}\right), \qquad 3.7$$

where r is the radius of the bubble embryo. Equation 3.25 states that the surface energy, and hence the free energy of bubble formation, is size-dependent. A similar analysis for $\left(\frac{\delta \Delta G}{\delta N_v}\right)_{T,P,N_s}$ and $\left(\frac{\delta \Delta G}{\delta N_s}\right)_{T,P,N_v}$ will yield conditions of chemical equilibrium $\mu_l = \mu_v = \mu_s$.

3.1.2 The Dividing Surface

The value of $\left(\frac{d\sigma}{dr}\right)$ in Eq. 3.7 depends on the placement of the *dividing surface* (DS), i.e., the interfacial boundary between liquid and vapour phases. The position of the dividing surface determines the volume of the old and new phases

at nucleation and the surface area of the new phase embryo (Kalikmanov, 2013). The choice of dividing surface establishes a connection between the mathematical model and experimentally measurable quantities and provides meaningful simplification of the problem (Kashchiev, 2003).

Amongst the various choices of DS, two are highlighted:

i) **The surface of tension (SoT)** (Gibbs, 1928). This choice states that a spherical membrane with no rigidity and uniform tension across the surface separates liquid and vapour phases. It is the only case where the surface tension is the same as the specific surface energy of a spherical embryo. (Kashchiev, 2003). The most important feature of the surface of tension is that it is defined such that $\left(\frac{d\sigma}{dr}\right) = 0$ and Eq. 3.7 is simplified to the Laplace equation of mechanical equilibrium (Vehkamäki, 2006).

ii) **The equimolecular dividing surface (EDS)** (Gibbs, 1928). The surface tension is independent of the radius of curvature of the embryo. The equimolecular surface is defined such that $N_s = 0$ and $N_v = N_l$ (Vehkamäki, 2006). In this case, the relationship between σ and r follows the generalised Laplace equation Eq. 3.7 and can only be determined by prior knowledge of the spatial profile of density fluctuations across the dividing surface. Such functions can only be obtained by statistical-molecular models and not by purely thermodynamic methods (Kashchiev, 2003). In this work, the surface of tension is the dividing surface of choice. The surface of tension is one whose thermodynamic and mechanical definitions are the same, and this is a valuable property for the development of hydrodynamic models for nucleation in *Chapter 5*.

3.1.3 The Critical Work of Nucleation

The size-dependent energy barrier for creating a stable phase in a metastable fluid is given by the work of nucleation. Employing the surface of tension as the DS of choice and replacing conditions of unstable equilibrium into Eq. 3.6 yields

$$W^* = \Delta G^* = \frac{2\sigma}{r^*}\left(\frac{4\pi}{3}\right)r^{*3} + \sigma 4\pi r^{*2} = \left(\frac{1}{3}\right)\sigma 4\pi r^{*2}, \quad 3.8$$

where r^* is the radius of the critical nucleus, also termed the critical size. In terms of the pressure in the liquid and vapour phases:

$$W^* = \left(\frac{16\pi}{3}\right)\frac{\sigma^3}{(P' - P_l)^2}. \quad 3.9$$

Where P' is the internal pressure in a critical nucleus. This form of the critical nucleation work has been extensively used in recent works on bubble nucleation in liquids (Caupin, 2005; Herbert, Balibar and Caupin, 2006; Davitt, Arvengas and Caupin, 2010). In short, the work W^* is an account of the energy needed to bring nanoscopic thermal fluctuations to a critical size r^* where the bubble nucleus has equal chances of spontaneous growth and collapse.

3.1.4 The Nucleation Rate

The critical work for nucleation is used to predict the nucleation rate. This is the net rate at which bubbles reach the critical size. The critical size r^* of a bubble is a threshold at which the system under consideration cannot be considered a single-phase system anymore. The nucleation rate is the rate at which the number of critical bubbles form per unit time and is proportional to the difference between the forward rates of vaporisation and the backward rates of condensation (Kashchiev, 2000; Vehkamäki, 2006). Assuming that the timescales of nucleation are much shorter than the tensile period of the ultrasound wave, the nucleation rate can be approximated as a stationary quantity (Davitt, Arvengas and Caupin, 2010). The validity of this approximation will be discussed in-depth in *Chapter 6*.

The nucleation rate is an equilibrium average in time and space for the number of critical nuclei formed in the system under consideration. At the critical size, the steady-state nucleation rate is usually represented as (Blander, 1979; Delale, Hruby and Marsik, 2003; Herbert, Balibar and Caupin, 2006; Vehkamäki, 2006; Davitt, Arvengas and Caupin, 2010)

$$J_{ss} = J_0 \exp\left(-\frac{W^*}{k_B T}\right). \qquad 3.10$$

In this equation, the pre-exponential term J_0 accounts for the average kinetic and spatial properties of nucleation, W^* is the critical work of nucleation defined in Eq. 3.9, k_B is Boltzmann's constant and T is the temperature of the medium. Equation 3.10 defines an upper mathematical bound for the nucleation rate since $J_{ss} \to J_0$ for $W^* \to 0$. By neglecting the effects of viscosity and inertia in the liquid (Kashchiev, 2000), J_0 can be defined in the form $J_0 = N_0\sqrt{\frac{2\sigma}{\pi m}}$, where $N_0 = \rho_L/m$, having ρ_L as the liquid density and m as the molecular mass of the liquid. J_0 has units of nuclei per unit volume and per unit time. The implications of this assumption will be discussed in detail in Chapter 5.

3.1.5 The Tensile Strength of Liquids

At sufficiently high nucleation rates, the control volume under consideration cannot be considered a single-phase volume anymore. The pressure and temperature in the liquid at this point are the nucleation threshold. For steady-state nucleation, the number of critical nuclei Σ formed in a volume V_0 during a time interval Δt_N can be approximated by

$$\Sigma = V_0 \int_0^{\Delta t_N} J_{ss}(P_l, T)dt, \qquad 3.11$$

where J_{ss} is the nucleation rate in a liquid at a pressure P_l and temperature T (Fisher, 1948). The quantity Δt_N has been referred to as the "mean-lifetime of the metastable fluid" (Baidakov, 2016), the "average time of formation of the first supercritical nucleus" (Schmelzer, Abyzov and Baidakov, 2017) or the "experiment/observation time" at the steady state (Herbert, Balibar and Caupin, 2006). Further consideration into the role of Δt_N in the nucleation process is given in Chapter 6.

The definition of J_{ss} in Eq. 3.11 is time-independent, but the acoustic field causes P_l and T to be transient. By assuming that the integration interval Δt_N is sufficiently small so that no appreciable changes in J_{ss} occur due to variations in T and P_l, Σ can be approximated as

$$\Sigma \cong J_{ss}^{*} V_0 \Delta t_N. \qquad 3.12$$

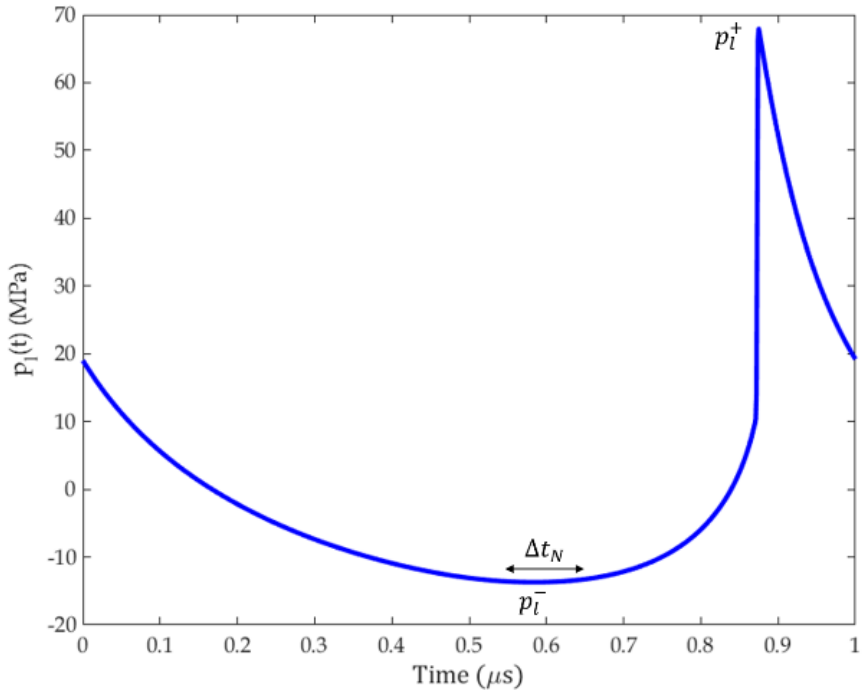

Figure 3-1. Simulated example of a focal waveform for HIFU propagation in water at 1 MHz.

Considering the formation of the first Σ nuclei, the detectable nucleation rate is defined as

$$J_{ss}^{*} = \frac{\Sigma}{V_0 \Delta t_N}, \qquad 3.13$$

where Σ is the nuclei in a volume V_0 after Δt_N seconds in an experiment. The appropriacy of this time-averaged approximation to ultrasound nucleation is also examined in Chapter 6.

Defining V_0 as a control volume where Σ bubbles nucleate after Δt_N seconds, the value of this parameter is assumed to be the volume within the -3 dB

drop in intensity at the transducer focus (Davitt, Arvengas and Caupin, 2010). Therefore, the choice of V_0 depends on the transducer geometry.

Given the nucleation rate J_{ss} that forms the first Σ nuclei in a time-volume setup $V_0 \Delta t_N$, a phenomenological approximation to the nucleation pressure threshold of a liquid can be obtained by solving Eqs. 3.31 and 3.28 in terms of the pressure in the liquid P_l. This approach for obtaining the temperature-dependent nucleation pressure threshold $P_l^N(T)$ was first employed in (Fisher, 1948) and has also been used in more recent work in bubble nucleation (Balibar and Caupin, 2003; Herbert, Balibar and Caupin, 2006).

Equating Eqs. 3.12 and 3.11, replacing the critical work of nucleation given by Eq. 3.9 and solving for P_l gives

$$P' - P_l^N = \left(\frac{16\pi\sigma^3}{3k_B T \ln\left(\frac{J_0 V_0 \Delta t_N}{\Sigma}\right)} \right)^{\frac{1}{2}}. \qquad 3.14$$

In this expression, P_l^N is the pressure P_l in the liquid at which an average of Σ nuclei appear during a time interval Δt_N in a homogeneous volume of liquid V_0 at a temperature T. A Poynting correction (Delale, Hruby and Marsik, 2003) allows the VLE pressure of the liquid to be used instead of the nucleus internal pressure P'. At high pressures, these are different quantities because of the assumption of unstable equilibrium used to obtain Eq. 3.9.

The pressure drop $(P' - P_l)$ can be accurately approximated by

$$(P' - P_l) = \zeta (P_v - P_l). \qquad 3.15$$

where $\zeta = 1 - \left(\frac{\rho_v}{\rho_l}\right) + \frac{1}{2}\left(\frac{\rho_v}{\rho_l}\right)^2$, and ρ_v and ρ_l denote the saturated densities of vapour and liquid water, respectively. The nucleation pressure threshold then assumes the form

$$P_l^N = P_v - \frac{1}{\zeta}\left(\frac{16\pi\sigma^3}{3k_B T \ln\left(\frac{J_0 V_0 \Delta t_N}{\Sigma}\right)}\right)^{\frac{1}{2}}. \qquad 3.16$$

This quantity can be evaluated by using standard thermodynamic quantities such as the VLE pressure of the liquid P_v and its density in the liquid and vapour phases. For the calculation of P', the IAPWS equations for the densities of the saturated liquid ρ_l and vapour phases of water ρ_v were employed as described in section 2.3.

3.2 The Surface Tension

The surface tension of a planar liquid-vapour interface of pure water is given by:

$$\sigma_\infty(T) = \sigma_1[1 - T_r]^{\sigma_2}[1 + \sigma_3(1 - T_r)], \qquad 3.17$$

where T_r is the reduced temperature, σ_1 = 235.8 × 10^{-3} Nm^{-1}, σ_2 =1.256 and σ_3 = -0.625. As established by the Gibbs phase rule (Turkevich and Mann, 1990), the surface tension of pure water depends only on the system's temperature (Takaishi, 1997). Alternatively, a strong pressure dependence on the liquid will be seen for water-gas mixtures, especially at low temperatures or high pressures (Chun and Wilkinson, 1995).

Pendant drop measurements of the surface tension of water-carbon dioxide systems report relaxation times up to fifteen minutes for the surface tension of water-gas mixtures to assume their pressure-dependent value (Hebach *et al.*, 2002). Considering that histotripsy nucleation takes place in timescales shorter than one second, it is assumed in this work that the effects of dissolved contaminant gas in the liquid are negligible in HIFU-induced nucleation.

3.2.1 Phenomenological Corrections to the Surface Tension

Finding an appropriate approximation for the surface tension is an essential step in implementing CNT (Bruot and Caupin, 2016). Approximations of the surface tension such as Equation 3.38 have been used to apply CNT in the modelling of bubble nucleation (Delale, Hruby and Marsik, 2003; Davitt, Arvengas and Caupin, 2010). When the planar surface tension of water is used in CNT, it is called a capillary approximation (Schmelzer and Baidakov, 2016). The assumption that the surface tension of critical nuclei equals that of a planar interface is not intrinsic to CNT. This approximation is often only made for the sake of heuristics (Schmelzer and Baidakov, 2016). The capillary approximation is known for predicting finite values of W^* at the spinodal liquid of stability, which is an nonphysical result (Cahn and Hilliard, 1959; Kashchiev, 2003). Furthermore, this approximation additionally carries the underlying assumption that the length of the nucleus wall is small compared to its volume. This is also known as the thin wall approximation (TWA) (Herbert, Balibar and Caupin, 2006).

3.2.2 Heterogeneous nucleation

If any substrates (impurities) are present in the fluid, the free energy of embryo formation takes a different form to that shown in Eq. 3.5

$$\Delta G = G - G_0 + \Delta\phi_s. \qquad 3.18$$

In this equation, the term $\Delta\phi_s = \phi_s - \phi_s^0$ accounts for the substrate's surface energy variation before and after nucleation. Substrates are different phases or molecular species which might act as preferential nucleation sites in the metastable phase.

For the case of pure substances, when no substrates are present, $\Delta\phi_s = 0$, and homogeneous nucleation (HON) is said to happen. If impurities are present, HON will still be energetically favoured for $\Delta\phi_s > 0$, where the substrate is said of the stabilising type. Stabilising impurities have been discussed in the context of HIFU-induced nucleation by (Davitt, Arvengas and Caupin, 2010). Alternatively, if $\Delta\phi_s < 0$, heterogeneous nucleation (HEN) will be the energetically favoured

process. Such is the case of destabilising impurities, which will be preferential nucleation sites because nucleation is less energetically demanding on their surface.

The critical work of nucleation in the presence of a substrate follows the same expression as Eq. 3.17, however, the surface tension takes the following form

$$\sigma_{HEN} = \Psi\sigma, \qquad 3.19$$

where Ψ is an activity factor depending on the geometry, surface energies and wetting angle of the substances in question (Fletcher, 1958; Kashchiev, 2000).

3.2.3 The Effective Surface Tension

Literature data on bubble nucleation in acoustic fields in the MegaHertz range is such that experiments usually do not surpass pressures of about – 40 MPa (Herbert, Balibar and Caupin, 2006; Davitt, Arvengas and Caupin, 2010; Caupin *et al.*, 2012; Maxwell *et al.*, 2013; Vlaisavljevich *et al.*, 2016). This contrasts to CNT predictions using a capillary assumption and quartz inclusion experiments, where water can be stretched to rarefactional pressures of about – 150 MPa (Azouzi *et al.*, 2013). Such discrepancy has been discussed in terms of destabilising impurities in the acoustic experiments or the presence of stabilising impurities in quartz inclusion experiments (Davitt, Arvengas and Caupin, 2010).

It has been shown that employing a scaling factor correcting the liquid surface tension or the nucleation work can help harmonise CNT predictions and experiments. Nucleation rates obtained in HIFU experiments at 1 MHz in ultra-purified water have been used in Eq. 3.19 in order to approximate an "effective value" of σ_∞ up to temperatures of 200 ˚C (Davitt, Arvengas and Caupin, 2010). The data obtained in these experiments showed agreement to a phenomenological implementation of CNT where the surface tension was scaled to 23.7% of the planar surface tension σ_∞. Similar experiments have been performed more recently up to 90˚C (Vlaisavljevich *et al.*, 2016), with scaling factors ranging from 25 to 27.5% of σ_∞. Furthermore, (Delale, Hruby and Marsik, 2003) have similarly

used a scaling factor on the critical work of nucleation to harmonise nucleation rate predictions with experimental values for liquid boiling. Values of $\Psi_{\mathrm{E}}(T)$ previously published in the literature use either a constant kinetic term (Vlaisavljevich, Lin, *et al.*, 2015) or obtained as a single value for a wide temperature range (Davitt, Arvengas and Caupin, 2010).

Here, a temperature-dependent scaling factor Ψ_{E} for the surface tension was calculated such that $\sigma_E = \Psi_{\mathrm{E}}\sigma_\infty$. This was achieved by optimising in $\Psi_{\mathrm{E}}(T)$ the absolute error between analytic predictions of Eq. 3.14 and experimental data for nucleation pressure thresholds in acoustic fields from Tables 2-1 through to 2-3. $\Psi_{\mathrm{E}}(T)$ was calculated by minimising $E(P_l^N)$. This scaling factor can be expressed as:

$$E(P_l^N) = \sqrt{(P_l^N(T, \Psi_E(T)) - P_{EXP}(T_{EXP}))^2}, \qquad 3.20$$

where P_{EXP} and T represent, respectively, experimental values of the nucleation pressure threshold and the temperature at which they were obtained. $P_L^N(T, \Psi_E(T))$ was calculated using Eq. 3.16. V_0 was approximated as an ellipsoidal focal volume within the - 3dB intensity drop region for a 2 MHz HIFU transducer such that $V_0 = 1.7299$ m^3. Δt_N is set as a tenth of the ultrasound wave period such that $\Delta t_N = \left(\frac{1}{10f}\right) = 5 \cdot 10^{-8}$ s. Properties of the Sonic Concepts H-Series (H148/H106/H102) are used throughout this manuscript due to their wide applicability in biomedical ultrasound research.

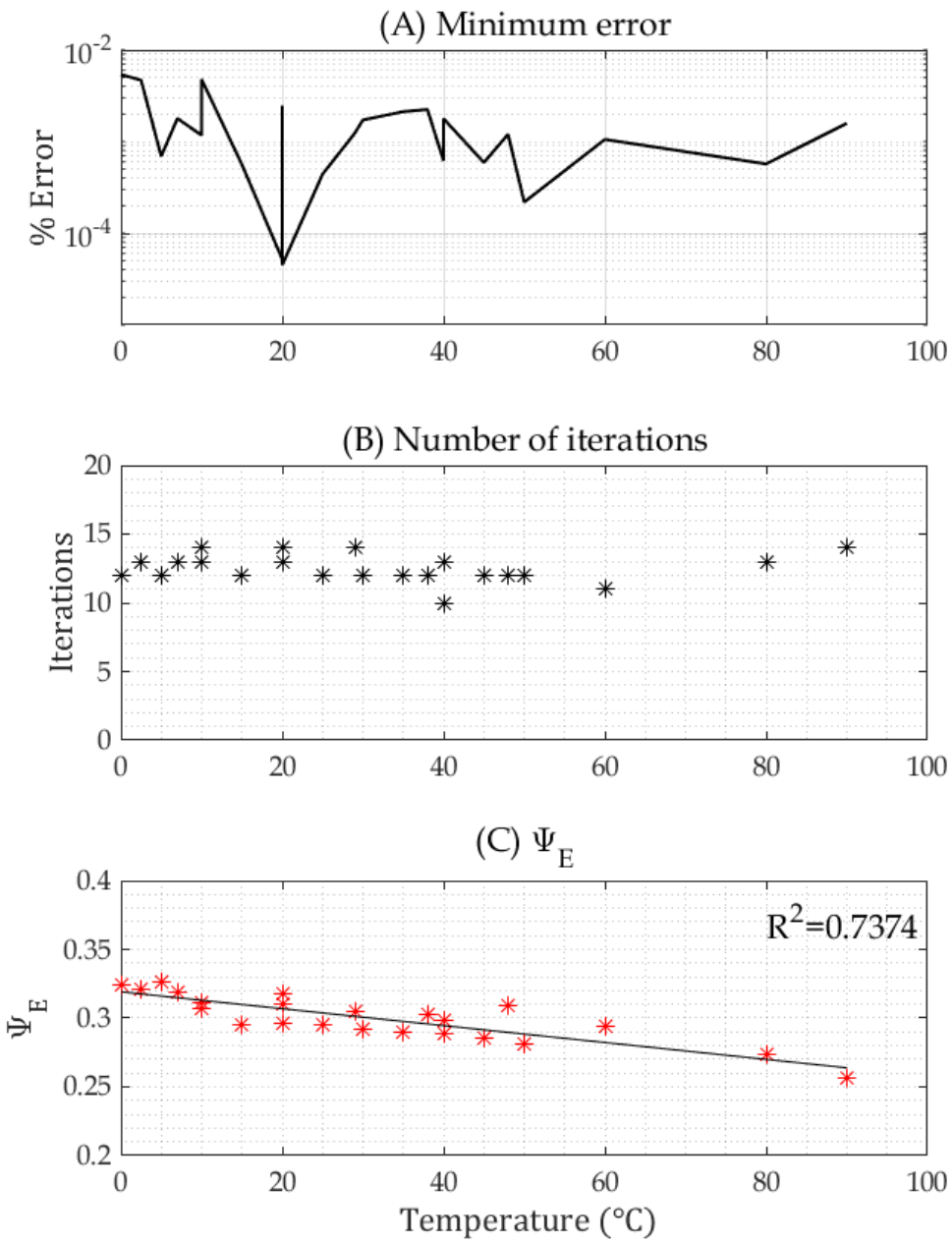

Figure 3-2. Error minimisation parameters for obtaining Ψ_E. (A) Percent error between analytical predictions and experimental values of P_l^N. (B) Number of iterations needed until minimum error was found. (C) Values of Ψ_E and linear regression of points. © 2021 IEEE. Reprinted, with permission, from de Andrade et. al, "Modeling the Physics of Bubble Nucleation in Histotripsy", IEEE Transactions on Ultrasonics, Ferroelectrics, and Frequency Control, September 2021.

In order to calculate temperature-dependent thermodynamic properties over a continuous temperature range, linear regression was used in order to obtain a first-order dependence of the optimised values $\Psi_E(T)$ on the liquid's temperature. For temperatures between 0 and 90 °C this reads:

$$\Psi_E(T) = 0.4869 - 6.1425 \cdot 10^{-4}(T + 273.15) \quad 3.21$$

It follows that the effective surface tension for HIFU-induced bubble nucleation is approximated as

$$\sigma = \Psi_E(T)\sigma_\infty(T) \quad 3.22$$

For temperature values between 90 and 110 °C, Ψ_E is extrapolated based on Eq. 3.21 with $R^2 = 0.7374$. For temperature values above 110 °C a conservative approach is taken and a constant $\Psi_E(T > 110°C) = \Psi_E(110°C)$ is assumed.

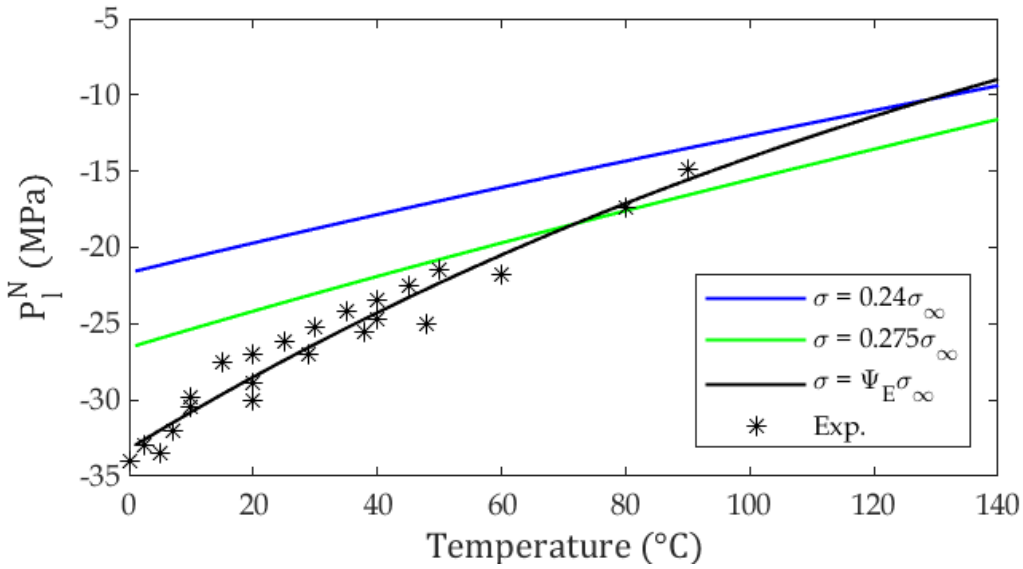

Figure 3-3. Comparison between CNT predictions of P_l^N at different Ψ_E. Blue and green curves represent a constant Ψ_E, 0.24 and 0.275 respectively, and black curve represents a temperature-dependent Ψ_E shown by Eq. 3.21. Asterisks denote experimental values of Ψ_E obtained from the literature. © 2021 IEEE. Reprinted, with permission, from de Andrade et. al, "Modeling the Physics of Bubble Nucleation in Histotripsy", IEEE Transactions on Ultrasonics, Ferroelectrics, and Frequency Control, September 2021.

Nucleation pressure thresholds are plotted as a function of temperature in Fig. 3-3, comparing the effects of the scaling quantity Ψ_E on the values of the nucleation pressure threshold. Asterisks represent experimental data for HIFU-induced bubble nucleation taken from the literature (Davitt, Arvengas and Caupin, 2010; Vlaisavljevich *et al.*, 2016). By employing the linear approximation for Ψ_E obtained in Eq. 3.21, it is possible to obtain nucleation pressure thresholds which are in close agreement with values reported in the literature throughout a

temperature range of interest in HIFU applications. Previously reported values for Ψ_E (0.24 and 0.275) are shown to underestimate the magnitude of P_l^N at low temperatures and to overestimate it at higher temperatures.

3.2.4 The validity of the capillary approximation

Figure 3-4 compares the predictions of P_l^N obtained from a planar surface tension (capillary assumption), a temperature-dependent effective surface tension $\sigma = \Psi_E \sigma_\infty$ with temperature-dependent values of the spinodal pressure of water at low temperatures numerically obtained from Waals-Cahn-Hilliard theory with the five-site transferable interaction potential (TIP5P) EoS (Caupin, 2005).

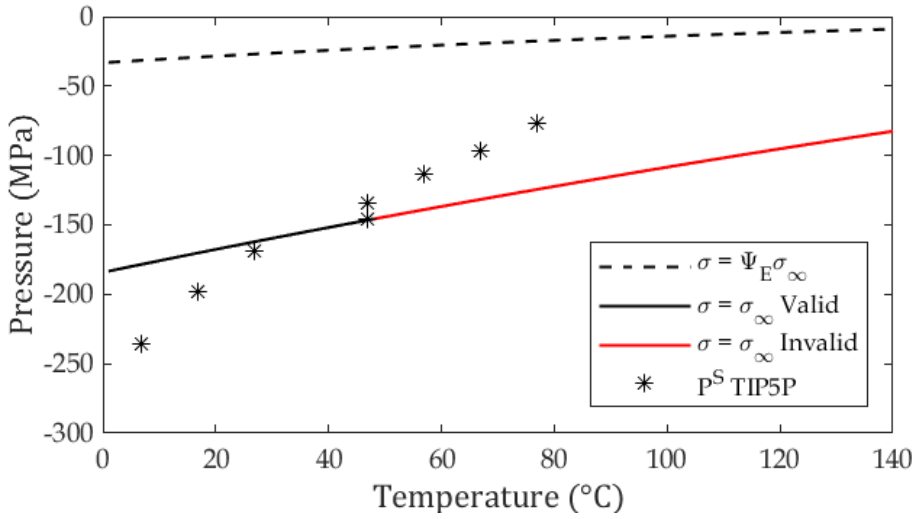

Figure 3-4. Comparison of values of P_l^N obtained by CNT with a capillary assumption (black and red curve) and obtained with an effective surface tension (dashed line). Asterisks represent the liquid spinodal of water obtained numerically with a TIP5P EoS. Values of P_l^N below values of the spinodal of water represent nonphysical predictions.

There is no consensus on the most appropriate computational model to be used when approximating the spinodal limit of water. The TIP5P model describes the properties of water within the realm of molecular dynamics at low temperatures with low computational costs. The parameters used in these models are fitted to reproduce bulk, macroscopic experimental properties of water such as liquid density and heat of vaporisation (Ouyang and Bettens, 2015). For example, a comparison of Speedy's EoS and the TIP5P has found qualitatively different predictions in temperature-dependent behaviour and suggested that comparison

of the simulation with available experimental data suggested the appropriacy of the TIP5P model for applications regarding the phase diagram of water (Caupin, 2005).

Results indicate the inappropriacy of CNT with a capillary approximation for modelling nucleation at low (< 40˚C) and medium (< 80˚C) temperatures. As discussed in the sections above, the temperature-dependent spinodal pressure defines an envelope around the regions where the fluid is unstable. Waals-Cahn-Hilliard theory predicts that the energy barrier to nucleation vanishes as the liquid pressure approaches spinodal pressures (Cahn and Hilliard, 1958; Cahn, 1959). When such is the case, liquids relax towards stability in an alternative process to nucleation, named spinodal decomposition. The spinodal pressure of water can then be used to assess the validity of CNT predictions (Debenedetti, 1996).

3.3 Regimens of bubble nucleation

In Fig. 3-5 the steady-state nucleation rate given by Eq. 3.27 is shown as a function of temperature for three pressure contours (-30, -15 and -5 MPa) in A, and as a function of pressure for three temperature contours (40, 100 and 200 °C) in B. These values are in units of the number of bubble nuclei per meter cubic per second. Nucleation rates at temperatures below 100 °C are only appreciable in the presence of high magnitude rarefactional pressures (< -15 MPa). On the other hand, at high temperatures (100 – 200 °C), nucleation rates plateau and present virtually no change as the liquid's pressure decreases. In this case, J_{ss} assumes asymptotic behaviour, close to its saturation value J_0. This suggests that at low temperatures, rarefactional pressures are the fundamental trigger for bubble nucleation (cavitation) and, at high temperatures, the degree of superheating is the controlling mechanism (boiling).

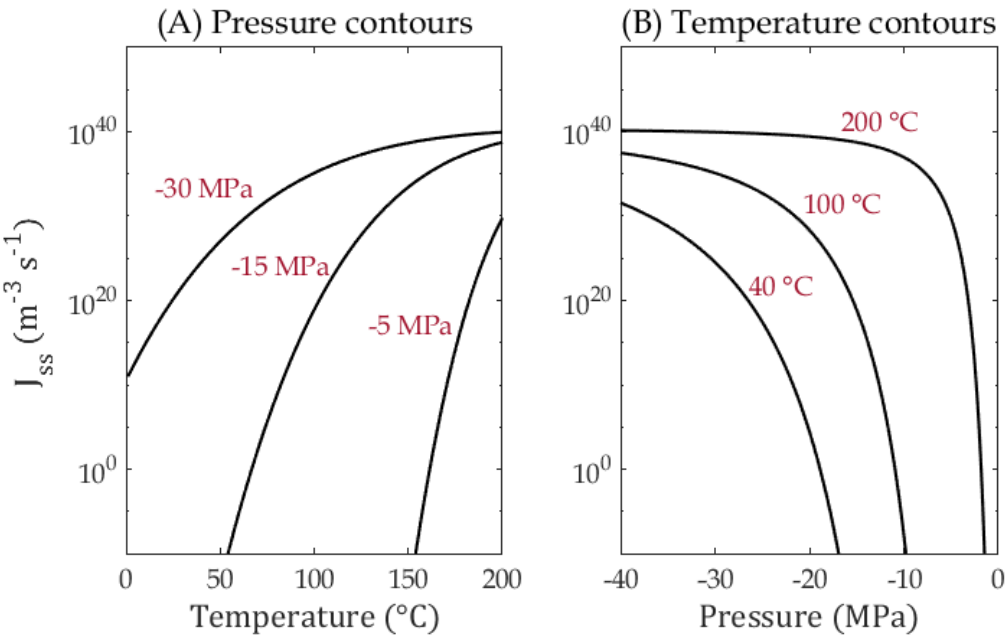

Figure 3-5. (A) Nucleation rate as a function of temperature with pressure contours. (B) Nucleation rate as a function of pressure with temperature contours. © 2021 IEEE. Reprinted, with permission, from de Andrade et. al, "Modeling the Physics of Bubble Nucleation in Histotripsy", IEEE Transactions on Ultrasonics, Ferroelectrics, and Frequency Control, September 2021.

The terms boiling and cavitation nucleation are traditionally used to describe bubble formation in liquids, many times without explicit distinction between them. Brennen (2009) proposed that the nomenclature "boiling" should only be used for cases where nucleation is triggered by a superheat ΔT at constant liquid pressure. Conversely, cavitation would be the phenomenon caused by a "tension", also termed rarefactional pressure (Kashchiev 2000), $\Delta P_l = P_v - P_l \geq 0$ at a constant temperature. In practice, it is challenging to design experiments that isolate the effects of both thermodynamic variables, and the distinction between the two phenomena is uncertain. Blander & Katz (1975) reported that at temperatures sufficiently close to the thermodynamic limit of superheat ($T \approx 0.89\, T_c$) nucleation rates increase approximately three or four orders of magnitude per degree Celsius. In such cases, it is appropriate to talk about the limits of superheating and boiling. Contrastingly, away from the thermodynamic limit of superheat ($T < 2T_c/3$), nucleation rates are only appreciable at negative pressures (Baidakov 2015). This happens because $P_l \gg P_v$, therefore the temperature-dependence of nucleation on the exponent of Equation 3.10 is significantly reduced. The surface tension term in W^* still has a negative derivative; however, this is of a much smaller magnitude.

At these conditions, it is meaningful to discuss the tensile strength and term the process as cavitation.

HIFU-induced bubble nucleation can be primarily driven by two factors, high-amplitude negative pressures or high temperatures. However, such distinction only becomes evident at temperatures around 150 °C. Therefore, Histotripsy protocols have been broadly named intrinsic pressure histotripsy and boiling histotripsy, deriving from the sense that bubble nucleation at high temperatures is termed boiling and bubble nucleation at lower temperatures and high-amplitude negative pressures is termed cavitation. Although results in Fig. 3-5 corroborate with this terminology, nucleation rates at 100 °C still present a non-zero derivative in pressure, indicating that this could be a pressure-threshold phenomenon facilitated by high temperatures.

3.4 Sensitivity to volume and time

The quantity Δt_N defines the time interval over which the first Σ bubbles nucleate. This quantity should be a fraction of the wave period estimated from the ultrasound frequency used (Bruot and Caupin, 2016). The choice of Δt_N needs to be such that variations in P_l and T are minimal so that these quantities can be assumed nearly constant, and their effects neglected. In Chapter 6, a quasi-stationary formulation of CNT is employed to quantify the relative timescales for heating and pressure oscillations that render the current implementation of CNT valid. Moreover, the parameter V_0 represents the experimental volume, i.e., the volume of the nucleating system under consideration. For nucleation induced by focused transducers, this parameter can be estimated using the focal volume of the transducer within the -3 dB region.

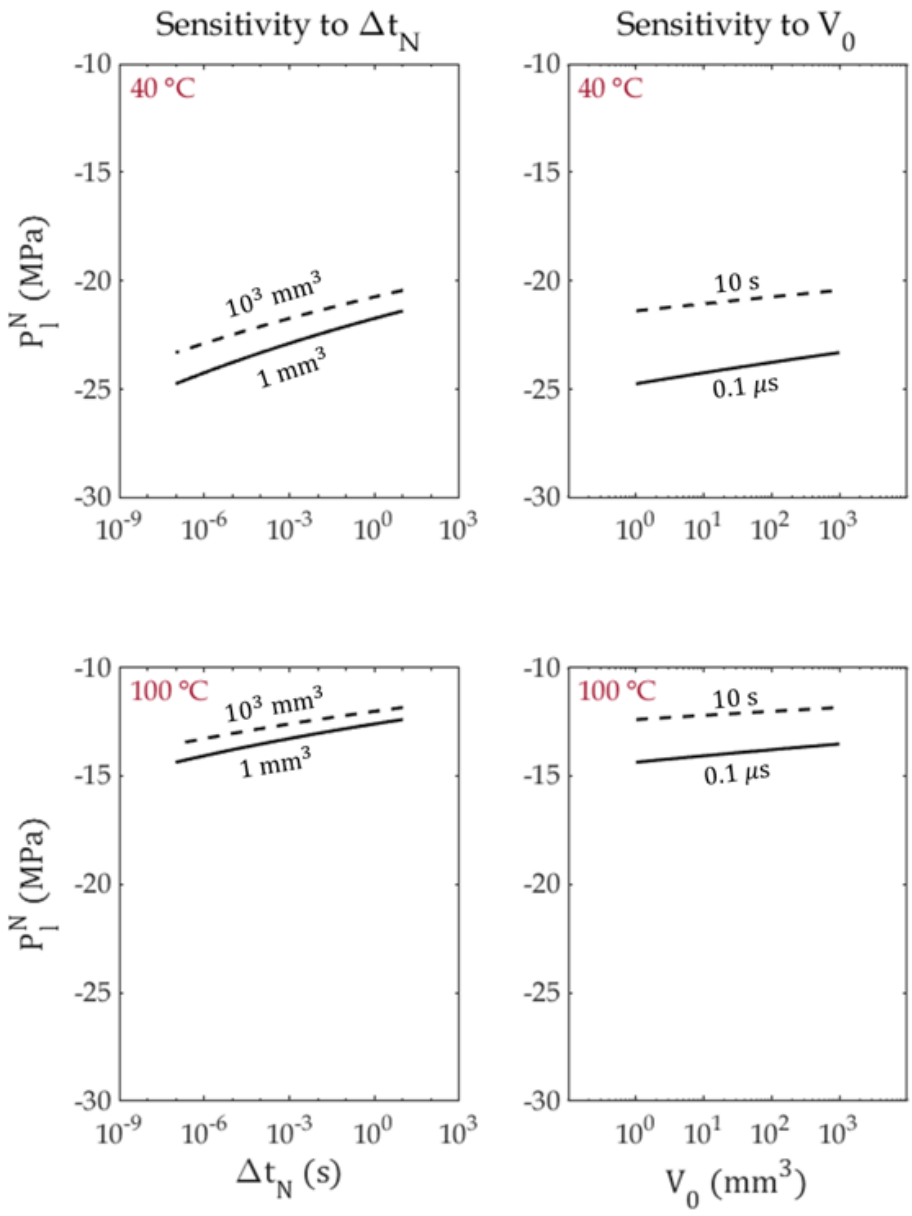

Figure 3-6. The effects of Δt_N (left column) and V_0 (right column) on P_l^N. Results in top row are obtained for $T = 40$ °C, results in bottom row are obtained for $T = 100$ °C. © 2021 IEEE. Reprinted, with permission, from de Andrade et. al, "Modeling the Physics of Bubble Nucleation in Histotripsy", IEEE Transactions on Ultrasonics, Ferroelectrics, and Frequency Control, September 2021.

By varying Δt_N between 0.1 μs and 1 s in Eq. 3.11 it was found that the magnitude of the nucleation pressure threshold monotonically decreases with increasing Δt_N. Similarly, by varying V_0 between 1 mm^3 and 1 cm^3 P_l^N also decreases monotonically with increasing V_0. This trend indicates that, at constant temperature, bubble nucleation is favoured at lower frequencies (< 10 MHz), since these would imply longer Δt_N and larger V_0. In Fig. 3-7, the maximum difference in

the value of P_l^N predicted by Equation 3.14 was plotted, that is $\Delta P_l^N = |P_l^N(1\ \mathrm{s}, 1\ \mathrm{cm}^3) - P_l^N(0.1\ \mu\mathrm{s}, 1\ \mathrm{mm}^3)|$. The effects of Δt_N (one tenth of the ultrasound central frequency) and V_0 (the ultrasound focal volume) are shown to decrease as the medium temperature increases.

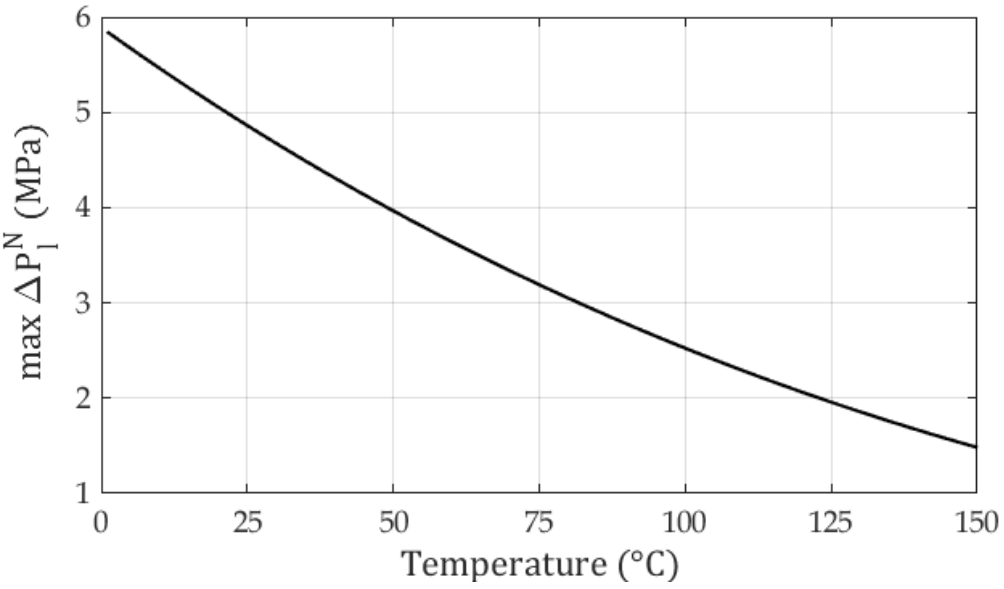

Figure 3-7. Maximum variation in P_l^N caused by the parametrisation of Δt_N and V_0. © 2021 IEEE. Reprinted, with permission, from de Andrade et. al, "Modeling the Physics of Bubble Nucleation in Histotripsy", IEEE Transactions on Ultrasonics, Ferroelectrics, and Frequency Control, September 2021.

3.5 Chapter Summary

In this Chapter, a thermodynamic model for bubble nucleation in constant pressure and temperature fields was developed using the classical nucleation theory. This model yields an estimate for the temperature dependence of the nucleation pressure threshold in water. Parameters such as the experiment time Δt_N and volume V_0 are included in the derivation of this model, under the simplifying assumption that pressure and temperature fields change sufficiently slowly to result in time-independent nucleation rates.

As a first validation step, predictions of the nucleation pressure threshold of water were compared to numerical predictions of the spinodal pressure of water obtained with the TIP5P model. Through this comparison, it was found that CNT yields nonphysical results when a capillary assumption is used. To circumvent this

problem, literature data on ultrasound-induced nucleation pressure thresholds outlined in Tables 2-1, 2-2 and 2-3 were used to evaluate a scaling factor for the surface tension of water. This scaling factor is positively correlated to the temperature of the liquid and was approximated linearly as shown in Eq. 3.21. The numerical procedure of linear fitting aimed at finding the values of Ψ_E that minimise the RMSE between experimental results and Eq. 3.16. Results obtained from this approximation were in better agreement with available experimental data than fixed scaling factors published in the literature.

Furthermore, numerical values of the nucleation rate were used to analyse the extent of the effects of rarefactional pressures and the degree of superheating in nucleation at different temperatures and pressures. It was found that the liquid pressure has a more significant effect on the nucleation rate at lower temperatures (< 40 ˚C). However, the degree of superheating was found to increase nucleation rates significantly at high temperatures (> 80 ˚C). Finally, the sensitivity of the predictions of P_l^N discussed in this Chapter to experimental parameters such as Δt_N and V_0 was analysed. It was shown that the magnitude of nucleation pressure thresholds decreases with increasing V_0 and Δt_N . These results suggest ultrasound frequencies below 10 MHz and larger HIFU focal volumes favour bubble nucleation.

A central simplifying assumption in this Chapter is that nucleation takes place during a finite, and very small, period of the ultrasound wave Δt_N where the ultrasound pressure P_l and the liquid temperature T can be assumed constant, therefore implying a steady-state nucleation rate J_{ss}. This simplification contains a range of conceptual issues for acoustic nucleation, because in ultrasound fields the pressure and temperature of the liquid constantly change. The mathematical validity of Chapter 3 with regards to the transiency of acoustic and thermal fields within the focus of high-intensity acoustic fields was analysed in detail in Chapter 6, which builds upon the hydrodynamic understanding of nucleation demonstrated in Chapter 5. Apart from the fundamental physics developed and discussed in Chapter 3, there are some important implications of how the understanding of bubble nucleation is advanced.

1. At the most essential level, nucleation means creating Σ bubbles within the focal volume of the transducer V_0 during a time interval Δt_N. This results in an experimentally verifiable nucleation rate $J_{ss} \approx \frac{\Sigma}{V_0 \Delta t_N}$ with the natural implications that (i) lower ultrasound frequencies prolong the interval Δt_N and increase the chance of nucleation, and (ii) smaller focal volumes will make nucleation more difficult, but they will reduce the chance of heterogeneous nucleation.
2. Nucleation must be seen as a thermodynamic process where both the temperature and pressure in the liquid are important variables. In water-like media, the pressure threshold that is necessary for nucleation will decrease with increasing temperature. Notably, the key parameter associated with a lowering of the magnitude of nucleation thresholds is the liquid surface tension.

The implications of Chapter 3 can be summarised in terms of how they advance the understanding of bubble nucleation as follows:

Fluids have an intrinsic type of energy that originates from thermal fluctuations and interactions between molecules. This intrinsic energy is of the order $k_B T$, and is manifested at the macroscopic scale in both mechanical and thermal form. The mechanical energy of fluids is observable through their volume and the pressure associated with that volume. Likewise, the thermal energy of fluids, which is based on the diffusivity of mechanical energy at the atomic scale, is manifested macroscopically as temperature. Both types of energy, although distinct in essence, interact via the manifestation of a pressure-volume-temperature relationship such equations of state.

Whenever energy is provided to a system, in the form of tensile pressures or heat deposition, the intrinsic energy fluctuations might be magnified causing a quantifiable change in the system. A cascade of rearrangements in the state of the system is then triggered, where nucleation is one of the possible outcomes. The fundamental question that Chapter 3 in this thesis addresses the magnitude of the energy disturbance necessary to cause a system to rearrange itself via bubble

nucleation. Any thermodynamic conceptualisation of energy must be followed by consideration on whether this energy can be used to carry out work (useful energy) or whether this energy has been dissipated from a process (entropy).

The entropy of a system behaves as an opposite of what is called the free energy of a system. The free energy of a system measures exactly the energy that can be used by the system to kickstart any processes. There are many ways to represent the free energy of a system which relate to the parameters in this system that can be experimentally controlled. In this dissertation, the Gibbs free energy was employed because this canonical thermodynamic potential has pressure and temperature as independent variables.

The Gibbs free energy is what drives the process of phase transformation according to nucleation theory. In this way, it can be argued that the point of minimum entropy in a system is the point where most of the energy in the system is useful, and a process (such as bubble nucleation) can be initiated. Conversely, the point of maximum entropy is the point where most energy within the system has been disorganised to a point where no work can be done with such energy. Most importantly, nucleation takes place in systems that are not in equilibrium. This means a pure fluid stretched below its vapour pressure or heated above its boiling point.

The tendency of a system to change phase via nucleation, or its deviation from equilibrium, can be quantified as the supersaturation, often denoted as $\Delta\mu$. The supersaturation measures the chemical potential of a system that can lead to chemical reactions or phase change. If one considers that vapour and liquid phases of a liquid are different chemical species, the supersaturation is applicable for pure fluids without impurities. The concept of phase equilibrium is then directly derived from the rationale above. If at the point where entropy is at its maximum, the free energy is at its minimum, this point is a point of equilibrium, where the system simply does not have a drive to change and is stable. The concept of "change" discussed above is restricted to the idea of changing phase.

In the literature review, the three manifestations of "stability" in a fluid were outlined as: (i) truly stable systems, such as water that has been left for days in a

glass; (ii) metastable systems, such as water that is heated above equilibrium conditions, or the focus of an ultrasound beam where negative pressures are present; and (iii) unstable systems which are systems that experience a sharp disruption to their equilibrium. The conclusion is that ultrasound fields cause a transient state of metastability in fluids during the tensile part of the ultrasound wave. Metastable states are *local* minima of the free energy of the system and are separated from the *global* minimum by an energy barrier. Provided that this energy barrier can be overcome by lowering pressures or raising temperatures, the system will move towards an equilibrium state where two phases coexist, even if momentarily, via the process of bubble nucleation. The bubble nucleation then takes place as the degree of metastability induced in a liquid surpasses a threshold where the naturally occurring thermal fluctuations of order $k_B T$ become significant. In his seminal work, Gibbs predicted that the energy of activation for new phase formation, denoted as $\frac{W^*}{k_B T}$ throughout this dissertation, will depend on the energetic requirements of creating a surface in the bulk of a liquid and the energy required for a nucleating bubble to create space for itself by pushing the surrounding liquid away. This means that much peer-reviewed work in the literature does not consider the possibility that the surface tension σ_E of a nanometric, quasi-spherical nucleating bubble is different from the surface tension of a planar water-vapour interface σ_∞.

In the present Chapter, this issue was addressed for the first time by:

I. Showing that the predictions of CNT using the surface tension of a planar water-vapour interface σ_∞ are far beyond the spinodal limit of stability of water for most temperatures, and therefore such models are conceptually incorrect.
II. Arguing that unless it is appropriate to model the surface tension as $\sigma_E = \Psi\sigma_\infty$, where Ψ is a temperature-dependent activity factor that provides a linear correction to the surface tension, which is consistent with the thermodynamic theory of nucleation.

Once these issues are discussed, Chapter 3 shows that it is possible to obtain a rigorous formulation of CNT that is parameterised by independent experimental results and valid throughout most of the pressure-temperature range of interest for histotripsy. The methodology in Chapter 3 was based on the work of Caupin, Arvengas, and co-workers in France (Balibar and Caupin, 2003; Caupin, 2005; Caupin and Herbert, 2006; Herbert, Balibar and Caupin, 2006; Davitt, Arvengas and Caupin, 2010; Arvengas, Davitt and Caupin, 2011; Caupin and Stroock, 2013; Bruot and Caupin, 2016), which aimed at exploring the physical properties of metastable water using ultrasound to induce metastability. These researchers suggested that, within ultrasound nucleation, a correction of the form $\sigma_E = \Psi\sigma_\infty$ was appropriate to explain the results of cavitation in ultra-purified water at 1.1 MHz. The theoretical framework used to justify this modelling strategy was inspired on the treatment of (Kashchiev, 2000, 2003; Delale, Hruby and Marsik, 2003) which attempted to find a thermodynamically consistent formulation of CNT that would not output results far below the spinodal of water. This work shows that a correction of the form $\sigma_E = \Psi\sigma_\infty$ is consistent with the fundamental theorems of nucleation, which are the very bridge between nucleation experiments and mathematical modelling. Finally, the main contribution of Chapter 3 is to propose an alternative hypothesis to a somehow dominant idea that the classical nucleation theory (CNT) is incompatible with the reality of cavitation experiments. In fact, this Chapter opens novel avenues of mathematical exploration for the effects of ultrasound focal volume, frequency, and medium parameters on the nucleation of bubbles in ultrasound.

Chapter 4

Numerical Simulation of Nucleation in Boiling Histotripsy

Acknowledgement: The contents of this chapter are based on (de Andrade et al., 2021). Figures 4-5, 4-9, 4-10, 4-11, 4-12, 4-13, 4-14 have been reproduced with authorisation of the publisher.

In Chapter 3, a thermodynamic approach was employed to develop a CNT model of ultrasound bubble nucleation. This model was parameterised with data from histotripsy and HIFU-induced nucleation experiments available in the literature. The underlying assumptions were of stationary nucleation and that the mean lifetime of the metastable fluid is so short that the gas content of the medium can be neglected.

In the current Chapter, the models developed in Chapter 3 are applied to boiling histotripsy pressure fields obtained numerically by solving the Khokhlov–Zabolotskaya–Kuznetsov (KZK) equation within a wide-angle approximation, and temperature fields computed by using the Bioheat transfer equation. This approach enables the modelling and visualisation of bubble nucleation in boiling histotripsy in time and space, allowing for the calculation of the pulse duration (minimum duty cycle) needed for bubble nucleation, the temperature distribution of the treatment zone at the time of nucleation, as well as the location where bubbles first nucleate and size of the critical bubble nucleus.

4.1 Introduction

The current rationale for parametrisation of histotripsy protocols is based on two general assumptions. The first is that bubble nucleation in soft tissue is comparable to bubble nucleation in untreated water volumes that boil at 100 ˚C under atmospheric pressure. The second is that if the pulse duration is not much longer than the time to boil, thermal damage in the resulting lesion will be negligible compared to the mechanical damage induced by bubble growth and its interaction with the acoustic field (Wang *et al.*, 2013). The main issue with the first hypothesis regards the slim chances of survival of unstable microbubbles in viable biological media. Gas bubbles in the absence of a stabilising force tend to dissolve in liquids due to Laplace pressure (Yount, 1979; Yount, Gillary and Hoffman, 1984; Blatteau *et al.*, 2006; Christopher E. Brennen, 2013b; Papadopoulou *et al.*, 2013). Moreover, biomolecular processes ensure that gas is transported out of solution within the human body in the form of acids or attached to proteins. In untreated water volumes, preferential nucleation sites are generally hydrophobic crevices where gas is trapped or free-flowing gas bubbles (Crum, 1982; Blatteau *et al.*, 2006; Christopher E. Brennen, 2013b). There is no evidence of the existence of such agents in soft tissue or interstitial fluid. A review of several studies concluded that no hydrophobic crevices had ever been observed in tissues or capillaries (Blatteau *et al.*, 2006).

Despite the availability of sophisticated methods for modelling the interactions between acoustic fields and bubbles (Lauterborn *et al.*, 2007; Lauterborn and Mettin, 2015), there remain unknowns regarding the thermodynamic conditions needed for the onset of nucleation in HIFU. Similarly, the specific contributions of both temperature and pressure to this process and their interactions are unexplored. Such gaps in understanding HIFU-induced nucleation hinder our ability to optimise histotripsy protocols for performance in current clinically available HIFU systems without time- and resource-demanding trials with in-vivo or ex-vivo set-ups.

4.2 Numerical simulation setup and convergence

The following sections detail a methodology for incorporating the model described in Chapter 3 into numerical simulations of acoustic propagation and heat deposition in boiling histotripsy. This model aims to compute nucleation pressure thresholds, the critical radius of nuclei and the critical work of nucleation as functions of spatially varying pressure and temperature pairs within the propagation region of focused ultrasound waves.

The initial step is to compute pressure fields resulting from a wide-angle parabolic approximation of the KZK equation using the HITU Simulator as described in section 2.1.5 of the literature review. This is a freeware MATLAB package that solves the 2D axisymmetric propagation of high-intensity acoustic sources over many layers of material. This software calculates acoustic quantities for each 2D element (z_i, r_j) in the grid, where i and j vary from one to the number of elements in the axial and radial directions of the grid, respectively. The pressure fields obtained from the acoustic simulation are used to compute spatially varying ultrasound heat deposition rates. Heat deposition rates are then fed onto simulations of heat deposition via Penne's BioHeat equation, as described in section 2.1.5 and 2.1.6. The numerical solver for the BioHeat equation is included within the software package HITU Simulator. Finally, after simulations for both acoustic propagation and heat deposition have been completed, pressures and temperatures for the discretised spatial elements are obtained. These spatially varying quantities are used in simulations of bubble nucleation with the equations described in Chapter 3. Figure 4-1 shows a flowchart of this numerical framework.

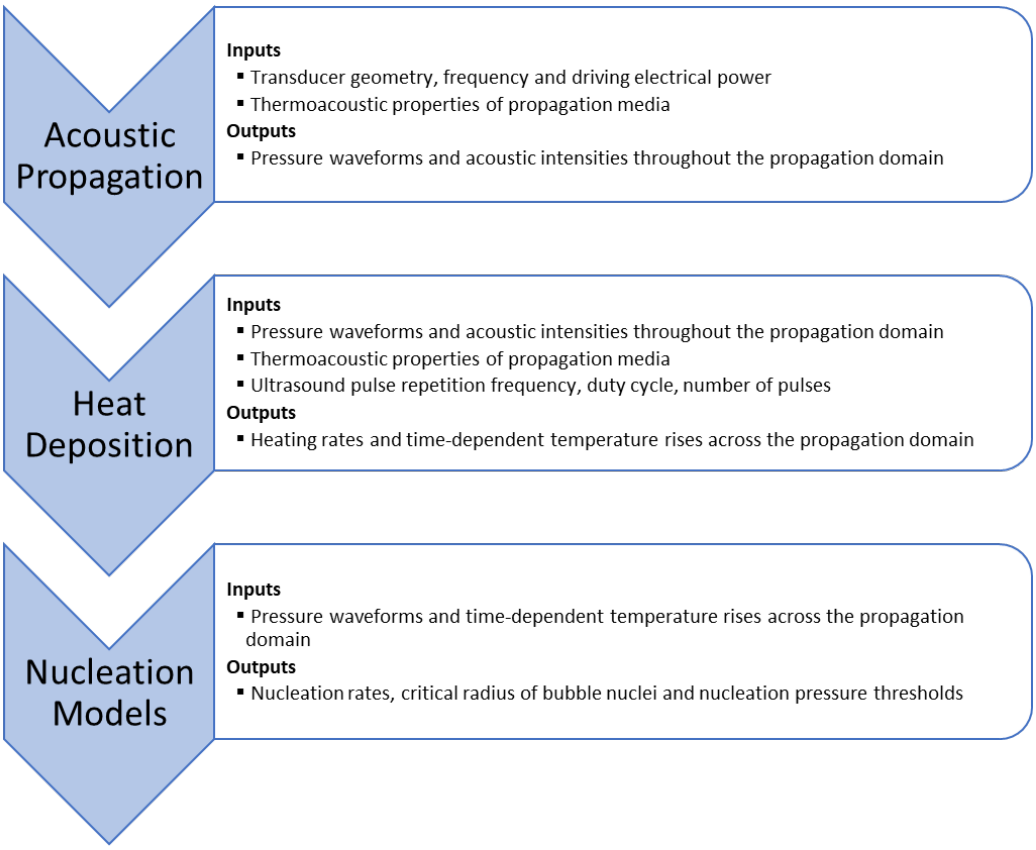

Figure 4-1. Flowchart of the procedure for numerically modelling bubble nucleation in histotripsy.

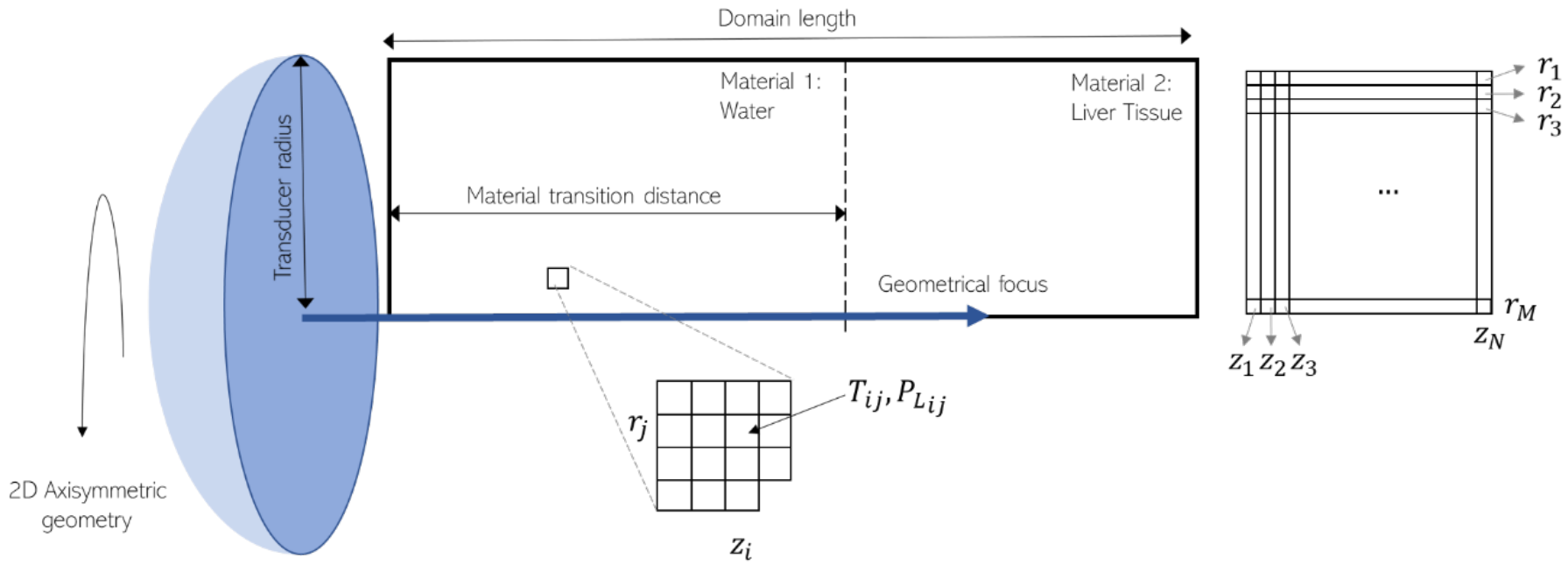

Figure 4-2. Schematic of acoustic simulation and discretisation of the domain.

The HITU Simulator first discretises the spatial domain according to the number of elements per wavelength in the radial and axial directions. Baseline simulations used 10 points per wavelength in the axial direction and 15 points per wavelength in the radial direction in the discretisation of the grid. These step sizes were chosen in order to produce a grid that can resolve the ultrasound focus at lengths below 1 mm. After discretising the spatial domain, the HITU Simulator marches forward in space, solving elements left-to-right in the axial direction and centre-up in the radial direction.

Acoustic propagation is then solved in the frequency domain for each element in the grid. Whenever the pressure in an element exceeds the Courant-Friedrichs-Lewy (CFL) condition for non-linearity, the solution is shifted to the time domain. The pressure waveform of that element is then computed by integrating Burger's equation. Subsequently, the element's pressure waveform is converted back to the frequency domain, and the code keeps marching forward in space. The time that each simulation takes will depend mostly on the size of the physical domain, the step size of the spatial mesh, and the number of harmonics employed. There is no specific rule for defining the exact number of harmonics needed for obtaining accurate solutions of the KZK equation (Soneson, 2009).

Convergence tests were carried out to define the ideal number of harmonics to be used in the simulations. Acoustic fields were computed at 32, 64, 128, 256, 512, 1024 and 2048 harmonics at 150 W input electrical power and assuming 85% efficiency for the 2 MHz transducer and at 300 W for the 1.1 MHz transducers. The number of harmonics used in the simulations followed a power of 2 to speed up fast Fourier transforms in the MATLAB code. Convergence was assumed fulfilled whenever doubling the number of harmonics resulted in an absolute difference smaller than 5% for key acoustic quantities such as heat deposition rate, acoustic intensity and peak negative focal pressure.

As shown in Fig. 4-3, key acoustic quantities in the calculation of nucleation pressure thresholds such as the focal peak negative pressure and focal heating rates converged monotonically for the increasing number of harmonics used in the simulations. At 512 harmonics, results were found to be within 5% difference from

simulations at 256 harmonics. The heating rate showed a slower convergence rate than both acoustic intensity and focal peak-negative pressure. This might have been caused by the frequency-dependence of the ultrasound absorption coefficient. Standard simulations throughout this manuscript were performed at 512 harmonics for both 1.1 and 2 MHz transducers.

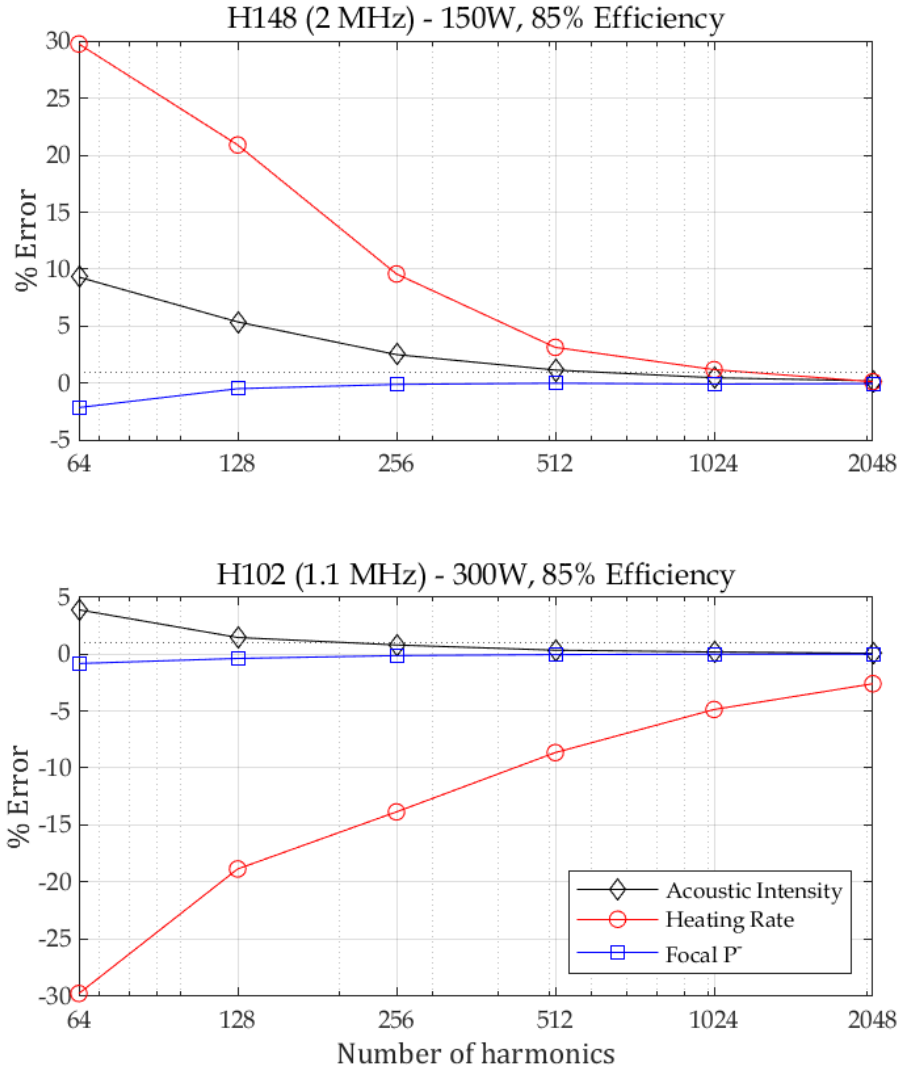

Figure 4-3. Numerical convergence of acoustic intensity (black diamonds), focal heating rates (red circles) and focal peak negative pressure (blue squares) in terms of the number of harmonics used in the acoustic simulations. The top plot displays results for a 2 MHz transducer driven at 150 W, and the bottom plot shows results for a 1.1 MHz transducer driven at 300 W electrical power.

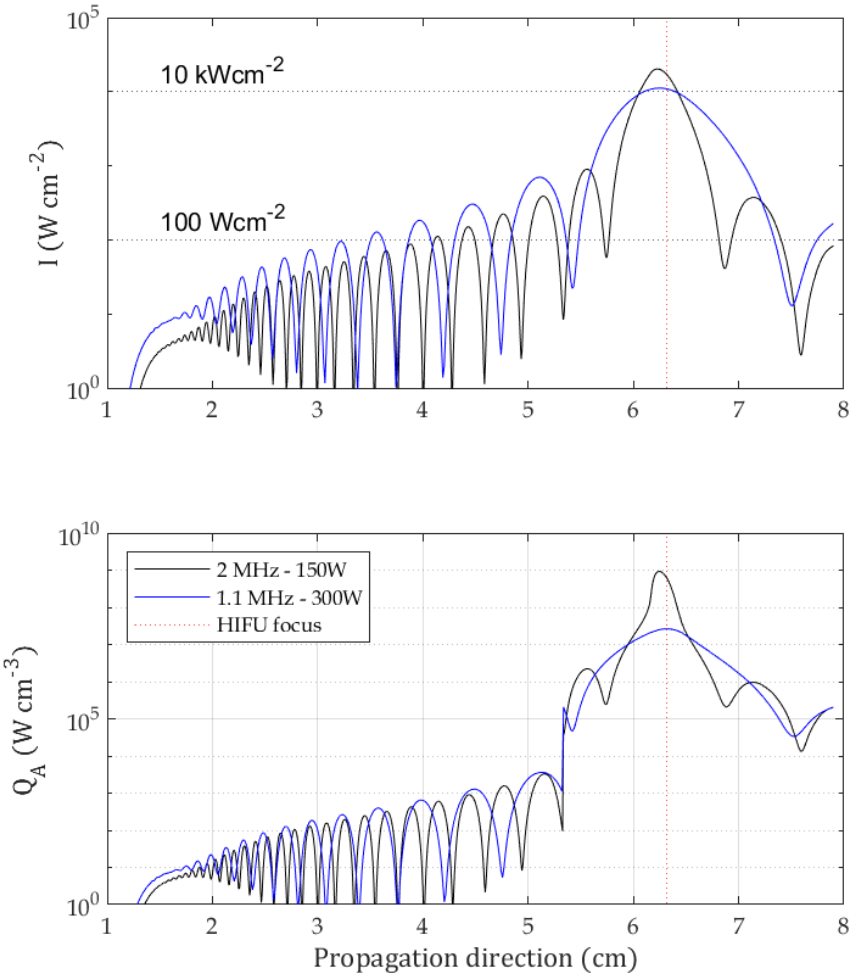

Figure 4-4. Plots of acoustic intensity (top) and focal heating rates (bottom) along the propagation axis. Black curves represent a 2 MHz transducer driven at 150 W, and blue curves show results for a 1.1 MHz transducer driven at 300 W. The red vertical dotted line shows the position of the HIFU focal plane. Black horizontal dotted lines represent the power output range of clinically available HIFU systems (Khokhlova *et al.*, 2015).

The power outputs of the transducers simulated herein are shown in Fig. 4-4. Acoustic intensity values for both transducers are measured within the output range of clinically available HIFU treatment systems along the propagation axis. These intensities are shown to be as high as acoustic intensities used in HIFU thermal ablation therapies; however, the short duty cycles involved in histotripsy might minimise any observable thermal effects.

4.3 Histotripsy Pressure and Temperature Fields

Propagation at 150 W input electrical power for the 2 MHz transducer (H148) and 300 W for the 1.1 MHz transducer (H102) showed that both transducers could generate focal acoustic intensities as high as 10 kW·cm^{-2}. Similarly, heating rates Q_A were found to be the greatest around the geometrical focus of both transducers. Focal heating rates observed for propagation at 2 MHz were about two orders of magnitude as high as those observed for 1.1 MHz. In Figure 4-5, waveforms for propagation at 2 and 1.1 MHz were plotted focally, as well as 0.5 cm pre- and post-focally.

Focal waveforms show the presence of shocks of higher magnitude for propagation at 2 MHz. Although both transducers have the same f-number, numerical simulation of focal quantities shows that key acoustic quantities for bubble nucleation such as the focal peak negative pressure and heat deposition rates differ by a large amount if both are driven at similar power outputs. Additional simulations for input electrical powers in the range of 200 – 400 W were carried for the 1.1 MHz transducer (H102) to match the focal peak-negative pressures and heating rates obtained with propagation at 2 MHz in the power range 100 – 200 W as shown in Fig. 4-7.

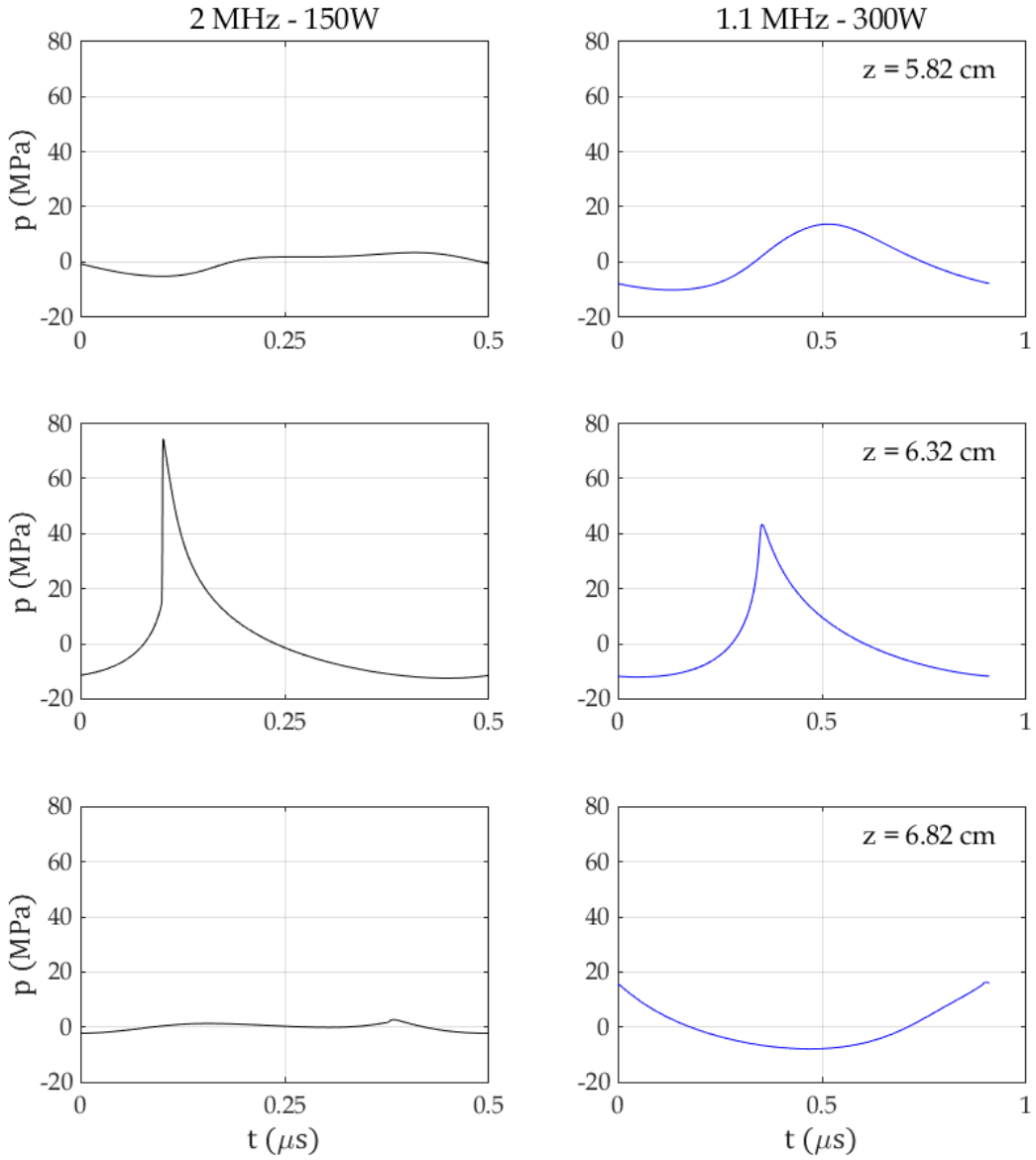

Figure 4-5. Plots of HIFU waveforms for 2 MHz at 150 W (left column) and 1.1 MHz at 300 W (right column). The input electrical powers have been chosen such that the numerical result achieves peak-positive and peak-negative pressures characteristic of boiling histotripsy. The top rows show pre-focal waveforms 5 mm away from the transducer geometrical focus, the middle rows display focal waveforms, and the bottom rows show post-focal waveforms 5 mm away from the focus.

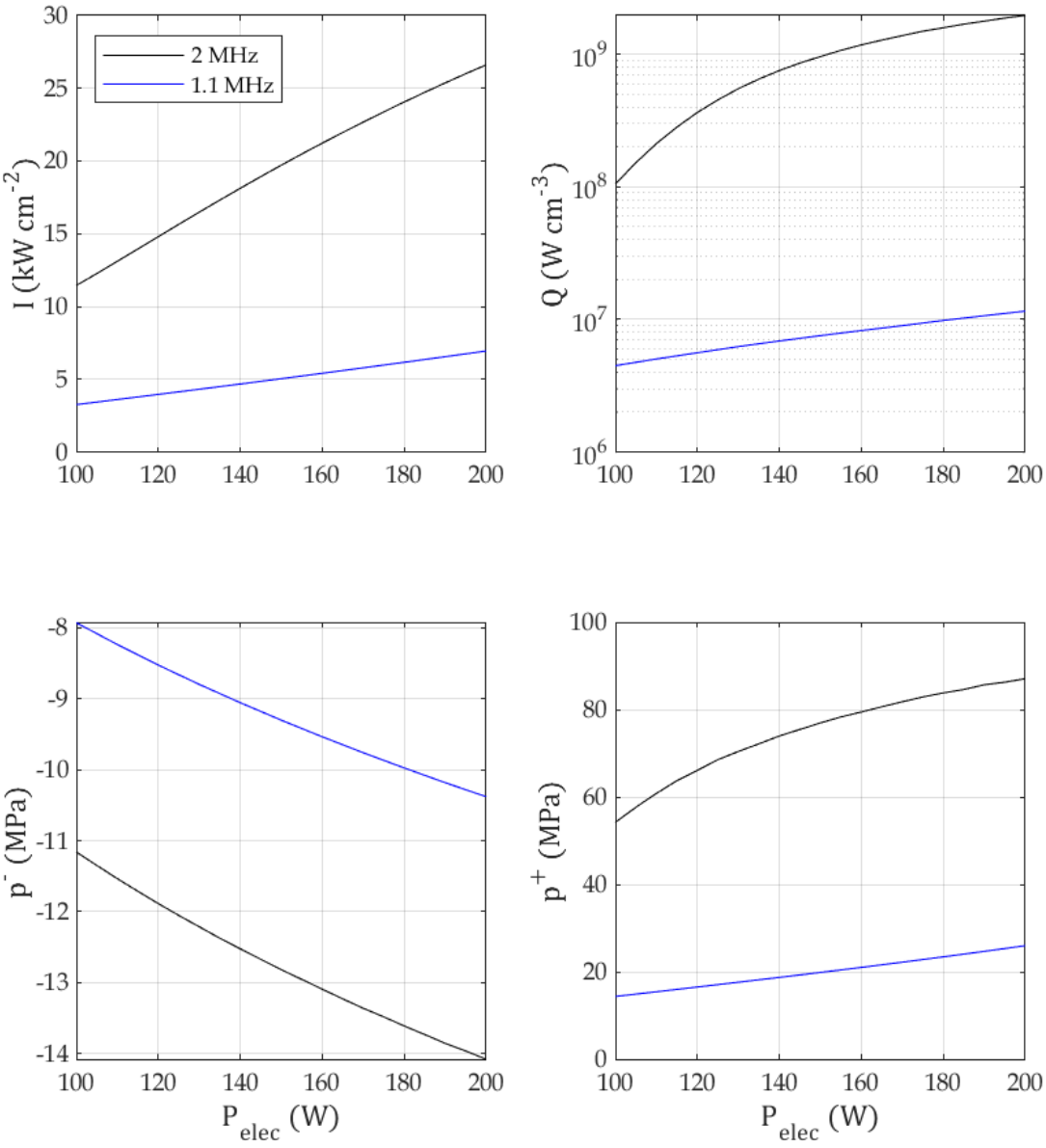

Figure 4-6. Comparison of key acoustic quantities between propagation at 2 MHz and 1.1 MHz as a function of input electrical power from 100 to 200 W. Black curves show results for the 2 MHz transducer, and blue curves show results for the 1.1 MHz transducer. Peak-negative and peak-positive focal pressures are shown in the second row of figures.

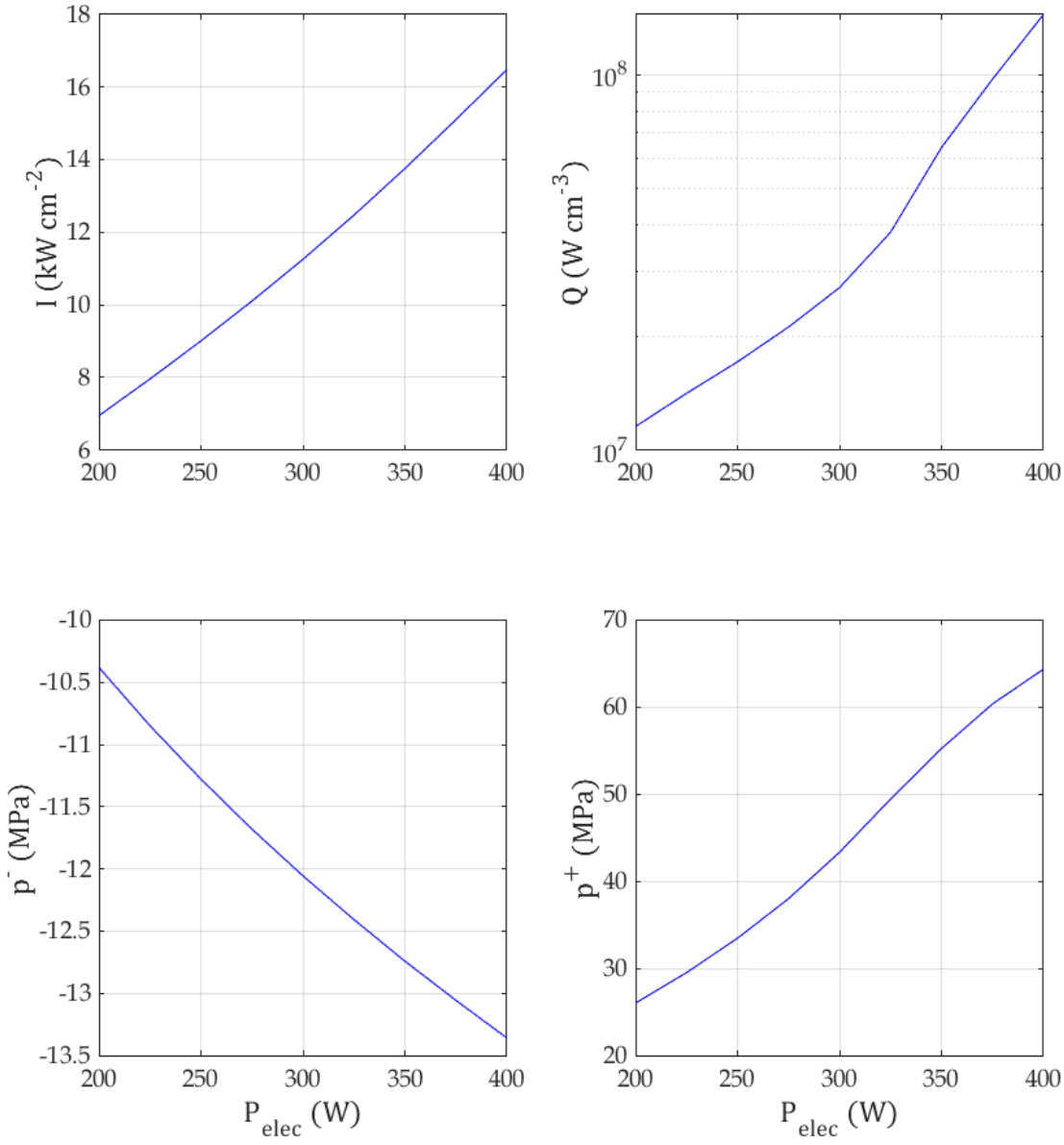

Figure 4-7. Key acoustic quantities for propagation at 1.1 MHz for input electrical powers between 200W and 400W.

Based on the magnitude nucleation thresholds obtained in Chapter 3, the window of input electrical powers for simulation in both transducers was defined as that which would result in focal peak negative pressures below – 10 MPa. Once this parameter window was defined for both transducers, the peak focal temperature was calculated using the Bioheat equation.

Heat deposition simulations were performed assuming an initial temperature of 20 °C in both the tissue volume and the perfusion fluid. The spatial grid for thermal simulations was coarsened by a factor of 2 in the axial direction

and by a factor of 3 in the radial direction in order to speed up calculations. The results shown in Fig. 4-8 display the maximum temperature at the treatment zone caused by HIFU heating. These results were obtained under the assumption that thermoacoustic properties of the medium are constant as temperature increases. This assumption was made to simplify the modelling and analysis of soft-tissue properties. Temperature values above the critical temperature of water (393.95 °C) were discarded.

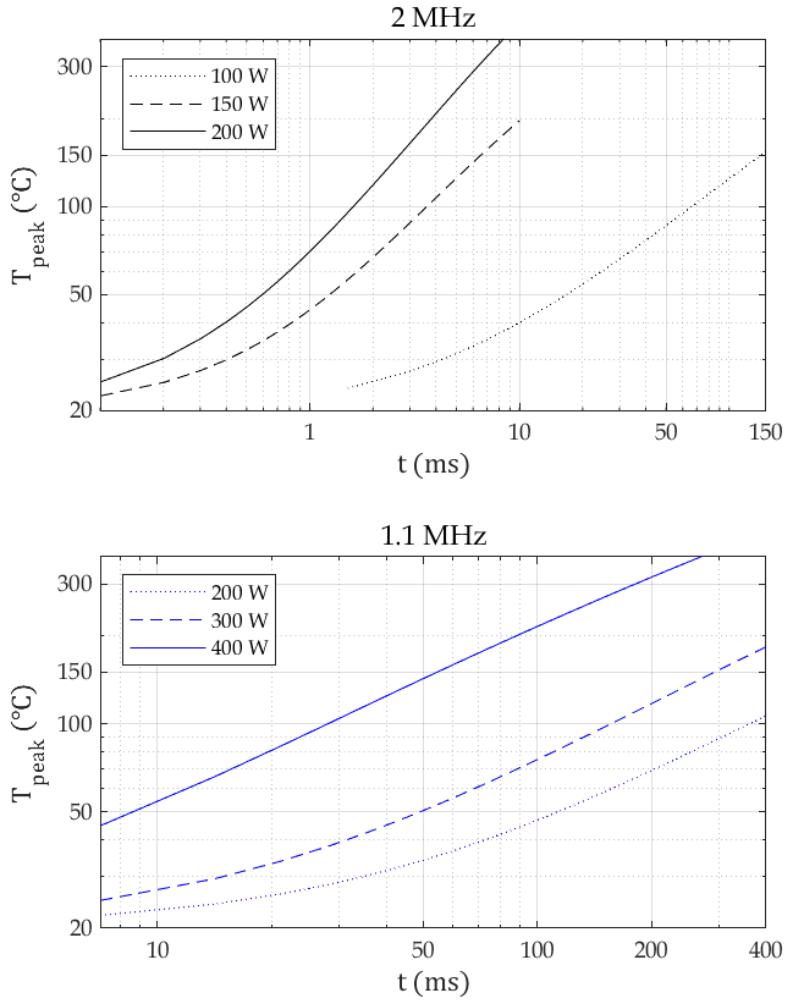

Figure 4-8. Peak focal temperatures as a function of pulse duration (sonication time). © 2021 IEEE. Reprinted, with permission, from de Andrade et. al, “Modeling the Physics of Bubble Nucleation in Histotripsy”, IEEE Transactions on Ultrasonics, Ferroelectrics, and Frequency Control, September 2021.

Figure 4-8 shows the dependence of the peak focal temperatures as a function of the pulse duration (sonication time). The pulse duration needed to reach temperatures around 100 °C was much shorter for propagation at 2 MHz compared

to 1.1 MHz. For input electrical powers of 150 and 200W, superheats of 100 °C were exceeded by the 2 MHz transducer in timescales as short as 10 ms. For the 1.1 MHz transducer, pulse durations as large as 200 ms were needed to exceed 100 °C for an input electrical power of 300 W. In the literature, it has been proposed that the formation of boiling bubbles in histotripsy depends on non-linear heating caused by the formation of a shockwave and that the absence of thermal damage is due to the capability of HIFU fields to heat the focal volume to around 100°C in a few milliseconds (Khokhlova *et al.*, 2015). Upon the nucleation of a bubble, HIFU focal heating is decreased due to scattering of the acoustic field from the boiling bubble and heat transfer into the bubble (Pahk *et al.*, 2018).

After the boiling bubble grows to a size that is comparable to the wavelength of the incoming acoustic field, this bubble acts as a scatterer and reflector of pressure waves due to the acoustic impedance mismatch between water vapour and soft tissue (Pahk *et al.*, 2017). This decreases acoustic intensities at the HIFU focus and creates pre-focal regions where the constructive interference between the incoming and reflected acoustic field can cause nucleation of a cavitation cloud (Pahk *et al.*, 2021).

4.4 Temperature Dependence of Pressure Thresholds

In Chapter 3, it was shown that HIFU-induced nucleation pressure thresholds could be modelled as a function of temperature upon appropriate parametrization of the medium's surface tension. In this section, Eq. 3.16 was used to predict the time dependence of the nucleation pressure threshold at the point of highest temperature within the HIFU focus obtained with the Bioheat equation.

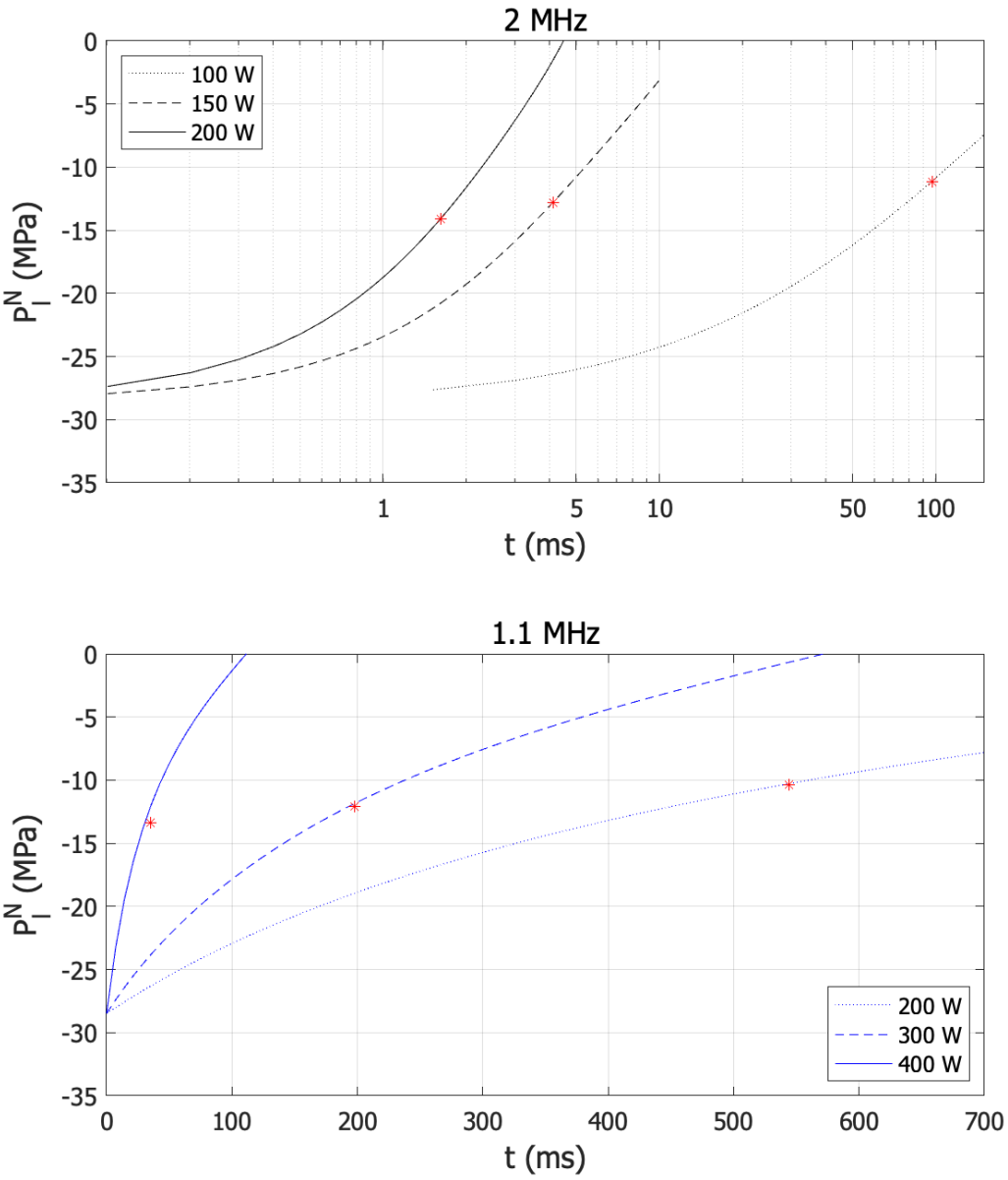

Figure 4-9. Focal nucleation pressure thresholds as a function of pulse duration (sonication time). Red asterisks denote focal peak-negative pressures for the equivalent input electrical power. © 2021 IEEE. Reprinted, with permission, from de Andrade et. al, "Modeling the Physics of Bubble Nucleation in Histotripsy", IEEE Transactions on Ultrasonics, Ferroelectrics, and Frequency Control, September 2021.

Figure 4-9 shows focal nucleation pressure thresholds for input electrical powers of 100, 150 and 200 W for the 2 MHz transducer and 200, 300 and 400 W for the 1.1 MHz transducer. Since the focal peak-negative pressure also depends on the electrical power provided to the transducer, these were indicated by red asterisks in the respective electrical power curve. These results agree with the

experiments of (Pahk *et al.*, 2015), where input electrical powers above 350 W were necessary for creating boiling histotripsy lesions in *ex-vivo* porcine liver with an H102 transducer.

Following from the assumptions in the derivation of Eq. 3.16, nucleation will happen in a time interval $\Delta t_N = 0.1 f_0$ after the focal nucleation pressure threshold is equal to the focal peak-negative pressure. These results show that the time needed for the nucleation of a boiling bubble decreases as heating rates are increased and as focal peak-negative pressures are lowered. Propagation at 1.1 MHz results in much longer times needed for bubble nucleation because heat deposition at these conditions is one to two orders of magnitude lower than at 2 MHz for lower input electrical powers.

4.4.1 Estimation of pulse-length required for nucleation

Traditionally, the pulse duration required for nucleation has been modelled as the time that the HIFU focus takes to reach 100 °C in the presence of shocks. By evoking weak shock theory (WST) (Canney, V. A. Khokhlova, *et al.*, 2010; Sapozhnikov, 2015), it is possible to approximate focal heating rates in focused ultrasound beams as

$$Q_{WS} = \frac{\beta f_0 (\Delta p)^3}{6 \rho_0^2 c_0^4} \qquad 4.1$$

where Δp is the magnitude of the incoming shock and β is the non-linearity parameter defined as 4.4 in simulations of propagation in the liver. The "time-to-boil" t_b can then be estimated by neglecting both diffusion and perfusion in Eq. 2.6 (Canney, V. A. Khokhlova, *et al.*, 2010; Khokhlova *et al.*, 2017):

$$Q_{WS} t_b = \Delta T \rho C. \qquad 4.2$$

This analytical model uses heating rates obtained from weak shock theory to approximate the time needed for boiling to occur. This approach relies on the assumption that entropy production at the shockwaves is negligible, and that the adiabatic equation of state can be used (Sapozhnikov, 2015). The main issue with

such an approach is that it neglects the effects of negative pressures in nucleation and thus underestimates the time for nucleation at low heating rates.

Estimation of the timescales required for boiling histotripsy considering the effects of the ultrasound focal peak-negative pressure can be done with the aid of CNT. Since the nucleation pressure is a temperature-dependent quantity, the nucleation pressure threshold can be calculated as a function of HIFU-induced heating, as displayed in Figure 4-10. This involves solving in time an equation of the type

$$p^- = P_l^N\left(T_{peak}(t)\right), \tag{4.3}$$

where p^- is the focal peak-negative acoustic pressure, P_l^N is defined by Eq. 3.16 and T_{peak} is obtained with the solution of the Bioheat equation. This equation is solved numerically in time, recording the value of t at which $P_l^N = p^-$. Results for this approach to the estimation of the timescales for the formation of the first bubbles are shown in Figure 4-10.

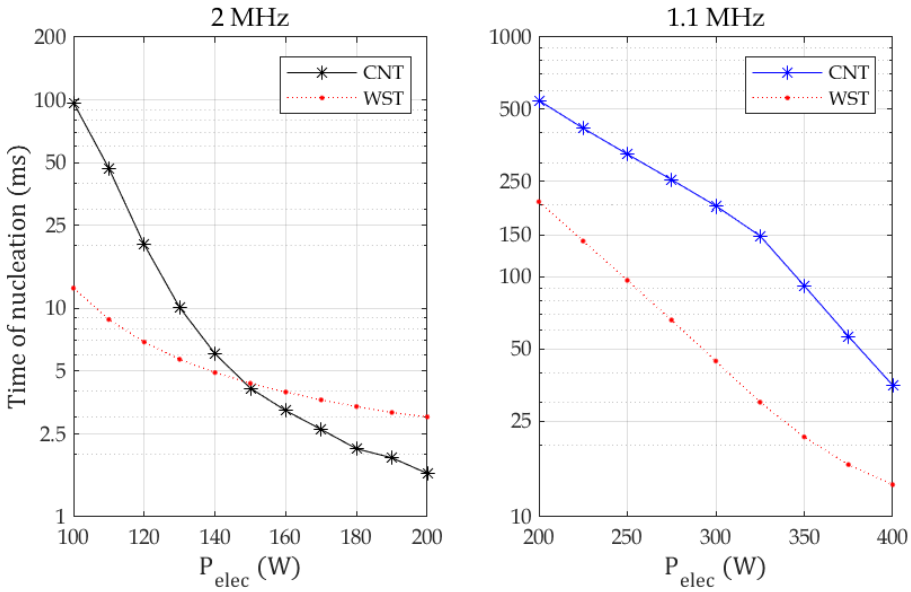

Figure 4-10. Time of nucleation as a function of input electrical power. © 2021 IEEE. Reprinted, with permission, from de Andrade et. al, “Modeling the Physics of Bubble Nucleation in Histotripsy”, IEEE Transactions on Ultrasonics, Ferroelectrics, and Frequency Control, September 2021.

Figure 4-10 shows a comparison of the time of nucleation calculated via CNT and the time to reach 100 °C shown in Eq. 4.3. The time needed for nucleation

decreases monotonically with increasing input electrical power for both transducers. In comparison with CNT results, the “time-to-boil” approach underestimates the time of nucleation at powers below 150 W for the 2 MHz transducer, and overestimates it at powers above 150 W. For propagation at 1.1 MHz Eq. 4.3 underestimates the time required for nucleation throughout the parameter space if compared to CNT. Physically, Eq. 4.3 overestimates focal heating by neglecting both heat diffusion and perfusion. Furthermore, the absence of terms regarding the pair of nucleation pressure and temperature in the liquid makes timescales shorter in regions where nucleation happens at temperatures higher than 100 °C and longer in regions where nucleation happens below it.

4.5 Spatial Profile of Nucleation

Focal temperature profiles right after the moment of nucleation are shown in Fig. 4-11 for propagation at 2 MHz and 150 W input electrical power ($t \approx 4.8$ ms) and 1.1 MHz and 300 W electrical power ($t \approx 240$ ms). In both simulations, the highest temperatures were in the range 100 – 120 °C. Heated regions were obtained as an ellipsoid around the HIFU focus. This spatial temperature profile is then used to calculate temperature-dependent nucleation pressure thresholds spatially, which can be seen in Fig. 4-10.

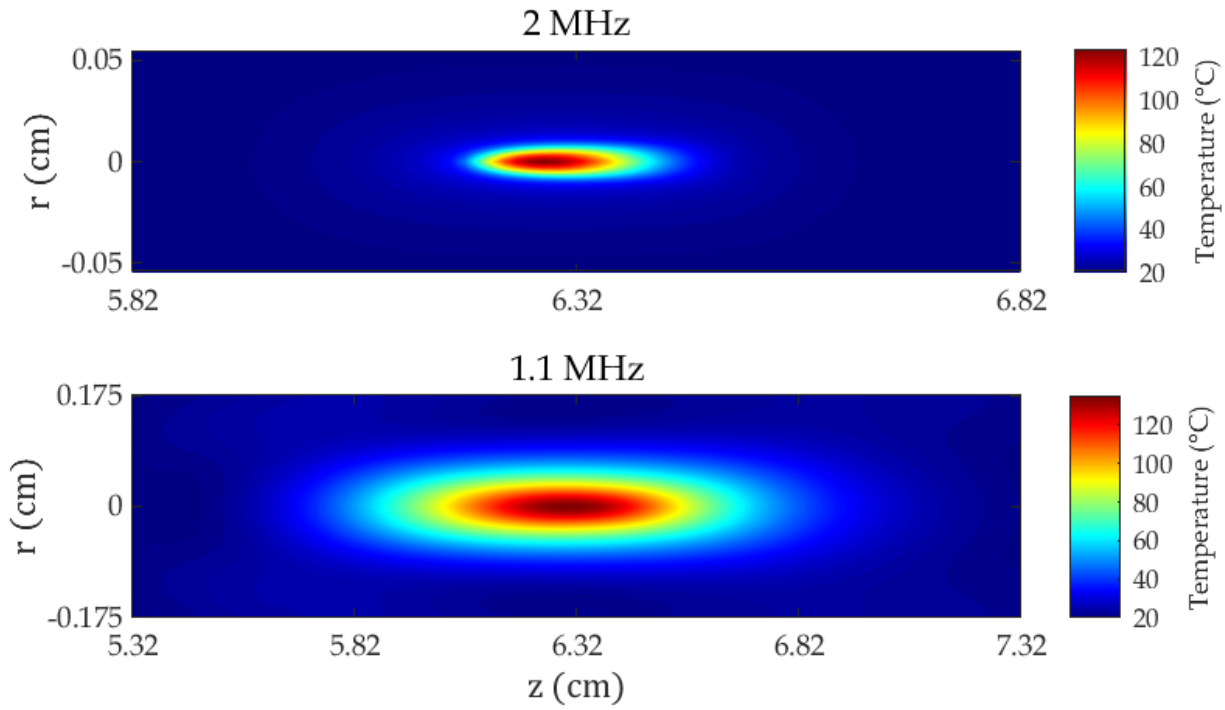

Figure 4-11. Focal temperature profile at the time of nucleation. The top figure shows temperature distribution after 4.8 ms of sonication at 2 MHz and 150W input electrical power. The bottom figure shows temperature profiles after 240 ms of sonication at 1.1 MHz with 300W input electrical power. © 2021 IEEE. Reprinted, with permission, from de Andrade et. al, "Modeling the Physics of Bubble Nucleation in Histotripsy", IEEE Transactions on Ultrasonics, Ferroelectrics, and Frequency Control, September 2021.

The spatial distribution of the nucleation pressure threshold shows contours of pressures with a similar shape to those created by heat deposition. These shapes are expected considering that Eq. 3.16 is solely temperature dependent. Nucleation then would take place within regions where the peak-negative acoustic pressure is below the pressure thresholds plotted. Results show that heat deposition facilitates nucleation by lowering thresholds and creates preferential nucleation sites around the regions of higher temperature. High-speed camera imaging of optically transparent tissue-mimicking gel phantoms has shown regions of highest heat deposition as the preferential site where vapour bubbles nucleate in boiling histotripsy (Pahk *et al.*, 2017).

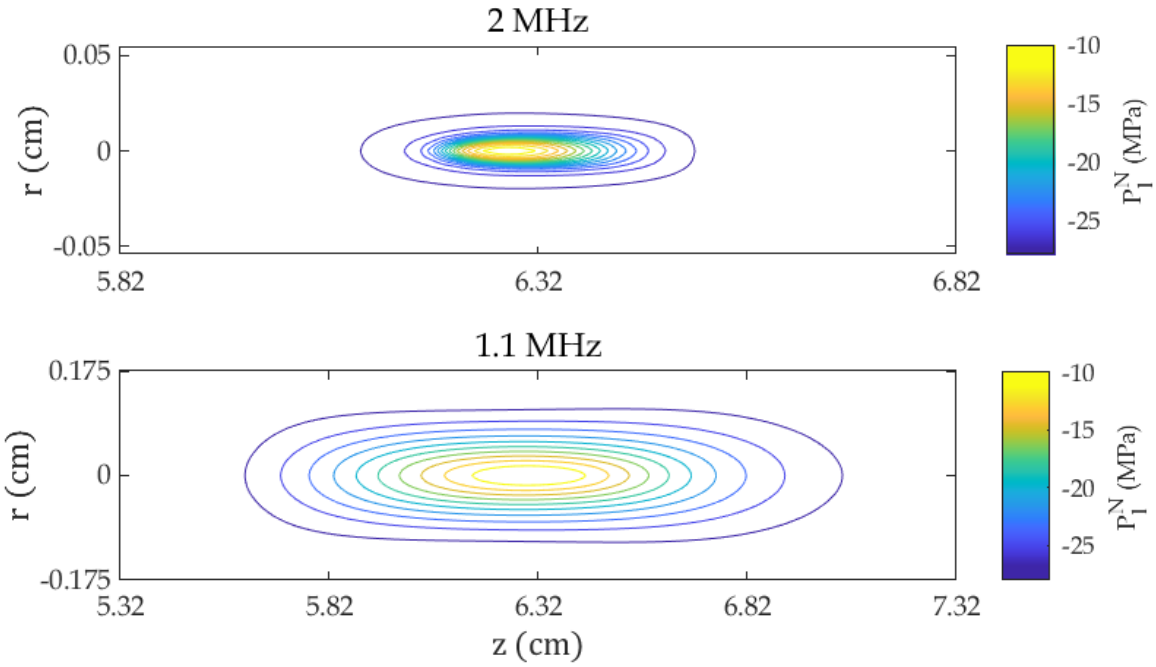

Figure 4-12. Temperature-dependent nucleation pressure thresholds at the time of nucleation. The top figure shows contours of nucleation pressure threshold distribution after 4.8 ms of sonication at 2 MHz and 150 W input electrical power. The bottom figure shows values of P_l^N after 240 ms of sonication at 1.1 MHz with 300 W input electrical power. © 2021 IEEE. Reprinted, with permission, from de Andrade et. al, "Modeling the Physics of Bubble Nucleation in Histotripsy", IEEE Transactions on Ultrasonics, Ferroelectrics, and Frequency Control, September 2021.

In both sets of results, a cigar-shaped region is observed, in agreement with previous numerical simulation of HIFU heat deposition and experiments in boiling histotripsy (Pahk *et al.*, 2017). It has been observed that boiling histotripsy lesions have a characteristic "tadpole" shape, consisting of a spherical "head" and an ellipsoidal "tail". This cigar-shaped nucleation region would be the location where the first boiling bubble forms and starts the process of mechanical fractionation of tissue (Pahk *et al.*, 2017).

Spatial nucleation rates are plotted in Figs. 4-13 and 4-14, compared to spatial temperature profiles and peak-negative acoustic pressures in the focal region. The highest nucleation rates were found to occur within a sub-volume of the HIFU focus, which coincides with the regions of highest temperature where the peak-negative pressure surpasses the nucleation pressure threshold. The bottom plot in Fig. 4-13 shows that although the lowest acoustic pressures happened

slightly pre-focally, these were insufficient to generate appreciable nucleation rates.

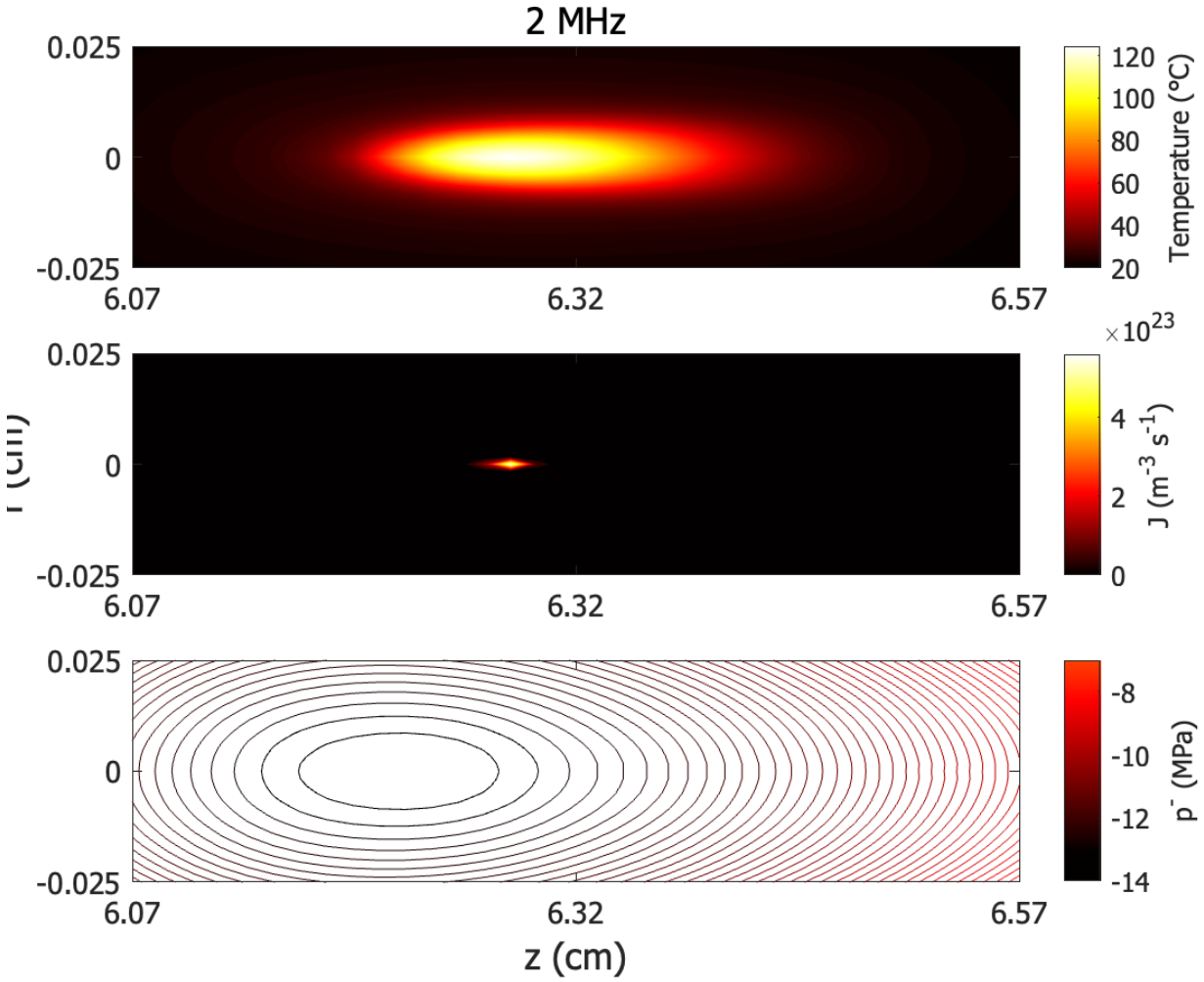

Figure 4-13. Overview of the bubble nucleation rate (middle figure) compared to temperature profiles (top) and peak negative acoustic pressures (bottom) at 4.8ms of sonication for propagation at 2 MHz and 150W input electrical power. © 2021 IEEE. Reprinted, with permission, from de Andrade et. al, "Modeling the Physics of Bubble Nucleation in Histotripsy", IEEE Transactions on Ultrasonics, Ferroelectrics, and Frequency Control, September 2021.

A similar trend was observed for both transducers simulated, having the preferential nucleation site within the regions of highest temperature. Since the nucleation pressure threshold is temperature-dependent, nucleation is spatially restricted to regions where the peak negative acoustic pressure overcomes the nucleation pressure threshold; however, these regions are not necessarily the regions of lowest acoustic pressure.

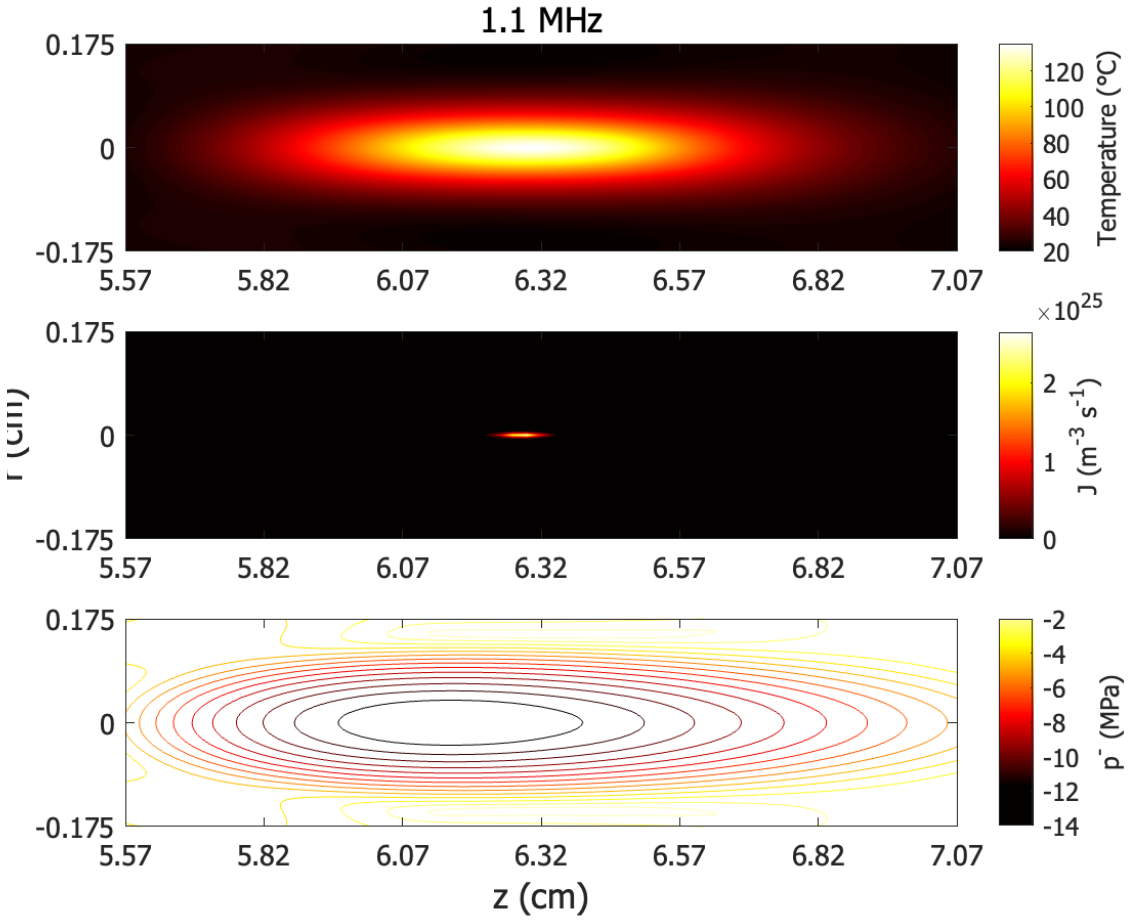

Figure 4-14. Overview of the bubble nucleation rate (middle figure) compared to temperature profiles (top) and peak negative acoustic pressures (bottom) at 240 ms of sonication for propagation at 1.1 MHz and 300W input electrical power. © 2021 IEEE. Reprinted, with permission, from de Andrade et. al, "Modeling the Physics of Bubble Nucleation in Histotripsy", IEEE Transactions on Ultrasonics, Ferroelectrics, and Frequency Control, September 2021.

The size distribution of critical bubble nuclei at the HIFU focus is shown in Fig. 4-15. These range from 6 – 10 mm in both sets of results, where the size of critical nuclei increases towards the regions of highest heat deposition. These results agree with those found in HIFU nucleation experiments in water (Davitt et al., 2010a). This could imply that the HIFU focus is the location where bubble nuclei have higher chances of merging and forming larger bubbles that are mechanically stable within the thermodynamic conditions imposed by HIFU pressure and temperature fields.

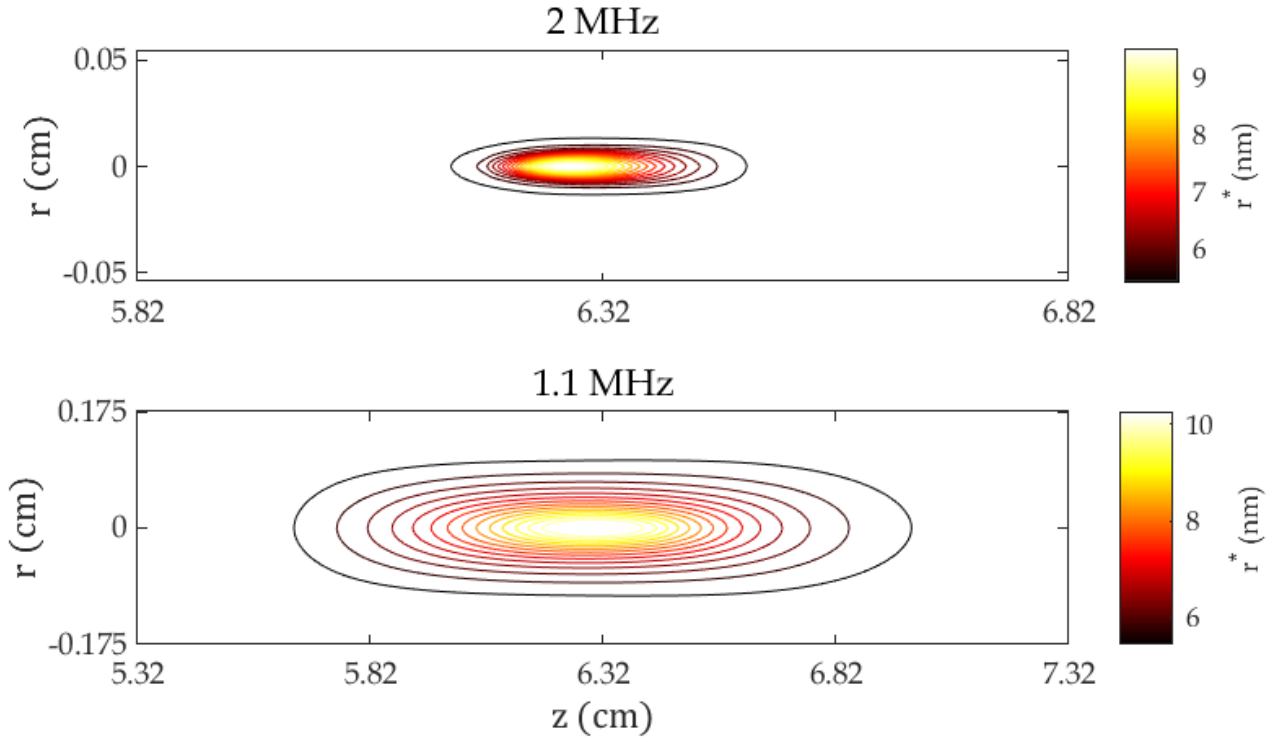

Figure 4-15. Size distribution of critical nuclei during of nucleation. © 2021 IEEE. Reprinted, with permission, from de Andrade et. al, "Modeling the Physics of Bubble Nucleation in Histotripsy", IEEE Transactions on Ultrasonics, Ferroelectrics, and Frequency Control, September 2021.

It is important to note that the ability of Eq. 3.7 to predict the size of critical nuclei shown in Fig. 4-15 has limitations. This is an equation that predicts the minimum size of bubble nuclei so that nucleation happens under the assumption that the surface tension is size-independent. It does not consider either inertial or viscous terms present in standard equations for bubble dynamics. This highlights the need to integrate these terms into CNT for appropriate modelling of bubble nucleation in terms of hydrodynamic quantities, which is done in Chapter 5. Numerical simulations of histotripsy bubble nuclei found that they grow by vapour transport (Bader and Holland, 2016). It has also been shown that the temperature field around these bubbles limits their growth (Kreider *et al.*, 2013; Pahk *et al.*, 2018). After the growth of these bubbles to dimensions like the wavelength of the acoustic field, these bubbles act as reflectors creating regions of extremely low negative pressure pre-focally where a cavitation cloud occurs (Pahk *et al.*, 2017).

4.6 Chapter Summary

The phenomenological implementation of CNT developed in *Chapter* 3 is applied to boiling histotripsy pressure and temperature fields and to bubble nucleation in soft tissue. This Chapter was developed following from the vastly studied solutions to the KZK equation, which is a specific case of the Westervelt equation (Soneson, 2017; Yuldashev et al., 2018). These models of acoustic propagation have been applied longitudinally to the modelling of highly focused acoustic beams and carries within itself the assumptions of axial symmetry along the propagation axis. Most notably, they yield pressure waveforms resulting ultrasound propagation in heterogeneous, sequential media and subsequent heat deposition caused by absorption of acoustic waves (Filonenko and Khokhlova, 2001). Acoustic propagation was simulated for two bowl-shaped transducers by solving a KZK-type equation with the HITU simulator operating at 2 MHz (Sonic Concepts. H148) and 1.1 MHz (Sonic Concepts, H102). Heat deposition was modelled with the Bioheat transfer equation. Nucleation theory models were then used to calculate quantities such as the nucleation rate, nucleation pressure threshold, radius of critical nuclei and the pulse durations required for a vapour bubble to form.

Results show that heat deposition in boiling histotripsy facilitates nucleation by decreasing focal nucleation pressure thresholds. With the present approach, it is possible to calculate the minimum pulse duration required to achieve nucleation in boiling histotripsy for a certain HIFU transducer. These results agreed with previous estimations of the time to boil in boiling histotripsy, decreasing monotonically with increasing input electrical power to the transducer. The present model shows that it is not sufficient to heat the HIFU focus up to 100° C in order to achieve repeatable bubble nucleation in histotripsy. The local nucleation of vapour bubbles happens because of the interaction of sufficiently high HIFU-induced temperatures and the tensile part of the ultrasound wave. This can inform the parametrisation of the duty cycle in boiling histotripsy protocols so that bubble

nucleation is consistently achieved and potential thermal damage to the treatment volume and intervening tissue is minimised.

Similar spatial trends in nucleation were observed for both transducers. The regions with highest nucleation rate were a sub-volume within the focal regions of high temperature. Nucleation is spatially restricted to regions where the peak negative acoustic pressure overcomes the temperature-dependent nucleation pressure threshold. However, these regions are not necessarily those of lowest acoustic pressure. The radius of focal critical nuclei obtained through the simulations presented in this Chapter ranged from 6 – 10 nm, in agreement with previous experimental investigation into HIFU-induced bubble nucleation. The size of critical nuclei was found to increase in regions of higher temperature around the HIFU geometrical focus. Overall, results indicate that it is not possible to detach the effects of focal pressure and temperatures induced by HIFU in the nucleation of bubbles.

Chapter 5

Hydrodynamic Nucleation in Ultrasound Fields

Acknowledgement: The contents of this chapter are based on (de Andrade *et al.*, 2022). Figures 5-2, 5-3, 5-4, 5-5, 5-6, 5-7 and 5-8 have been reproduced here with authorisation of the publisher.

In Chapter 3, a thermodynamic formulation of CNT optimised for ultrasound nucleation was derived. This formulation of CNT was applied to boiling histotripsy protocols in Chapter 4, revealing temporal and spatial trends of nucleation within the ultrasound focus. The theory derived in Chapter 3 is a thermodynamic theory, which considers vapour transport to be the sole mechanism involved in nuclei growth. However, it is known that bubble growth is jointly determined by hydrodynamic effects via the acoustic field and thermal effects controlled by the liquid temperature (Church, 2002). This means that the formulation of CNT presented in Chapter 3 yields nucleation rates which ignore the effects of the acoustic field in the initial stages of growth of nuclei. In Chapter 4, the nucleation models developed in Chapter 3 were applied to the numerical simulation of boiling histotripsy protocols. It was found that boiling bubbles would first nucleate at the regions of highest heat deposition at the ultrasound focus (de Andrade *et al.*, 2021), even though there were regions of peak negative pressure with higher amplitude within the field.

High-speed camera imaging of boiling histotripsy in transparent tissue phantoms provides evidence that both cavitation and boiling might occur in boiling histotripsy (Pahk *et al.*, 2017). The constructive interactions of the pressure waves reflected by boiling bubbles with the incoming acoustic field can create pre-focal regions of negative pressure that surpass the medium's intrinsic pressure

threshold, resulting in a cavitation cloud (Pahk *et al.*, 2021). Such tensile pressure regions have been observed in linear and non-linear acoustic reflection simulations from a boiling histotripsy vapour bubble (Pahk et al., 2021, 2017). The possibility of distinct nucleation regimes within boiling histotripsy protocols warrants interest in the physics of bubbles nucleated throughout physiological, hyperthermic and boiling temperatures. Herein, the role of thermal, inertial, and viscous effects in ultrasound-induced bubble nucleation are analysed. We employ a hydrodynamic formulation of classical nucleation theory, where the dynamics of spherical bubbles is considered by including the Rayleigh-Plesset (Prosperetti, 1982) equation into the kinetic terms of a CNT model. This model is based on the hydrodynamic approach of Zeldovich developed in 1942 (Zeldovich, 2015), further developed by Kagan and discussed in detail by Blander and Katz (Blander, 1979; Katz and Blander, 1973).

This formulation adds to the current understanding of ultrasound bubble nucleation by (i) accounting for the dynamics of bubbles throughout their nucleation window (Church, 2002), (ii) yielding nucleation rates that are fully pressure-dependent and are not limited by vaporisation rates (de Andrade et al., 2021, 2019), and (iii) quantifying physical similarities and differences between "boiling" and "cavitation" bubbles (Kreider *et al.*, 2011). In addition, the present theory yields three non-dimensional quantities which provide information on the underlying mechanism controlling bubble nucleation when applied to histotripsy protocols. These quantities show how the balance between viscous and inertial forces affects the kinetics of bubble nucleation and how thermal mechanisms play a role in the quantity and size of nucleated bubbles.

5.1 The Governing Equation of Nucleation

The models discussed in Chapter 3 and 4 were based on well-known derivations and equations for bubble nucleation in the presence of tensile pressures. This model only accounts for uniform growth of nuclei via vapour transport and correlates the radius of a critical nucleus with its internal number of molecules via an ideal gas law and basic equations from liquid kinetics. The model

in Chapter 3 is a purely thermodynamic model, similar to the model obtained by Gibbs in his seminal works (Gibbs, 1928, 1878). However, it is possible to obtain this model purely in kinetic terms. Here, the interest is understanding the kinetic development of nucleation, which warrants a more fundamental approach. Physically, the model in Chapters 3 and 4 measures the number of nuclei of size r^* that are produced from t_0 to $t = t_0 + \Delta t_N$.

5.2 Growth by vapour transport

The problem of determining vapour transport rates across an interface given a supersaturation is one that can be approached with a macroscopic kinetic theory of mass transport. Therefore, the derivations within this section will focus on the kinetics involved in the time evolution of embryos through attachment and detachment of single vapour molecules. This implies that the process of nucleation occurs as a series of single reactions between monomers, i.e., single vapour molecules, and polymers, which are clusters of vapour molecules within the bulk of a liquid phase.

Herein, it is assumed that the ever-changing thermal fluctuations in the liquid create a distribution of nuclei with distribution $Z(n,t)$. This function represents the concentration of embryos with n internal molecules throughout the development of time t in an experiment. It will be convenient to denote the true transient distribution of an embryo with n molecules as $Z(n,t) = Z_n(t)$ for a concise notation. However, one might also wonder the exact nature of these n-sized embryos.

In Chapter 3, it was discussed how the Gibbs free energy of the system leads to the formation of extremely small bubbles, that trigger nucleation upon growing to a certain critical size r^*. From a thermodynamic point of view, these are transient, short-lived formations that happen due to the molecular movement in the liquid, which has a characteristic magnitude of $k_B T$. However, these events happen randomly in space and time, meaning that in any liquid, even at equilibrium, there are short-lived fluctuations in density that can be understood as bubble embryos.

If one averages the number of fluctuations of all sizes that take place within a long observation time and divides this by the volume under investigation, the result is a time-independent, spatially-averaged equilibrium distribution of nuclei $C(n,t) = C_n(t)$. The first mathematical challenge is then finding a way to represent the unknown true distribution of nuclei $Z_n(t)$ from the equilibrium distribution $C_n(t)$, however this will be discussed later in this Chapter.

5.2.1 Transition frequencies

We can model nucleation as the process where embryos with initial distribution $Z(n,0) \equiv Z_n(0)$ is subjected to a certain growth law $v = f\left(\frac{dn}{dt}, n, \frac{dr}{dt}, r, \ldots\right)$ towards $Z_{n^*}(\Delta t_N)$ after a time interval Δt_N. The growth law then acts as a characteristic line over which the initial distribution $Z_n(0)$ travels in time until it becomes $Z_{n^*}(\Delta t_N)$, as illustrated in Figure 5-2. This characteristic line is a mathematical relationship between the radius of nuclei and time and takes on as many independent variables as needed for the description of the growth of embryos, although this was simplified as the rate of vaporisation into bubble nuclei in Chapter 3.

If nucleation is seen as the transformation of a naturally-occurring unsteady distribution of n-sized nuclei $Z_n(t) \equiv Z(n,t)$ into one that can be detected experimentally, this process fundamentally depends on the amount of growth Δn that a nucleus needs to undertake within a time interval $\Delta t_N = \frac{\Delta n}{v}$ so that the initial population embryos of radius $n = n_0$ at $t = 0$ grows to a critical size n^* at $t = \Delta t_N$. Therefore, the quantity $Z_n(\Delta t_N) - Z_n(0)$ measures the variation in the distribution of nuclei of all sizes n in a time interval Δt_N, with rate $\frac{Z_n(\Delta t_N) - Z_n(0)}{\Delta t_N}$. If one assumes vaninshingly small intervals Δt_N, this becomes the derivative $\frac{dZ_n(t)}{dt} \equiv \frac{\partial Z(n,t)}{\partial t}$.

By focusing on how the concentration of embryos of n internal molecules changes in time, it can be noticed that it is simply the rate of arrivals at the size n subtracted by the rate of departures from size n. Let us denote the rate of arrivals as $f(n,t) \equiv f_n$, denoting the frequency where n-sized embryos gain one vapour

molecule, and the rate of departures as $g(n,t) \equiv g_n$, denoting the frequency where n-sized embryos lose one vapour molecule. This leads to an expression of the form

$$\frac{dZ_n}{dt} = f_{n-1}Z_{n-1} + g_{n+1}Z_{n+1} - (f_n + g_n)Z_n. \tag{5.1}$$

This equation means that the rate of arrivals at the size n will be given by the forward rate of $n-1$ sized nuclei growing into n added to the backward rate of $n+1$ sized nuclei shrinking into n. The rate of departures is given by n sized nuclei either growing or shrinking away from n. Thus, the net movement of the cluster on the (n,t) plane is given by the drift $f_n - g_n$.

5.2.2 Equilibrium

We now make use of the equilibrium distribution of nuclei $C(n,t)$ as nuclei sizes are conserved in equilibrium. The number of nuclei that grow from the size n is balanced by the number of nuclei that shrink into n and that the number of nuclei that grow into n is balanced by the number of nuclei that shrink from n.

$$C(n,t) = C_0 \exp\left(-\frac{W(n,t)}{k_B T}\right). \tag{5.2}$$

The equilibrium concentration of nuclei is fundamentally time-independent, but whenever there are changes to the supersaturation of the medium via transient temperature $T(t)$ or pressure fields $P_l(t)$, the work of nucleation $W(n)$ can be defined as $W(n,t)$.

The conservation of sizes in equilibrium is summarised by the identities

$$\begin{aligned} f_n C_n = g_{n+1}C_{n+1} \;\therefore\; g_{n+1} &= \frac{f_n C_n}{C_{n+1}}, \\ f_{n-1}C_{n-1} = g_n C_n \;\therefore\; g_n &= \frac{f_{n-1}C_{n-1}}{C_n}. \end{aligned} \tag{5.3}$$

If these identities are replaced in Eq. 5.1:

$$\begin{aligned}\frac{dZ_n}{dt} &= f_{n-1}Z_{n-1} + \frac{f_nC_n}{C_{n+1}}Z_{n+1} - f_nZ_n - \frac{f_{n-1}C_{n-1}}{C_n}Z_n \\ &= f_{n-1}C_{n-1}\left(\frac{Z_{n-1}}{C_{n-1}} - \frac{Z_n}{C_n}\right) - f_nC_n\left(\frac{Z_n}{C_n} - \frac{Z_{n+1}}{C_{n+1}}\right),\end{aligned} \quad 5.4$$

the following Euler forward steps in size are obtained

$$\frac{Z_{n-1}}{C_{n-1}} - \frac{Z_n}{C_n} = \frac{\partial}{\partial n}\left[\frac{Z(n,t)}{C(n,t)}\right][(n-1)-n] = -\frac{\partial}{\partial n}\left[\frac{Z(n,t)}{C(n,t)}\right], \quad 5.5$$

and

$$\frac{Z_n}{C_n} - \frac{Z_{n+1}}{C_{n+1}} = \frac{\partial}{\partial n}\left[\frac{Z(n,t)}{C(n,t)}\right][n-(n+1)] = -\frac{\partial}{\partial n}\left[\frac{Z(n,t)}{C(n,t)}\right]. \quad 5.6$$

Therefore,

$$\frac{\partial Z(n,t)}{\partial t} = \frac{\partial}{\partial n}\left[\frac{Z(n,t)}{C(n,t)}\right](f_nC_n - f_{n-1}C_{n-1}). \quad 5.7$$

Once again, the implicit differential in this equation is

$$\begin{aligned}&\frac{\partial}{\partial n}\left[\frac{Z(n,t)}{C(n,t)}\right](f_nC_n - f_{n-1}C_{n-1}) \\ &\qquad = \frac{\partial}{\partial n}\left\{f_nC_n\frac{\partial}{\partial n}\left[\frac{Z(n,t)}{C(n,t)}\right]\right\}[n-(n-1)] \\ &\qquad = \frac{\partial}{\partial n}\left\{f_nC_n\frac{\partial}{\partial n}\left[\frac{Z(n,t)}{C(n,t)}\right]\right\}.\end{aligned} \quad 5.8$$

This is the general form of the governing equation of nucleation

$$\frac{\partial Z(n,t)}{\partial t} = \frac{\partial}{\partial n}\left\{f(n,t)C(n,t)\frac{\partial}{\partial n}\left[\frac{Z(n,t)}{C(n,t)}\right]\right\}. \quad 5.9$$

5.2.3 Nucleation rates

Now it is of interest to obtain the number of super nuclei that appear within a fixed volume V_0 after a time interval Δt_N. Knowing that if $Z(n,t)$ is a density function of n-sized nuclei at the time t, the nuclei that are greater than the critical size can be quantified with the integral

$$\Sigma(t) = V_0 \int_{n^*}^{M} Z(n,t)\, dn, \tag{5.10}$$

where the time derivative $\frac{d\Sigma}{dt} \equiv J(t)$ is precisely the rate at which nuclei greater than the critical size are formed in time, i.e., the time-dependent nucleation rate $J(t)$. M is the total number of molecules in the system, and $Z_M(t) \approx 0$ is a fair assumption, stating that there is never a nucleus that comprises all molecules in the control volume under consideration.

It is then necessary to find an approximation for $Z(n)$ in terms of the equilibrium distribution $C(n^*)$ in the vicinity of the critical size. Knowing that the equilibrium distribution is defined as $C(n) = C_0 \exp\left(-\frac{W(n)}{k_B T}\right)$, where $C_0 = \left(\frac{\rho_l}{m}\right)$, $W(n)$ can be expanded in a second-order Taylor series around n^*.

$$W(n) = W^* + \left(\frac{1}{2}\right)\left(\frac{d^2W}{dn^2}\right)_{n=n^*} (n-n^*)^2. \tag{5.11}$$

This approximation is fundamental towards obtaining an understanding of nucleation around the critical region, yielding an explicit dependence of $C(n)$ on n for nucleating embryos around the critical size n^*:

$$C(n) = C(n^*) \exp[\beta^2 (n-n^*)^2]. \tag{5.12}$$

The quantity $\beta = \sqrt{\frac{-\left(\frac{d^2W}{dn^2}\right)_{n=n^*}}{2k_BT}}$ is a geometrical characterization of the curvature of $W(n)$, and a greater value of β corresponds to a sharper maximum of $W(n)$ at n^*. Since $C(n,t)$ has a sharp maximum at $n = n^*$, all values of $C(n,t)$ away from the critical point will approach zero. Since vaporisation rates $f(n,t)$ are finite, $f^*(t)C^*(t)$ is a good approximation as shown by (Kashchiev 1968). Since the approximation of $C_n(t)$ in Eq. 5.12 has a sharp maximum at $n = n^*$, the critical values of this integral can be taken leading to the simplified form

$$\begin{aligned} J(t) &= \left(\frac{1}{\mathrm{V}_0}\right)\frac{d\Sigma(t)}{dt} = \int_{n^*}^{M}\frac{\partial C(r,t)}{\partial t}dn \\ &= \int_{n^*}^{M}\frac{\partial}{\partial n}\left\{f(n,t)C(n,t)\frac{\partial}{\partial n}\left[\frac{Z(n,t)}{C(n,t)}\right]\right\}dn \\ &= -f^*(t)C^*(t)\left\{\frac{\partial}{\partial n}\left[\frac{Z(n,t)}{C(n,t)}\right]\right\}_{n=n^*} + Z^*\frac{dn^*}{dt}. \end{aligned} \qquad 5.13$$

At this point, the rate J_{ss} in which Σ nuclei within a volume V_0 over a time interval Δt_N, defined as

$$J_{ss} = \frac{\Sigma}{V_0\Delta t_N} \approx -f^*C^*\left[\frac{d}{dn}\left(\frac{Z_n}{C_n}\right)\right]_{n=n^*}, \qquad 5.14$$

to which an analytical expression has been obtained by Zeldovich (Kashchiev, 2000) by integrating Eq. 5.9 for a steady state process, i.e., $\frac{\partial Z}{\partial t} = 0$, obtaining:

$$\frac{Z_n}{C_n} = \frac{\int_n^M [f(m)C(m)]^{-1}dm}{\int_1^M [f(m)C(m)]^{-1}dm}. \qquad 5.15$$

By taking the derivative of this expression with respect to the size n and evaluating at $n = n^*$, a general form of J_{ss} is derived:

$$J_{ss} = \frac{\Sigma}{V_0 \Delta t_N} \approx \int_1^M \frac{dn}{f(n)C(n)} = zf^*C^*. \qquad 5.16$$

Which is Equation 3.28 for the case of vaporisation.

5.2.4 The critical region

If one looks at the equilibrium concentration of critical nuclei in a metastable liquid, there will be a certain critical region with width $\Delta^* = n_2 - n_1$ in which nuclei will be energetically equivalent. This happens because when $|W^* - W(n)| < k_B T$ for any size n such that $n_1 < n < n_2$ (Kashchiev 2000). Since the nucleation rate has a peak at the critical value W^* with sharpness defined by $\beta = \sqrt{-\frac{\left(\frac{d^2W}{dr^2}\right)_{r=r^*}}{2k_BT}}$, the region Δ^* centered around r^* (Debenedetti, 1991) will influence the final nucleation rates as not all nuclei will be able to cross this region without randomly fluctuating back to subcritical sizes.

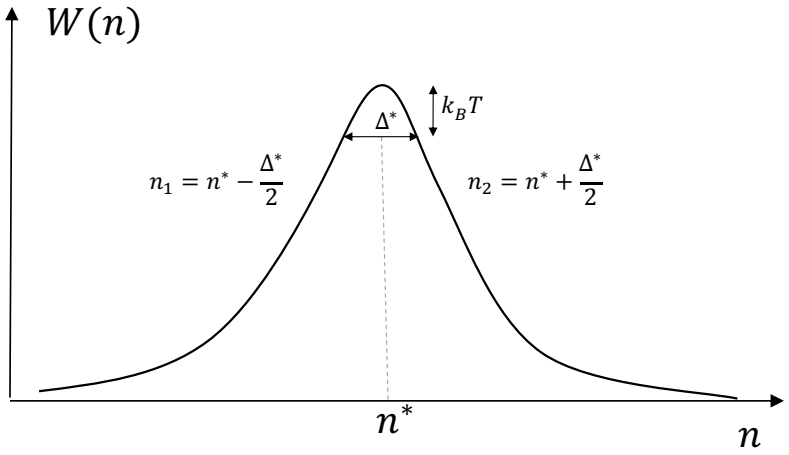

Figure 5-1. Illustration of the critical region.

The definition of Δ^* as given by (Kashchiev 2000) is

$$\Delta^* = \frac{\sqrt{\pi}}{\beta}. \qquad 5.18$$

This definition of the critical region has been implicitly considered in the derivations of Chapters 3 – 4, however omitted for the sake of simplicity. This quantity has an important physical implication with regards to the number of embryos that grow onto supercritical sizes. If nuclei within the size range $n_1 < n < n_2$ are energetically equivalent, that is, a change from n_1 to n_2 and vice-versa requires less free energy than the naturally occurring thermal fluctuations of the medium with magnitude $k_B T$, then some embryos of sizes between n^* and $n^* + \frac{\Delta^*}{2}$ are not "safe", and might be randomly reduced to subcritical sizes between $n^* - \frac{\Delta^*}{2}$ and n^* by intrinsic thermal fluctuations in the medium. This physical mechanism is summarised in z, the Zeldovich factor of nucleation. This factor is inversely proportional to the width of the critical region as $z = \frac{1}{\Delta^*}$ and is related to the probability that a thermally activated random walk of nuclei in size space will result in spontaneous growth of nuclei.

5.3 Combined vapour transport and acoustic growth

As mentioned earlier, the models of ultrasound nucleation discussed in Chapters 3 and 4 (de Andrade et al., 2021, 2019) were based on the Szilard model, where nucleation is thought to be a series of reactions between monomers ($n = 1$ molecule clusters) and polymers ($n > 1$ molecule clusters). This results in a steady-state nucleation rate that carries the assumption that nuclei can only grow via the evaporation of the surrounding liquid phase. Nonetheless, the influence of the liquid vapour pressure in nucleation decreases at lower temperatures and might become insignificant compared to very large tensile pressures at play, as discussed in (de Andrade *et al.*, 2021). It is now of interest to understand how one can apply macroscopic properties of bubble dynamics to understand the growth of bubble nuclei. This will now be done by using the approach of (Zeldovich, 2015) to approximate the continuous size transition $r_n \rightleftarrows r_{n+1}$ in the radial coordinate r instead of the discrete transition $n \rightleftarrows n + 1$ in the size coordinate n.

The first physical factor to consider is that there is an idealised relationship between the radius of a bubble embryo and the number of internal molecules it contains via the ideal gas law $PV = nk_BT$. Therefore, a change of coordinates from (n, t) to (r, t) can be applied to Eq. 3.9. It is critical to notice that as a bubble embryo transitions from a size n to $n + 1$, the differential at play is $\Delta n = 1$ in the discrete n coordinate system, however Δn is equivalent to an unknown number of radial variations dr in the continuous coordinate r as illustrated by Figure 5-2.

One can then assume that the transition from n to $n + 1$, or from n to $n - 1$, has a fundamental length scale $l_r = r(n + 1) - r(n)$, where $r(n)$ is a relationship derived from the ideal gas law. This length scale is useful in changing the independent variables of Equation 5.9 from n to r, since Eq. 5.5 will be equivalent to

$$\frac{Z_{r-l_r}}{C_{r-l_r}} - \frac{Z_r}{C_r} = \frac{\partial}{\partial r}\left[\frac{Z(r,t)}{C(r,t)}\right][(r - l_r) - r] = -\frac{\partial}{\partial r}\left[\frac{Z(r,t)}{C(r,t)}\right] l_r. \tag{5.19}$$

Similarly, Eq. 5.6 becomes

$$\begin{aligned} \frac{\partial}{\partial r}\left[\frac{Z(r,t)}{C(r,t)}\right] &= \left(f_r C_r - f_{r-l_r} C_{r-l_r}\right) \\ &= \frac{\partial}{\partial r}\left\{f_r C_r \frac{\partial}{\partial r}\left[\frac{Z(r,t)}{C(r,t)}\right] l_r\right\}[r - (r - l_r)] \\ &= \frac{\partial}{\partial r}\left\{f_r l_r^2 C_r \frac{\partial}{\partial r}\left[\frac{Z(r,t)}{C(r,t)}\right]\right\} \end{aligned} \tag{5.20}$$

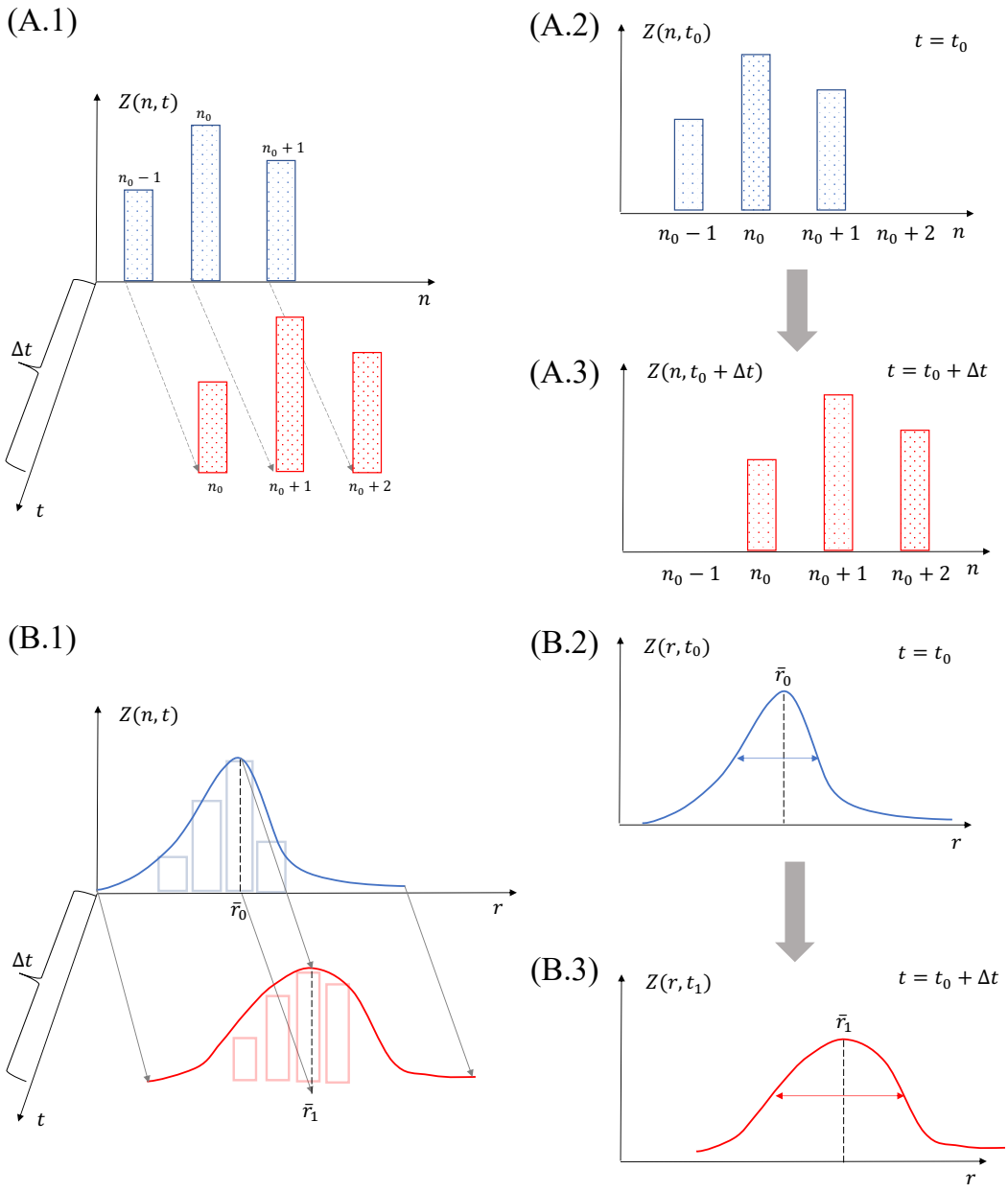

Figure 5-2. Schematic of the evolution of a nuclei distribution within the Szilard model (A.1, A.2, and A.3), where nuclei grow one molecule at a time and nuclei sizes are a discrete variable n compared to the evolution of a distribution within the Zeldovich model (B.1, B.2, and B.3) where nuclei grow hydrodynamically and nuclei sizes are a continuous variable r. The center of mass of the continuous distribution of nuclei is given by Eq. 6, and the width of the distribution is a measure of the diffusivity given by Eq. 10.

The quantity $f_r l_r^2$ therefore has units of a diffusion coefficient and the governing equation can be rewritten as

$$\frac{\partial Z(r,t)}{\partial t} = \frac{\partial}{\partial r}\left\{ DC(r,t)\frac{\partial}{\partial r}\left[\frac{Z(r,t)}{C(r,t)}\right]\right\}. \quad 5.21$$

In the case where $C(r,t)$ is a constant, this reduces to Fick's law:

$$\frac{\partial Z(r,t)}{\partial t} = D\frac{\partial^2 Z(r,t)}{\partial r^2} \quad 5.22$$

The diffusion coefficient in Eq. 5.21 has a very specific physical meaning. It is the spread in bubble embryo size that is caused by a growth law acting on these nuclei within the critical region. As a mathematical analogy, the Szilard model is a linear translation of a probability mass function $C(n,t)$ of nuclei sizes that acts on a characteristic line $v = f(\frac{dn}{dt})$, translating a discrete distribution in space.

Alternatively, the Zeldovich model in Equation 5.21 employs $Z(r,t)$ as a probability mass function of a distribution that changes central value and spread through time. The time-dependence of its central value is advected on a characteristic curve $v = f(\frac{dr}{dt}, r, \dots)$ with a spread that is given by D. In summary, the hydrodynamic model assumes that the distribution of bubble embryos behaves like a distribution with a certain mean that varies along $v = f(\frac{dr}{dt}, r, \dots)$ and spreads with standard deviation D. This process is analogous to the convection of a substance along an axis with flow velocity v and diffusivity D.

It is now interesting to understand the central value $\bar{r}$ of the hydrodynamic distribution $Z(r,t)$, via the rate $\frac{d\bar{r}}{dt}$. The expected value $\bar{r}$ for the average nucleus radius is then obtained as the centre of mass of $Z(r,t)$

$$\bar{r} = \int_{-\infty}^{+\infty} Z(r,t) r dr \left(\int_{-\infty}^{+\infty} Z(r,t) dr \right)^{-1} \quad 5.23$$

where $\int_{-\infty}^{+\infty} Z(r,t)dr$ is the total number of nuclei, which is always conserved by assuming that there are no bubble-bubble interactions. Evaluating the time derivative of both sides of this expression:

$$\left(\int_{-\infty}^{+\infty} Z(r,t)dr\right)\frac{d\bar{r}}{dt} = \int_{-\infty}^{+\infty}\left[\frac{\partial Z(r,t)}{\partial t}r + Z(r,t)\frac{dr}{dt}\right]dr$$

$$= \left\{rDC(r,t)\frac{\partial}{\partial r}\left[\frac{Z(r,t)}{C(r,t)}\right] - DZ(r,t)\right\}_{-\infty}^{+\infty} \qquad 5.24$$

$$+ \int_{-\infty}^{+\infty}\frac{Z(r,t)}{C(r,t)}\frac{\partial}{\partial r}[DC(r,t)]\,dr + \int_{-\infty}^{+\infty} Z(r,t)\frac{dr}{dt}\,dr.$$

The terms $\left\{rDC(r,t)\frac{\partial}{\partial r}\left[\frac{Z(r,t)}{C(r,t)}\right] - DZ(r,t)\right\}_{-\infty}^{+\infty}$ and $\int_{-\infty}^{+\infty} Z(r,t)\frac{dr}{dt}\,dr$ vanish at the limits of integration (Zeldovich, 2015), leading to the expression:

$$\left(\int_{-\infty}^{+\infty} Z(r,t)dr\right)\frac{d\bar{r}}{dt} = \int_{-\infty}^{+\infty}\frac{Z(r,t)}{C(r,t)}\frac{\partial}{\partial r}[DC(r,t)]\,dr. \qquad 5.25a$$

Now, by taking the derivative of both sides of this equation with respect to the size variable r, and replacing $\int_{-\infty}^{+\infty} Z(r,t)dr = N_T$:

$$N_T\frac{d\dot{\bar{r}}}{dr} = \frac{Z(r,t)}{C(r,t)}\frac{\partial}{\partial r}[DC(r,t)] \qquad 5.25b$$

which relates how the average embryo velocity $\dot{\bar{r}} \equiv \left(\frac{\partial \bar{r}}{\partial t}\right)$ changes as a function of embryo sizes within the distribution Z. If D is a measure of spread of the distribution $Z(r,t)$, it is assumed that the variations of D with respect to r are negligible compared to the other derivatives at play so that this process can be analysed as steady-state. This results in the expression

$$\frac{d\dot{\bar{r}}}{dr} = \left[\frac{Z(r,t)}{N_T}\right] D \frac{\partial}{\partial r}[\ln C(r,t)], \tag{5.26}$$

Equation 5.21 can now be developed one step further:

$$\begin{aligned}
\frac{\partial Z(r,t)}{\partial t} &= \frac{\partial}{\partial r}\left\{DC(r,t)\frac{\partial}{\partial r}\left[\frac{Z(r,t)}{C(r,t)}\right]\right\} \\
&= \frac{\partial}{\partial r}\left\{DC(r,t)\left[\frac{1}{C(r,t)}\frac{\partial Z(r,t)}{\partial r} - Z(r,t)\left[\frac{1}{C(r,t)}\right]^2\frac{\partial C(r,t)}{\partial r}\right]\right\} \\
&= -\frac{\partial}{\partial r}\left\{Z(r,t)v - D\frac{\partial Z(r,t)}{\partial r}\right\}.
\end{aligned} \tag{5.27}$$

Equation 5.27 models the convection of $Z(r,t)$ with advective term $v = D\frac{\partial}{\partial r}[\ln C(r,t)]$ and diffusion coefficient D. This makes the evolution of the centre of the distribution be such that $N_T\frac{d\dot{\bar{r}}}{dr} = Z(r,t)v$. Here, there are two factors at play in changing Z. The first, is that these embryos have a certain drift velocity v that causes them to grow when $v > 0$, to shrink when $v < 0$, and to stay at the same size when $v = 0$. This drift-type velocity translates the concentration Z horizontally as shown in Figure 5-2. The second important factor is assuming that by subjecting the nuclei population to a pressure P_l and a temperature T, one might cause a diffusion in nucleus sizes with coefficient D. That is, the pressure field might make nuclei oscillate around a mean radius, and very small oscillations do not result in mass transfer into the nucleus, but in a spread of the possible sizes of the nucleus around a mean equilibrium value.

This means that the growth law does not change the nuclei population discretely, and that the diffusion coefficient spreads the size distribution around a mean value $\bar{r}$ for the nuclei radius. The mean radius changes as a function of time following the integral equation 5.25 involving the diffusivity and the equilibrium concentration of nuclei. This is analogous to the convective diffusion of a substance within a cylinder in the presence of fluid flow, where the flow velocity is here represented by v.

The connection between macroscopic and microscopic behaviour in the hydrodynamic theory is given by the diffusion coefficient D, which following from $v = D\frac{\partial}{\partial r}[\ln C(r,t)]$ is of the form (Zeldovich, 2015)

$$D_n = \frac{v_n}{\frac{\partial}{\partial n}[\ln C(n,t)]} = -\frac{k_B T \dot{n}}{\frac{dW}{dn}} = -\frac{k_B T \dot{n}\left(\frac{dn}{dr}\right)}{\frac{dW}{dr}} \qquad \text{5.28-A}$$

$$D_r = \frac{v_r}{\frac{\partial}{\partial r}[\ln C(r,t)]} = -\frac{k_B T \dot{r}}{\frac{dW}{dr}} \qquad \text{5.28-B}$$

The most important feature of these expressions is that there is no advection of the nuclei population at the critical point, where $\frac{dW}{dr} = \frac{dW}{dn} = 0$, hence $\dot{n} = \dot{\bar{r}} = 0$. Eqs. 5.28a and 5.28b also tell us that the diffusion in nuclei size represented by D is proportional to the velocity at which the distribution travels the (r,t) or (n,t) planes, and that size diffusion will be largest for bubbles with high wall velocities.

In both cases of vapour and hydrodynamic growth, Eqs. 5.28 – A and B are a natural extension of the formula obtained by Einstein for the diffusion of a solute in a liquid solvent. Most importantly, there is a singularity in D^*. Since the variable r changes at much shorter timescales than n, it is of interest to check how radial changes affect the vapour flux. This is done by evaluating the critical diffusivity in Eq. 5.28-A as a limit with respect to the critical radius by using L'Hôpital's rule

$$D^* = \lim_{r \to r^*} D = \frac{k_B T \left(\frac{d\dot{n}}{dr}\right)^* \left(\frac{dn}{dr}\right)^*}{\left(\frac{d^2 W}{dr^2}\right)^*}, \qquad \text{5.29}$$

where $\left(\frac{dn}{dr}\right)$ is obtained from the ideal gas law.

The immediate next step (Blander, 1979) is to connect both radial oscillation and vaporisation rates at the critical size via the derivative $\left(\frac{\partial \dot{n}}{\partial r}\right)^*$ by using the law of ideal gases $PV = nk_B T$, and $\left(\frac{\partial v}{\partial r}\right)^*$ by using the Rayleigh-Plesset (RP) equation.

Since $v = f(\frac{dr}{dt}, r, \dots)$ is a wall velocity that needs to be applicable to all embryos in the cluster, it is clear that $v \equiv \dot{r}$, where $\dot{r} = \dot{r}(\frac{d^2r}{dt^2}, \frac{dr}{dt}, r, \dots)$ is the bubble wall velocity. This differs from $\dot{\bar{r}} \equiv \left(\frac{\partial \bar{r}}{\partial t}\right)$ in the sense that $v \equiv \dot{r}$ is a size-dependent velocity, and $\dot{\bar{r}} \equiv \left(\frac{\partial \bar{r}}{\partial t}\right)$ is an averaged, distribution-dependent velocity via $\frac{d\dot{\bar{r}}}{dr} = \left[\frac{Z(r,t)}{N_T}\right] v$.

However, in resorting to the RP equation, it is assumed that variations in the microscopic system (that cannot be observed) are equivalent to variations in the macroscopic system that can be observed. The Rayleigh-Plesset equation establishes that the difference in pressure $\Delta P = P' - P_l$ within and outside of a spherical bubble in an isothermal, incompressible liquid is given as (Lauterborn and Mettin, 2015):

$$P' = P_l + \frac{2\sigma}{r} + \rho_l r\ddot{r} + \frac{3}{2}\rho_l \dot{r}^2 + 4\eta\frac{\dot{r}}{r} \qquad 5.30$$

Where $\eta = \eta(T)$ is the liquid's temperature-dependent viscosity, $\dot{r}$ is the bubble wall's velocity and $\ddot{r}$ is its acceleration. If length scales of r are much smaller than the ultrasound wavelenght, $\frac{\partial P_l}{\partial r} \to 0$. By employing the chain rule $\ddot{r} = \frac{\partial \dot{r}}{\partial r}\frac{\partial r}{\partial t}$ to take the derivative of Eq. 5.30 with respect to r and evaluate it at the critical size:

$$\left(\frac{\partial P'}{\partial r}\right)^* = -\frac{2\sigma}{r^{*2}} + \rho_l r^* \left[\left(\frac{d\dot{r}}{dr}\right)^*\right]^2 + 4\eta\frac{1}{r^*}\left(\frac{d\dot{r}}{dr}\right)^*. \qquad 5.31$$

The first and second terms on the right-hand side of Eq. 5.31 represent inertial and mechanical effects, whilst the third term accounts for viscous effects. Furthermore, the rate of vapour transport $\dot{n} = \frac{\partial n}{\partial t}$ can be modelled in the presence of heat transfer from the liquid into the bubble as (Blander, 1979)

$$\dot{n} = \frac{A(P_v - P')}{(1+\delta)\sqrt{2\pi m k_B T}} \tag{5.32}$$

where the non-dimensional factor $(1+\delta)$ accounts for a decrease in the influx $\dot{n}$ of molecules caused by enthalpy transport. Vapour transport into the bubble creates an enthalpy flux across the surface area A. The enthalpy of vapour is higher than that of liquid water, causing vapour to carry heat from the liquid into the bubble core. This transport cools the bubble surroundings from T to T_i. The quantity δ is non-dimensional and is of the form (Blander, 1979)

$$\delta = \sqrt{\frac{2k_B}{\pi m T}}\left(\frac{\Delta H_v}{k_B T}\right)^2 \left(\frac{\sigma}{\kappa b}\right), \tag{5.33}$$

where κ is the thermal conductivity of the liquid [W·m^{-1}·K^{-1}] , ΔH_v [J] is the enthalpy of vaporisation of water, and $b = \frac{\Delta P}{P'}$ is the order of magnitude of the underpressure caused by the ultrasound wave in comparison to the nucleus internal pressure P'. The case where vapour carries insignificant heat through the bubble surface arises at $\lim_{\delta \to 0} \dot{n}$.

By taking the derivative of $\dot{n}$ with respect to r at the critical size r^* and removing vanishingly terms:

$$\left(\frac{d\dot{n}}{dr}\right)^* = \frac{A^*}{(1+\delta)\sqrt{2\pi m k_B T}}\left\{\frac{2\sigma}{r^{*2}} - 4\eta\frac{1}{r^*}\left(\frac{d\dot{r}}{dr}\right)^* - \rho_L r^*\left[\left(\frac{d\dot{r}}{dr}\right)^*\right]^2\right\}. \tag{5.34}$$

This model can be closed by using an ideal gas law, such that $\dot{n}$ can be obtained in terms of the bubble radius and its derivatives in time

$$\dot{n} = \frac{\partial}{\partial t}\left(\frac{4}{3}\pi r^3 \frac{P'}{k_B T}\right) \tag{5.35}$$

By taking the derivative of Eq. 5.35 with respect to r, replacing Eq. 5.31 for $\frac{\partial P'}{\partial r}$ then evaluating at the critical size yields:

$$\left(\frac{d\dot{n}}{dr}\right)^{*} = \frac{4\pi}{3k_B T}\left\{3P_l r^{*2}\left(\frac{d\dot{r}}{dr}\right)^{*} + 4\sigma r^{*}\left(\frac{d\dot{r}}{dr}\right)^{*} + 4\eta r^{*2}\left[\left(\frac{d\dot{r}}{dr}\right)^{*}\right]^{2} + \rho_l r^{*4}\left[\left(\frac{d\dot{r}}{dr}\right)^{*}\right]^{3}\right\}. \quad 5.36$$

Using Eqs. 5.36 and 5.34, defining $\Gamma = (1+\delta)\sqrt{\frac{2\pi m}{k_B T}}$ and $\mathrm{X} = \left(\frac{1}{4}\right)\Gamma r^{*}\left(\frac{d\dot{r}}{dr}\right)^{*}$ as auxiliary variables for ease of notation, the model is finalised as:

$$\Phi_2 \mathrm{X}^3 + \left(\frac{8}{9}\right)\Phi_1\left(1 + \frac{27}{32}\frac{\Phi_2}{\Phi_1}\right)\mathrm{X}^2 + \left(\frac{2}{3}\right)\left(\frac{3-b}{b} + \Phi_1\right)\mathrm{X} - \frac{1}{2} = 0. \quad 5.37$$

Where the non-dimensional parameters Φ_1 and Φ_2 are defined as

$$\frac{6\eta}{\sigma\Gamma} = \Phi_1, \quad 5.38$$

and

$$\frac{16\rho_l r^{*}}{3\sigma\Gamma^2} = \Phi_2. \quad 5.39$$

Φ_1 represents the ratio between viscous and thermal effects in bubble nucleation, and Φ_2 represents the ratio between inertial and thermal effects. One non-dimensional group of interest is the ratio $\frac{\Phi_1^2}{\Phi_2} = \frac{27}{4}\left(\frac{\eta^2}{\sigma\rho_l r^{*}}\right)$. If this quantity is much greater than unity, Eq. 5.37 can be reduced to a second-order approximation for nucleation controlled by viscous forces (Blander, 1979):

$$\mathrm{Y}^2 + \left(\frac{3}{4\Phi_1}\right)\left(\frac{3-\mathrm{b}}{\mathrm{b}} + \Phi_1\right)\mathrm{Y} - \frac{9}{16\Phi_1} = 0. \quad 5.40$$

5.4 Dimensional analysis

The extent where viscous effects dominate over surface tension and inertial effects in ultrasound nucleation can be visualised as a function of pressure and temperature in Figure 5-3. In this figure, the black solid curve represents the ultrasound temperature-dependent nucleation pressure threshold as calculated from Eq. 3.34, and the coloured contours illustrate values of the ratio Φ_1^2/Φ_2. The quantity Φ_1^2/Φ_2 is analogous to the inverse of the Laplace number, where $\frac{\Phi_1^2}{\Phi_2} \propto \mathrm{La}^{-1} = \frac{27}{4}\frac{\eta^2}{\sigma\rho_l r^*}$. At values of $\frac{\Phi_1^2}{\Phi_2} > 1$, one can say that viscosity dominates over the joint effects of surface tension and inertia in bubble nucleation.

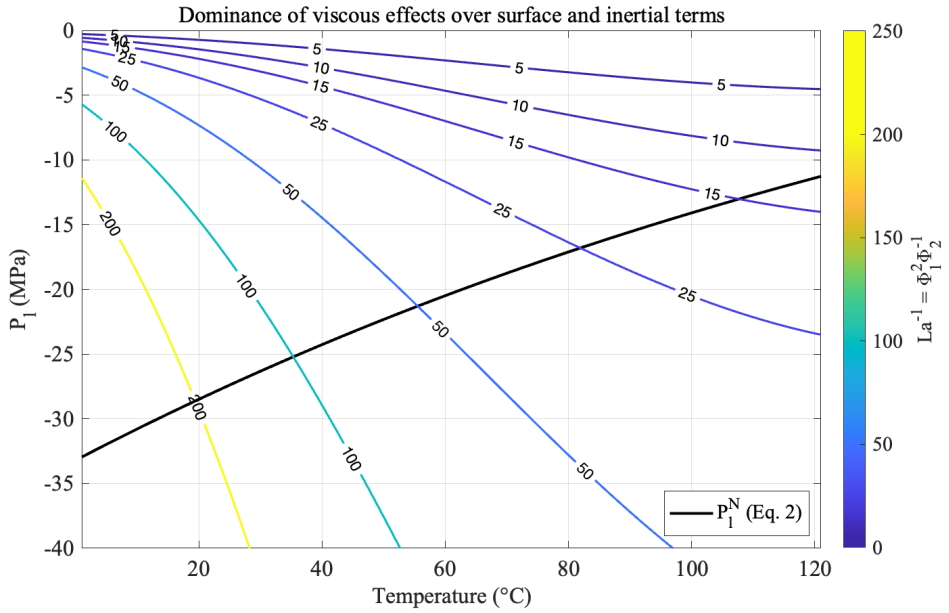

Figure 5-3. Values of the ratio Φ_1^2/Φ_2 across the histotripsy pressure and temperature range. Higher values of Φ_1^2/Φ_2 indicate that viscous effects dominate over the joint effects of surface tension and inertia.

Figure 5-3 shows that the dominance of viscosity is particularly visible at low temperatures, indicating that nucleation in cavitation-based histotripsy methods is controlled by the liquid viscosity to a greater extent than the hydrodynamic effects of surface tension and inertia at the bubble surface. In particular, the ratio Φ_1^2/Φ_2 stays within the range 200 – 100 for normothermic temperatures (20 to 40 °C) and around histotripsy intrinsic threshold pressures (-40 to -25 MPa). At higher

temperatures, viscous effects are less pronounced, and the ratio Φ_1^2/Φ_2 stays within the range of 25 – 10 around pressure-temperature pairs compatible with boiling histotripsy bubble nucleation, from 80 to 120 °C and from -5 to -25 MPa.

Similarly, the order of magnitude of the effects of heat transport given by $\log_{10}\delta$ is shown as a function of pressure and temperature in Figure 5-4. In this figure, the black curve represents the ultrasound temperature-dependent nucleation pressure threshold as calculated by Eq. 3.34, and the coloured contours illustrate values of the quantity $\log_{10}\delta$. Positive values of $\log_{10}\delta$ will indicate extensive influence of enthalpy transport across the bubble surface in the nucleation process. As proposed by (Blander, 1979; Katz and Blander, 1973), enthalpy transport across the nucleus surface will cool down the surrounding liquid. This effect causes the liquid to lose supersaturation in the vicinity of critical bubbles via an increase in the energy barrier to nucleation ΔG^*. This effect will favour the growth of the first bubbles to nucleate in detriment of a decrease in the number of bubbles nucleated subsequently.

According to the results shown in Fig. 5-4, such heat transport effects are more pronounced at temperatures above 40 °C. In particular, the order of magnitude of δ increases by a factor of three in the temperature range 60 - 100 °C. Conversely, at temperatures below 40 °C, the effects of heat transport seem to be negligible, and the order of magnitude of δ ranges from 10^{-2} to 10^{0}. The immediate physical implication of this analysis is that nucleation at low temperatures, like cavitation-based histotripsy, occurs in a regime where the nucleation of the first few nuclei does not hinder the nucleation of subsequent nuclei. This is an environment where it is thermodynamically favourable for nucleation to occur in densely populated clouds of small bubbles. Conversely, nucleation favours smaller quantities of bubbles above 9 nm at high temperatures as shown in Fig. 4-15.

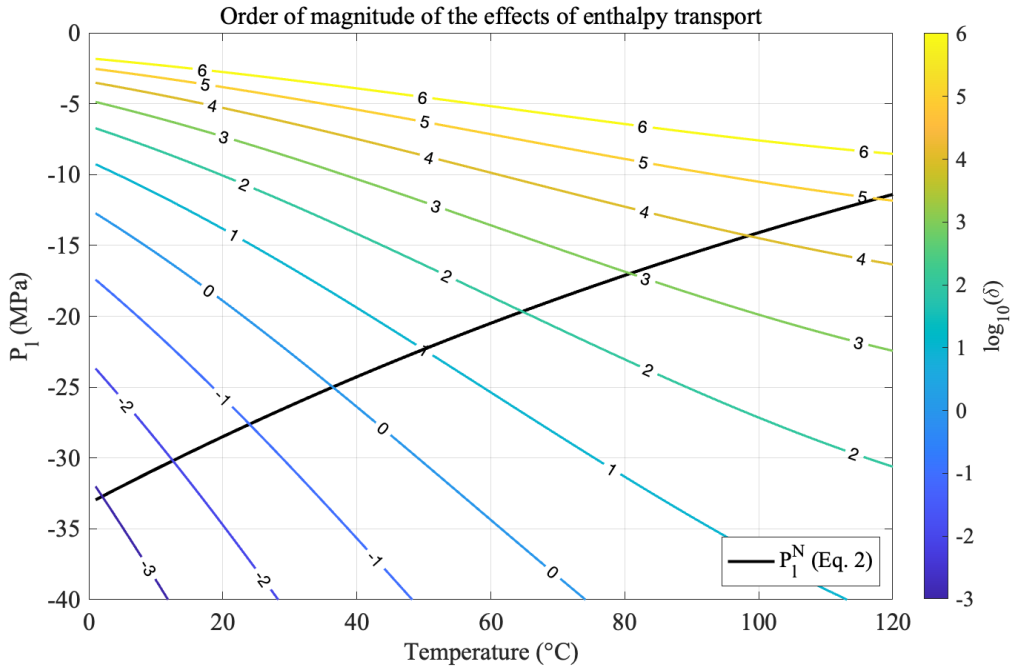

Figure 5-4. Values of $\log_{10}\delta$ across the histotripsy pressure and temperature range. Positive values of $\log_{10}\delta$ indicate that enthalpy transport at the bubble surface decreases the total number of bubbles nucleated because thermal energy is redirected onto making existing critical bubbles larger.

5.5 The effects of enthalpy transport

Figure 5-5-A illustrates critical values of the constant $(\delta + 1)$ as a function of temperature. These are the values of $\delta^* = \delta(P_l^N, T^N)$ calculated at pressure-temperature pairs obtained with Eq. 3.34. This non-dimensional term appears in the definition of $\dot{n}$ because of the effects of heat and vapour transport into the bubble nucleus. The enthalpy of vapour is higher than that of liquid water, and as water changes from liquid to a vapour phase, it absorbs thermal energy from the surroundings of the bubble nucleus (Blander, 1979). It can be observed in Figure 5-5-A that this effect increases with increasing temperature, which results in a decrease in the nucleation rate of vapour bubbles shown in Figure 5-5-C. As numerical examples, the ratio $\frac{1}{1+\delta}$ takes on values of 0.9664 at 20 °C, 0.3996 at 40 °C, 0.0240 at 60 °C, and 9.4466×10^{-5} at 100 ˚C . Figure 5-5-C then shows that this effect reduces nucleation rates by 60% at 40˚C and by over 99% around 100˚C. These results again suggest that dense cavitation clouds appearing at low temperatures are a consequence of negligible vapour transport into the nuclei

population characterised by small values of δ. This is a case in which the nucleation of bubbles does not change the free energy ΔG^* available for new bubbles to nucleate.

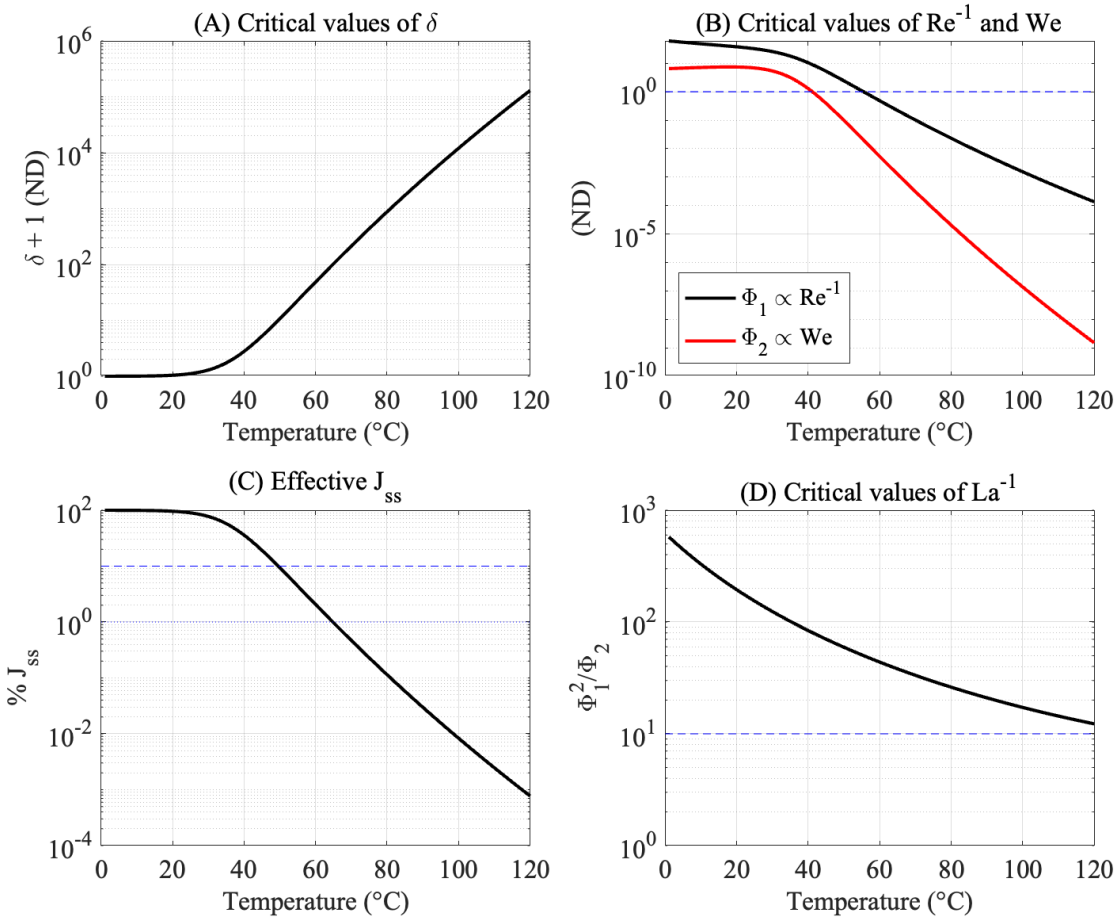

Figure 5-5. (A) Values of the term $(\delta + 1)$ representing the enthalpy flux across the bubble surface over the (P_l^N, T^N) nucleation curve, (B) values of Φ_1 and Φ_2 over (P_l^N, T^N) (C) percent estimate of the effective value of J_{ss} due to the effect of enthalpy transport, and (D) values of the ratio Φ_1^2/Φ_2 over the (P_l^N, T^N) curve.

Moreover, critical values of the constants Φ_1 and Φ_2 are plotted as functions of temperature in Fig. 5-5-B. These non-dimensional terms originate from the non-linear ordinary differential equations in Eqs. 5.37 and 5.40, which describe hydrodynamic effects in bubble nucleation. If analysed in terms of the Reynolds number Re and the Weber number We, these results indicate that viscous forces dominate over inertial forces at low temperature, as shown by $\Phi_1 \propto \mathrm{Re}^{-1}$, however $\Phi_2 \propto \mathrm{We}$ indicates that inertial effects overshadow surface tension effects at lower

temperature. It is important to highlight that the definition of both Φ_1 and Φ_2 is inversely proportional to δ, and the decrease of these quantities at high temperatures is likely to be linked to an increase in the extent of enthalpy transport effects via high values of δ as shown in Fig. 5-5-A. More information can be drawn from these results by then analysing Fig. 5-5-D. These results show that the dominance of viscosity over both surface tension and inertia reduces with increasing temperature.

5.6 The mechanisms and timescales of nuclei growth

In Figure 5-6, the critical diffusivity $D^*$is calculated along (P_L^N, T^N) for the mechanisms of vapour and hydrodynamic growth with and without the presence of enthalpy transport. In this figure, curves shown in black represent values of X, Y and $\dot{n}$ as given by Eqs. 5.32 – 5.40 for the case where enthalpy transport is present, characterised by $\delta > 0$. Conversely, curves shown in red represent the cases where enthalpy transport is neglected, which is characterised by $\delta = 0$.

Eq. 3.37 is a third order polynomial, therefore it has at least one real root of X, whereas the other two roots might be either a pair of real roots or a pair of complex conjugate roots. Moreover, Eq. 3.40 has one pair of real roots, where one is positive, and the other is negative. In this figure, we show results for the largest real-valued positive roots of X and Y. In accordance with Figure 5-5-D, where $\frac{\Phi_1^2}{\Phi_2} \gg 1$ throughout the temperature range of interest, we can observe that there is no appreciable distinction between hydrodynamic growth dominated by viscosity and that dominated by inertial effects.

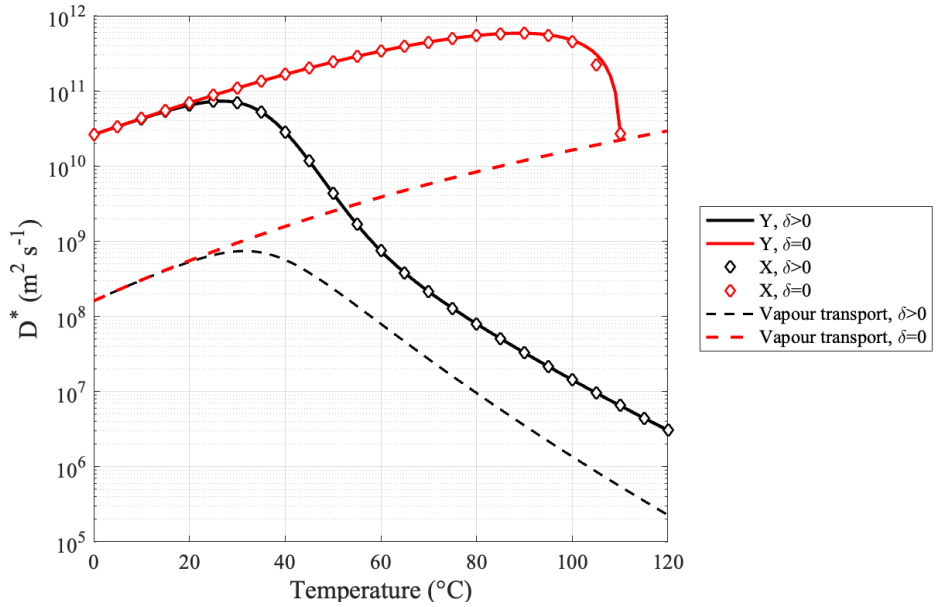

Figure 5-6. Critical diffusivity coefficients for vapour transport, heat transport and hydrodynamic growth. Red curves represent nuclei growth in the absence of enthalpy transport, whilst black curves represent growth in the presence of enthalpy transport. The largest real-valued positive solutions for X and Y from Eqs. 18 and 22, respectively, are selected as representing solutions for the third and second-order hydrodynamic approaches.

These results show that hydrodynamic nuclei growth rates are at least one order of magnitude greater than growth caused solely by vapour transport throughout the temperature range of interest. Moreover, the results illustrated in Figure 5-6 show that the mechanism of enthalpy transport greatly reduces nuclei growth as given by the critical diffusivity in Eq. 5.29. The critical diffusivity coefficients present a turning point around 30˚C, which if analysed in conjunction with the inflection point in Fig. 4-A, might be interpreted as the point where enthalpy transport starts to play a role in nucleation. We can observe close agreement between the third and second-order hydrodynamic approximations throughout the 0 – 120˚C temperature range, regardless of the presence of enthalpy transport. This behaviour can be explained by the results shown in Fig. 5-5-D, showing that the Laplace number $\frac{\Phi_1^2}{\Phi_2} \gg 1$ for the temperature range considered, and thus viscous effects dominate the process.

5.7 Comparing ultrasound nucleation results

In Figure 5-7, the constant δ is compared to histotripsy experimental protocols in the literature. It can be observed that all normothermic intrinsic pressure threshold histotripsy protocols take place at pressure-temperature pairs where δ ranges from 10^{-2} to 10^{0}. On the other hand, most boiling histotripsy protocols are performed at pressure-temperature pairs where δ ranges from 10^{2} to 10^{5}. This is evidence that there is considerable vapour and heat transfer into the bubble in boiling histotripsy protocols, which, as exemplified by Fig. 5-5-C, causes a decrease in the net number of bubbles nucleated.

This result agrees with high-speed imaging of boiling histotripsy protocols, where boiling bubbles appear in greater size but smaller quantities at the distal side of the focal region (Pahk *et al.*, 2017). On the other hand, small values of δ at intrinsic histotripsy pressure-temperature pairs suggests that no significant heat transport takes place into the nuclei, and these are free to nucleate in higher quantities. Again, this correlates with documented experimental results, which report the appearance of densely populated clouds of bubbles for intrinsic threshold histotripsy (Pahk et al., 2017; Xu et al., 2007, 2006).

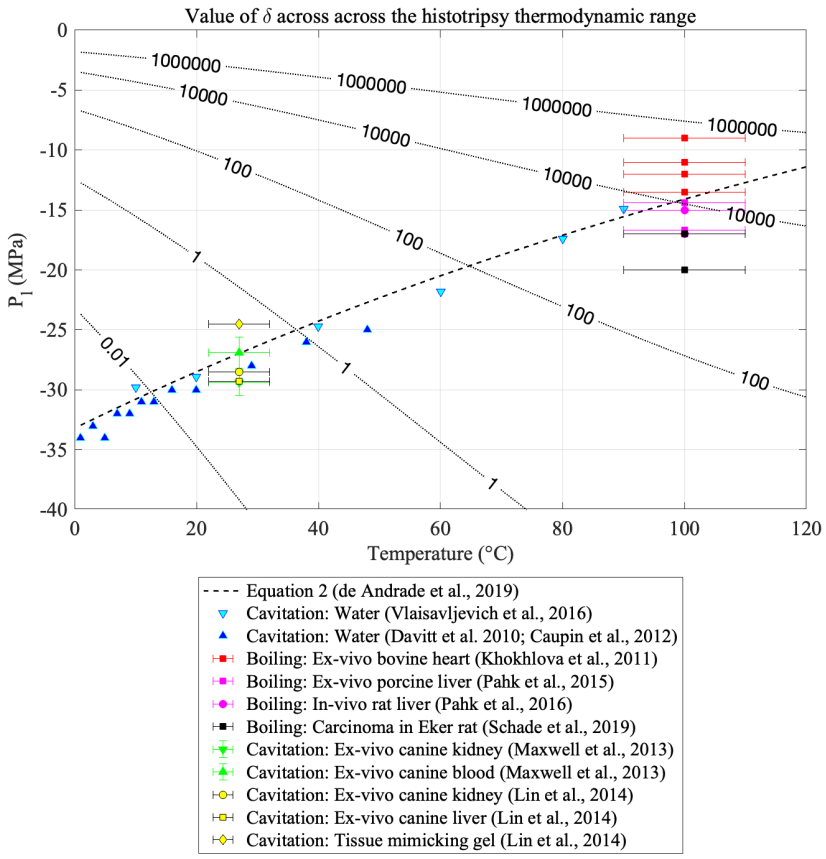

Figure 5-7. Values of δ across the histotripsy range of pressures and temperatures. Equation 2 in (de Andrade *et al.*, 2019) refers to Equation 3.16 in this thesis.

Finally, Figure 5-8 shows values of the ratio Φ_1^2/Φ_2 as compared to histotripsy protocols. These results show Φ_1^2/Φ_2 assumes values within the range 200 – 100 when bubble nucleation occurs within the pressure range from -40 to -20 MPa, indicating that the liquid's viscosity plays a significant effect in nucleation at these pressure-temperature pairs. Conversely, when bubble nucleation takes place within the pressures ranging from -20 to 0 MPa and temperatures within 80 to 120 °C, Φ_1^2/Φ_2 assumes values between 25 – 10, indicating that the liquid's viscosity has a less pronounced effect in bubble nucleation at higher temperatures. Concerning histotripsy, these results indicate that the liquid's viscosity plays a significant effect in defining nucleation pressure thresholds for cavitation-based histotripsy approaches, and this effect is less critical for boiling histotripsy.

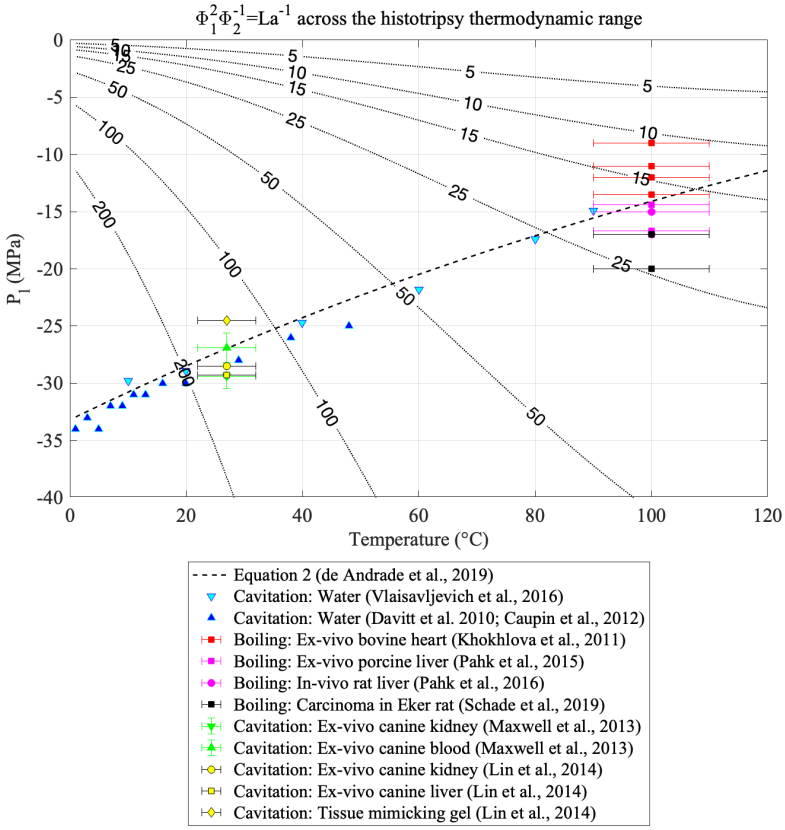

Figure 5-8. Values of Φ_1^2/Φ_2 across the histotripsy range of pressures and temperatures. Equation 2 in (de Andrade *et al.*, 2019) refers to Equation 3.16 in this thesis.

5.8 Chapter Overview

In this Chapter, the hydrodynamic theory of nucleation developed by Zeldovich (Zeldovich, 2015) and furthered by Kagan and Blander (Blander, 1979) was applied to analyse the role of thermal and hydrodynamic constraints on the growth of bubbles in ultrasound nucleation using histotripsy as a case-study. The Zeldovich theory is one that circumvents the need for a priori information on the initial distribution of bubbles by analysing how the size distribution of nuclei $Z(r,t)$ evolves in time as compared to the equilibrium distribution of nuclei $C(r,t)$ from liquid kinetics. This is a convenient mathematical framework since it is applicable to distributions of all sizes and shapes if one can establish a relationship between the nuclei population under consideration to an equilibrium population of nuclei.

The present work furthers our understanding in ultrasound bubble nucleation by relating the direct effects of ultrasound pressure fields characterised by the drift v to near-equilibrium effects characterised by the critical diffusivity D in terms of the liquid's temperature. This allows us to construct a fundamental set of equations which yields non-dimensional measures of the relative effects of constraints such as viscosity, inertia, surface tension and enthalpy transport in bubble nucleation. When compared to documented experimental data in bubble nucleation and histotripsy, these metrics outline well-defined parameter windows where nucleation takes place via equivalent mechanisms. The immediate implication of these results is that metrics such as Eqs. 5.33 – 5.40 can be used to compare the equivalence and similarity of protocols for ultrasound bubble nucleation in water.

It is important to outline that amongst all constraints analysed for bubble nucleation, the surface tension of bubble nuclei is the only one that is present in the two fundamental components of nucleation, acting both as a kinetic term and an energetic term. The surface tension acts as an energetic term because it is very closely related to the energy barrier that needs to be overcome such that nucleation takes place. Alternatively, the surface tension affects the kinetics of bubble nucleation because it is an active term in determining both the radial dynamics of bubbles as given by the Rayleigh-Plesset equation, and the extent to which enthalpy transport decreases vaporisation rates into bubble nuclei. Therefore, it is important to highlight that, although the viscosity of the surrounding liquid is the dominant factor with respect to the growth of bubble nuclei, the surface tension remains the most critical parameter in nucleation, because the nucleation rate depends on it exponentially as shown in Chapter 3.

Finally, the present model is based on several existing models in the literature which were often developed as local approximations. For example, as discussed in (de Andrade et al., 2021, 2019), our thermodynamic model of bubble nucleation assumes an isobaric and isothermal liquid, so that the work of nucleation can be constructed via the Gibbs free energy potential. For this assumption to be valid, the nucleation pressure threshold described by Eq. 3.34 is

obtained within one tenth of the acoustic cycle (approximately 50 ns), such that the pressures and temperatures in the surrounding liquid can be considered constant.

5.9 Chapter Summary

A hydrodynamic model for ultrasound-induced bubble nucleation was obtained by including the effects of the liquid's viscosity and inertia via the Rayleigh-Plesset equation in a classical nucleation theory model. In addition, the effects of heat transport into the bubble were accounted for by including a model of enthalpy transport across the bubble surface. This approach was instrumental in calculating the critical diffusivity of nucleation, which affects the rate at which bubbles nucleate and grow in ultrasound pressure and temperature fields.

With the hydrodynamic approach considered herein, it is possible to classify bubble nucleation in terms of its dominant mechanism. Bubble nucleation at temperatures below 30 °C is shown to be largely dependent on the liquid's viscosity, with negligible influence of inertial effects or heat transport. On the other hand, bubble nucleation at high temperatures has a much weaker dependence on viscous constraints in the liquid and is mainly controlled by heat transport into the bubble.

We found that the timescales for hydrodynamic growth, as imposed by the radial oscillations of critical nuclei, are at least two orders of magnitude smaller than those that are characteristic of vaporisation-dominated growth. This means that bubble nuclei first grow via hydrodynamic factors, which are supplemented by vapour transport over longer timescales.

Notably, the enthalpy transport effect is a possible explanation of the mechanism involved in the formation of cavitation clouds in ultrasound-induced nucleation. At higher temperatures, vapour flux into the bubble reduces the temperature of its surroundings because the enthalpy of vapour is greater than the enthalpy of liquid water. This cooling effect decreases the supersaturation around boiling bubbles, which then appear in greater size and smaller quantities. Conversely, negligible enthalpy transport at temperatures below 30˚C leads to

higher nucleation rates of smaller bubbles, resulting in the nucleation of clusters of small gas pockets, where a local nucleation event does not affect the likelihood of nucleation in its surroundings.

Chapter 6

The Timescales of Quasi-Stationary Acoustic Nucleation

In previous Chapters, efforts were focused into understanding how classical nucleation theory (CNT) can model the energy requirements for ultrasound bubble nucleation (Chapter 3) and be applied to characteristic histotripsy pressure and temperature fields (Chapter 4). Results showed evidence that CNT can accurately model ultrasound nucleation pressure thresholds by applying a linear temperature-dependent correction to the bulk surface tension of water (de Andrade et al., 2021, 2019). Moreover, these models were expanded to account for how thermal and hydrodynamic effects can improve the description and clarify the constraints to bubble nucleation and growth in Chapter 5 (de Andrade *et al.*, 2022). An important finding of this Chapter is that intrinsic and boiling bubble nucleation interact distinctively with the surrounding hydrodynamics and temperature field. In cavitation, i.e., nucleation at low temperatures and high magnitude tensile pressures, hydrodynamic factors are dominant, and the liquid viscosity is the main constraint to nuclei growth. Conversely, at higher temperatures, enthalpy transport from the liquid into the bubble is the dominating constraint in nucleation. This happens as vapour transport into the bubble cools the surrounding liquid and prevents the formation of new bubble nuclei in the vicinity of an already existing vapour bubble.

At the core of these models of nucleation is the assumption that nucleation takes place at much shorter timescales than those of pressure variations or temperature rises in the medium. This assumption is materialised by the need of defining a minimal observable timescale Δt_N for nucleation to happen at the trough

of an ultrasound wave where fluid pressure and temperatures are roughly constant (de Andrade et al., 2021, 2019).

A fundamental aspect of such models is the relationship between the equilibrium distribution of bubble nuclei $C(r,t)$, and the real distribution under consideration $Z(r,t)$. The former can be described within the theoretical framework of continuous thermodynamics. The latter is often unknown *a priori* and one needs to find regimen where there is a mathematical relationship between the unknown $Z(r,t)$ and the idealised $C(r,t)$. This relationship describes how one understands the transient state of the nucleating system in an experimental distribution $Z(r,t)$ in terms of the equilibrium state that can be fully described with thermodynamic theory and liquid kinetics (Blander, 1979; Zeldovich, 2015).

In general cases, nucleation is considered a phenomenon that takes place at constant supersaturation $\Delta\mu$, where the chemical potential μ is a metric of the tendency of the liquid to change into another phase. The supersaturation of a nucleating liquid is a measure of how much the pressure and temperature to which the liquid is subjected to is different to those at thermodynamic equilibrium (Kashchiev, 2000, 1970, 1969a). Therefore, a model that considers constant supersaturation is of debatable validity for nucleation under an acoustic field because both pressure and temperature change as functions of time, however at different timescales.

In the present Chapter, the hydrodynamic approach of Zeldovich (Zeldovich, 2015) and a transient treatment of nucleation (Kashchiev, 1970, 1969a, 1969b; Schmelzer et al., 2017) are applied to determine the thermodynamic time and length scales at which ultrasound-induced nucleation occurs. By identifying the timescales of nucleation, it is possible to quantify the minimal timestep, or experimental sampling frequency, needed to accurately model the evolution of the process in time. These timescales are obtained in terms of the ultrasound fundamental frequency and waveform, as well as the heat deposition caused by a focus ultrasound wave. We then quantify the appropriacy of using a steady-state nucleation rate to model a phenomenon that happens while pressure and temperature vary at different rates. This is done by measuring whether, within the

timescales of ultrasound propagation, the real distribution of nuclei $Z(r,t)$ has sufficient time to adjust into the equilibrium concentration $C(r,t)$, which can be obtained by thermodynamic formulae. This Chapter will explore the parameter window ranging from 0 to 120˚C in temperature to identify temperature-dependent behaviour. Finally, numerically obtained ultrasound focal pressure and temperature fields are applied to visualise and discuss the effects of different waveforms in nucleation.

6.1 Quasi-stationary in transient acoustic fields

A generalised equation for nucleation at varying supersaturation has been obtained by (Kashchiev, 1970). This equation considers that the diffusivity of nucleation discussed in Chapter 5 can be modelled as a time-dependent quantity and is obtained via the hydrodynamic approach of (Zeldovich, 2015) which considers the size of embryos r as a continuous variable. Kashchiev augmented the Zeldovich equation as

$$\frac{\partial Z(r,t)}{\partial t} = \frac{\partial}{\partial r}\left\{D(t)C(r,t)\frac{\partial}{\partial r}\left[\frac{Z(r,t)}{C(r,t)}\right]\right\}, \qquad 6.1$$

where the only change from Eq. 5.9 given Chapter 5 is that $D \equiv D(t)$ is a transient quantity instead of a constant as defined by Eq. 5.29.

We start working with this equation by considering nucleation taking place in a closed system such that mass conservation can be assumed. Moreover, it is assumed that temperature and pressure in the liquid are known functions of time $T(t)$ and $P_l(t)$, as shown in Chapter 4. Considering a true size distribution of nuclei $Z(r,t)$, nucleation obeys the boundary conditions

$$
\begin{aligned}
&Z(r,0) = 0, && (r_1 < r \leq r_2),\\
&Z(r_1,t) = C(r_1,t), &&\\
&Z(r_2,t) = 0, &&
\end{aligned}
\qquad 6.2
$$

where r_2 represents the maximum embryo radius in the liquid, and r_1 is the minimum radius of the volume occupied by an embryo with one molecule or less. These boundary conditions are equivalent to stating that there are no nuclei at the start of the process, but as time develops, there will be, at least, an equilibrium concentration of subcritical embryos of a certain radius r_1 that is linked to the smallest radius possible for an embryo in the liquid.

6.1.1 Quasi-stationary distribution of nuclei

Following the steps described by (Kashchiev, 1970), it is then useful to introduce an auxiliary function $Y(r,t)$ such that $Y(r,t) = \frac{Z(r,t)}{C(r,t)}$. This transforms the boundary conditions in 6.2 to

$$
\begin{aligned}
&Y(r,0) = 0,\\
&Y(r_1,t) = 1,\\
&Y(r_2,t) = 0.
\end{aligned}
\qquad 6.3
$$

If we evaluate Equations 6.1 – 6.3, taking 5.13 into account, we obtain:

$$
\begin{aligned}
&\frac{\partial Y(r,t)}{\partial t} + \frac{\partial \ln C^*(t)}{\partial t} Y = \left[\frac{1}{C^*(t)}\right] \frac{\partial}{\partial r}\left[D^*(t) C^*(t) \frac{\partial Y(r,t)}{\partial r}\right]\\
&\frac{\partial Y(r,t)}{\partial t} + \frac{\partial \ln C^*(t)}{\partial t} Y = D^*(t) \frac{\partial^2}{\partial r^2} Y(r,t)
\end{aligned}
\qquad 6.4
$$

The solution of Equation 6.4 under the boundary conditions 6.3 is not known. However, the greatest contributions to its solution are obtained within the critical region, where $r^* - \frac{\Delta^*}{2} < r < r^* + \frac{\Delta^*}{2}$. Within this region, all sizes r are energetically equivalent via detailed equilibrium, so the approximations $D(r,t) \approx D(r^*,t) \equiv D^*(t)$, and $C(r,t) \approx C(r^*,t) \equiv C^*(t)$ hold with sufficient accuracy

(Kashchiev 2000). Thus, the boundary conditions in 6.3 can be shifted to their equivalents around the critical region:

$$\begin{aligned} Y(r,0) &= 0, \\ Y(r_1,t) &= 1, \\ Y(r_2,t) &= 0. \end{aligned} \qquad 6.5$$

Where $r_1 = r - \frac{\Delta^*}{2}$ and $r_2 = r + \frac{\Delta^*}{2}$. Equation 6.4 can then be rearranged as:

$$\frac{\partial Y}{\partial t} = D^*(t)\frac{\partial^2 Y}{\partial r^2} - \frac{\partial}{\partial t}\left(\frac{-W^*(t)}{k_B T(t)}\right) Y(r,t) \qquad 6.6$$

Our aim now is obtaining the conditions at which $W^*(t) \equiv W^*(P_l(t), Y(t))$, varies sufficiently slowly with time so that the true size distribution of embryos $Z(r,t)$ approaches the equilibrium distribution $C(r,t)$. This is only true when $\frac{\partial Y}{\partial t} \equiv \frac{\partial}{\partial t}\left[\frac{Z(r,t)}{C(r,t)}\right] = 0$. That is, we can find a solution for 6.6 when the ratio between the true size distribution Z and the equilibrium size distribution C is constant in time.

Therefore, the solutions of Eq. 6.6 which allow for $\frac{\partial Y}{\partial t} = 0$ to be a good approximation are named *quasi*-stationary solutions, and are denoted by $y = \frac{Z_q(t)}{C(r,t)}$, forming the ordinary differential equation with respect to r

$$y'' + \chi^2 y = 0 \qquad 6.7$$

This equation is subject to the conditions $y(r_1) = 1$ and $y(r_2) = 0$, where primes represent derivatives with respect to the size variable r. This is clearly an ordinary harmonic equation with wavenumber χ, where:

$$\chi^2 = \frac{1}{D^*(t)}\left\{\frac{d}{dt}\left[\frac{W(t)}{k_B T(t)}\right]\right\}_{r=r^*}. \qquad 6.8$$

It is also evident from 6.8 that χ^2 depends implicitly on liquid pressure $P_l(t)$ through W^* and $D^*(t)$. The solutions of 6.7 can then be shown to be of the form:

$$y = \frac{1}{2\cos\frac{\chi\Delta^*}{2}} \tag{6.9}$$

this solution can be used to derive an approximation for the time-dependent quasi-stationary distribution of critical nuclei $Z_q(t)$, which is a subset of the solutions Z of Eq. 6.1 within the critical region:

$$Z_q(t) = \frac{C^*(t)}{2}\frac{1}{\cos\left(\frac{\chi\Delta^*}{2}\right)}. \tag{6.10}$$

The second term on the right-hand side of 6.10 can be approximated in a second order Taylor series expansion around zero with truncation error $E(\chi^3\Delta^{*3})$:

$$Z_q(t) = \frac{C^*(t)}{2}\left[1 + \frac{\chi^2\frac{\Delta^{*2}}{4}}{2} + E\left(\chi^3\Delta^{*3}\right)\right], \tag{6.11}$$

this approximation holds with good accuracy provided that

$$\chi^2\frac{\Delta^{*2}}{4} < 1. \tag{6.12}$$

Therefore, Eq. 6.12 shows the conditions where the transient distribution of nuclei $Z(r,t)$ varies sufficiently slow with time such that it approximates the time-dependent distribution Z_q that can be obtained solely in terms of the equilibrium distribution $C^*(t)$.

6.2 The fundamental timescale of nucleation

This condition of convergence for the Taylor series expansion of y is arguably the central result of this Chapter, since it illustrates how slowly the work of nucleation and the temperature need to change in time for a quasi-stationary assumption to be valid:

$$\frac{d}{dt}\left[\frac{W(t)}{k_B T(t)}\right]_{r=r^*} < \frac{4D^*(t)}{\Delta^{*2}(t)}. \tag{6.13}$$

Most importantly, this equation contains a fundamental timescale of the process of nucleation given by

$$\tau = \frac{\Delta^{*2}}{4D^*}, \tag{6.14}$$

The quantity τ is the time-lag of nucleation and defines the timescales at which a metastable system approaches steady-state nucleation rates.

The full transient solution of 6.1 then comprises two terms. The first, is given by the quasi-stationary solution accounting for nucleation rates that adjust sufficiently quickly to changes in the supersaturation at any time t that is similar or greater than τ. The second includes effects that will appear at shorter timescales, which appropriately model any events taking place when $t < \tau$. Using this principle, a time-dependent solution for Eq. 6.1 was given by (Kashchiev, 1969a)as:

$$J(t) = J_{ss}(t)\left[1 + 2\sum_{k=1}^{\infty}(-1)^k \exp\left(-\frac{k^2 t}{\tau}\right)\right]. \tag{6.15}$$

This is a widely adopted expression for both theoretical and experimental treatment of non-stationary nucleation (Schmelzer et al., 2017; Schmelzer and Baidakov, 2016). Analysis of Eq. 6.15 shows that at sufficiently small values of τ,

or say sufficiently large values of t, the term $\sum_{k=1}^{\infty}(-1)^k \exp\left(-\frac{k^2 t}{\tau}\right)$ vanishes and the transient nucleation rate approaches the quasi-stationary rate $J_{qs}(t)$. The quasi-stationary rate, in this case, is given by

$$J_{qs}(t) = z(t)D^*(t)C^*(t) = A(t)\exp\left[-\frac{W^*(t)}{k_B T(t)}\right], \qquad 6.16$$

where $A(t) = \frac{C_0 D^*(t)}{\Delta^*(t)} \propto \frac{C_0 \Delta^*(t)}{\tau(t)}$. This expression very clearly relates the nucleation rate to the velocity of nuclei crossing the critical region Δ^* within the timescale τ. Thus, investigating the effects of a time-varying supersaturation via a quasi-stationary formulation is a fundamental, and dominating, component in understanding transient ultrasound-induced bubble nucleation at macroscopical length scales.

6.2.1 Timescales of isothermal nucleation

In the case where heating rates are negligible, $\frac{dT}{dt} \to 0$ and nucleation is caused solely by the acoustic field. By the chain rule, we obtain $\left|\frac{d}{dt}\left[\frac{W^*(t)}{k_B T}\right]\right| = \frac{1}{k_B T}\left|\left(\frac{dW}{dP_l}\right)^* \dot{P}_l(t)\right|$, and by calculating $\left(\frac{dW}{dP_l}\right)^* = \frac{32\pi}{3}\left(\frac{\sigma}{P'-P_l}\right)^3$, we obtain:

$$\left|\dot{P}_l\right| < \frac{3}{32\pi^3}\frac{k_B T}{\tau}\left(\frac{P' - P_l}{\sigma}\right)^3 \qquad 6.17$$

If we define $\Delta P = P' - P_l$, the quantity ϵ_P that needs to be smaller than zero so that nucleation occurs as a quasi-stationary process is given as

$$\epsilon_P = \left|\dot{P}_l\right| - \frac{3}{32\pi^3}\frac{k_B T}{\tau}\left(\frac{\Delta P}{\sigma}\right)^3 \qquad 6.18$$

6.2.2 Timescales in the presence of acoustic heating

Acoustic heat deposition is a result of the attenuation of acoustic waves as they propagate in thermoviscous media. Here, we employ the approach of (Filonenko and Khokhlova, 2001) to calculate heating rates resulting from linear and non-linear acoustic propagation. We employ the heat transfer equation to evaluate temperature rises at the focus of a bowl-shaped transducer as:

$$\frac{\partial T}{\partial t} = \kappa \nabla^2 T + \frac{q}{c_V}, \tag{6.19}$$

where κ is the thermal conductivity of the medium, c_V is the heat capacity at constant volume, and q is the acoustic volumetric heating rate. Here, we are interested in the case where most contributions to $\frac{\partial T}{\partial t}$ originate from acoustic heating, hence we neglect the effects of thermal diffusivity and employ the approximation

$$\frac{\partial T}{\partial t} \approx \frac{q}{c_V}. \tag{6.20}$$

The expression for the source q depends on the propagation regime. At sufficiently high-power outputs, ultrasound propagation results in the formation of shockwaves which are readily absorbed by the medium and turned into heat. Focal heating rates can then be evaluated through an analytic expression based on weak shock theory (Filonenko and Khokhlova, 2001):

$$q_N = \frac{\beta f_0 A_S^3}{6 c_0^4 \rho_l^2}, \tag{6.21}$$

where β is the coefficient of non-linearity of the medium, f_0 is the fundamental HIFU frequency, $A_S = P_l^+ - P_l^-$ is the peak-to-peak focal shock amplitude, c_V is the heat capacity at constant volume and c_0 is the sound speed of the medium.

In cases where the derivative $\frac{\partial T}{\partial t}$ is not negligible, quasi-stationary nucleation should be analysed in terms of both pressure and temperature variations with time. The inequality 6.13 then reads

$$\left|\frac{d}{dt}\left[\frac{W^*(t)}{k_B T(t)}\right]\right| = \left|\frac{\partial}{\partial P_l}\left(\frac{W^*}{k_B T}\right)\frac{dP_l}{dt} + \frac{\partial}{\partial T}\left(\frac{W^*}{k_B T}\right)\frac{dT}{dt}\right| < \frac{1}{\pi^2 \tau}. \qquad 6.22$$

Assuming a nucleus in mechanical equilibrium with the pressure field $r^* = 2\sigma/\Delta P$, where $\Delta P = P' - P_l$, this becomes

$$\left|\frac{d}{dt}\left[\frac{W^*(t)}{k_B T(t)}\right]\right| = \frac{16\pi\sigma^2}{k_B T \Delta P^2}\left|\frac{2\sigma \dot{P}_l}{3\Delta P} + \left(\frac{d\sigma}{dT} - \frac{2\sigma}{3\Delta P}\frac{dP'}{dT} - \frac{\sigma}{T}\right)\frac{q}{c_V}\right|. \qquad 6.23$$

Using the relationship $\frac{dP'}{dt} = \left(\frac{dP'}{dT}\right) q/c_V = \dot{P}'$ yields

$$\left|\frac{2\sigma \dot{P}_l(t)}{3\Delta P} + \left(\frac{d\sigma}{dT} - \frac{2\sigma}{3\Delta P}\frac{dP'}{dT} - \frac{\sigma}{T}\right)\frac{q}{c_V}\right| < \frac{k_B T \Delta P^2}{16\pi^3 \tau \sigma^2}. \qquad 6.24$$

We then define the quantity ϵ_H that needs to be smaller than zero so that nucleation occurs as quasi-stationary in the presence of heating as:

$$\epsilon_H = \left|\dot{P}_l + \frac{3\Delta P}{2\sigma}\frac{q}{c_V}\left(\frac{d\sigma}{dT} - \frac{2\sigma}{3\Delta P}\frac{dP'}{dT} - \frac{\sigma}{T}\right)\right| - \frac{3}{32\pi}\frac{k_B T}{\tau}\left(\frac{\Delta P}{\sigma}\right)^3. \qquad 6.25$$

6.3 Numerical results and discussion

As defined by Eqs. 5.18 and 6.14, the width of the critical region can be used to calculate the nucleation time-lag. The nucleation time-lag τ is a measure of the diffusivity of nuclei sizes D^* with respect to the characteristic length they will diffuse over, which is given by Δ^*. It is important to notice that Eq. 6.14 is effectively a Fourier-number, and that many approximations can be found in the literature for different limiting cases.

In Figure 6-1, five cases of interest are plotted and compared for the attention of the reader. The blue curve shows the expression obtained by (Kashchiev, 2000) for the case where bubble nuclei grow solely by the attachment of single vapour molecules and is used as a baseline for the other results. The orange curve is reproduced from a previous work (de Andrade *et al.*, 2022), where we used the simpler approximation $\tau = 10/D^*$, which considers that about 10% of bubble nuclei can safely cross the critical region defined by Δ^* and go towards spontaneous growth (Kashchiev, 2000).

The remaining three curves, τ_1, τ_2 and τ_3 respectively in yellow, purple, and green, are obtained with the more exact approximation given by Equation 6.14. There are three different values for this quantity due to the three distinct solutions that are possible for D^* when one accounts for how bubble dynamics and hydrodynamic effects change the behaviour of acoustic nucleation (de Andrade *et al.*, 2022). Throughout this work, we employ the curve τ_2 (referred from now on simply as τ) for analysis of results since this is the largest solution of D^* which is strictly real and positive.

Figure 6-1 shows that the fundamental timescales of nucleation depend on the underlying mechanism of bubble growth. The nucleation time-lag calculated with a hydrodynamic approximation has a global minimum between 20 – 40 ˚C, and then increases with increasing temperature, ranging between 10^{-4} and 10 μs. This is in contrast with the approximation for sole vapour transport, where τ increases monotonically with increasing temperature. This qualitative difference is caused by the maximum in the critical diffusion coefficient characteristic of bubbles nucleating in hydrodynamic fields, i.e., when one accounts for radial dynamics when modelling the growth of bubble nuclei (de Andrade *et al.*, 2022). Such turning point is associated with the effects of enthalpy transport into nuclei as they grow, which cools the surroundings of critical nuclei and subsequently decrease nucleation rates. More importantly, the difference of about three orders of magnitude in the nucleation time-lag between ambient (20 - 40 ˚C) and boiling (around 100˚C) temperatures suggests that ultrasound bubble nucleation at high

temperatures has a longer intrinsic timescale, and that transient approaches are more appropriate for bubbles at high temperatures.

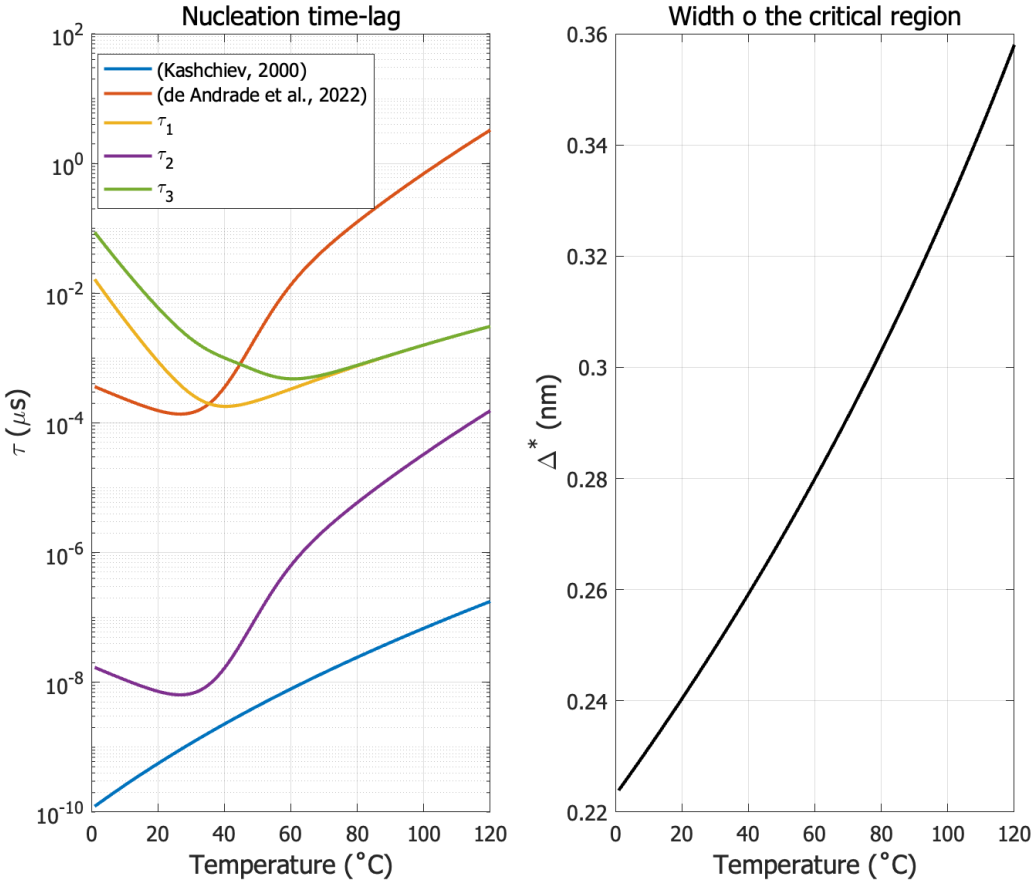

Figure 6-1. (A) Nucleation time-lag τ in microseconds as a function of temperature for several approximations in the literature and (B) Width of the nucleation critical region in nanometres as a function of temperature. All quantities are calculated at the nucleation pressure threshold $P_l^N(T)$.

Moreover, the width of the critical nucleation region is also plotted as a function of temperature at every temperature-dependent nucleation pressure point $P_l^N(T)$ in Figure 6-1. This figure shows an increasing trend for Δ^* with respect to temperature, with magnitudes between 0.22 – 0.36 nm throughout the 0 – 120 ˚C temperature range. As discussed in (de Andrade et al., 2022; Zeldovich, 2015), naturally occurring fluctuations within the critical region $r^* \pm \frac{\Delta^*}{2}$ can stop bubble nucleation from taking place should such fluctuations bring bubbles to subcritical sizes. The region around the critical radius where such fluctuations are important is given by Δ^*. The length of the critical region shows how Brownian fluctuations in the liquid, which are of the order of $k_B T$, are manifested as variations of radius in

a critical bubble. Therefore, Δ^* is the minimal timescale that can be resolved for nucleating bubbles within the scope of the CNT model employed herein.

The most important application of the approach discussed in this Chapter is in determining whether nucleation takes place as a quasi-stationary process. A quasi-stationary process is one where although the main variables of interest P_l and T are time-dependent, their derivative in time is sufficiently small such that the quasi-stationary rate can be approximated at every point in time t as $J_{qs}(t) = J_{ss}(P_l(t), T(t))$. A quasi-stationary approximation has a strict mathematical meaning that $\frac{\partial}{\partial t}\left[\frac{Z(r,t)}{C(r,t)}\right] \to 0$, which is subject to the inequalities in Eqs. 6.18 and 6.25 being true. Given that this condition is satisfied, the approximations discussed in the previous Chapters of this thesis (de Andrade et al., 2021, 2019) are appropriate and hold with accuracy.

To evaluate such appropriacy, the focal pressure waveforms obtained from non-linear ultrasound propagation are shown in Figures 6-2 and 6-3 for ultrasound central frequencies of 2 and 1.1 MHz respectively. In these figures, the focal waveform is plotted in black, and the periods where quasi-stationary nucleation holds via $\epsilon_P < 0$ are highlighted in red. These periods were calculated by replacing the numerically obtained focal waveforms into Eqs. 6.18 and 6.25 and retrieving the periods where ϵ_P is smaller than zero.

Figures 6-2 and 6-3 show that quasi-stationary nucleation holds throughout most of the tensile period of non-linear focal waveforms and is not restricted to the tensile part of an ultrasound wave for the case of propagation at 1.1 MHz. We can observe in Figs. 6-2 and 6-3 that since the validity of a steady-state approximation to nucleation is dependent on the time derivative of the pressure field, steady-state nucleation will hold at periods where the pressure is changing sufficiently slowly with respect to time. Naturally, these are the periods around the bottom-most of the tensile part of the focal waveform where the pressure field is not changing too fast with respect to time.

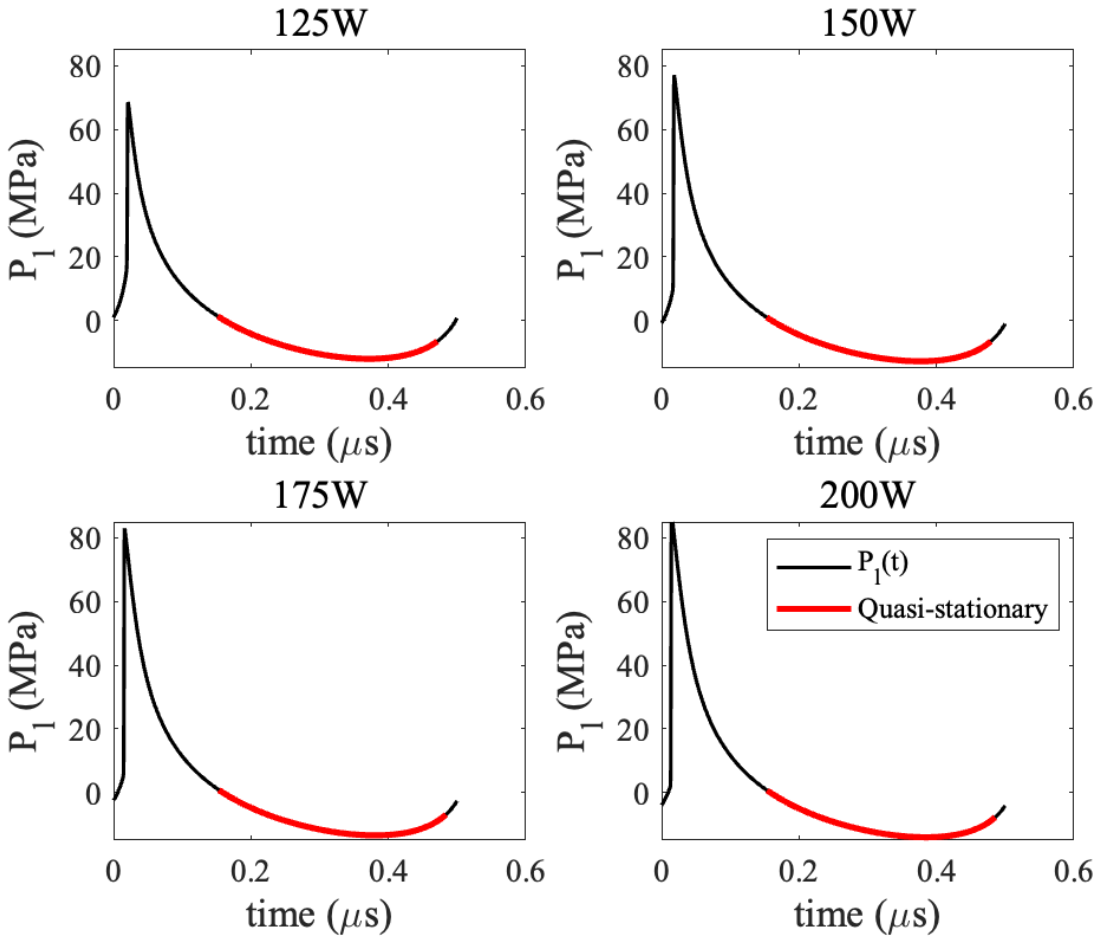

Figure 6-2. Illustration of the portions of a focal waveform generated by a 2 MHz transducer (black) where quasi-stationary nucleation is valid (red) for different input electrical powers to the transducer: 125, 150, 175 and 200 W.

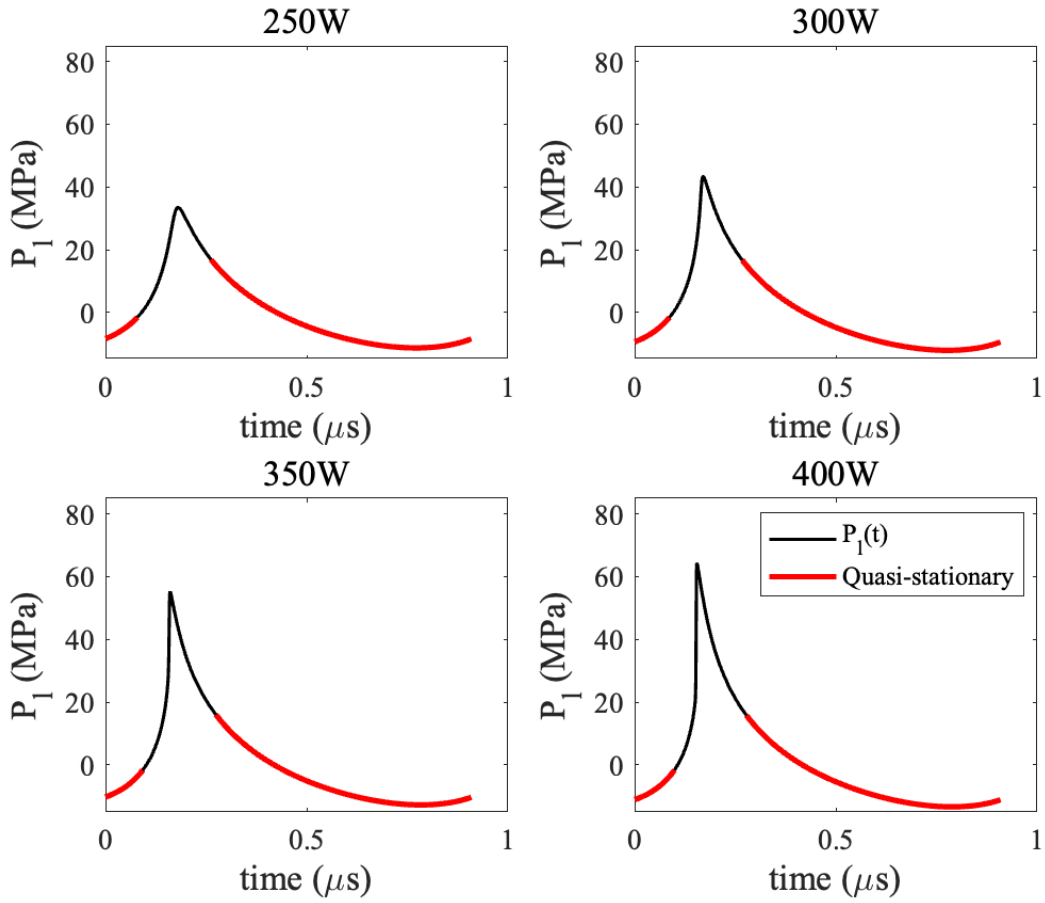

Figure 6-3. Illustration of the portions of a focal waveform generated by a 1.1 MHz transducer (black) where quasi-stationary nucleation is valid (red) for different input electrical powers to the transducer: 250, 300, 350 and 400 W.

The results displayed above show that although bubble nucleation occurs with certainty (Arvengas et al., 2011; Caupin et al., 2012; Caupin and Herbert, 2006; Davitt et al., 2010a, 2010b; Herbert et al., 2006)after a certain threshold is overcome, this is not a discontinuous phenomenon. Provided that the inequality $\epsilon_P < 0$ holds, there is a time-invariant proportionality between the distribution of bubble nuclei under investigation Z and the equilibrium concentration of critical bubbles C^*. This implies that, at every moment in time, the distribution of bubble nuclei in the liquid is synchronised to the acoustic field and can rearrange itself within timescales that do not significantly affect the rate at which they will nucleate.

A summary of the total nucleation period Δt_N as a function of temperature and input electrical power to the transducer is given in Fig. 6-4 for propagation at both 1.1 and 2 MHz. For the 2 MHz case, we simulated nucleation within the 100

– 200 W input electrical power range as this has been shown to be sufficient for bubble nucleation in previous works (de Andrade *et al.*, 2021). Likewise, we confined the parameter window for input electrical power to 200 – 400 W for sonication at 1.1 MHz since these yield higher heating rates and peak-negative focal pressure amplitudes that are compatible with the requirements of bubble nucleation.

The results in Figure 6-4 show that in the presence of time-dependent pressure and temperature fields, the time Δt_N where quasi-stationary nucleation takes place is often a fraction of the ultrasound wave period. This nucleation time decreases with increasing temperatures and increases with increasing electrical power provided to the transducer. In Fig. 6-4, solid lines represent the values of Δt_N obtained within the validity of Eq. 6.18 for $\epsilon_P < 0$ within isothermal acoustic fields. Alternatively, the dashed lines show the values of Δt_N obtained within the validity of Eq. 6.25, in the presence of acoustic heating.

These results show that the total time where quasi-stationary nucleation takes place is decreased in the presence of acoustic heat deposition. This difference is moderately small at low temperatures but increases at higher temperatures. These results do not speak about how long it takes for nucleation to take place. Rather, they describe how much time within the period of the acoustic wave a quasi-stationary formulation of nucleation is valid. Having that in mind, Fig. 6-4 implies that when both the focal pressure and temperature are changing, the system will spend more time relaxing into the time-specific thermodynamic state and less time nucleating bubbles at a fixed rate, i.e., the rate is continuously changed with time. An immediate implication of this result is the confirmation of the appropriacy of the timescales used to parametrise a CNT model of ultrasound bubble nucleation in previous Chapters (de Andrade et al., 2022, 2021, 2019) $\Delta t_N = 0.05$ μs which is the lower limit for the case of propagation at 2 MHz at 120 $^{\circ}$C in Figure 6-4.

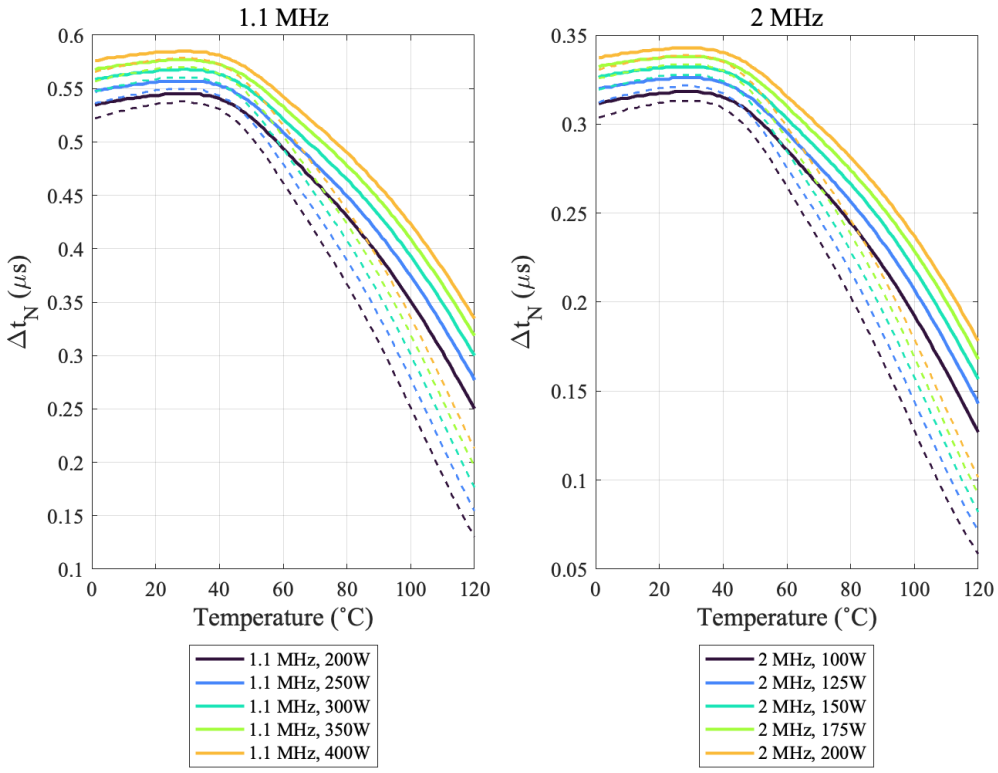

Figure 6-4. The relationship between the total steady-state nucleation time within a focal waveform to temperature at various electrical power inputs for 1.1 and 2 MHz transducers. Solid lines represent trends for isothermal nucleation, dashed lines represent trends for nucleation in the presence of heat deposition. Colours identify the input electrical power provided to the transducer in both scenarios.

6.4 Chapter Summary

In this Chapter, we applied a transient treatment of nucleation to evaluate the fundamental time and length scales of nucleation in non-linear acoustic fields. By using a second-order approximation to the equilibrium solution of the generalised Zeldovich equation, we were able to derive the conditions at which quasi-stationary nucleation takes place by relating changes in the acoustic field and focal temperature to the nucleation time-lag. These models were applied to numerically obtained non-linear acoustic fields given by a wide-angle implementation of the KZK solution solved with 512 harmonics at 1.1 and 2 MHz.

We found that quasi-stationary nucleation is valid throughout the tensile part of focal shockwaves on high intensity focused ultrasound fields due to the elongated tensile period of shockwaves. When measuring the period of validity of

quasi-stationary nucleation in focal waveforms, we found this to decrease with increasing temperature and to increase linearly with increasing electrical power provided to the transducer. These results provide numerical evidence that:

- quasi-stationary nucleation regimens can be achieved within a single cycle of non-linear ultrasound waves at 1.1 and 2 MHz for a wide range of temperatures and electrical power inputs to the transducer.
- non-linear distortion and shockwave formation favour quasi-stationary nucleation at the tensile part of an acoustic shockwave.
- quasi-stationary nucleation holds for a significant part of the tensile period of an acoustic wave at low temperatures.
- the effects of acoustic heat deposition are more evident at high temperatures, where they decrease the total time where a quasi-stationary approximation is valid.

The present results confirm the validity of the steady-state approach to bubble nucleation described in (de Andrade et al., 2022, 2021, 2019). Finally, this model predicts that thermal fluctuations in the liquid can cause variations between 0.22 to 0.36 nm in the radius of nucleating bubbles.

Chapter 7

Thesis summary and Future work

This Chapter is formed by four reflective essays where the original Chapters in this dissertation are reviewed, discussed, and contextualised. Future directions of research are given for each Chapter.

7.1 Chapter 3

Chapter 3 in this dissertation was dedicated to a review of first-order phase transitions, its associated thermodynamics, and applications in developing understanding of the energetic requirements of bubble nucleation in ultrasound. The main novel contribution of Chapter 3 is to demonstrate that upon rigorous physics reasoning and parametrisation with experimental data, the classical nucleation theory (CNT) can be harmonised with the reality of cavitation experiments, especially those of histotripsy methods. The results in Chapter 3 open novel avenues of mathematical exploration for the effects of ultrasound focal volume, frequency, and medium parameters on the nucleation of bubbles in ultrasound.

Chapter 3 was built on the cornerstone of the canonical work of Gibbs in the equilibrium of two-phase liquids (Gibbs, 1878). Additionally, it was developed considering more recent seminal work in metastable liquids and bubble nucleation such as that of (Debenedetti, 2020; Kashchiev, 2000; Skripov Kondor Reuven. Slutzkin Dinah., 1974). The skeleton of the mathematical model in Chapter 3 considers that nuclei grow solely by the attachment of vapour molecules and that hydrodynamic constraints do not play a role in the kinetics of bubble nucleation. These assumptions are closely scrutinised in Chapter 5, where a more complete overview of the mechanisms of bubble nucleation and growth is given. In Chapter

3, nucleation is defined as a response to the system being provided with sufficient energy in the form of heat or tensile pressures. The key quantities explored in Chapter 3 are metrics of free energy, which is the energy a system has available to do work and change phases.

The novel contributions to the field brought about by Chapter 3 in this thesis can be outlined as:

- The novel development and demonstration from first principles of a rigorous theory of thermodynamic equilibrium of phases for single-component systems with the aid of the classical nucleation theory.
- A novel comparison, discussion and integration of empirical work on the acoustics of metastable water with experiments on histotripsy, resulting in a general framework for the analysis of bubble nucleation at constant pressure and temperature.
- For the first time, a mathematical framework that erases the conceptual boundaries drawn by homogeneous and heterogeneous nucleation events was derived and applied to ultrasound-induced nucleation, demonstrating the concept of an activity coefficient in the equations used in the classical nucleation theory.
- For the first time, a linear dependence of the surface activity coefficient on the liquid's temperature has been evaluated in terms of experimental data in histotripsy and pure water.
- A novel demonstration of the limits of validity of the classical nucleation theory with respect to the spinodal envelope of water as parameterised by Speedy's equation of state and the TIP5P molecular dynamic model.
- The first demonstration of the sensitivity of the classical nucleation theory to experimentally relevant quantities such as the mean lifetime of the metastable fluid and the focal volume.
- The demonstration of different sensitivities of this mathematical framework to changes in pressure and temperature, shedding light on

the physical mechanisms responsible for phenomena such as boiling and cavitation.

7.1.1 Future work on Chapter 3

The models presented in Chapter 3 make the simplifying assumption that soft tissue shares the thermodynamic properties of water in nucleation. Future work extending and validating the models designed in Chapter 3 of this thesis should include formulations that account for the presence of dissolved gas in the medium.

As a proof-of-concept model, a thermodynamic description of vapour-liquid equilibrium in a mixture of H_2O and CO_2 at temperature T and ambient pressure $P \geq 0$ following that of (Carey, 1988b; Carroll, Slupsky and Mather, 1991) is described below. The solvent (water) is modelled as

$$x_1 P_v = y_1 \phi_1 P, \tag{7.1}$$

and the solute (carbon dioxide) is modelled as

$$x_2 H_{21} = y_2 \phi_2 P. \tag{7.2}$$

Where x_i is the liquid molar fraction of component i and y_i is the vapour molar fracion of the same component. $P_{v,1}$ is the vapour pressure of water given by Eq. 7.3 and H_{21} is the temperature-dependent Henry constant for the system H_2O + CO_2. ϕ_i represents the fugacity of the ith component.

$$\ln\left(\frac{H_{21}(T)}{1\ \mathrm{MPa}}\right) = h_1 + \frac{h_2}{T} + \frac{h_3}{T^2} + \frac{h_4}{T^3}, \tag{7.3}$$

where T is temperature in Kelvin, and the coefficients h_i can be found in Table 6-3. A temperature-dependent $H_{21}(T)$ valid from 0 to 160 ˚C atmospheric pressures and below is given by (Carroll, Slupsky and Mather, 1991).

Table 7-1. Coefficients for Equation 7.3 (Carroll, Slupsky and Mather, 1991).

h_1	-6.8346
h_2	$1.2817 \cdot 10^4$
h_3	$-3.7668 \cdot 10^6$
h_4	$2.9970 \cdot 10^8$

The fugacity coefficients are defined as the ratio of fugacities of pure components in vapour and liquid phases as $\phi_1 = \frac{\phi_1^v}{\phi_1^l}$ and $\phi_2 = \phi_2^v$. This makes it possible to employ the approach of (Peng and Robinson, 1976b) to calculate pure substance fugacity coefficients. The Peng-Robinson equation stablishes that in the vapour phase:

$$\ln \phi^v = Z^v - 1 - \ln(Z^v - B) - \frac{A}{2\sqrt{2}B} \ln\left(\frac{Z^v + \left(1 + \sqrt{2}B\right)}{Z^v + \left(1 - \sqrt{2}B\right)}\right), \qquad 7.4$$

and in the liquid phase:

$$\ln \phi^l = Z^l - 1 - \ln(Z^l - B) - \frac{A}{2\sqrt{2}B} \ln\left(\frac{Z^l + \left(1 + \sqrt{2}B\right)}{Z^l + \left(1 - \sqrt{2}B\right)}\right), \qquad 7.5$$

where Z is the compressibility factor of the Peng-Robinson cubic EoS described by the equation

$$Z^3 - (1 - B)Z^2 + (A - 3B^2 - 2B)Z - (AB - B^2 - B^3) = 0, \qquad 7.6$$

where $A = \frac{aP}{(RT)^2}$ and $B = \frac{bP}{RT}$.

The smallest real solution of Eq. 7.6 defines Z^v and the largest real solution defines Z^l. Therefore, using the condition that $\sum_i y = \sum_i x_i = 1$, the temperature-dependent equilibrium concentration of dissolved CO_2 in water x_2 is given by the solution of the linear system:

$$\begin{bmatrix} P_v\phi_1 & 0 & -P & 0 \\ 0 & \frac{H_{21}}{\phi_2} & 0 & -P \\ 1 & 1 & 0 & 0 \\ 0 & 0 & 1 & 1 \end{bmatrix} \begin{bmatrix} x_1 \\ x_2 \\ y_1 \\ y_2 \end{bmatrix} = \begin{bmatrix} 0 \\ 0 \\ 1 \\ 1 \end{bmatrix}. \quad 7.7$$

By calculating x_i and y_i through a model such as the one presented in Eq. 7.7, it is possible to reframe Equation 3.6 in this thesis to account for the gas content of the medium undergoing nucleation. This would allow for numerically evaluating the effect of dissolved gasses in the critical size of bubble nuclei, the energy barrier to bubble nucleation, potential variations of the scaling factor for the surface tension in terms of the gas composition of the liquid, as well as understanding how the equilibrium pressure of dissolved gas in soft tissue behaves as a function of temperature.

7.2 Chapter 4

Chapter 4 in this dissertation discussed, for the first time, the application of thermodynamic models of phase equilibrium to numerically obtained pressure and temperature fields that are characteristic of boiling histotripsy. At the forefront of the results in Chapter 4 is the idea that an appropriate understanding of pressure and temperature fields is essential for the description of bubble nucleation, especially in boiling histotripsy (Canney et al., 2010b; de Andrade et al., 2021; Khokhlova et al., 2019a). For the case of boiling histotripsy, the model developed in Chapter 4 interacts with the theory laid out in Chapter 3 by enabling the solution of the equation $P_l^N(T) = P_l(t)$, where one can identify the moment where nucleation takes place by identifying the time t where the temperature $T = T(t)$ and acoustic pressure $P_l = P_l(t)$ satisfy the thermodynamic conditions for nucleation by exceeding the temperature-dependent threshold $P_l^N(T)$.

The results in Chapter 4 consist of a series of spatial-temporal trends in bubble nucleation that can serve as a distinctive metric of what exactly the ultrasound pulse is doing within the heterogeneous reality of surgical targets. As an example, we could consider the heterogeneity of soft tissue, which comprises

portions of parenchyma intertwined with connective tissue. Although basic metrics such as attenuation parameters and the speed of sound are obtained for a mean tissue sample, it is obvious that the bulk of interstitial fluid and cells has different thermoviscous properties than collagen and connective tissue. Although most methods of analysis are currently limited by the mean-field character of the approximations available for such constants, Chapter 4 establishes a framework where one could investigate whether nucleation would be quantitatively different at the interface between soft tissue and connective tissue, or around fatty regions within an organ. The most important message of this Chapter is that, once one knows the material at hand and the properties of the acoustic field in appropriate detail, it is possible to plan and optimise experiments and procedures considering the classical nucleation theory.

The most distinctive numerical result in Chapter 4 is shown in Figure 4-13, where there is a mismatch between the region of highest nucleation rates and the region of lowest peak-negative pressures. This mismatch can be interpreted with the theory in Chapter 3 in simple terms: preferential nucleation sites are not necessarily the regions of lowest acoustic pressure, but rather the regions where the interaction between tensile acoustic pressures and temperature allows for bubble nucleation to take place. This approach allows the parametrisation of boiling histotripsy protocols, or rather, of any histotripsy protocol where one first employs the effects of acoustic heat deposition to lower the nucleation pressure threshold $P_l^N(T)$ and then applies the tensile part of an ultrasound wave to trigger the process of nucleation. Therefore, Chapter 4 contributes toward the applicability of the models developed herein by relating the basic parameters of experiments such as electrical power input, pulse repetition frequency, and duty cycle, to the nucleation metrics predicted by CNT. Although the applicability of this Chapter is tentatively worded for boiling histotripsy, its implications are wide. Upon appropriate validation this approach can be envisioned to serve as a tool for protocol planning of histotripsy procedures where it is not trivial to propagate high-intensity waves through surrounding organs, for example through the skull or ribcage.

The novel contributions to the field brought about by Chapter 4 in this thesis can be outlined as:

- The development of a novel computational algorithm that integrates simulations of acoustic propagation, acoustic heat deposition, temperature-dependent thermodynamic properties, and metrics of bubble nucleation.
- The development of a novel numerical methodology for the parametrisation of boiling histotripsy protocols, where it is possible to identify the thermodynamic conditions where boiling bubbles have the highest likelihood to form within a histotripsy pressure field.
- The demonstration of a novel methodology for optimising boiling histotripsy pulse durations and duty cycles, where it is possible to calculate the time taken for the formation of the first bubble nucleus without evoking the assumption that bubble nucleation will always take place at 100 ˚C irrespective of time and length-scales of the application at hand.
- A compound novel visualization of the thermodynamic variables involved in the process of bubble nucleation, demonstrating that the synergetic interaction of pressure and temperature within the HIFU focus can surpass the isolated effects of either pressure or temperature separately on the nucleation rate.
- A novel prototype numerical framework for clinical protocol planning of boiling histotripsy surgery, where it would be possible to estimate the energetic requirements for bubble nucleation within a surgical target.

7.2.1 Future work on Chapter 4

The numerical framework presented in Chapter 4 integrates simulations of acoustic propagation, acoustic heat deposition, temperature-dependent thermodynamic properties, and metrics of bubble nucleation. This framework can be augmented with a more complex formulation of bubble nucleation that considers the effects of dissolved gasses presented in 7.1. For example:

- Future studies should aim to calculate the local differences in chemical potential between the vapour and liquid phases of water and gas mixtures. This involves a detailed analysis of the thermodynamic equilibrium conditions under varying temperatures and pressures, which are influenced by ultrasound-induced heating (Carroll, Slupsky and Mather, 1991). By understanding these differences in chemical potential, it will be possible to predict more accurately where and when nucleation is likely to occur within the tissue. This requires the integration of more sophisticated thermodynamic models into the existing numerical framework, allowing for a more nuanced simulation of bubble nucleation processes.
- The possibility of changes in gas concentration due to temperature gradients, known as the Soret effect, presents a possible area of investigation (Rahman and Saghir, 2014; Guo *et al.*, 2018; Bekezhanova and Goncharova, 2020). This phenomenon, where dissolved gases migrate along temperature gradients, could significantly impact the distribution of gases within tissues exposed to focused ultrasound. Future work will explore how these temperature-induced concentration gradients affect the likelihood and locations of bubble nucleation. This involves developing models that can simulate the diffusion of gases in response to temperature gradients created by ultrasound heating, providing insights into how to manipulate these effects to optimize therapeutic outcomes.
- Another promising avenue is the modelling of local pH modulation within the ultrasound focus by altering gas saturation concentrations as a function of temperature (Krieg *et al.*, 2014). This aspect is particularly relevant for treatments targeting the acidic microenvironments of tumors, where pH modulation could enhance the efficacy of certain therapies. Future models will need to account for the solubility of gases like CO2, which can significantly affect pH levels, and how these solubility changes with temperature. This

requires a multidisciplinary approach, combining acoustic physics, thermodynamics, and biochemistry to develop a comprehensive model of pH modulation through focused ultrasound.

- Finally, future work will model the spatial pressure thresholds for nucleation in the presence of dissolved gases (Wilemski, 1983; Oxtoby and Kashchiev, 1994; Vehkamäki, 2006). This involves determining the conditions under which dissolved gases come out of solution to form bubbles, considering both the acoustic pressures applied and the effects of dissolved gases on the nucleation process. By accurately modelling these pressure thresholds, it will be possible to predict and control the formation of bubbles within targeted tissues, optimizing the therapeutic effects of focused ultrasound treatments.

7.3 Chapter 5

When analysing expressions for the nucleation rate in CNT in Chapters 3 and 4, it is evident that most kinetic models for nuclei growth focus solely on the case of vapour transport. This is probably because, historically, it has been easier to study the effect of a superheat in nucleation than the effect of tensile pressures on bubble formation, and molecular detachment is the most direct effect of superheating in a fluid. In Chapter 5, the hydrodynamic theory of nucleation developed by Zeldovich and furthered by Kagan and Blander was applied in analysing the role of thermal and hydrodynamic constraints on the growth of bubbles in ultrasound nucleation using histotripsy as case-study. This means that instead of analysing the vaporisation rate $\frac{dn}{dt}$ this Chapter aimed at establishing an understanding of the radial growth of critical nuclei $v_r = \frac{dr}{dt}$.

An implicit simplifying assumption omitted from Chapters 3 and 4, was that the liquid could be instantly brought to an equilibrium concentration of nuclei. The equilibrium concentration can be exemplified as the case where one lowers the pressure in a liquid, and the density in a closed control volume within this liquid

subsequently decreases. From this decreased density, the intermolecular spaces increase, making room for empty pockets to be formed from the Brownian motion of molecules. This is an idealised model for homogeneous, well-characterised fluids with an equilibrium distribution $C(r,t)$. However, the reality of any fluid is that it contains impurities which will alter the profile of the real distribution of nuclei $Z(r,t)$ contained within it. Therefore, the only appropriate treatment of nucleation for realistic fluids depends on understanding how the liquid looks like at the microscopic scale.

The theory developed in Chapter 5 is one that circumvents the need for having a priori information on the initial distribution of bubbles. This theory uses principles of statistics and transport phenomena to describe how the size distribution of nuclei $Z(r,t)$ evolves in time as compared to the equilibrium distribution of nuclei $C(r,t)$ from liquid kinetics. This is a convenient mathematical framework since it is applicable to distributions of all sizes and shapes if one can establish a mathematical relationship between the nuclei population under consideration to an equilibrium population of nuclei.

The novelty brought by the work described in Chapter 5 is that it represents the distribution of bubbles across sizes within a mass conservation law. The conservative nature of the governing equation of nucleation (Eq. 5.9) makes it analogous to the evolution of a pulse modelled by Burgers' equation, where dissipation occurs due to a certain diffusion coefficient D^* and the advective term v_r is non-linear. At this point, it is possible to merge the Rayleigh-Plesset equation into CNT. If the Rayleigh-Plesset equation describes how bubbles respond to an acoustic field with a certain size-dependent velocity $\frac{dr}{dt}$, then this equation is applicable in finding the advective term v_r in Zeldovich's theory, which is simply the characteristic equation over which the nuclei population will be advected.

Chapter 5 furthers our understanding in ultrasound bubble nucleation by relating the direct effects of ultrasound pressure fields characterised by the drift v_r to near-equilibrium effects characterised by the critical diffusivity D^* in terms of the liquid's temperature. This Chapter comprises a theory that accounts for the fluctuational drift of bubbles up to nearly critical sizes, and for the size diffusion that

occurs around the critical size, i.e. when the intrinsic thermal fluctuations in the liquid $k_B T$ are the defining factor for nucleation to happen. This framework allows the construction of a fundamental set of equations which yields non-dimensional measures of the relative effects of constraints such as viscosity, inertia, surface tension and enthalpy transport in bubble nucleation. When compared to documented experimental data in bubble nucleation and histotripsy, these metrics outline well-defined parameter windows where nucleation takes place via equivalent mechanisms. The immediate implication of these results is that metrics such as Eqs. 5.33 – 5.40 can be used to compare the equivalence and similarity of protocols for ultrasound bubble nucleation in water.

It is important to outline that amongst all constraints analysed for bubble nucleation, the surface tension of bubble nuclei is the only one that is present in the two fundamental components of nucleation, acting both as a kinetic term and an energetic term. The surface tension acts as an energetic term because it is very closely related to the energy barrier that needs to be overcome such that nucleation takes place. Likewise, the surface tension affects the kinetics of bubble nucleation because it is an active term in determining both the radial dynamics of bubbles as given by the Rayleigh-Plesset equation, and the extent to which enthalpy transport decreases vaporisation rates into bubble nuclei. Therefore, it is important to highlight that, although the viscosity of the surrounding liquid is the dominant factor with respect to the growth of bubble nuclei, the surface tension remains the most critical parameter in nucleation, because the nucleation rate depends on it exponentially as shown in Chapter 3.

The most interesting paradox that is posed by Equations 5.29 and 5.34 is that, in the idealised case, there is a direct relationship between vaporisation rates and the radial oscillations of a bubble. Although very basic, this statement can be interrogated with the question “Does the bubble radius change because of the internal number of molecules in a bubble or does the internal number of molecules change because of the radius?”. This is a fundamental question that shapes and limits the analysis of the mathematics in Chapter 5 of this thesis. The primary step into an answer is given by the results of this Chapter, which depend on the

temperature at which the system is being observed. At low temperatures, viscous effects dominate bubble nucleation and absorb kinetic energy from radial oscillations such that bubble contents are always “catching up” with the bubble size. Alternatively, at high temperatures, enthalpy transport into the bubble decreases the supersaturation around a critical nucleus, bringing nucleation to a halt. In this case, the radius of the bubble is controlled by the rate at which its contents change.

The novel contributions to the field brought about by Chapter 5 in this thesis can be outlined as:

- For the first time, a hydrodynamic model of bubble nuclei populations is derived within the application of ultrasound-induced nucleation. This includes a novel visualization of the growth of bubble populations in terms of advective and diffusive transport mechanisms.
- For the first time, metrics representing the magnitude at which enthalpy transport constrains the formation of bubbles has been developed, explored and demonstrated for ultrasound-induced bubble nucleation. It has been shown, for the first time, that this mechanism is a viable explanation for the difference in size and behaviour between boiling histotripsy vapour bubbles and histotripsy cavitation clouds.
- For the first time, a mathematical model of bubble nucleation has integrated the Rayleigh-Plesset Equations to the Classical Nucleation Theory for the process of bubble nucleation.
- For the first time, it was demonstrated that boiling and intrinsic pressure histotripsy protocols can be discerned with respect to dimensional analysis. Most importantly, this is a novel way of quantifying the character of bubbles as they nucleate.
- Fort the first time, it was demonstrated that a second-order hydrodynamic approximation to bubble critical diffusivities is in excellent agreement with the third-order approximation.
- For the first time, it was demonstrated that when only the effects of vapour transport are taken into account at low temperatures, these

yield nucleation rates that are significantly lower than those obtained by considering the effects of pressure fields.

7.3.1 Future work on Chapter 5

The hydrodynamic model presented in Chapter 5 integrates kinetic aspects of hydrodynamic nucleation into the calculation of nucleation rates. These models highlight that enthalpy of vaporisation can play an important role in reducing nucleation rates around a critical nucleus. By augmenting the fundamental thermodynamic model in Chapter 3 to account for dissolved gas, it is possible to arrive at an additional nondimensional factor δ_2 for Equation 5.32. This happens by acknowledging that while the water vapour transport rate into the critical nucleus core is

$$\dot{n}_1 = \frac{A}{(1+\delta_1)\sqrt{2\pi m k_B T}}\left[\frac{x_1}{\phi_1}P_v - y_1 P'\right], \tag{7.8}$$

the rate of gas transfer will be given by

$$\dot{n}_2 = \frac{A}{\sqrt{2\pi m k_B T}}\left[\left(\frac{x_2 H_{21}}{\phi_2}\right)_s - y_2 P'\right]. \tag{7.9}$$

This implies the existence of a second non-dimensional factor, such as that introduced in 5.33 that arises from heat transfer caused by the process of gas dissolution. Such work would be an important extension to the work in this thesis and other seminar works in the field (Katz and Blander, 1973; Blander, 1979; Zeldovich, 2015).

7.4 Chapter 6

A critical aspect of Zeldovich's theory of bubble formation is that by establishing a relationship between the real distribution of nuclei in a liquid $Z(r,t)$ and the equilibrium one $C(r,t)$ the adjustment of the former onto the latter requires time. The specific magnitude of this relaxation period needs to be conservatively

accounted for with the slowest process involved in nucleation, which is size diffusion as discussed in Chapter 5. This means that there is a Fourier-type number that relates the timescales at which bubble size diffusion takes place. At the centre of Chapter 6, is the idea that the key kinetic component of nucleation, the critical diffusivity D^*, shapes the speed at which any concentration of nuclei rearranges into an equilibrium concentration, which can be analysed mathematically within the scope of liquid kinetics. The mathematical validity of this idea underpins the transient validity of *all* mathematical models derived within this thesis. Starting with Chapter 3, where it was proposed that at the most essential level, nucleation is the process of creating Σ bubbles within the focal volume of the transducer V_0 during a time interval Δt_{N}, which results in a steady-state nucleation rate $J_{\mathrm{ss}} \approx \frac{\Sigma}{V_0 \Delta t_N}$.

A critical interrogation of this statement needs to lead to questioning on how the time interval Δt_N is determined. On the one hand, this interval needs to be sufficiently small such that first-order approximations hold with sufficient accuracy. Likewise, this time interval needs to be significantly smaller than the acoustic period $\frac{1}{f}$ such that neither the acoustic pressure P_l or the focal temperature T change significantly over the duration of Δt_N. Provided that all these assumptions hold true, one can evaluate a linear steady-state nucleation rate as $J_{ss} \approx \frac{\Sigma}{V_0 \Delta t_N}$. This approximation is the key to defining what is meant by a "nucleation pressure threshold" in Chapter 3. On the other hand, this interval needs to be sufficiently big so that a detailed time-series measurement of the nucleation rate can be obtained.

In Chapter 6, the concept of quasi-stationary nucleation was applied to gauge and confirm the mathematical validity of results obtained in Chapters 3 through 5. Quasi-stationary nucleation is a special case of transient nucleation where, at every moment in time, the nucleation rate is very close to the steady-state nucleation rate at that pressure and temperature. During quasi-stationary nucleation, the system spends very little time doing rearrangements that will enable the formation of critical bubbles and spends most of the time nucleating them. Although the assumption of equilibrium is ubiquitous in the derivations of Chapter 3, the concept of equilibrium is also largely associated with the limit of a property

at $t \to \infty$. Thus, it would be simply irresponsible to apply a steady-state analysis dependent on equilibrium quantities to a process that is, by definition, highly transient with frequencies within the MegaHertz range.

The main finding of Chapter 6 is that the total time available for nucleation Δt_N is a quantity that depends on a range of parameters such as temperature and pressure magnitude, but mostly on the acoustic waveform. The results in Chapter 6 show that when the pressure wave changes sufficiently slow with time the system can quickly rearrange itself to the acoustic field, and nucleation is not hindered by the transiency of pressure and temperature. Most importantly, Chapter 6 shows that the elongated tensile period of shockwaves characteristic of high-intensity focused ultrasound are favourable to nucleation by prolonging the period of exposure to negative pressures with minimal changes to the equilibrium distribution of nuclei.

The novel contributions to the field brought about by Chapter 6 in this thesis can be outlined as:

- For the first time, a quasi-stationary model of bubble nucleation in acoustic fields was developed. This model includes considerations that are valid for the analysis of the metastability induced by time-dependent pressure and/or temperature fields.
- For the first time, it was demonstrated that the classical nucleation theory has timescales that are compatible with those of high-intensity ultrasound fields.
- For the first time, it was demonstrated that quasi-stationary nucleation takes place at the tensile part of acoustic waves. This confirms the validity of the models developed and discussed in Chapters 3 – 5 for application in ultrasound-induced nucleation.
- For the first time, the effects of temperature on the mean lifetime of a metastable fluid were calculated and evaluated as a function of temperature, and it was demonstrated that it decreases with increasing temperatures.

The quasi-stationary model presented in Chapter 6 elucidates the effects of time-varying temperature and pressure fields in the nucleation process and establish a comparison between steady-state and transient nucleation rates. These models can be extended to scenarios where dissolved gas is present, evaluating the minimal timescales for establishing the quasi-stationary regimes of nucleation for which the work in this thesis is mathematically valid.

References

Ando, K., Liu, A.Q. and Ohl, C.D. (2012) 'Homogeneous nucleation in water in microfluidic channels', *Physical Review Letters*, 109(4). Available at: https://doi.org/10.1103/PhysRevLett.109.044501.

de Andrade, M.O. *et al.* (2019) 'The effects of ultrasound pressure and temperature fields in millisecond bubble nucleation', *Ultrasonics Sonochemistry*, 55(October 2018), pp. 262–272. Available at: https://doi.org/10.1016/j.ultsonch.2019.01.019.

de Andrade, M.O. *et al.* (2021) 'Modelling the Physics of Bubble Nucleation in Histotripsy', *IEEE Transactions on Ultrasonics, Ferroelectrics, and Frequency Control*, p. 1. Available at: https://doi.org/10.1109/TUFFC.2021.3097118.

de Andrade, M.O. *et al.* (2022) 'Mechanisms of Nuclei Growth in Ultrasound Bubble Nucleation', *Ultrasonics Sonochemistry*, p. 106091. Available at: https://doi.org/https://doi.org/10.1016/j.ultsonch.2022.106091.

Apfel, R.E. and Holland, C.K. (1991) 'Gauging the likelihood of cavitation from short-pulse, low-duty cycle diagnostic ultrasound', *Ultrasound in Medicine & Biology*, 17(2), pp. 179–185. Available at: https://doi.org/10.1016/0301-5629(91)90125-G.

Arvengas, A., Davitt, K. and Caupin, F. (2011) 'Fiber optic probe hydrophone for the study of acoustic cavitation in water', *Review of Scientific Instruments*, 82(3), p. 34904. Available at: https://doi.org/10.1063/1.3557420.

Azhari, H. (2010) 'Safety and Therapeutic Applications', in *Basics of Biomedical Ultrasound for Engineers*. Hoboken, NJ, USA: John Wiley & Sons, Inc., pp. 287–312. Available at: https://doi.org/10.1002/9780470561478.ch12.

Azouzi, M.E.M. *et al.* (2013) 'A coherent picture of water at extreme negative pressure', *Nature Physics*, 9(1), pp. 38–41. Available at: https://doi.org/10.1038/nphys2475.

Bader, K.B. *et al.* (2012) 'The effect of static pressure on the strength of inertial cavitation events', *The Journal of the Acoustical Society of America*, 132(4), pp. 2286–2291. Available at: https://doi.org/10.1121/1.4750494.

Bader, K.B. *et al.* (2019) 'Histotripsy-enhanced thrombolysis', *The Journal of the Acoustical Society of America*, 145(3), pp. 1746–1747. Available at: https://doi.org/10.1121/1.5101403.

Bader, K.B. and Holland, C.K. (2016) 'Predicting the growth of nanoscale nuclei by histotripsy pulses', *Physics in Medicine and Biology*, 61(7), pp. 2947–2966. Available at: https://doi.org/10.1088/0031-9155/61/7/2947.

Bader, K.B., Vlaisavljevich, E. and Maxwell, A.D. (2019) 'For Whom the Bubble Grows: Physical Principles of Bubble Nucleation and Dynamics in Histotripsy Ultrasound Therapy', *Ultrasound in Medicine & Biology*, 45(5), pp. 1056–1080. Available at: https://doi.org/10.1016/j.ultrasmedbio.2018.10.035.

Baidakov, V.G. (2016) 'Spontaneous cavitation in a Lennard-Jones liquid: Molecular dynamics simulation and the van der Waals-Cahn-Hilliard gradient theory', *Journal of Chemical Physics*, 144(7), p. 74502. Available at: https://doi.org/10.1063/1.4941689.

Bailey, M.R. *et al.* (2003) 'Physical mechanisms of the therapeutic effect of ultrasound (a review)', *Acoustical Physics*, pp. 369–388. Available at: https://doi.org/10.1134/1.1591291.

Balibar, S. and Caupin, F. (2003) 'Metastable liquids', *Journal of Physics: Condensed Matter*, 15(1), pp. S75–S82. Available at: https://doi.org/10.1088/0953-8984/15/1/308.

Barnett, S.B. *et al.* (1994) 'Current status of research on biophysical effects of ultrasound', *Ultrasound in Medicine and Biology*, 20(3), pp. 205–218. Available at: https://doi.org/10.1016/0301-5629(94)90060-4.

Bawiec, C.R. *et al.* (2021) 'Inertial Cavitation Behaviors Induced by Nonlinear Focused Ultrasound Pulses', *IEEE Transactions on Ultrasonics,*

Ferroelectrics, and Frequency Control [Preprint]. Available at: https://doi.org/10.1109/TUFFC.2021.3073347.

Beegle, B.L., Modell, M. and Reid, R.C. (1974) 'Thermodynamic stability criterion for pure substances and mixtures', *AIChE Journal*, 20(6), pp. 1200–1206. Available at: https://doi.org/10.1002/aic.690200621.

Bekezhanova, V.B. and Goncharova, O.N. (2020) 'Influence of the Dufour and Soret effects on the characteristics of evaporating liquid flows', *International Journal of Heat and Mass Transfer*, 154, p. 119696. Available at: https://doi.org/10.1016/j.ijheatmasstransfer.2020.119696.

Blander, M. (1979) 'Bubble nucleation in liquids', *Advances in Colloid and Interface Science*, 10(1), pp. 1–32. Available at: https://doi.org/10.1016/0001-8686(79)87002-5.

Blatteau, J.E. *et al.* (2006) 'Gas nuclei, their origin, and their role in bubble formation', *Aviation Space and Environmental Medicine*, 77(10), pp. 1068–1076.

Boissenot, T. *et al.* (2016) 'Ultrasound-triggered drug delivery for cancer treatment using drug delivery systems: From theoretical considerations to practical applications', *Journal of Controlled Release*, 241, pp. 144–163. Available at: https://doi.org/10.1016/j.jconrel.2016.09.026.

Brennen, Christopher Earls (2013) *Cavitation and bubble dynamics*, *Cavitation and Bubble Dynamics*. Cambridge: Cambridge University Press. Available at: https://doi.org/10.1017/CBO9781107338760.

Brennen, Christopher E. (2013a) 'Dynamics of Oscillating Bubbles', in *Cavitation and Bubble Dynamics*. Cambridge: Cambridge University Press, pp. 89–109. Available at: https://doi.org/10.1017/cbo9781107338760.005.

Brennen, Christopher E. (2013b) *Phase Change, Nucleation, and Cavitation*, *Cavitation and Bubble Dynamics*. Cambridge: Cambridge University Press. Available at: https://doi.org/10.1017/cbo9781107338760.002.

Brennen, Christopher E. (2013c) ‘Spherical Bubble Dynamics’, in *Cavitation and Bubble Dynamics*. Cambridge: Cambridge University Press, pp. 30–58. Available at: https://doi.org/10.1017/cbo9781107338760.003.

Briggs, L.J. (1950) ‘Limiting negative pressure of water [2]’, *Journal of Applied Physics*, 21(7), pp. 721–722. Available at: https://doi.org/10.1063/1.1699741.

Bruot, N. and Caupin, F. (2016) ‘Curvature Dependence of the Liquid-Vapor Surface Tension beyond the Tolman Approximation’, *Physical Review Letters*, 116(5), p. 56102. Available at: https://doi.org/10.1103/PhysRevLett.116.056102.

Cahn, J.W. (1959) ‘Free energy of a nonuniform system. II. Thermodynamic basis’, *The Journal of Chemical Physics*, 30(5), pp. 1121–1124. Available at: https://doi.org/10.1063/1.1730145.

Cahn, J.W. and Hilliard, J.E. (1958) ‘Free energy of a nonuniform system. I. Interfacial free energy’, *The Journal of Chemical Physics*, 28(2), pp. 258–267. Available at: https://doi.org/10.1063/1.1744102.

Cahn, J.W. and Hilliard, J.E. (1959) ‘Free energy of a nonuniform system. III. Nucleation in a two-component incompressible fluid’, *The Journal of Chemical Physics*, 31(3), pp. 688–699. Available at: https://doi.org/10.1063/1.1730447.

Canney, M.S. *et al.* (2008) ‘Acoustic characterization of high intensity focused ultrasound fields: A combined measurement and modeling approach’, *The Journal of the Acoustical Society of America*, 124(4), pp. 2406–2420. Available at: https://doi.org/10.1121/1.2967836.

Canney, M.S., Khokhlova, V.A., *et al.* (2010) ‘Shock-Induced Heating and Millisecond Boiling in Gels and Tissue Due to High Intensity Focused Ultrasound’, *Ultrasound in Medicine & Biology*, 36(2), pp. 250–267. Available at: https://doi.org/10.1016/j.ultrasmedbio.2009.09.010.

Canney, M.S., Khokhlova, T.D., *et al.* (2010) ‘Tissue Erosion Using Shock Wave Heating and Millisecond Boiling in HIFU Fields’, in *AIP Conference Proceedings*. AIP, pp. 36–39. Available at: https://doi.org/10.1063/1.3367183.

Carey, V.P. (1988a) ‘The properties of gases & liquids’, *Experimental Thermal and Fluid Science*, 1(4), p. 409. Available at: https://doi.org/10.1016/0894-1777(88)90021-0.

Carey, V.P. (1988b) ‘The properties of gases & liquids’, *Experimental Thermal and Fluid Science*, 1(4), p. 409. Available at: https://doi.org/10.1016/0894-1777(88)90021-0.

Carroll, J.J., Slupsky, J.D. and Mather, A.E. (1991) ‘The Solubility of Carbon Dioxide in Water at Low Pressure’, *Journal of Physical and Chemical Reference Data*, pp. 1201–1209. Available at: https://doi.org/10.1063/1.555900.

Carstensen, E.L. (1987) ‘Acoustic cavitation and the safety of diagnostic ultrasound’, *Ultrasound in Medicine and Biology*, 13(10), pp. 597–606. Available at: https://doi.org/10.1016/0301-5629(87)90057-3.

Caupin, F. (2005) ‘Liquid-vapor interface, cavitation, and the phase diagram of water’, *Physical Review E - Statistical, Nonlinear, and Soft Matter Physics*, 71(5), p. 051605. Available at: https://doi.org/10.1103/PhysRevE.71.051605.

Caupin, F. *et al.* (2012) ‘Exploring water and other liquids at negative pressure’, *Journal of Physics: Condensed Matter*, 24(28), p. 284110. Available at: https://doi.org/10.1088/0953-8984/24/28/284110.

Caupin, F. (2015) ‘Escaping the no man’s land: Recent experiments on metastable liquid water’, *Journal of Non-Crystalline Solids*, 407, pp. 441–448. Available at: https://doi.org/10.1016/j.jnoncrysol.2014.09.037.

Caupin, F. and Herbert, E. (2006) ‘Cavitation in water: a review’, *Comptes Rendus Physique*, 7(9–10), pp. 1000–1017. Available at: https://doi.org/10.1016/j.crhy.2006.10.015.

Caupin, F. and Stroock, A.D. (2013) ‘The Stability Limit and other Open Questions on Water at Negative Pressure’, in *Advances in Chemical Physics*. Hoboken, NJ, USA: John Wiley & Sons, Inc., pp. 51–80. Available at: https://doi.org/10.1002/9781118540350.ch3.

Chun, B.S. and Wilkinson, G.T. (1995) 'Interfacial Tension in High-Pressure Carbon Dioxide Mixtures', *Industrial and Engineering Chemistry Research*, 34(12), pp. 4371–4377. Available at: https://doi.org/10.1021/ie00039a029.

Church, C.C. (2002) 'Spontaneous homogeneous nucleation, inertial cavitation and the safety of diagnostic ultrasound', *Ultrasound in Medicine & Biology*, 28(10), pp. 1349–1364. Available at: https://doi.org/10.1016/S0301-5629(02)00579-3.

Cleveland, R.O. and McAteer, J.A. (2012) 'Physics of Shock-Wave Lithotripsy', in *Smith's Textbook of Endourology*. Oxford, UK: Wiley-Blackwell, pp. 527–558. Available at: https://doi.org/10.1002/9781444345148.ch49.

Coleman, A.J. and Saunders, J.E. (1993) 'A review of the physical properties and biological effects of the high amplitude acoustic fields used in extracorporeal lithotripsy', *Ultrasonics*, 31(2), pp. 75–89. Available at: https://doi.org/10.1016/0041-624X(93)90037-Z.

Copelan, A. *et al.* (2015) 'High-Intensity Focused Ultrasound: Current Status for Image-Guided Therapy', *Seminars in Interventional Radiology*, 32(4), pp. 398–415. Available at: https://doi.org/10.1055/s-0035-1564793.

Coussios, C.C. and Roy, R.A. (2008) 'Applications of acoustics and cavitation to noninvasive therapy and drug delivery', *Annual Review of Fluid Mechanics*, 40(1), pp. 395–420. Available at: https://doi.org/10.1146/annurev.fluid.40.111406.102116.

Crum, L.A. (1982) 'Nucleation and stabilization of microbubbles in liquids', *Applied Scientific Research*, 38(1), pp. 101–115. Available at: https://doi.org/10.1007/BF00385941.

Dalecki, D. (2004) 'Mechanical bioeffects of ultrasound', *Annual Review of Biomedical Engineering*, 6(1), pp. 229–248. Available at: https://doi.org/10.1146/annurev.bioeng.6.040803.140126.

Davitt, K. *et al.* (2010) 'Equation of state of water under negative pressure', *Journal of Chemical Physics*, 133(17), p. 174507. Available at: https://doi.org/10.1063/1.3495971.

Davitt, K., Arvengas, A. and Caupin, F. (2010) 'Water at the cavitation limit: Density of the metastable liquid and size of the critical bubble', *EPL (Europhysics Letters)*, 90(1), p. 16002. Available at: https://doi.org/10.1209/0295-5075/90/16002.

Debenedetti, P.G. (1988) 'Thermodynamic stability of single-phase fluids and fluid mixtures under the influence of gravity', *The Journal of Chemical Physics*, 89(11), pp. 6881–6888. Available at: https://doi.org/10.1063/1.455725.

Debenedetti, P.G. (2020) *Metastable Liquids*, *Metastable Liquids*. Princeton University Press. Available at: https://doi.org/10.2307/j.ctv10crfs5.

Delale, C.F., Hruby, J. and Marsik, F. (2003) 'Homogeneous bubble nucleation in liquids: The classical theory revisited', *Journal of Chemical Physics*, 118(2), pp. 792–806. Available at: https://doi.org/10.1063/1.1525797.

Ferrara, K., Pollard, R. and Borden, M. (2007) 'Ultrasound microbubble contrast agents: Fundamentals and application to gene and drug delivery', *Annual Review of Biomedical Engineering*, 9(1), pp. 415–447. Available at: https://doi.org/10.1146/annurev.bioeng.8.061505.095852.

Filonenko, E.A. and Khokhlova, V.A. (2001) 'Effect of acoustic nonlinearity on heating of biological tissue by high-intensity focused ultrasound', *Akusticheskij Zhurnal*, 47(4), pp. 541–550.

Fisher, J.C. (1948) 'The fracture of liquids', *Journal of Applied Physics*, 19(11), pp. 1062–1067. Available at: https://doi.org/10.1063/1.1698012.

Fletcher, N.H. (1958) 'Size effect in heterogeneous nucleation', *The Journal of Chemical Physics*, 29(3), pp. 572–576. Available at: https://doi.org/10.1063/1.1744540.

Fowlkes, J.B. and Holland, C.K. (2000) 'Mechanical bioeffects from diagnostic ultrasound: AIUM consensus statements. American Institute of

Ultrasound in Medicine.', in *Journal of ultrasound in medicine : official journal of the American Institute of Ultrasound in Medicine*. NIH Public Access, pp. 69–72. Available at: https://doi.org/10.7863/jum.2000.19.2.69.

Fry, F.J. *et al.* (1977) 'Biological effects of ultrasonic energy on living mammals.', *Ultrasound in medicine & biology*, 2(4), p. 351. Available at: https://doi.org/10.1016/0301-5629(77)90041-2.

Fry, W.J. *et al.* (1950) 'Physical Factors Involved in Ultrasonically Induced Changes in Living Systems: I. Identification of Non-Temperature Effects', *Journal of the Acoustical Society of America*, 22(6), pp. 867–876. Available at: https://doi.org/10.1121/1.1906707.

G R ter Haar and S Daniels (1981) 'Evidence for ultrasonically induced cavitation in vivo', *Physics in Medicine & Biology*, 26(6), pp. 1145–1149. Available at: https://doi.org/10.1088/0031-9155/26/6/013.

Gallo, P. *et al.* (2016) 'Water: A Tale of Two Liquids.', *Chemical reviews*, 116(13), pp. 7463–7500.

Galloway, W.J. (1954) 'An Experimental Study of Acoustically Induced Cavitation in Liquids', *Journal of the Acoustical Society of America*, 26(5), pp. 849–857. Available at: https://doi.org/10.1121/1.1907428.

Gateau, J. *et al.* (2011) 'Combined passive detection and ultrafast active imaging of cavitation events induced by short pulses of high-intensity ultrasound', *IEEE Transactions on Ultrasonics, Ferroelectrics, and Frequency Control*, 58(3), pp. 517–532. Available at: https://doi.org/10.1109/TUFFC.2011.1836.

Geoghegan, R. *et al.* (2022) 'Methods of monitoring thermal ablation of soft tissue tumors – A comprehensive review', *Medical Physics*. Available at: https://doi.org/10.1002/mp.15439.

Gibbs, J.W. (1878) 'On the equilibrium of heterogeneous substances', *American Journal of Science*, s3-16(96), pp. 441–458. Available at: https://doi.org/10.2475/ajs.s3-16.96.441.

Gibbs, J.W. (1928) *The collected works of J. W. Gibbs: Thermodynamics*, *London, Longmans, Green, & co.*

González, M.A. *et al.* (2014) 'Detecting vapour bubbles in simulations of metastable water', *The Journal of Chemical Physics*, 141(18), p. 18C511. Available at: https://doi.org/10.1063/1.4896216.

Greenspan, M. and Tschiegg, C.E. (1967) 'Radiation-induced acoustic cavitation; apparatus and some results', *Journal of Research of the National Bureau of Standards, Section C: Engineering and Instrumentation*, 71C(4), p. 299. Available at: https://doi.org/10.6028/jres.071c.024.

Greenspan, M. and Tschiegg, C.E. (1982) 'Radiation-induced acoustic cavitation; Threshold versus temperature for some liquids', *The Journal of the Acoustical Society of America*, 72(4), pp. 1327–1331. Available at: https://doi.org/10.1121/1.388415.

Guggenheim, E.A. (1950) 'Thermodynamics. An Advanced Treatment for Chemists and Physicists', *Zeitschrift für Naturforschung A*, 5(4), pp. 236–236. Available at: https://doi.org/10.1515/zna-1950-0413.

Guo, H. *et al.* (2018) 'Soret effect on the diffusion of CO2 in aqueous solution under high-pressure', *International Journal of Heat and Mass Transfer*, 117, pp. 966–971. Available at: https://doi.org/10.1016/j.ijheatmasstransfer.2017.10.058.

ter Haar, G. *et al.* (1982) 'Ultrasonically induced cavitation in vivo', *British Journal of Cancer*, 45(Suppl. 5), pp. 151–155.

ter Haar, G. and Coussios, C. (2007) 'High intensity focused ultrasound: Physical principles and devices', *International Journal of Hyperthermia*, 23(2), pp. 89–104. Available at: https://doi.org/10.1080/02656730601186138.

Hall, T.L. *et al.* (2009) 'Histotripsy of the Prostate: Dose Effects in a Chronic Canine Model', *Urology*, 74(4), pp. 932–937. Available at: https://doi.org/10.1016/j.urology.2009.03.049.

Haworth, K.J. *et al.* (2012) 'Passive imaging with pulsed ultrasound insonations', *The Journal of the Acoustical Society of America*, 132(1). Available at: https://doi.org/10.1121/1.4728230.

Hebach, A. *et al.* (2002) 'Interfacial tension at elevated pressures-measurements and correlations in the water + carbon dioxide system', *Journal of Chemical and Engineering Data*, 47(6), pp. 1540–1546. Available at: https://doi.org/10.1021/je025569p.

Hedrick, W.R. and Hykes, D.L. (1991) 'Biologic Effects of Ultrasound: V. Clinical Safety', *Journal of Diagnostic Medical Sonography*, 7(6), pp. 333–338. Available at: https://doi.org/10.1177/875647939100700603.

Herbert, E., Balibar, S. and Caupin, F. (2006) 'Cavitation pressure in water', *Physical Review E*, 74(4), p. 041603. Available at: https://doi.org/10.1103/PhysRevE.74.041603.

Hill, C.R. (1982) 'Ultrasound biophysics: a perspective.', *The British journal of cancer Supplement*, 5, pp. 46–51.

Holland, C.K. and Apfel, R.E. (1989) 'An improved theory for the prediction of microcavitation thresholds', *IEEE Transactions on Ultrasonics, Ferroelectrics and Frequency Control*, 36(2), pp. 204–208. Available at: https://doi.org/10.1109/58.19152.

Holland, C.K.S. (1989) 'Thresholds of transient cavitation produced by pulsed ultrasound in a controlled nuclei environment', *The Journal of the Acoustical Society of America*, 86(2), pp. 844–844. Available at: https://doi.org/10.1121/1.398215.

Hoogenboom, M. *et al.* (2015) 'Mechanical High-Intensity Focused Ultrasound Destruction of Soft Tissue: Working Mechanisms and Physiologic Effects', *Ultrasound in Medicine and Biology*, 41(6), pp. 1500–1517. Available at: https://doi.org/10.1016/j.ultrasmedbio.2015.02.006.

Huang, H.W. and Horng, T.L. (2015) 'Bioheat Transfer and Thermal Heating for Tumor Treatment', *Heat Transfer and Fluid Flow in Biological Processes*, pp. 1–42. Available at: https://doi.org/10.1016/B978-0-12-408077-5.00001-8.

Hwang, J.H. *et al.* (2006) 'Correlation between inertial cavitation dose and endothelial cell damage in vivo', *Ultrasound in Medicine and Biology*, 32(10), pp. 1611–1619. Available at: https://doi.org/10.1016/j.ultrasmedbio.2006.07.016.

Izadifar, Z., Babyn, P. and Chapman, D. (2019) 'Ultrasound Cavitation/Microbubble Detection and Medical Applications', *Journal of Medical and Biological Engineering*. Springer Berlin Heidelberg, pp. 259–276. Available at: https://doi.org/10.1007/s40846-018-0391-0.

Izadifar, Zahra *et al.* (2020a) 'An introduction to high intensity focused ultrasound: Systematic review on principles, devices, and clinical applications', *Journal of Clinical Medicine*. MDPI. Available at: https://doi.org/10.3390/jcm9020460.

Izadifar, Zahra *et al.* (2020b) 'An introduction to high intensity focused ultrasound: Systematic review on principles, devices, and clinical applications', *Journal of Clinical Medicine*, 9(2). Available at: https://doi.org/10.3390/jcm9020460.

Kalikmanov, V.I. (2013) 'Nucleation theory', *Lecture Notes in Physics*, 860, pp. 1–331. Available at: https://doi.org/10.1007/978-90-481-3643-8.

Kashchiev, D. (1969a) 'Solution of the non-steady state problem in nucleation kinetics', *Surface Science*, 14(1), pp. 209–220. Available at: https://doi.org/10.1016/0039-6028(69)90055-7.

Kashchiev, D. (1969b) 'Solution of the non-steady state problem in nucleation kinetics', *Surface Science*, 14(1), pp. 209–220. Available at: https://doi.org/10.1016/0039-6028(69)90055-7.

Kashchiev, D. (1970) 'Nucleation at time-dependent supersaturation', *Surface Science*, 22(2), pp. 319–324. Available at: https://doi.org/10.1016/0039-6028(70)90085-3.

Kashchiev, D. (2000) *Nucleation*. 1st edn. Edited by D. Kashchiev. Institute of Physical Chemistry, Bulgarian Academy of Sciences: Butterworth-Heinemann (Basic Theory with Applications).

Kashchiev, D. (2003) 'Thermodynamically consistent description of the work to form a nucleus of any size', *The Journal of Chemical Physics*, 118(4), pp. 1837–1851. Available at: https://doi.org/10.1063/1.1531614.

Katz, J.L. and Blander, M. (1973) 'Condensation and boiling: Corrections to homogeneous nucleation theory for nonideal gases', *Journal of Colloid And Interface Science*, 42(3), pp. 496–502. Available at: https://doi.org/10.1016/0021-9797(73)90035-0.

Khokhlova, T.D., Canney, M.S., *et al.* (2011) 'Controlled tissue emulsification produced by high intensity focused ultrasound shock waves and millisecond boiling', *The Journal of the Acoustical Society of America*, 130(5), pp. 3498–3510. Available at: https://doi.org/10.1121/1.3626152.

Khokhlova, T.D., Simon, J.C., *et al.* (2011) '*In vivo* tissue emulsification using millisecond boiling induced by high intensity focused ultrasound.', *The Journal of the Acoustical Society of America*, 129(4_Supplement), pp. 2477–2477. Available at: https://doi.org/10.1121/1.3588149.

Khokhlova, T.D. *et al.* (2017) 'Dependence of Boiling Histotripsy Treatment Efficiency on HIFU Frequency and Focal Pressure Levels', *Ultrasound in Medicine and Biology*, 43(9), pp. 1975–1985. Available at: https://doi.org/10.1016/j.ultrasmedbio.2017.04.030.

Khokhlova, V. *et al.* (2014) 'Monitoring boiling histotripsy with bubble-based ultrasound techniques', *The Journal of the Acoustical Society of America*, 136(4), pp. 2301–2301. Available at: https://doi.org/10.1121/1.4900325.

Khokhlova, V. *et al.* (2016) ' Pilot in vivo studies on transcutaneous boiling histotripsy in porcine liver and kidney ', *The Journal of the Acoustical Society of America*, 140(4), pp. 3030–3030. Available at: https://doi.org/10.1121/1.4969401.

Khokhlova, V.A. *et al.* (2006) 'Effects of nonlinear propagation, cavitation, and boiling in lesion formation by high intensity focused ultrasound in a gel phantom', *The Journal of the Acoustical Society of America*, 119(3), pp. 1834–1848. Available at: https://doi.org/10.1121/1.2161440.

Khokhlova, V.A. *et al.* (2015) 'Histotripsy methods in mechanical disintegration of tissue: Towards clinical applications', *International Journal of Hyperthermia*, 31(2), pp. 145–162. Available at: https://doi.org/10.3109/02656736.2015.1007538.

Khokhlova, V.A., Schade, G.R., *et al.* (2019) 'Pilot in vivo studies on transcutaneous boiling histotripsy in porcine liver and kidney', *Scientific Reports*, 140(1), pp. 3030–3030. Available at: https://doi.org/10.1038/s41598-019-56658-7.

Khokhlova, V.A., Bawiec, C.R., *et al.* (2019) 'Real-time imaging and control of boiling histotripsy lesion formation using Doppler ultrasound', *The Journal of the Acoustical Society of America*, 146(4), pp. 2992–2992. Available at: https://doi.org/10.1121/1.5137355.

Kim, T.-H. and Kim, H.-Y. (2012) 'Observations of Disruptive Bubble Behavior and Micro-Pattern Damage in Ultrasonic Cleaning', in *8th International Symposium on Cavitation*. Singapore: Research Publishing Services, pp. 274–276. Available at: https://doi.org/10.3850/978-981-07-2826-7_007.

Kooiman, K. *et al.* (2020) 'Ultrasound-Responsive Cavitation Nuclei for Therapy and Drug Delivery', *Ultrasound in Medicine & Biology*, 46(6), pp. 1296–1325. Available at: https://doi.org/10.1016/j.ultrasmedbio.2020.01.002.

Kreider, W. *et al.* (2011) 'The dynamics of histotripsy bubbles', in *AIP Conference Proceedings*, pp. 427–430. Available at: https://doi.org/10.1063/1.3607944.

Kreider, W. *et al.* (2013) 'Rectified growth of histotripsy bubbles', in *Proceedings of Meetings on Acoustics*. Available at: https://doi.org/10.1121/1.4800326.

Krieg, B.J. *et al.* (2014) 'In vivo predictive dissolution: Transport analysis of the CO2, bicarbonate in vivo buffer system', *Journal of Pharmaceutical Sciences*, 103(11). Available at: https://doi.org/10.1002/jps.24108.

Lauterborn, W. *et al.* (2007) 'Acoustic cavitation, bubble dynamics and sonoluminescence', *Ultrasonics Sonochemistry*, 14(4), pp. 484–491. Available at: https://doi.org/10.1016/j.ultsonch.2006.09.017.

Lauterborn, W. and Mettin, R. (2015) 'Acoustic cavitation: Bubble dynamics in high-power ultrasonic fields', in *Power Ultrasonics: Applications of High-Intensity Ultrasound*. Elsevier, pp. 37–78. Available at: https://doi.org/10.1016/B978-1-78242-028-6.00003-X.

Lienhard, J.H., Shamsundar, N. and Biney, P.O. (1986) 'Spinodal lines and equations of state: A review', *Nuclear Engineering and Design*, 95(C), pp. 297–314. Available at: https://doi.org/10.1016/0029-5493(86)90056-7.

Lin, K.W. *et al.* (2014) 'Histotripsy beyond the intrinsic cavitation threshold using very short ultrasound pulses: Microtripsy', *IEEE Transactions on Ultrasonics, Ferroelectrics, and Frequency Control*, 61(2), pp. 251–265. Available at: https://doi.org/10.1109/TUFFC.2014.6722611.

Mancia, L. *et al.* (2017) 'Predicting Tissue Susceptibility to Mechanical Cavitation Damage in Therapeutic Ultrasound', *Ultrasound in Medicine and Biology*, 43(7), pp. 1421–1440. Available at: https://doi.org/10.1016/j.ultrasmedbio.2017.02.020.

Mancia, L. *et al.* (2019) 'Modeling tissue-selective cavitation damage', *Physics in Medicine and Biology*, 64(22). Available at: https://doi.org/10.1088/1361-6560/ab5010.

Maxwell, A. *et al.* (2012) 'Disintegration of Tissue Using High Intensity Focused Ultrasound: Two Approaches That Utilize Shock Waves', *Acoustics Today*, 8(4), p. 24. Available at: https://doi.org/10.1121/1.4788649.

Maxwell, A.D. *et al.* (2011) 'Cavitation clouds created by shock scattering from bubbles during histotripsy', *The Journal of the Acoustical Society of America*, 130(4), pp. 1888–1898. Available at: https://doi.org/10.1121/1.3625239.

Maxwell, A.D. *et al.* (2013) 'Probability of Cavitation for Single Ultrasound Pulses Applied to Tissues and Tissue-Mimicking Materials', *Ultrasound in Medicine & Biology*, 39(3), pp. 449–465. Available at: https://doi.org/10.1016/j.ultrasmedbio.2012.09.004.

McLaughlan, J. *et al.* (2010) 'A study of bubble activity generated in ex vivo tissue by high intensity focused ultrasound', *Ultrasound in Medicine and Biology*, 36(8), pp. 1327–1344. Available at: https://doi.org/10.1016/j.ultrasmedbio.2010.05.011.

Menzl, G. *et al.* (2016) 'Molecular mechanism for cavitation in water under tension', *Proceedings of the National Academy of Sciences of the United States of America*, 113(48), pp. 13582–13587. Available at: https://doi.org/10.1073/pnas.1608421113.

Meroni, D. *et al.* (2022) 'Sonoprocessing: From Concepts to Large-Scale Reactors', *Chemical Reviews*. Available at: https://doi.org/10.1021/acs.chemrev.1c00438.

Miller, D.L. (1987) 'A review of the ultrasonic bioeffects of microsonation, gas-body activation, and related cavitation-like phenomena', *Ultrasound in Medicine and Biology*, 13(8), pp. 443–470. Available at: https://doi.org/10.1016/0301-5629(87)90110-4.

Miller, D.L. *et al.* (2012) 'Overview of therapeutic ultrasound applications and safety considerations', *Journal of Ultrasound in Medicine*, 31(4), pp. 623–634. Available at: https://doi.org/10.7863/jum.2012.31.4.623.

Miller, M.W. and Brayman, A.A. (1997) 'Biological effects of ultrasound. The perceived safety of diagnostic ultrasound within the context of ultrasound biophysics: A personal perspective', *Echocardiography*, 14(6 PART I), pp. 615–627. Available at: https://doi.org/10.1111/j.1540-8175.1997.tb00771.x.

Miller, M.W., Miller, D.L. and Brayman, A.A. (1996) 'A review of in vitro bioeffects of inertial ultrasonic cavitation from a mechanistic perspective', *Ultrasound in Medicine and Biology*, 22(9), pp. 1131–1154. Available at: https://doi.org/10.1016/S0301-5629(96)00089-0.

Mitragotri, S. (2005) 'Healing sound: The use of ultrasound in drug delivery and other therapeutic applications', *Nature Reviews Drug Discovery*, 4(3), pp. 255–260. Available at: https://doi.org/10.1038/nrd1662.

O'Brien Jr, W.D. (2007) 'Ultrasound{\textendash}biophysics mechanisms', *Progress in biophysics and molecular biology*, 93(1–3), pp. 212–255.

O'Donnell, M., Jaynes, E.T. and Miller, J.G. (1981) 'Kramers-kronig relationship between ultrasonic attenuation and phase velocity', *Journal of the Acoustical Society of America*, 69(3), pp. 696–701. Available at: https://doi.org/10.1121/1.385566.

Ouyang, J.F. and Bettens, R.P.A. (2015) 'Modelling water: A lifetime enigma', *Chimia*, 69(3), pp. 104–111. Available at: https://doi.org/10.2533/chimia.2015.104.

Oxtoby, D.W. and Kashchiev, D. (1994) 'A general relation between the nucleation work and the size of the nucleus in multicomponent nucleation', *The Journal of Chemical Physics*, 100(10), pp. 7665–7671. Available at: https://doi.org/10.1063/1.466859.

Pahk, K.J. *et al.* (2015) 'Ultrasonic histotripsy for tissue therapy', *Journal of Physics: Conference Series*, 581(1). Available at: https://doi.org/10.1088/1742-6596/581/1/012001.

Pahk, K.J. *et al.* (2016) 'A Novel Approach to Ultrasound-Mediated Tissue Decellularization and Intra-Hepatic Cell Delivery in Rats', *Ultrasound in Medicine and Biology*, 42(8), pp. 1958–1967. Available at: https://doi.org/10.1016/j.ultrasmedbio.2016.03.020.

Pahk, K.J. *et al.* (2017) 'Numerical and Experimental Study of Mechanisms Involved in Boiling Histotripsy', *Ultrasound in Medicine and Biology*, 43(12), pp. 2848–2861. Available at: https://doi.org/10.1016/j.ultrasmedbio.2017.08.938.

Pahk, K.J. *et al.* (2018) 'Bubble dynamics in boiling histotripsy', *Ultrasound in Medicine and Biology*, 44(12), pp. 2673–2696. Available at: https://doi.org/10.1016/j.ultrasmedbio.2018.07.025.

Pahk, Kisoo Joo *et al.* (2019) 'Boiling Histotripsy-induced Partial Mechanical Ablation Modulates Tumour Microenvironment by Promoting Immunogenic Cell Death of Cancers', *Scientific Reports*, 9(1), pp. 1–9. Available at: https://doi.org/10.1038/s41598-019-45542-z.

Pahk, Ki Joo *et al.* (2019) 'Mechanical damage induced by the appearance of rectified bubble growth in a viscoelastic medium during boiling histotripsy exposure', *Ultrasonics Sonochemistry*, 53(January), pp. 164–177. Available at: https://doi.org/10.1016/j.ultsonch.2019.01.001.

Pahk, K. J. *et al.* (2019) 'The effects of the size of a boiling bubble on lesion production in boiling histotripsy', in *Journal of Physics: Conference Series*. Available at: https://doi.org/10.1088/1742-6596/1184/1/012007.

Pahk, K J (2021) 'Control of the dynamics of a boiling vapour bubble using pressure-modulated high intensity focused ultrasound without the shock scattering effect: A first proof-of-concept study', *Ultrasonics Sonochemistry*, 77(May), p. 105699. Available at: https://doi.org/10.1016/j.ultsonch.2021.105699.

Pahk, K. J. (2021) 'Evidence of the formation of the shock scattering induced violent cavitation cluster during boiling histotripsy insonation: A numerical case study', in *Journal of Physics: Conference Series*. Available at: https://doi.org/10.1088/1742-6596/1761/1/012006.

Pahk, K.J. *et al.* (2021) 'The interaction of shockwaves with a vapour bubble in boiling histotripsy: The shock scattering effect', *Ultrasonics Sonochemistry*, 70(June 2020), p. 105312. Available at: https://doi.org/10.1016/j.ultsonch.2020.105312.

Paliwal, S. and Mitragotri, S. (2008) 'Therapeutic opportunities in biological responses of ultrasound', *Ultrasonics*, 48(4), pp. 271–278. Available at: https://doi.org/10.1016/j.ultras.2008.02.002.

Papadopoulou, V. *et al.* (2013) 'A critical review of physiological bubble formation in hyperbaric decompression', *Advances in Colloid and Interface Science*, 191–192, pp. 22–30. Available at: https://doi.org/10.1016/j.cis.2013.02.002.

Parsons, J.E. *et al.* (2006) 'Pulsed cavitational ultrasound therapy for controlled tissue homogenization', *Ultrasound in Medicine and Biology*, 32(1), pp. 115–129. Available at: https://doi.org/10.1016/j.ultrasmedbio.2005.09.005.

Peng, D.-Y. and Robinson, D.B. (1976a) 'A New Two-Constant Equation of State', *Industrial & Engineering Chemistry Fundamentals*, 15(1), pp. 59–64. Available at: https://doi.org/10.1021/i160057a011.

Peng, D.-Y. and Robinson, D.B. (1976b) 'A New Two-Constant Equation of State', *Industrial & Engineering Chemistry Fundamentals*, 15(1), pp. 59–64. Available at: https://doi.org/10.1021/i160057a011.

Pitzer, K.S. (1955) 'The Volumetric and Thermodynamic Properties of Fluids. I. Theoretical Basis and Virial Coefficients', *Journal of the American Chemical Society*, 77(13), pp. 3427–3433. Available at: https://doi.org/10.1021/ja01618a001.

Pitzer, K.S. *et al.* (1955) 'The Volumetric and Thermodynamic Properties of Fluids. II. Compressibility Factor, Vapor Pressure and Entropy of Vaporization', *Journal of the American Chemical Society*, 77(13), pp. 3433–3440. Available at: https://doi.org/10.1021/ja01618a002.

Plesset, M.S. (1949) 'The Dynamics of Cavitation Bubbles', *Journal of Applied Mechanics*, 16(3), pp. 277–282. Available at: https://doi.org/10.1115/1.4009975.

Plesset, M.S. and Chapman, R.B. (1971) 'Collapse of an initially spherical vapour cavity in the neighbourhood of a solid boundary', *Journal of Fluid*

Mechanics, 47(2), pp. 283–290. Available at: https://doi.org/10.1017/S0022112071001058.

Prosperetti, A. (1982) 'A generalization of the Rayleigh-Plesset equation of bubble dynamics', *Physics of Fluids*, 25(3), pp. 409–410. Available at: https://doi.org/10.1063/1.863775.

Rahman, M.A. and Saghir, M.Z. (2014) 'Thermodiffusion or Soret effect: Historical review', *International Journal of Heat and Mass Transfer*, 73, pp. 693–705. Available at: https://doi.org/10.1016/j.ijheatmasstransfer.2014.02.057.

Redlich, O. and Kwong, J.N.S. (1949) 'On the thermodynamics of solutions. V. An equation of state. Fugacities of gaseous solutions', *Chemical Reviews*, 44(1), pp. 233–244. Available at: https://doi.org/10.1021/cr60137a013.

Roberts, W.W. *et al.* (2006) 'Pulsed cavitational ultrasound: A noninvasive technology for controlled tissue ablation (histotripsy) in the rabbit kidney', *Journal of Urology*, 175(2), pp. 734–738. Available at: https://doi.org/10.1016/S0022-5347(05)00141-2.

Roberts, W.W. (2014) 'Development and translation of histotripsy: Current status and future directions', *Current Opinion in Urology*, pp. 104–110. Available at: https://doi.org/10.1097/MOU.0000000000000001.

Sankin, G.N. and Teslenko, V.S. (2003) 'Two-threshold cavitation regime', *Doklady Physics*, 48(12), pp. 665–668. Available at: https://doi.org/10.1134/1.1639433.

Sapozhnikov, O.A. (2015) 'High-intensity ultrasonic waves in fluids: Nonlinear propagation and effects', *Power Ultrasonics: Applications of High-Intensity Ultrasound*, (1971), pp. 9–35. Available at: https://doi.org/10.1016/B978-1-78242-028-6.00002-8.

Schade, G.R. *et al.* (2019) 'Boiling Histotripsy Ablation of Renal Cell Carcinoma in the Eker Rat Promotes a Systemic Inflammatory Response', *Ultrasound in Medicine and Biology*, 45(1), pp. 137–147. Available at: https://doi.org/10.1016/j.ultrasmedbio.2018.09.006.

Schmelzer, J.W.P., Abyzov, A.S. and Baidakov, V.G. (2017) 'Time of Formation of the First Supercritical Nucleus, Time-lag, and the Steady-State Nucleation Rate', *International Journal of Applied Glass Science*, 8(1), pp. 48–60. Available at: https://doi.org/10.1111/ijag.12243.

Schmelzer, J.W.P. and Baidakov, V.G. (2016) 'Comment on "Simple improvements to classical bubble nucleation models"', *Physical Review E*, 94(2), p. 026801. Available at: https://doi.org/10.1103/PhysRevE.94.026801.

Schuster, T.G. *et al.* (2018) 'Histotripsy Treatment of Benign Prostatic Enlargement Using the Vortx Rx System: Initial Human Safety and Efficacy Outcomes', *Urology*, 114, pp. 184–187. Available at: https://doi.org/10.1016/j.urology.2017.12.033.

Siedek, F., Yeo, S.Y., Heijman, E., Grinstein, O., Bratke, G., Heneweer, C., Puesken, M., Persigehl, T., Maintz, D. and Grüll, H. (2019) 'Magnetic Resonance-Guided High-Intensity Focused Ultrasound (MR-HIFU): Overview of Emerging Applications (Part 2)', *RoFo Fortschritte auf dem Gebiet der Rontgenstrahlen und der Bildgebenden Verfahren*. Georg Thieme Verlag, pp. 531–539. Available at: https://doi.org/10.1055/a-0817-5686.

Siedek, F., Yeo, S.Y., Heijman, E., Grinstein, O., Bratke, G., Heneweer, C., Puesken, M., Persigehl, T., Maintz, D. and Grull, H. (2019) 'Magnetic Resonance-Guided High-Intensity Focused Ultrasound (MR-HIFU): Technical Background and Overview of Current Clinical Applications (Part 1)', *RoFo Fortschritte auf dem Gebiet der Rontgenstrahlen und der Bildgebenden Verfahren*. Georg Thieme Verlag, pp. 522–530. Available at: https://doi.org/10.1055/a-0817-5645.

Skripov Kondor Reuven. Slutzkin Dinah., V.P. (1974) *Metastable liquids*. New York; Chichester; Jerusalem; London: Wiley ; Israel Program for Scientific Translations.

Soneson, J.E. (2009) 'A user-friendly software package for HIFU simulation', in *AIP Conference Proceedings*, pp. 165–169. Available at: https://doi.org/10.1063/1.3131405.

Soneson, J.E. (2017) ‘Extending the Utility of the Parabolic Approximation in Medical Ultrasound Using Wide-Angle Diffraction Modeling’, *IEEE Transactions on Ultrasonics, Ferroelectrics, and Frequency Control*, 64(4), pp. 679–687. Available at: https://doi.org/10.1109/TUFFC.2017.2654125.

Speedy, R.J. (1982) ‘Stability-limit conjecture. An interpretation of the properties of water’, *Journal of Physical Chemistry*, 86(6), pp. 982–991. Available at: https://doi.org/10.1021/j100395a030.

Speedy, R.J. (2002) ‘Limits of Stability for Liquids Under Tension’, in *Liquids Under Negative Pressure*, pp. 1–12. Available at: https://doi.org/10.1007/978-94-010-0498-5_1.

Strasberg, M. (1959) ‘Onset of Ultrasonic Cavitation in Tap Water’, *Journal of the Acoustical Society of America*, 31(2), pp. 163–176. Available at: https://doi.org/10.1121/1.1907688.

Stride, E. and Saffari, N. (2003) ‘Microbubble ultrasound contrast agents: A review’, *Proceedings of the Institution of Mechanical Engineers, Part H: Journal of Engineering in Medicine*, 217(6), pp. 429–447. Available at: https://doi.org/10.1243/09544110360729072.

Styn, N. *et al.* (2011) ‘Histotripsy homogenization of the prostate: Thresholds for cavitation damage of periprostatic structures’, *Journal of Endourology*, 25(9), pp. 1531–1535. Available at: https://doi.org/10.1089/end.2010.0648.

Takaishi, Y. (1997) ‘New IAPWS Releases on Surface Tensions of Ordinary Water and Heavy Water Substances’, *Review of High Pressure Science and Technology/Koatsuryoku No Kagaku To Gijutsu*, 6(1), pp. 46–51. Available at: https://doi.org/10.4131/jshpreview.6.46.

Tomita, H. *et al.* (2009) ‘Direct observation of single bubble cavitation damage for MHz cleaning’, *Solid State Phenomena*, 145–146, pp. 3–6. Available at: https://doi.org/10.4028/www.scientific.net/SSP.145-146.3.

Turkevich, L.A. and Mann, J.A. (1990) 'Pressure Dependence of The Interfacial Tension between Fluid Phases. 1. Formalism and Application to Simple Fluids', *Langmuir*, 6(2), pp. 445–456. Available at: https://doi.org/10.1021/la00092a027.

Vehkamäki, H. (2006) *Classical nucleation theory in multicomponent systems*. 1st edn, *Classical Nucleation Theory in Multicomponent Systems*. 1st edn. Berlin: Springer Berlin Heidelberg. Available at: https://doi.org/10.1007/3-540-31218-8.

Vlaisavljevich, E. *et al.* (2013) 'Image-guided non-invasive ultrasound liver ablation using histotripsy: Feasibility study in an invivo porcine model', *Ultrasound in Medicine and Biology* [Preprint]. Available at: https://doi.org/10.1016/j.ultrasmedbio.2013.02.005.

Vlaisavljevich, E. *et al.* (2014) 'Effects of tissue mechanical properties on susceptibility to histotripsy-induced tissue damage', *Physics in Medicine and Biology*, 59(2), pp. 253–270. Available at: https://doi.org/10.1088/0031-9155/59/2/253.

Vlaisavljevich, E., Xu, Z., *et al.* (2015) 'Effects of thermal preconditioning on tissue susceptibility to histotripsy', *Ultrasound in Medicine and Biology*, 41(11), pp. 2938–2954. Available at: https://doi.org/10.1016/j.ultrasmedbio.2015.07.016.

Vlaisavljevich, E., Lin, K.W., *et al.* (2015) 'Effects of tissue stiffness, ultrasound frequency, and pressure on histotripsy-induced cavitation bubble behavior', *Physics in Medicine and Biology*, 60(6), pp. 2271–2292. Available at: https://doi.org/10.1088/0031-9155/60/6/2271.

Vlaisavljevich, E. (2015) 'Investigations of the Cavitation and Damage Thresholds of Histotripsy and Applications in Targeted Tissue Ablation', *ProQuest Dissertations and Theses*, p. 436. Available at: https://search.proquest.com/docview/1728125368?accountid=10394%0Ahttp://linksource.ebsco.com/linking.aspx?sid=ProQuest+Dissertations+%26+Theses+Global&fmt=dissertation&genre=dissertations+%26+theses&issn=&volume=&issue=&date=2015-01-01&spage=&title=Invest.

Vlaisavljevich, E., Aydin, O., *et al.* (2015) 'The role of positive and negative pressure on cavitation nucleation in nanodroplet-mediated histotripsy', *Physics in Medicine and Biology*, 61(2), pp. 663–682. Available at: https://doi.org/10.1088/0031-9155/61/2/663.

Vlaisavljevich, E. *et al.* (2016) 'Effects of Temperature on the Histotripsy Intrinsic Threshold for Cavitation', *IEEE Transactions on Ultrasonics, Ferroelectrics, and Frequency Control*, 63(8), pp. 1064–1077. Available at: https://doi.org/10.1109/TUFFC.2016.2565612.

Vlaisavljevich, E. *et al.* (2017) 'Effects of f-number on the histotripsy intrinsic threshold and cavitation bubble cloud behavior', *Physics in Medicine and Biology*, 62(4), pp. 1269–1290. Available at: https://doi.org/10.1088/1361-6560/aa54c7.

Wagner, W. and Pruß, A. (2002) 'The IAPWS formulation 1995 for the thermodynamic properties of ordinary water substance for general and scientific use', *Journal of Physical and Chemical Reference Data*, 31(2), pp. 387–535. Available at: https://doi.org/10.1063/1.1461829.

Wang, Y.-N. *et al.* (2013) 'Histological and Biochemical Analysis of Mechanical and Thermal Bioeffects in Boiling Histotripsy Lesions Induced by High Intensity Focused Ultrasound', *Ultrasound in Medicine & Biology*, 39(3), pp. 424–438. Available at: https://doi.org/10.1016/j.ultrasmedbio.2012.10.012.

Wang, Y.-N. *et al.* (2014) 'Tissue decellularization with boiling histotripsy and the potential in regenerative medicine', *The Journal of the Acoustical Society of America*, 136(4), pp. 2278–2278. Available at: https://doi.org/10.1121/1.4900233.

Wang, Y.N. *et al.* (2018) 'Mechanical decellularization of tissue volumes using boiling histotripsy', *Physics in Medicine and Biology*, 63(23), p. 235023. Available at: https://doi.org/10.1088/1361-6560/aaef16.

Ward, M. and Wu, J. (1999) 'Ultrasound-induced cell lysis and sonoporation enhanced by contrast agents', *The Journal of the Acoustical Society of America*, 106(4), pp. 2230–2230. Available at: https://doi.org/10.1121/1.427585.

Waters, K.R. *et al.* (2000) 'On the applicability of Kramers–Krönig relations for ultrasonic attenuation obeying a frequency power law', *The Journal of the Acoustical Society of America*, 108(2), pp. 556–563. Available at: https://doi.org/10.1121/1.429586.

Wilemski, G. (1983) 'Composition of the critical nucleus in multicomponent vapor nucleation', *The Journal of Chemical Physics*, 80(3), pp. 1370–1372. Available at: https://doi.org/10.1063/1.446822.

Williams, A.R. (1986) 'In vitro biological effects of ultrasound', *Ultrasound in Medicine and Biology*, 12(9), pp. 685–686. Available at: https://doi.org/10.1016/0301-5629(86)90278-4.

Williams, R.P. *et al.* (2023) 'The histotripsy spectrum: differences and similarities in techniques and instrumentation', *International Journal of Hyperthermia*. Available at: https://doi.org/10.1080/02656736.2023.2233720.

Wu, J. and Nyborg, W.L. (2008) 'Ultrasound, cavitation bubbles and their interaction with cells', *Advanced Drug Delivery Reviews*, 60(10), pp. 1103–1116. Available at: https://doi.org/10.1016/j.addr.2008.03.009.

Xu, J. *et al.* (2014) 'Dependence of ablative ability of high-intensity focused ultrasound cavitation-based histotripsy on mechanical properties of agar', *The Journal of the Acoustical Society of America*, 136(6), pp. 3018–3027. Available at: https://doi.org/10.1121/1.4898426.

Xu, J., Bigelow, T.A. and Lee, H. (2013) 'Effect of pulse repetition frequency and scan step size on the dimensions of the lesions formed in agar by HIFU histotripsy', *Ultrasonics*, 53(4), pp. 889–896. Available at: https://doi.org/10.1016/j.ultras.2012.12.011.

Xu, Z. *et al.* (2003) 'Controlled ultrasound tissue erosion', *Proceedings of the IEEE Ultrasonics Symposium*, 1(6), pp. 732–735. Available at: https://doi.org/10.1109/tuffc.2004.1304271.

Xu, Z., Fowlkes, J.B., Rothman, E.D., *et al.* (2005) 'Controlled ultrasound tissue erosion: The role of dynamic interaction between insonation and

microbubble activity', *The Journal of the Acoustical Society of America*, 117(1), pp. 424–435. Available at: https://doi.org/10.1121/1.1828551.

Xu, Z., Fowlkes, J.B., Ludomirsky, A., *et al.* (2005) 'Investigation of intensity thresholds for ultrasound tissue erosion', *Ultrasound in Medicine and Biology*, 31(12), pp. 1673–1682. Available at: https://doi.org/10.1016/j.ultrasmedbio.2005.07.016.

Xu, Z. *et al.* (2006) 'High speed imaging of bubble clouds in pulsed cavitational ultrasound therapy - Histotripsy', in *Proceedings - IEEE Ultrasonics Symposium*. IEEE, pp. 293–296. Available at: https://doi.org/10.1109/ULTSYM.2006.86.

Xu, Z. *et al.* (2007) 'High speed imaging of bubble clouds generated in pulsed ultrasound cavitational therapy - Histotripsy', *IEEE Transactions on Ultrasonics, Ferroelectrics, and Frequency Control*, 54(10), pp. 2091–2101. Available at: https://doi.org/10.1109/TUFFC.2007.504.

Yount, D.E. (1979) 'Skins of varying permeability: A stabilization mechanism for gas cavitation nuclei', *Journal of the Acoustical Society of America*, 65(6), pp. 1429–1439. Available at: https://doi.org/10.1121/1.382930.

Yount, D.E., Gillary, E.W. and Hoffman, D.C. (1984) 'A microscopic investigation of bubble formation nuclei', *Journal of the Acoustical Society of America*, 76(5), pp. 1511–1521. Available at: https://doi.org/10.1121/1.391434.

Yuldashev, P. V., Mezdrokhin, I.S. and Khokhlova, V.A. (2018) 'Wide-Angle Parabolic Approximation for Modeling High-Intensity Fields from Strongly Focused Ultrasound Transducers', *Acoustical Physics*, 64(3), pp. 309–319. Available at: https://doi.org/10.1134/S1063771018030168.

Zeldovich, Y.B. (2015) '10. On the Theory of New Phase Formation. Cavitation', in R.A. Sunyaev (ed.) *Selected Works of Yakov Borisovich Zeldovich, Volume I*. Princeton: Princeton University Press, pp. 120–137. Available at: https://doi.org/10.1515/9781400862979.120.

Zhang, X. *et al.* (2015) 'Noninvasive thrombolysis using histotripsy beyond the intrinsic threshold (microtripsy)', *IEEE Transactions on Ultrasonics, Ferroelectrics, and Frequency Control*, 62(7), pp. 1342–1355. Available at: https://doi.org/10.1109/TUFFC.2015.007016.

Appendix 1: MATLAB Code

Appendix 1: MATLAB Code

The MATLAB code in this thesis is available online for review and replication of the results presented in this thesis. The code is hosted on UCL's OneDrive platform, accessible via the following link:

https://liveuclac-my.sharepoint.com/:f:/g/personal/ucemoli_ucl_ac_uk/En4-UBx5b45EtLedUZ60QWEBr6ARmddK4hx-czLMcVol2g?e=6kSjBL

Please note that the folder is set to 'view only' to ensure the integrity of the code.